Freie Universität Berlin

Dissertation

The Shkoder Peja Normal Fault system at the Dinaric-Hellenic Junction: a structural and thermochronological study

vorgelegt von

Marc Ulrich Grund

Zur Erlangung des Doktorgrades der Naturwissenschaften (Dr. rer. nat.) im

Fachbereich Geowissenschaften

Institut für Geologische Wissenschaften

Fachrichtung Tektonik und Sedimentäre Systeme

Publikationsort: Berlin
Einreichung der Dissertation: 29.11.2022
Die Disputation erfolgte am 10.03.2023 in Berlin-Lankwitz.

28th April 2018, sunset at Mt. Cukali (1721 m), Albania

“Chi va piano va sano e va lontano”

“Those who go slowly go healthy and get ahead”

Eidesstattliche Erklärung

Hiermit erkläre ich, Marc Ulrich Grund, dass diese Doktorarbeit mit dem Titel „The Shkoder Peja Normal Fault system at the Dinaric-Hellenic Junction: a structural and thermochronological study“ ausschließlich auf Grundlage der angegebenen Hilfsmittel und Hilfen selbstständig von mir verfasst wurde. Die Rolle von mir als Autor/Co-Autor in den in dieser Arbeit enthaltenen Manuskripten ist im Kapitel „Organization of the thesis“ erläutert. Die Arbeit wurde nicht in einem früheren Promotionsverfahren eingereicht.

Diese Arbeit wurde vom Promotionsausschuss des Fachbereichs Geowissenschaften

am 06.12.2022 zum Promotionsverfahren zugelassen.

Erstgutachter: Prof. Dr. Mark R. Handy

Zweitgutachter: Prof. Dr. Kamil Ustaszewski

Weitere Mitglieder des Betreuungsteams:

Dr. Jörg Giese

Dr. Lorenzo Gemignani

Dr. Jan Pleuger

Die Disputation erfolgte am 10.03.2023.

Berlin, den 14.04.2023

Marc Ulrich Grund

Abstract

This doctoral thesis presents new thermochronological and thermometric data, cross-sections, and plate reconstructions on the kinematics and age of orogen-parallel extension and arc formation, as well as studies of basin and landscape evolution at the junction of the Dinaric and Hellenic orogens.

The Dinaric-Hellenic mountain belt bends some 30° where two fault systems transect the orogen: (1) the Shkoder-Peja Normal Fault system (SPNF); (2) the Shkoder Peja Transfer Zone (SPTZ) that dextrally offsets the Dinaric-Hellenic nappes by ~75 km. The SPNF is a composite structure that cuts Dinaric folds and nappe contacts. It comprises four segments that were active under ductile-brittle conditions and downthrow the West Vardar Ophiolite in the hanging wall while exhuming two domes with anchizonal-to-lower greenschist-facies metamorphism in the footwall.

Peak-metamorphic temperatures of ~280°C from RSCM (Raman spectroscopy of carbonaceous matter) analysis of the mélange of the ophiolite nappe atop the Dinaric nappe stack were attained during obduction in latest Jurassic-Early Cretaceous time, followed by cooling of the ophiolithic mélange to <180°C ((U/Th)-He zircon ages; ZHe) in Cretaceous (~125-100 Ma) time. The offset of the ophiolite front along the SPTZ is attributed to re-activation of an Early Mesozoic rift transfer zone in the Adriatic margin during Eocene subduction of the Pindos Ocean. This subduction involved a clockwise rotation of the Hellenides with respect to the Dinarides around a pole at the NW end of the then-existing Krasta-Cukali basin.

Stratigraphic criteria indicate that thrusting and nappe stacking beneath the emplaced ophiolite in the Internal Dinarides initiated in Late Cretaceous time. Contours of peak temperature in the nappe stack cross the thrust contacts, with a maximum temperature of ~460°C reached in the Decani Dome, in the footwall of the SPNF. The arcuate peak-temperature contours around the perimeter of the dome indicate that the attainment of peak-temperatures pre-dates Decani doming. There, the nappes underwent extensional mylonitic shearing (~300-350°C) and cooling to < 240°C at ~70 Ma (zircon fission track ages; ZFT) at temperatures somewhat less than those attained in the dome itself. This suggests that doming and extensional mylonitic shearing were broadly coeval. This attributes to extension in a back-arc setting to the east of the then-active accretion-subduction front. This first pulse of doming and extension at the Dinaric-Hellenic junction in the Late Cretaceous (80-70 Ma) occurred in the upper plate of the SW-propagating orogenic front.

Nappe stacking in the External Dinarides continued throughout Middle Eocene to Early Oligocene time according to stratigraphic criteria. Peak-temperatures in the External Dinaric nappes were lower (~180-280°C) than in the Internal Dinarides and correspond to a burial depth of ~6-10 km. Peak temperatures were attained after nappe stacking and the formation of the Cukali Dome in the SW footwall of the SPNF, as contours here transect both the nappe contacts and the Cukali Dome. Cooling below ~180°C (57-43 Ma, ZHe) and ~110°C (35-21 Ma, apatite fission track ages) suggests that the Dinaric nappes cooled slowly after Early Eocene time.

The two prominent Decani and Cukali Domes locate in the SPNF footwall and are accompanied by their segments: the Cukali-Tropoja Fault and the Decani Shear Zone, whereas the latter represents the oldest SPNF part that hosts the aforementioned Decani Dome in its footwall. The Cukali-Tropoja Fault and a late ductile-brittle phase of the Decani Shear Zone formed during a post-nappe stacking phase of orogen-parallel extension and clockwise rotation, with a minimum of ~2500 m vertical offset. Extension north of the SPNF is attributed to detachment of part of the Adriatic slab beneath the internal Dinarides that triggered magmatism, core complex formation and uplift.

The second pulse of SPNF doming and extension occurred sometime between 32 and 16 Ma, and is attributed to rollback subduction of the untorn part of the Adriatic slab beneath the Hellenides towards the SW. This phase involved localized subsidence of Neogene basins at the Dinaric-Hellenic junction coupled with accelerated post-Paleogene clockwise oroclinal bending. However slower cooling (3.0-3.2°C/Ma) in vicinity to the Dinaric-Hellenic junction after Eocene time corresponds to an average denudation rate of 0.1-0.2 mm/yr, equivalent to removal of ~1.6–3.2 km of overburden since ~16 Ma. Faster, tectonically induced cooling and denudation at shorter timescales is possible, but beyond the detectability of our applied methods.

The Dukagjini Fault, with about ~1000 m vertical throw, now covered by Pliocene sediments, represents the youngest segment of the SPNF and is largely responsible for the formation of the Western Kosovo Basin, as evidenced by the oldest Middle Miocene syntectonic sediments in the basin.

To bridge the gap between the Neogene uplift, exhumation and deformation history of the Dinaric-Hellenic junction and the influence of the SPNF on the recent landscape evolution, the sediments of the sedimentary basins preserved today and the present-day geomorphology were analyzed. Analysis of fluvial morphology of the Drin River system reveals higher values of river slope indices ($k$sn) and χ (Chi) between the SPNF and the Drin drainage divide. The drainage divide is predicted to be migrating away from the SPNF, except at its NE end. The Western Kosovo Basin and Tropoja Basin contain flat-lying late Pliocene-to-Holocene sedimentary rocks deposited well after the main fault activity and immediately after the LGM. These layers document an early Pleistocene transition from lacustrine to fluvial conditions that reflects a sudden change from internal to external drainage of paleo-lakes. In the Tropoja Basin these layers were incised to form three generations of river terraces, interpreted to reflect episodic downstream incision during re-organization of the paleo-Drin River drainage system. ^{36}Cl-cosmogenic-nuclide depth-profile ages of the two youngest of these terraces (~12 and ~8 ka) correlate with periods of wetter climate and increased sediment transport in post-LGM time. The incision rate (~12 mm/yr) is significantly greater than reported in central and southern Albania. Thus, glacial/interglacial climatic variability, hinterland erosion and baselevel changes appear to have regulated basin filling and excavation cycles when the rivers draining the basins became part of the river network emptying into the Adriatic Sea. These dramatic morphological changes occurred long after SPNF related normal faulting. However, the SPNF provided a structural and erosional template upon which climate-induced erosion in Holocene time effected reorganization of the regional drainage pattern. The arc of the main drainage divide around the SPNF deviates from the general coincidence of this divide with the NW-SE trend of the Dinaric-Hellenic mountain chain. This arc encompasses the morphological imprint left by the rollback subduction of the Adriatic plate beneath the northwestern Hellenides, and thus represents a witness to the structural evolution of the Dinaric-Hellenic junction, which began over 100 million years ago and is still evident in the landscape today.

Zusammenfassung

In dieser Dissertation werden neue thermochronologische und thermometrische Daten, Profilschnitte und Plattenrekonstruktionen zur Kinematik und zum Alter der orogenparallelen Ausdehnung und Bogenbildung sowie Untersuchungen zur Becken- und Landschaftsentwicklung an der Nahtstelle des Dinarisch-Hellenischen Orogens vorgestellt.

Der dinarisch-hellenische Gebirgsgürtel ist um etwa 30° gekrümmt, wo zwei Störungssysteme das Orogen durchschneiden: (1) das Shkoder-Peja Normal Fault System (SPNF); (2) die Shkoder-Peja Transfer Zone (SPTZ), die die dinarisch-hellenischen Deckenstapel um etwa 75 km dextral versetzt. Die SPNF ist eine zusammengesetzte Struktur, die dinarische Falten und Deckenkontakte schneidet. Sie umfasst vier Segmente, die unter duktil-spröden Bedingungen aktiv waren und den West Vardar Ophiolite im Hangenden abschieben, während sie zwei Dome mit anchizonaler bis niedriggradigen grünschieferfazieller Metamorphose im Liegenden exhumieren.

Nach RSCM-Analysen (Raman spectroscopy of carbonaceous matter) wurden während der Obduktion im späten Jura und in der frühen Kreidezeit maximale Metamorphosetemperaturen von ~ 280 °C in in der Mélange des Ophioliten über dem dinarischen Deckenstapel erreicht, gefolgt von einer Abkühlung der ophiolithischen Mélange auf <180 °C ((U/Th) -He-Zirkonalter; ZHe) in der Kreidezeit (~125-100 Ma). Der Versatz der Ophiolith-Front entlang der SPTZ wird auf die Reaktivierung einer frühmesozoischen Rift-Transferzone am adriatischen Kontinentalrand während der eozänen Subduktion des Pindos-Ozeans zurückgeführt. Bei dieser Subduktion rotierten die Helleniden gegenüber den Dinariden im Uhrzeigersinn um einen Pol am nordwestlichen Ende des damals existierenden Krasta-Cukali-Beckens.

Stratigraphische Kriterien deuten darauf hin, dass die Überschiebung und die Deckenstapelung unter dem Ophiolit in den inneren Dinariden in der späten Kreidezeit begann. Die Konturen der Spitzentemperaturen im Deckenstapel schneiden die Überschiebungskontakte, wobei die Höchsttemperatur von ~460°C im Decani-Dom im Liegenden der SPNF erreicht wird. Die bogenförmigen Konturen der Spitzentemperaturen um den Dom herum weisen darauf hin, dass das Erreichen der Spitzentemperaturen vor der Aufdomung geschah. Dort erfuhren die Decken Dehnung und eine mylonitische Scherung (~300-350°C) sowie eine Abkühlung auf < 240°C bei ~70 Ma (Zirkonspaltspurenalter; ZFT) bei Temperaturen, die etwas niedriger waren als die im Dom selbst erreicht wurden. Das deutet darauf hin, dass die Aufdomung und die mylonitische Scherung im Großen und Ganzen zeitgleich stattfanden. Dies ist auf die Ausdehnung in einem Back-Arc-Setting östlich der damals aktiven Akkretions- und Subduktionsfront zurückzuführen. Dieser erste Impuls von Aufdomung und Extension am dinarisch-hellenischen Übergang in der späten Kreidezeit (80-70 Ma) fand in der oberen Platte der nach SW propagierenden Orogenesefront statt.

Die Deckenstapelung in den äußeren Dinariden setzte sich nach stratigraphischen Kriterien während des gesamten mittleren Eozäns bis zum frühen Oligozän fort. Die Spitzentemperaturen in den äußeren Dinariden waren niedriger (~180-280°C) als in den inneren Dinariden und entsprechen einer Versenkungstiefe von ~6-10 km. Die Spitzentemperaturen wurden nach der Stapelung der Decken und der Bildung des Cukali-Doms im SW Hangendblock der SPNF erreicht, da die Konturen hier sowohl die Deckenkontakte als auch den Cukali-Dom durchschneiden. Die Abkühlung unter ~180°C (57-43 Ma, ZHe) und ~110°C (35-21 Ma, Apatitspaltspurenalter) deutet darauf hin, dass die dinarischen Decken nach dem frühen Eozän langsam abkühlten.

Die beiden markanten Decani- und Cukali-Dome befinden sich im Liegenden der SPNF und werden von ihren Segmenten begleitet: der Cukali-Tropoja-Störung und der Decani-Scherzone, wobei letztere den ältesten Teil des SPNF darstellt, die den bereits erwähnten Decani-Dome in ihrem Liegenden beherbergt. Die Cukali-Tropoja-Störung und eine späte duktil-spröde Phase der Decani-Scherzone bildeten sich während einer post-

Deckenstapelungsphase mit orogenparalleler Ausdehnung und Rotation im Uhrzeigersinn, mit einem Minimum von ~2500 m vertikalem Versatz. Die Ausdehnung weiter nördlich der SPNF wird auf die Ablösung eines Teils der adriatischen Platte unter den inneren Dinariden zurückgeführt, die Magmatismus, Kernkomplexbildung und Hebung auslöste.

Der zweite Impuls der SPNF-Aufdomung und Ausdehnung fand irgendwann zwischen 32 und 16 Ma statt und wird der Rollback-Subduktion des nicht abgerissenen Teils der adriatischen Platte unter den Helleniden in Richtung SW zugeschrieben. In dieser Phase kam es zu einer lokalen Absenkung der neogenen Becken an der dinarischen und hellenischen Grenze in Verbindung mit einer beschleunigten postpaläogenen orogenen Biegung und Rotation im Uhrzeigersinn. Die langsamere Abkühlung (3,0-3,2°C/Ma) in der Nähe des dinarisch-hellenischen Übergangs nach dem Eozän entspricht einer durchschnittlichen Denudationsrate von 0,1-0,2 mm/Jahr, was einer Abtragung von ~1,6-3,2 km Deckgebirge seit ~16 Ma entspricht. Eine schnellere, tektonisch bedingte Abkühlung und Denudation auf kürzeren Zeitskalen ist möglich, liegt aber außerhalb der Nachweisbarkeit unserer angewandten Methoden.

Die Dukagjini-Störung mit einem vertikalen Versatz von etwa 1000 m, die heute von pliozänen Sedimenten bedeckt ist, stellt das jüngste Segment des SPNF dar und ist weitgehend für die Bildung des westlichen Kosovo-Beckens (Western Kosovo Basin) verantwortlich, was die ältesten syntektonischen Sedimente aus dem mittleren Miozän in diesem Becken belegen.

Um die Lücke zwischen der neogenen Hebungs-, Exhumierungs- und Deformationsgeschichte des dinarisch-hellenischen Übergangs und dem Einfluss des SPNF auf die jüngste Landschaftsentwicklung zu schließen, wurden die Ablagerungen der heute erhaltenen Sedimentbecken und die heutige Geomorphologie analysiert. Die Analyse der Flussmorphologie des Drin-Flusssystems zeigt höhere Werte der Flussneigungsindizes (ksn) und χ (Chi) zwischen dem SPNF und der Drin-Wasserscheide. Es wird vorhergesagt, dass sich die Wasserscheide von der SPNF wegbewegt, außer an ihrem nordöstlichen Ende. Das westliche Kosovo-Becken und das Tropoja-Becken enthalten flachliegende Sedimentgesteine aus dem späten Pliozän bis Holozän, die lange nach der Hauptverwerfungsaktivität der SPNF und unmittelbar nach dem LGM abgelagert wurden. Diese Schichten dokumentieren einen frühpleistozänen Übergang von lakustrinen zu fluvialen Bedingungen, der einen plötzlichen Wechsel von interner zu externer Entwässerung von Paläoseen widerspiegelt. Im Tropoja-Becken wurden diese Schichten so eingeschnitten, dass sie drei Generationen von Flussterrassen bildeten, was als Ausdruck eines episodischen Einschnitts flussabwärts während der Reorganisation des Paläo-Drin-Flusses interpretiert wird. Die 36Cl-Kosmogen-Nuklid-Tiefenprofil-Alter der beiden jüngsten dieser Terrassen (~12 und ~8 ka) korreliert mit Perioden feuchteren Klimas und erhöhtem Sedimenttransport in der Zeit nach dem LGM. Die Einschnittrate (~12 mm/Jahr) ist deutlich höher als in Zentral- und Südalbanien. Somit scheinen glaziale/interglaziale Klimaschwankungen, Erosion im Hinterland und Änderungen des Meeresspiegels die Zyklen der Beckenfüllung und -aushebung gesteuert zu haben, als die Flüsse, die die Becken entwässern, Teil des Flussnetzes wurden das in die Adria mündet. Diese dramatischen morphologischen Veränderungen traten lange nach der SPNF-bedingten Abschiebungsaktivität auf. Die SPNF bildete somit eine strukturelle und erosive Vorlage bzw. Schablone, auf der die klimabedingte Erosion im Holozän eine Neuordnung des regionalen Entwässerungsmusters bewirkte. Der Bogen der Hauptwasserscheide um die SPNF weicht von der allgemeinen Koinzidenz dieser Wasserscheide mit dem NW-SO-Trend der dinarischen und hellenischen Gebirgskette ab. Dieser Bogen umfasst den morphologischen Abdruck, den die Rollback-Subduktion der adriatischen Platte unter den nordwestlichen Helleniden hinterlassen hat, und ist somit ein Zeuge der strukturellen Entwicklung des dinarisch-hellenischen Übergangs, die vor über 100 Millionen Jahren begann und noch heute in der Landschaft sichtbar ist.

Abstrakt

Kjo tezë doktorature paraqet të dhëna të reja lidhur me termokronologjinë dhe termometrinë, prerjet gjeologjike, rindërtimin e kinematikës së pllakave si dhe moshën e shtrirjes dhe të harkimit të orogjenit-paralel, si dhe mbi evolucionin e basenit dhe peisazhit në pjesën e bashkimit të orogjenit Dinarid dhe atij Helenid.

Brezi malor Dinarid-Helenid përkulet me rreth 30° dhe dy sisteme prishjesh e përshkojnë orogjenin: (1) sistemi i prishjes normale Shkodër-Pejë (Shkoder-Peja Normal Fault system SPNF); (2) zona e transferimit të Shkodër-Pejës (Shkoder Peja Transfer Zone SPTZ) e cila ekuilibron djathtas napën Dinarido-Helenide me ~75 km. SPNF është një strukturë e përbërë që pret rrudhat Dinaride dhe kontaktet e napës. Ai përfshin katër segmente që kanë qenë aktivë në kushte duktile-të brishtë dhe "kanë hedhur" ofiolitin e Vardarit Perëndimor në "murin" e krijuar, gjatë kohës që zhvarroseshin dy kupola me facie metamorfike të tipit ankizonal-shiste të gjelbra në pjesën e poshtme.

Temperaturat e pikut metamorfik prej ~ 280°C nga analizat RSCM (spektroskopia Raman e lëndës karbonike) e melanzhit të napës ofiolitike, në kulmin e napës Dinaride u arritën gjatë obduksionit në fund të Jurasik-Kretak i Hershëm, e ndjekur nga ftohja e melanzhit ofiolitik në <180°C ((U/Th)-He mosha e zirkonit; ZHe) në Kretak (~125-100 milionë vjet). Kompensimi i frontit të ofiolitit përgjatë SPTZ i atribuohet riaktivizimit të një zone rifti në skajin e Adriatikut gjatë Mesozoit të Hershëm, në subduksionin e Eocenit të Oqeanit Pindos. Ky subduksion përfshinte një rrotullim të Helenideve në drejtim orar në lidhje me Dinaridet rreth një poli në skajin veriperëndimor të basenit të atëhershëm të Krasta-Cukalit.

Kriteri stratigrafik tregon se hipja dhe grumbullimi i napës nën ofiolitin e vendosur në Dinaridet e Brendshme filloi gjatë Kretakut të vonshëm. Konturet e temperaturës së pikut në napë gjenden në kontaktet e hipjes, me një temperaturë maksimale prej ~460°C , e arritur në Kupolën e Deçanit, në pjesën e poshtme të SPNF. Konturet të temperaturës së pikut në hark, rreth perimetrit të kupolës tregojnë se temperaturat e pikut janë arritur para Kupolës së Deçanit. Atje, napa iu nënshtrua *extensional mylonitic shearing* (~ 300-350 ° C) dhe ftohjes në < 240 °C në ~ 70 milionë vjet (mosha e përcaktuar nëpërmjet gjurmës së ndarjes së zirkonit; ZFT) në temperatura disi më të ulëta se ato të arritura në kupolë. Kjo sugjeron se krijimi i kupolës dhe *extensional mylonitic shearing* kanë qenë bashkëkohore. Ne ia atribuojmë ato shtrirjes në një mjedis të tipit *back-arc* (pas harkor) në lindje të frontit aktiv të grumbullim-subduksionit të atëhershëm. Ky puls i parë për krijimin e kupolës dhe shtrirjes në bashkimin Dinarido-Helenid në Kretakun e vonshëm (80-70 milionë vjet) ndodhi në pllakën e sipërme të frontit orogjenik që përhapet në SW.

Grumbullimi i napës në Dinaridet e Jashtme vazhdoi gjatë gjithë Eocenit të Mesëm deri në Oligocenin e Hershëm duke u bazuar në kriterin stratigrafik. Temperaturat e pikut në napën e jashtme Dinaride ishin më të ulëta (~180-280°C) në krahasim me Dinaridet e Brendshme dhe korrespondojnë me një thellësi groposjeje prej ~ 6-10 km. Temperaturat e pikut u arritën pas grumbullimit të napës dhe formimit të kupolës së Cukalit në pjesën e poshtme jugperëndimore të SPNF, pasi konturet këtu presin si kontaktet e napës ashtu edhe Kupolën e Cukalit. Ftohja nën ~ 180°C (57-43 milionë vjet, ZHe) dhe ~ 110°C (35-21 milionë vjet, moshat sipas gjurmës së ndarjes së apatitit) sugjeron që napa Dinaride u ftoh ngadalë pas Eocenit të Hershëm.

Dy kupolat e spikatura të Deçanit dhe Cukalit ndodhen në pjesën e poshtme të SPNF dhe shoqërohen nga segmentet e tyre: prishja Cukal-Tropojë dhe *shear zone* e Deçanit, ndërsa kjo e fundit përfaqëson pjesën më të vjetër të SPNF dhe në pjesën e poshtme të saj gjendet Kupola e lartpërmendur e Deçanit. Prishja e Cukal-Tropojës dhe një fazë e mëvonshme duktile-e brishtë e *shear-zone* së Deçanit u formuan gjatë një faze grumbullimi post-napë të zgjerimit orogjen-paralel *(orogen-parallel extension)* dhe rrotullimit në drejtim orar,

me një zhvendosje vertikale minimale prej ~2500 m. Zgjerimi në veri të SPNF i atribuohet shkëputjes së një pjese të pllakës së Adriatikut nën Dinaridet e brendshme që shkaktoi magmatizëm, formimin e një kompleksi bërthamë dhe ngritjen përfundimtare.

Pulsi i dytë i formimit të kupolës dhe zgjerimit të SPNF ndodhi diku midis 32 dhe 16 milion vite më parë, dhe i atribuohet kthimit mbrapsht të pjesës së pashkatërruar të pllakës së Adriatikut poshtë Helenideve drejt jugperëndimit. Kjo fazë përfshin uljen e lokalizuar të baseneve Neogjene në bashkimin Dinarido-Helenid të shoqëruar me përkulje oroklinale të përshpejtuar pas Paleogjenit në drejtim orar. Megjithatë, ftohja më e ngadaltë (3,0-3,2°C/Ma) në afërsi të kryqëzimit Dinarido-Helenid pas Eocenit korrespondon me një normë mesatare denudimi prej 0,1-0,2 mm/vit, ekuivalente me heqjen e ~1,6-3,2 km të mbingarkesës që nga ~ 16 milionë vite. Ftohja dhe denudimi më i shpejtë, i nxitur tektonikisht në periudha më të shkurtra kohore është e mundur, por shkon përtej mundësisë së detektimit nga metodat e përdorura nga ne.

Prishja e Dukagjinit, me hedhje vertikale rreth ~ 1000 m, tani e mbuluar nga sedimentet e Pliocenit, përfaqëson segmentin më të ri të SPNF dhe është kryesisht përgjegjës për formimin e Basenit të Kosovës Perëndimore, siç dëshmohet nga sedimentet më të vjetra sintektonike të Miocenit të Mesëm në basen.

Për të kapërcyer hendekun midis ngritjes gjatë Neogjenit, historisë së zhvarrosjes dhe deformimit tek bashkimi Dinarido-Helenid si dhe i ndikimit të SPNF në evolucionin e peisazhit deri në ditët e sotme, u analizuan sedimentet e ruajtura në basenet sedimentare dhe gjeomorfologjia e sotme. Analiza e morfologjisë lumore të sistemit të lumit Drin zbulon vlera më të larta të indekseve të pjerrësisë së lumit (ksn) dhe χ (Chi) midis SPNF dhe ndarjeve të drenazhimit të Drinit. Ato parashikohet të migrojnë larg SPNF-së, me përjashtim të skajit verilindor të saj. Baseni i Kosovës Perëndimore dhe baseni i Tropojës përmbajnë shkëmbinj sedimentarë me shtrirje horizontale nga Plioceni i Vonshëm deri në Holocen të depozituar pas aktivitetit të prishjes kryesore dhe menjëherë pas LGM. Këto shtresa dokumentojnë një kalim gjatë Pleistocenit të hershëm nga kushte liqenore në ato lumore, çka pasqyron një ndryshim të papritur nga drenazhimi i brendshëm në të jashtëm të paleo-liqeneve. Në basenin e Tropojës, këto shtresa janë ndërprerë duke formuar tre breza tarracash lumore, të interpretuara për të pasqyruar ndërprerjen episodike në rrjedhën e poshtme gjatë riorganizimit të sistemit të drenazhimit të lumit paleo-Drin. Nëpërmjet metodës së *^{36}Cl-cosmogenic-nuclide* është dhënë mosha e dy prej tarracave më të reja (~ 12.000 dhe ~ 8.000 vjet), moshë e cila lidhet me periudhë klime më të lagësht dhe transport më të lart të sedimenteve, post-LGM.

Shkalla e tretjes (~12 mm/vit) është dukshëm më e madhe se sa raportohet në Shqipërinë qendrore dhe jugore. Kështu, ndryshimet klimaterike akullnajore/ndërglaciale, erozioni në brendësi të tokës dhe ndryshimet në nivelin bazë duket se kanë rregulluar ciklet e mbushjes dhe gërryerjes së baseneve, kur lumenjtë që derdheshin në basen u bënë pjesë e rrjetit të lumenjve që derdheshin në detin Adriatik. Këto ndryshime morfologjike të theksuara shumë, ndodhën shumë kohë pas prishjes normale të lidhur me SPNF. SPNF siguroi një model strukturor dhe erozional mbi të cilin erozioni i shkaktuar nga klima në kohën e Holocenit ndikoi në riorganizimin e modelit rajonal të drenazhimit. Harku i ndarjes kryesore të drenazhimit rreth SPNF-së devijon nga rregulli i përgjithshëm i kësaj ndarjeje, me trend VP-JL të vargut malor Dinarido-Helenid. Ky hark përfshin gjurmën morfologjike të lënë nga zhytja mbrapsht e pllakës së Adriatikut nën Helenidet veriperëndimore, dhe kështu ai përfaqëson një dëshmi të evolucionit strukturor të bashkimit Dinarido-Helenid, i cili filloi mbi 100 milion vjet më parë dhe është ende i dukshëm në peizazhet e sotme.

Acknowledgements

This work is dedicated to my parents who have always supported and encouraged me to study. They taught me that education is a key to a happy, beautiful and carefree life. And they were right.

First of all, I would like to thank Saskia for standing by me for the last 13 years, always supporting me during my studies and in life, distracting me from stupid ideas and giving me the most beautiful gift I could ever imagine, our little Mathilda. Dear Mathilda came in the middle of the schedule of this thesis and turned our lives upside down, but she made our lives even more worth living and she is my biggest inspiration.

Of course, a doctoral thesis cannot be written without the excellent supervision and tireless support of the supervisors, and so I would like to thank Mark, Jörg, Lorenzo and Jan for mentoring me, challenging me and keeping me on my toes over the past five years. We had ups and downs, different opinions and endless, sometimes recurring discussions, but we never lost the thread and finally I finished this thesis. Thank you all for your perseverance and tenacity, I really benefited from your knowledge and experience, not only in scientific issues, and I really enjoyed the time in our group at FU Berlin. I would also like to thank all my colleagues and friends at the Lankwitz campus, especially Julian, Philip, Arthur, Peter, Benjamin, Charlotte, Iris, Robert, Carolin, Vincent, Sascha, Alex, Alex, Martina, Juliane, Anne, Eline and the rest of our group for a nice and collegial working atmosphere. I would also like to thank Ed Sobel and Hannah Pomella for assisting me with the methodological and laboratory work on this thesis.

Finally, I would like to thank the rest of my family, friends, and fellow students for support, relaxation, vacations, nice evenings, and a great time as a student. Thank you all.

Organization of the thesis

This thesis consists of six chapters. The first chapter introduces the reader to the study area and to the regional geology, explains the scientific questions and introduces the methods used to answer them. Chapter II analyzes the large-scale structures of the Dinaric-Hellenic junction (manuscript in review, IJES) and presents plate tectonic reconstructions and resulting models. This chapter is based on my fieldwork and data compilations along the SPNF. The basis of the maps and profile sections presented in the chapter is composed of the results of my fieldwork, mapping, and my research of the existing data sets. From these results, I developed the models, maps and figures presented in this chapter and the geologic interpretations derived from them. Chapter III provides maximum temperature estimates and presents a new synthesis of the thermochronological data at the Dinaric-Hellenic junction (soon to be published in a peer-reviewed journal). The samples, which are the basis of the thermochronological and thermometric results, and from which the cooling ages and maximum temperatures presented in the chapter result, were taken by me during several field campaigns and for the most part processed, examined, analyzed, evaluated and interpreted by me in the laboratory. From these results I developed the models, maps and figures presented in the chapter and the geological interpretations derived from them. Chapter IV (published in the journal Frontiers in Earth Science; M.U. Grund as co-author) deals with the evolution of landscape morphology and the resulting geomorphological features in relation to tectonic and climatic changes along the Dinarides-Hellenides orogen. The basis for this publication was, among other things, intensive fieldwork, sampling and detailed mapping that I accompanied during three field campaigns and on the basis of which three final theses were written. On the basis of these and my fieldwork, new structural geological datasets were created, which form the basis for the current maps and figures of this chapter and its appendix, which I helped to create and on which the further analyses, discussion and interpretation of this chapter are partly based. Chapter V summarizes the results of this thesis and Chapter VI provides a brief outlook on possible future work.

The organization of this thesis and the titles of the chapters included in the thesis builds up as follows:

Chapter I: Introduction

Chapter II: Faulting, basin formation and orogenic arcuation at the Dinaric - Hellenic junction (northern Albania and Kosovo)

Marc U. Grund[1], Jörg Giese[2], Lorenzo Gemignani[1], Mark R. Handy[1], Jan Pleuger[1] & Kujtim Onuzi[3]

(1) Freie Universität Berlin, Institut für Geologische Wissenschaften, Berlin, Germany, (2) Geological Survey of Norway -NGU- Trondheim, Norway, (3) Polytechnic University of Tirana, Institute of Geosciences, Tiranë, Albania

In review in *International Journal of Earth Sciences*, submitted 19.04.2022.
This manuscript is currently in the peer-review process in the journal *"International Journal of Earth Sciences"*. The copyrights of this manuscript are held by Springer Nature. The peer-reviewed article of the same name is expected to be published in *"International Journal of Earth Sciences"* in 2023.

Chapter III: Thermal record of obduction, nappe stacking and orogen-parallel extension at the Dinaric - Hellenic junction

Marc U. Grund[1], Jörg Giese[2], Lorenzo Gemignani[1], Mark R. Handy[1], Jan Pleuger[1], Edward Sobel[3], Sascha Zertani[4], Julian Hülscher[1], Philip Groß[5] & Hannah Pomella[6]

(1) Freie Universität Berlin, Institute of Geological Sciences, Berlin, Germany, (2) Geological Survey of Norway -NGU- Trondheim, Norway, (3) University Potsdam, Institute of Geosciences, Potsdam, Germany, (4) University of Oslo, Department of Geosciences, Oslo, Norway, (5) Heidelberg University, Earth Sciences, Heidelberg, Germany, (6) University Innsbruck, Department of Geology, Innsbruck, Austria

Submitted soon in a peer-reviewed journal.

Chapter IV: Response of drainage pattern and basin evolution to tectonic and climatic changes along the Dinarides-Hellenides orogen

L. Gemignani[1], B. Mittelbach[1-2†], D. Simon[1], A. Rohrmann[1], **M. U. Grund[1]**, A. Bernhardt[1], K. Hippe[1], J. Giese[1-3†], M. R. Handy[1]

(1)Institut für Geologische Wissenschaften, Freie Universität Berlin, Berlin, Germany, (2) Department of Earth Sciences, ETH-Zürich, Switzerland, (3) The Geological Survey of Norway (NGU), NO-7491 Trondheim, Norway, †*Current Address*.

Published in: *Frontiers in Earth Science, Front. Earth Sci. 10:821707. doi:10.3389/feart.2022.821707*
DOI: https://doi.org/*10.3389/feart.2022.821707*

Chapter V: Conclusions

Chapter VI: Outlook

Table of content

Chapter I: Introduction

The Earth is a dynamic planet. Endogenous processes in the Earth's interior that drive continental drift (Wegener 1912, 2001) provide dynamic motion and deformation of the lithosphere. Continental and oceanic crust above the upper mantle generate processes and phenomena associated with plate tectonics, including the formation of mountain belts (orogenesis) by the pressure of colliding continents, and the most common forms of volcanism and earthquakes. Despite forming due to horizontal compressional forces (Dewey and Bird 1970) that drive crustal shortening and thickening, mountain belts often also record synorogenic extension (Dewey 1988; Rossetti et al. 1999). Explanations for such synorogenic intramontane extension range from forced lateral extrusion, involving strike-slip and orogen-parallel normal faulting in front of an indenter (Tapponnier et al. 1986; Ratschbacher et al. 1991), to lateral spreading due to a difference in gravitational potential energy between high and low elevation regions (Dewey 1988; Molnar and Lyon-Caen 1988). Synorogenic extension is also a common feature of oroclines (Marshak 1988; Rosenbaum 2014), which are a first-order feature of the Alpine-Mediterranean mountain belts (Rosenbaum & Lister, 2004, Fig. 1.1)

Various mechanisms have been proposed for oroclinal bending, from opposing subduction polarity, along-strike switches in subduction polarity (e.g., Vignaroli et al., 2008, 2009) to along-strike variation in the rates of subduction, rollback and/or collision (Malo et al. 1995; Spikings et al. 2001; Sekine et al. 2010; Pearce et al. 2012; Yabe et al. 2014; Plunder et al. 2018). Regardless of the driving force, syn-orogenic extension and orogenic arcuation are often associated with crustal exhumation and rapid erosional and tectonic denudation, particularly in the footwalls of large normal faults (Grasemann and Mancktelow 1993; Fügenschuh et al. 1997; Scharf et al. 2013a). The Dinaric-Hellenic orogen is part of the European Alpine mountain belt, running for more than 1500 km along the Adriatic Coast. The Dinarides are the dominant mountain range of southeastern Europe, forming the climatic, cultural, and scenic border between the Mediterranean region and the inland of Eastern Europe. South of the Dinarides are the Hellenides, which extend in a similarly pronounced manner, crossing most of Albania and western Greece in a south-southeasterly direction to the island of Crete (Fig 1.1). The junction of the Dinarides and Hellenides is recognizable as a change in the trend of the orogens: The Dinarides, north of the junction strike roughly WNW-ESE, whereas the Hellenides south of the junction strike NNW-SSE. The most prominent structure characterizing the Dinaric-Hellenic junction is the Shkoder Peja Normal Fault system, (SPNF), a crustal scale normal fault, which has a length of about 120 km from southwest to northeast and which is accompanied by other extensional structures in its footwall and hanging walls.

The strongest amplitude of arcuation of the Hellenides with respect to the Dinarides also occurs along the SPNF, which marks the southern boundary of some Dinaric nappes. Likewise, obducted ophiolites are located about 75 km farther west in the Hellenides than north of the SPNF in the Dinarides (Fig. 1.1). In addition to map-scale surface structural and geological features along and across the SPNF, changes across the Dinaric-Hellenic junction appear to continue at depth as seen in tomographic models. P-wave tomography models show a positive anomaly beneath the northwestern Hellenides, interpreted as a ~400 km southeast-dipping slab retreating to the southwest. In contrast, below the Dinarides the convergence is strongly oblique and the slab anomaly (~150 km) is not as long (Bijwaard and Spakman 2000; Piromallo and Morelli 2003). The Dinaric-Hellenic junction may therefore be related to altered plate geometries and associated changes in the geodynamics of the Adriatic subduction zone of the eastern Adriatic, over which the Dinarides and Hellenides were accreted. The Adriatic slab evolution and timing of key tectonic events remains uncertain, Eocene slab tearing and probably break-off with increasing length of the Hellenic slab south of the SPNF is proposed by Handy, et al. (2019).

This doctoral thesis focusses on the Dinaric-Hellenic junction as changes in orogenic structure to the north and south of the junction have sparked debate about how continental crust responds to mantle restructuring, and in particular about the role of extension during subduction. The origin of extensional faults and associated basins across the Dinarides and Hellenides is controversial, with several competing drivers proposed that point toward changes in the slab configuration below the orogen. Upper-plate extension has been invoked to explain basins affecting the Internal Dinarides (van Hinsbergen et al. 2005); Dinaric slab delamination has been invoked as a cause of Oligo-Miocene core-complex formation and uplift of marine terraces (Schefer et al. 2011; Balling et al. 2021) and rollback of the SW-retreating Hellenic slab segment may have caused Mio-Pliocene late orogenic extension in north-eastern Albania (Muceku et al. 2008). Handy et al. 2019 present evidence for the SPNF as a primarily Neogene structure that accommodated CW rotation, including evidence for earlier rotation and orogen-parallel extension on the SPNF and clockwise oroclinal bending and SPNF-related orogen-normal extension. Further, foreland basins formed in Mio-Pliocene time (Periadriatic Foredeep, Tirana Basin) are thought to have been partly uplifted and exposed during Plio-Pleistocene convergence (Robertson and Shallo 2000).

The formation history of the Dinarides and Hellenides is considered since the Mesozoic, in the Early Triassic the eastern Mediterranean region experienced rifting and magmatism at the eastern margin of the Adriatic microplate (Robertson and Shallo 2000), followed by spreading of the Neotethys in Early to Late Jurassic times. Subsequent intra-oceanic obduction occurred in Middle Jurassic, then parts of the Neotethyan lithosphere were obducted in Late Jurassic onto the former passive Adriatic continental margin (Babić et al. 2002), and formed the West Vardar Ophiolite. Continued Alpine collision from Late Eocene time onwards involved nappe stacking (Schmid et al. 2008), with subdivision of the Dinaric-Hellenic nappe stack into an internal zone marked by Eocene folding and out-of-sequence thrusting of low-grade units and an external zone with Oligocene-Miocene to recent thrusting (Tari 2002). The Dinarides, like the Hellenides, consist of accreted continental nappes derived from Adria, with thick Mesozoic platform carbonates and interbedded deep-sea sediments making up the bulk of the lithologies. These thick sediments are partly deposited on Variscan basement, which is mainly found in the eastern part of the Dinarides and Hellenides. The continental sediments are partly overlain by the West Vardar Ophiolite. The Sava Suture delimits the Adriatic units to the east and also represents the boundary to accreted European lithosphere. The Adriatic nappes are stacked in a westerly direction, and thrusted onto the undeformed Adriatic margin (Schmid, et al., 2008). Although convergence between the Adriatic and Europe continues today (Grenerczy et al. 2005), the main phase of overthrusting likely occurred from the Late Cretaceous and end of Paleogene (Schmid et al. 2008; Handy et al. 2019; van Unen et al. 2019).

In this thesis, I focus on the structural evolution of the Dinaric-Hellenic junction and the role of the SPNF. I investigate the Mesozoic-Cenozoic origins of the Dinaric-Hellenic junction and I present measured geological cross sections through the different segments of the SPNF based on new field data and geological mapping, and quantify throw along the SPNF. I investigate both the history of the Shkoder Peja Lineament (SPL), a precursor of the SPNF, and the evidence of past rotations along this structure to present plate tectonic reconstructions that serve as a basis for models of the evolution of the Dinaric-Hellenic junction.

In the past, the SPNF was often proposed to be a simple structure (e.g., Kissel and Speranza 1995; van Hinsbergen et al. 2005) which superficially represents a lineament at the junction between the Dinarides and Hellenides. On closer inspection, it becomes apparent that the SPNF is structurally complex and that no reliable information has been provided so far on the timing of the direct activity of this structure. Furthermore, possible pre-existing structures, which may explain the dextral offset of the ophiolite front, have been only proposed based on discontinuity of Mesozoic strata on either side of the lineament (Aubouin and Dercourt 1975). There is also no information on the detailed structure of the SPNF, including a clear assignment, delineation, and naming of its fault segments, and quantified amounts of vertical throw along the SPNF.

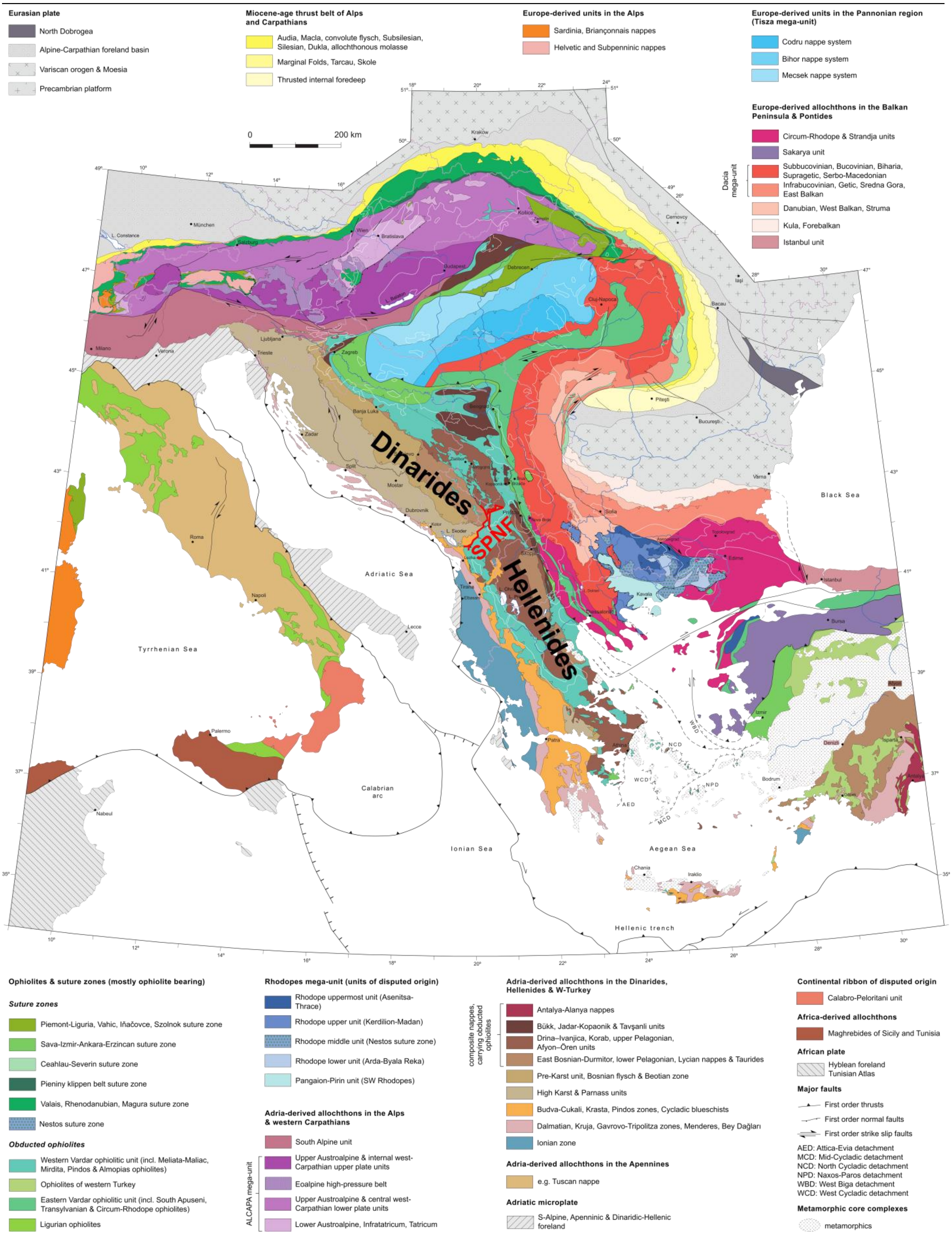

Fig. 1.1: Tectonic units of the Alpine collision zone between Eastern Alps and western Turkey (Schmid et al. 2020) and the extent of the Dinaric-Hellenic orogen. Thick red line marks the extent of the Shkoder Peja Normal Fault system (SPNF). The Schmid et al. 2020 article and the map shown here are available for download in various high-resolution file formats, including shapefiles for GIS applications, at https://www.researchgate.net/ on the personal page of Jan Pleuger, Freie Universität Berlin and in the attached digital data medium.

The SPNF is not a simple fault structure because it hosts at least two dome structures (Cukali and Decani Domes) in its footwall and two sedimentary basins (Tropoja and Western Kosovo Basin) in its hanging wall, some of which were formed at different stages of activity of the present-day exposed fault (Handy et al. 2019). The sedimentary basins have not yet been studied in detail for possible connections in their formation history with the SPNF. The present landscape along the SPNF is characterized by the rugged and towering *Albanian Alps* in the footwall of the SPNF and by gentler hills and sedimentary basins in the hanging wall. The possible influence of the fault system on present-day landscape forms and the present-day river network has also received little or no attention.

In the following chapters, I investigate the cooling history of the Dinaric-Hellenic junction using low-temperature thermochronology and thermometry. I sampled along and across the SPNF and applied zircon and apatite fission track dating as well as (U/Th)-He dating on zircons to cover a temperature range of >240°C to <60°C for the cooling history of the Dinaric-Hellenic junction. Furthermore, I applied RSCM (Raman spectroscopy of carbonaceous material) to the samples to determine the maximum temperature that each sample reached. This innovative combination of low-temperature thermochronology with RSCM thermometry allows to gain deep insights into the formation history of the orogen, maximum burial temperatures and derived burial depths of nappes. I discuss evidence for early orogenic back-arc extension and interpret and discuss cooling rates of the Dinaric-Hellenic junction. I compare peak temperatures and cooling at the SPNF with Neogene cooling patterns in the Hellenides and in the Dinarides. Finally, the influence of the SPNF on the Neogene and recent landscape at the Dinaric-Hellenic junction is examined. The migration of knickpoints and rivers is studied, and models for the evolution of river courses and the formation of possible paleolakes and build and integrated with the formation of sedimentary basins partly based on ^{36}Cl dated fluvial terraces from the Tropoja Basin. Furthermore, this work demonstrates that the present landscape at the SPNF was formed by a complex interplay of tectonic, climatic, and sedimentary processes, and that the SPNF represents a structural and erosional template on which climate-driven erosion since the Holocene has caused restructuring of the regional drainage pattern, thus indirectly imprinting fault activity on the present-day geomorphology. The integration of large-scale plate tectonic processes with the formation, rotation, arcuation and genesis of orogens is considered, as well as the structural deformation, denudation and uplift of nappes and the resulting geomorphological emergence of sedimentary basins and landscapes along the Dinaric-Hellenic junction.

This doctoral thesis was initiated by Mark R. Handy and is based on the DFG research project "Slab tearing or slab retreat as triggers of extension at the Dinaric-Hellenic transition?" which was implemented by Jörg Giese (Freie Universität Berlin and Geological Survey of Norway -NGU- Trondheim, Norway), Mark R. Handy (Freie Universität Berlin) and Jan Pleuger (Freie Universität Berlin). Lorenzo Gemignani became part of the project in 2018 and provided significant support during the field campaign in 2019 and the AFT fission track analysis, as well as with supervision and the solicitation of research funding. Ed Sobel led the ZHe analyses and assisted with the AFT fission track analysis. Hannah Pomella provided the ZFT fission track analysis data and assisted with the fine separation of heavy minerals. The German Research Foundation (DFG) supported this project (Grants: Gi 825/4-1; No. Ha 21/21-1; No. Pl 534/3-1), as well as the Freie Universität Berlin and PROMOS (DAAD) in the form of subsidized field and mapping trips with MSc students from the Freie Universität Berlin. The TCN ages were made possible by a grant from RADIATE (Grant Agreement No. 19001937) to Lorenzo Gemignani.

Chapter II: Faulting, basin formation and orogenic arcuation at the Dinaric - Hellenic junction (northern Albania and Kosovo)

Marc U. Grund[1], Jörg Giese[2], Lorenzo Gemignani[1], Mark R. Handy[1], Jan Pleuger[1] & Kujtim Onuzi[3]

(1) Freie Universität Berlin, Institut für Geologische Wissenschaften, Berlin, Germany, (2) Geological Survey of Norway -NGU- Trondheim, Norway, (3) Polytechnic University of Tirana, Institute of Geosciences, Tiranë, Albania

In review in *International Journal of Earth Sciences*, submitted 19.04.2022.
This manuscript is currently in the peer-review process in the journal *"International Journal of Earth Sciences"*. The copyrights of this manuscript are held by Springer Nature. The peer-reviewed article of the same name is expected to be published in *"International Journal of Earth Sciences"* in 2023.

Abstract

The Dinaric-Hellenic mountain belt bends some 30° where two fault systems transect the orogen: (1) the Oligo-Miocene Shkoder-Peja Normal Fault system (SPNF); (2) the Eo-Oligocene dextral Shkoder Peja Transfer Zone (SPTZ) that offsets the Dinaric-Hellenic nappes by ~75 km. This offset is attributed to activation of an Early Mesozoic rift transfer zone in the Adriatic margin during Eocene subduction of the Pindos Ocean. This subduction involved an initial clockwise rotation of the Hellenides with respect to the Dinarides around a pole at the NW end of the Krasta-Cukali basin. The younger SPNF is a composite structure comprising five segments: Four of these were active under ductile-brittle conditions and downthrow the West Vardar Ophiolite in the hanging wall and exhume domes with anchizonal-to-lower greenschist-facies metamorphism in the footwall. These structures formed during a first-phase of orogen-parallel extension and clockwise rotation beginning at ~27 Ma. Extension is attributed to detachment of part of the Adriatic slab beneath the internal Dinarides that triggered magmatism, core complex formation and uplift. A second phase was accommodated by the fifth segment of the SPNF: a subsurface normal fault bordering syn-rift, mid-late Miocene sediments in the Western Kosovo Basin. This phase involved localized subsidence of Neogene basins at the Dinaric-Hellenic junction coupled with accelerated clockwise oroclinal bending. The driving force for clockwise rotation during both phases is thought to be post-Paleogene bending and rollback of the untorn part of the Adriatic slab beneath the Hellenides.

Introduction

Orogenic arcs, also called oroclinal bends or oroclines (Marshak 1988; Rosenbaum 2014), are a first-order feature of the Alpine-Mediterranean mountain belt (Rosenbaum & Lister, 2004, Fig. 2.1a). These range from the tight loops of the Western Alps, Carpathians and Calabria, to more modest bends, for example, along the Dinarides and Hellenides mountain belt that borders the Adriatic Plate (Fig. 2.1a). Various mechanisms have been proposed for oroclinal bending, from opposing subduction polarity (e.g., Vignaroli et al., 2008, 2009) to along-strike variation in the rates of subduction and/or collision (Malo et al. 1995; Spikings et al. 2001; Sekine et al. 2010; Pearce et al. 2012; Yabe et al. 2014; Plunder et al. 2018). Another explanation is that curvilinear paleogeography of margins and ocean-continent transitions (e.g. Malinverno & Ryan, 1986; Royden & Burchfiel, 1989) reflect lateral changes in the depth and geometry of basal detachments in orogens (e.g. Chiarabba et al., 2009; Lacombe & Mouthereau, 2002; Li & Mitra, 2017; Robert et al., 2011). What distinguishes the Dinaric-Hellenic bend from the aforementioned arcs is that it coincides with an orogen-parallel change in the mode of Neogene plate convergence, from retreating subduction, collision and slab bending in the Hellenides (Hollenstein et al., 2008; Kahle et al., 2000; Royden & Papanikolaou, 2011) to oblique dextral collision and slab tearing in the Dinarides (Wortel and Spakman 2000; Rosenbaum and Lister 2004; Handy et al. 2019). In this paper, we use the term "Dinaric-Hellenic junction" to refer to the segment of the orogen at the border of Albania and Kosovo where an oroclinal bend of about 30° is located (Fig. 2.1b).

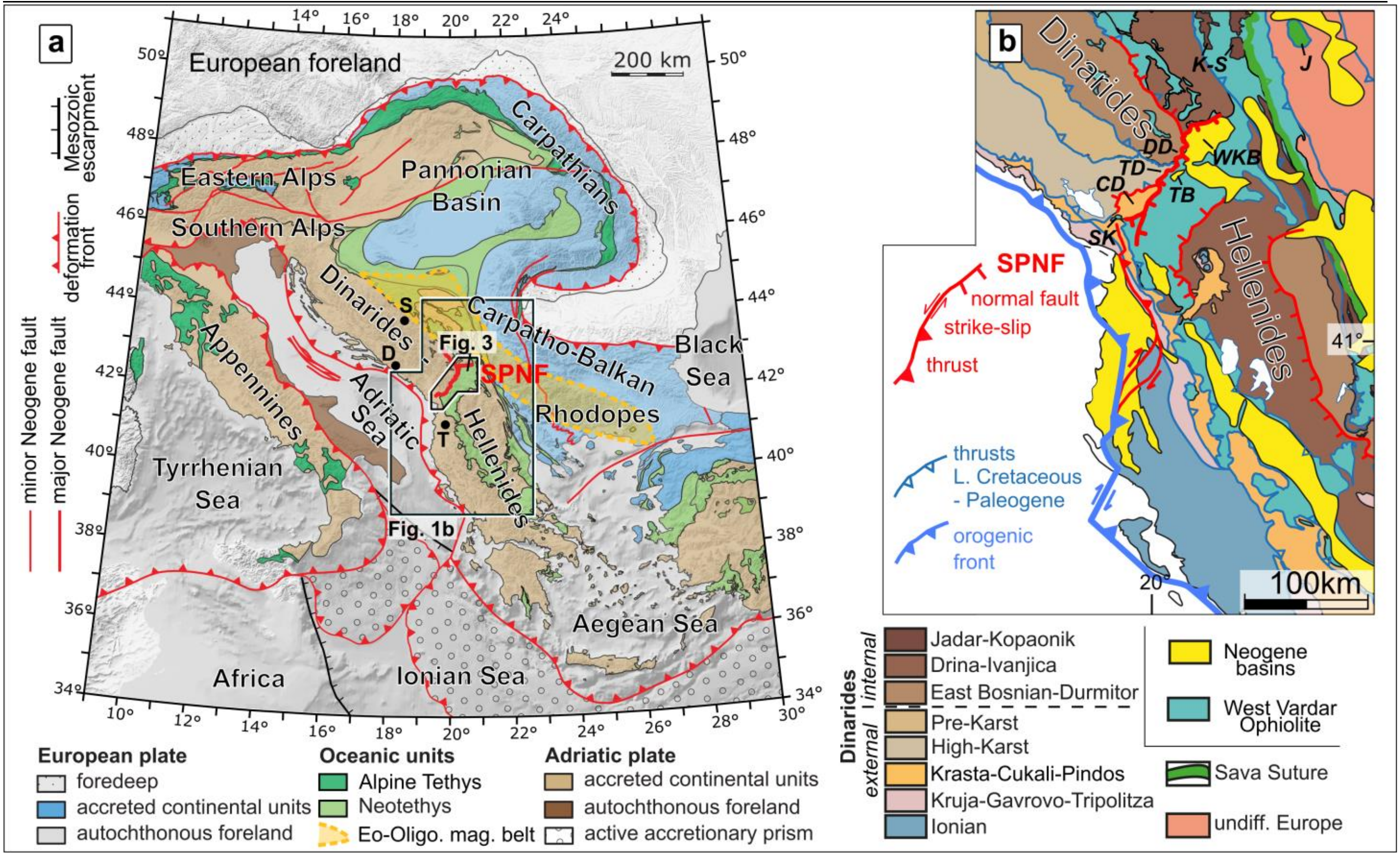

Fig. 2.1: (a) Alpine orogens of the central Mediterranean and their accreted European (blue) and Adriatic (brown) crust. Boxed areas show locations of Figs. 2.1b and 2.3. Belt of Eocene-Oligocene magmatism (pale orange) discussed in text and compiled from Handy et al. (2015, their Fig. 3). Cities: D = Dubrovnik, S = Sarajevo, T = Tirana. (b) Dinaric-Hellenic junction with SPNF system (thick red line) and the associated structures: SK = Shkoder Klippe; CD = Cukali Dome; TB = Tropoja Basin; TD = Tropoja Dome; DD = Decani Dome; WKB = Western Kosovo Basin. K-S = Kopaonik and Studenica core-complexes with Oligo-Miocene intrusions and in the southern Dinarides compiled from Schefer et al. (2011), J = Jastrebac core-complex (Marović et al. 2007). Nappes, Neogene basins, orogenic front, thrusts and normal faults modified from Schmid et al. (2020, 2008). Note that Fig. 1b and 3 in Fig. 2.1 refers to Fig. 2.1 b and 2.3 in this thesis.

Orogenic bending at the Dinaric-Hellenic junction reaches back to pre-Neogene time, as revealed by paleomagnetic studies indicating block rotation since the Late Cretaceous (Kissel et al. 1995; Márton et al. 2003, 2014; Handy et al. 2019). Metamorphic core complexes in the internal Dinarides (Fig. 2.1b) document post-nappe extension in late Paleogene time (Schefer et al. 2011; Schefer 2012; Stojadinovic et al. 2013, 2016; Mladenović et al. 2015; Erak et al. 2016). This was roughly coeval with subduction of an arm of the Neotethyan Ocean, relics of which are preserved in the Hellenic nappes (Pindos unit) and equivalent units in the Dinarides (Krasta-Cukali-Pindos unit in Fig. 2.1b, van Hinsbergen et al., 2020; Schmid et al., 2020, 2008)). The relationship of these events to the pre-Neogene component of oroclinal bending is unclear. A main goal of this paper is therefore to examine the spatial-temporal evolution of the faults marking the Dinaric-Hellenic junction in order to ascertain the causes of bending, and if possible, to determine how orogenic crust responds to along-strike changes in plate convergence. The clockwise bend of the Dinaric-Hellenic orogen coincides with a system of normal faults that cut across the NE-dipping Dinaric-Hellenic nappe pile of Late Cretaceous to Paleogene age (faults marked in red in Fig. 2.1b, e.g., Schmid et al. 2008). The main fault in this system is the Shkoder-Peja* Normal Fault or SPNF (Fig. 2.1) that juxtaposes the Dinaric nappe stack in its footwall with the structurally highest nappe, the West Vardar Ophiolite, in its hanging wall. The name stems from the cities of Shkoder and Peja, respectively, in northern Albania and western Kosovo located near the ends of this SE-dipping normal fault.

In using the term "Dinaric-Hellenic junction", we purposefully avoid the expression "Albanides" sometimes used for this segment (Cvijić 1901; von Nopcsa 1905; Meço and Aliaj 2000), because the overall sequence of nappes is the same along the chain in the southeastern Dinarides and northwestern Hellenides (Schmid et al.

2020). These geological terms should be distinguished from the local geographical names for the mountain range, *Albanian Alps* or *Accursed Mountains (Bjeshkët e Nemuna)*, for the mountain range in this area. The nappe stack beneath the West Vardar Ophiolite on either side of the SPNF comprises sheets of late Paleozoic basement, Mesozoic platform carbonates and Paleogene flysch derived from the early Mesozoic Adriatic continental margin (Louis 1927; Babić et al. 2002; Gawlick et al. 2008; Schmid et al. 2008; Bortolotti et al. 2013; Scherreiks et al. 2014).

** Shkodra–Pejë (definite Albanian form), Skadar–Peć (Serbo-Croatian), Scutari-Peć (Italian) or Shkoder-Peja (Albanian-English).*

The SPNF system coincides with the 30° bend of the mountain belt observed in map view (Fig. 1a), suggesting that this fault system is associated with orogenic arcuation (van Hinsbergen et al., 2005; Kissel et al., 1995; Speranza et al., 1995). Indeed, Handy et al. (2019) proposed that the fault is not strictly a normal fault, but accommodated scissor-like motion with top-SE downthrow of the hanging wall block increasing northeastwards away from a vertical rotation pole near Shkoder (Fig. 2.2). The amount of rotation is poorly constrained due to the absence of structural markers and thermochronological studies on either side of the fault. An orogen-parallel change in Mesozoic facies across the SPNF (von Nopcsa 1905; Aubouin and Dercourt 1975) precludes the use of stratigraphy and nappe contacts as markers. The only thermochronological data available so far (zircon U–Th)/He, ZHe, and apatite fission-track, AFT, Muceku et al., 2006, 2008) indicate rapid exhumation of ~1.2 mm/year (Muceku et al. 2008) and cooling of units to the SE of the SPNF in early Pliocene time (4-6 Ma). This overlaps with the age of syn-extensional sediments (Mio-Pliocene) in basins discordantly overlying the West Vardar Ophiolites in the hanging wall of the SPNF (marked yellow in Fig. 2.1b).

Another puzzling feature of the Dinaric-Hellenic junction is a dextral offset of the West Vardar Ophiolite sheet by some 75 km in map view (Fig. 2.1). This offset gave rise to the idea of the “transversale de Scutari-Pec” (Aubouin and Dercourt 1975) or Shkoder-Peja Transverse Zone (SPTZ, Handy et al., 2019) which is truncated by, and therefore older than, the SPNF (Handy et al. 2019). Three structural domes in the footwall of the SPNF, the Cukali, Tropoja and Decani Domes (Fig. 2.1b and Fig. 2.3), deform and therefore post-date the Dinaric-Hellenic nappe stack, but their kinematic relationship to the SPTZ and SPNF is enigmatic. It is tempting to relate doming to footwall exhumation along the SPNF (Handy et al. 2019), but the domes affect different levels of the nappe stack, suggesting varied amounts of exhumation along the SPNF.

The hanging wall of the SPNF contains several Neogene fresh-water basins (Neubauer et al. 2015; Gemignani et al. 2022), the largest of which is the Western Kosovo Basin (Fig. 2.1b and Fig. 2.3). Middle Miocene clastics in this basin (Elezaj 2009; Elezaj and Kodra 2012) have been used to date downthrow of the hanging wall of the SPNF (Handy et al. 2019), but the Plio-Pleistocene strata (Knobloch et al. 2006; Legler et al. 2006; Elezaj 2009; Elezaj and Kodra 2012) are not visibly in contact with surface exposures of the SPNF mapped so far. Either the SPNF comprises several coeval branches, or these faults formed at different times and their spatial proximity is coincidental.

Finally, the Dinarides-Hellenides junction coincides with changes in the depth and orientation of positive P-wave anomalies in the mantle, with a short Dinaric slab anomaly north of the junction contrasting with a longer slab anomaly in the south that trends north-south (Bijwaard and Spakman, 2000; Handy et al. 2019). Debate centres on the causes of this subcrustal change in structure and its relationship to structures at the surface. Did a southward propagating tear or breakoff of the Dinaric slab (Wortel and Spakman 2000) lead to nucleation of the SPNF, in turn facilitating orogenic arcuation? Or was the arcuation induced by faster rollback of the originally longer Hellenic slab segment as proposed by Handy et al. (2019)? Geodetic studies show that ongoing arcuation and orogen-parallel extension of the Hellenides is limited to the north by the SPNF system (e.g. D'Agostino et al., 2020; Jouanne et al., 2012), suggesting that this system is still accommodating arcuation today. Another goal of this paper is therefore to clarify the relationship of fault kinematics to patterns of doming, exhumation and basin subsidence at the surface and to subduction of lithosphere at depth.

This study presents structural and kinematic evidence to test the hypothesis that today`s bend in the Dinarides-Hellenides chain is a long-lived, partly pre-Neogene feature that nucleated along an inherited rift transfer within the Adriatic margin. In *Structure and history of the Dinaric-Hellenic nappes*, we introduce key features of the Dinaric-Hellenic junction as a prelude to new field evidence in *Structures and kinematics* that the SPNF is not a single fault, but a composite structure comprising several distinct segments. *Age and kinematics of faulting, doming and basin formation* discusses how these segments accommodated varied amounts of orogen-normal and parallel extension, doming, as well as why Neogene sedimentary basins can be attributed to activity of one segment of the SPNF. Age constraints compiled in *A model for arc-parallel extension and orogenic arcuation* provide the basis for a new conceptual model of faulting and basin formation. It is argued that strike-slip activity of the SPTZ was associated with minor oroclinal bending during differential shortening of the Dinarides and Hellenides in Late Cretaceous time. Most clockwise bending was accommodated later by normal faulting on the SPNF during two phases, the first during late Paleogene detachment and retreat of the Adriatic slab beneath the Dinarides and the second during Neogene rollback subduction of Neotethys (Handy et al. 2019), part of the Greater Adria Plate (van Hinsbergen et al., 2020).

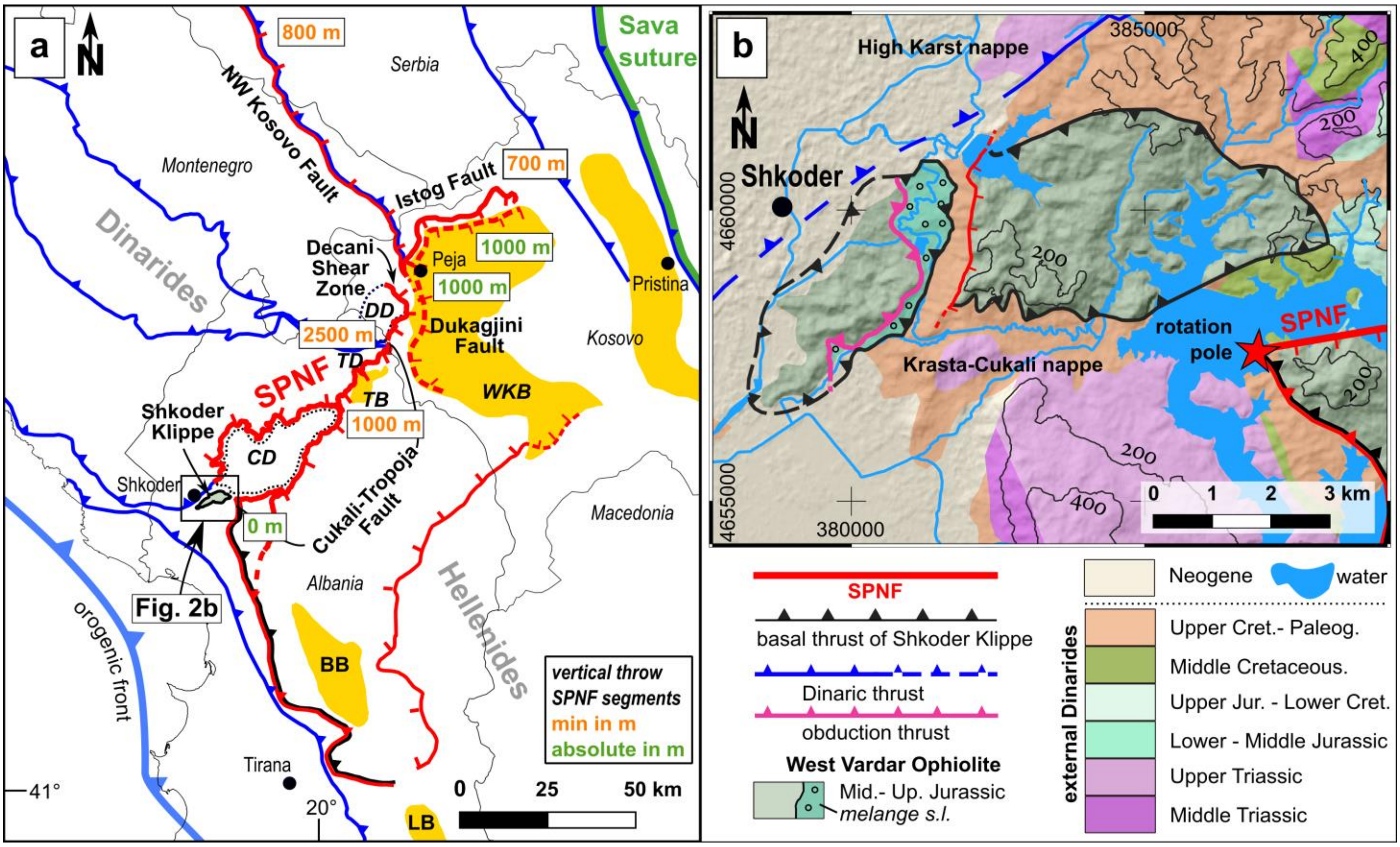

Fig. 2.2: Faults at the Dinaric-Hellenic junction: (a) SPNF system (thick red line), Dinaric thrusts (dark blue) and present orogenic front (pale blue). SV = Sava Suture, Dashed line represents the Dukagjini Fault beneath in the Western Kosovo Basin (WKB). Neogene basins in yellow: TB = Tropoja Basin; BB = Burrel Basin; LB = Librazhd Basin. Major structures in the footwall of the SPNF: Cukali Dome (CD), Tropoja Dome (TD) and Decani Dome (DD). Box indicates location of (b) Shkoder Klippe near city of Shkoder in northern Albania. SPNF rotation pole from Handy et al. (2019). Tectonic units from Schmid et al. (2020, 2008). Hillshade model and contour lines in (a) are extracted from ASTER GDEM (Abrams et al. 2020). Map in (b) is simplified from Groß et al. (2014). Note that Fig. 2b in Fig. 2.2 refers to Fig. 2.2 b in this thesis.

Structure and history of the Dinaric-Hellenic nappes

To grasp the full extent of faulting at the Dinaric-Hellenic junction, it is necessary to understand the structure of the nappe pile truncated by the SPTZ and SPNF. The highest nappe in this pile, the West Vardar Ophiolite, is the only reliable structural marker for these faults, being dextrally offset along the SPTZ and vertically downthrown to the SE along the SPNF (Schmid et al. 2008; Handy et al. 2019; van Hinsbergen et al. 2020). We follow geochemical, structural and stratigraphic arguments supporting the idea that the Neotethyan ophiolite belts of the Dinarides and northern Hellenides, including the West Vardar Ophiolite, originated from a single, oceanic basin (Bortolotti et al. 2004, 2013, Schmid et al., 2008) of early-middle Jurassic age (Halamić et al. 1999; Liati et al. 2004; Ozsvárt et al. 2012; Lugović et al. 2015). The West Vardar Ophiolite was obducted SW-ward onto the Adriatic passive margin of lower-mid Triassic age (Ferriere et al., 2016; Gawlick et al., 2008; Haas et al., 2019; Halamić et al., 1999; Sudar et al., 2013) in Late Jurassic to Early Cretaceous time (Pamić, 2002; Scherreiks et al., 2014; Tremblay et al., 2015) as documented by Ar-Ar amphibole ages from its metamorphic sole (Dimo-Lahitte et al. 2001; Borojević Šoštarić et al. 2014) and biostratigraphic ages in its sub-ophiolitic mélange (Vishnevskaya et al. 2009). The internal Dinaric nappes (Schmid et al. 2008, 2020) underlying the West Vardar Ophiolite and derived from the Adriatic passive margin (Fig. 2.3, Jadar-Kopaonik, Drina-Ivanjica-Korab = Upper Pelagonian nappe, East Bosnian-Durmitor = Lower Pelagonian nappe) were subsequently imbricated with the obducted West Vardar Ophiolite sheet during SW-directed Dinaric thrusting in Paleogene time (Schmid et al. 2020). Collision initiated in Late Cretaceous time with closure of parts of a somewhat younger branch of Neotethys called the Sava Ocean (Sava Suture in Figs. 2.1 and 2.2, , Dimitrijević, 1997; van Hinsbergen et al., 2020; Schmid et al., 2008, their Fig. 5h). Dinaric thrusting continued until early Oligocene time in the external nappes of the Dinarides (Pre-Karst, High Karst, Krasta-Cukali, Kruja and Ionian units in Fig. 2.3; (Xhomo et al. 2002; Tari 2002; Schmid et al. 2008)) as constrained by the youngest biostratigraphic age of flysch underlying the basal thrust of each nappe. These nappes are deformed by the aforementioned domes, Cukali, Tropoja and Decani Domes, located in the footwall of the SPNF (Figs. 2.3 and 2.4). Also in the footwall of the SPNF near Shkoder is a small klippe of West Vardar Ophiolite that directly overlies Eocene flysch of the Krasta-Cukali nappe (Figs. 2.2, 2.3 and 2.4). This klippe, the Shkoder Klippe (*Structures and kinematics, Fig. 2.2*), has great significance in the following chapters for determining strike-slip motion on the SPTZ.

The Hellenic nappes south of the SPTZ and SPNF have the same basic structure as the Dinaric nappes, except that the Krasta-Cukali nappe is exposed in a tectonic window (Peshkopie Window, Fig. 2.3, inset map) surrounded by the Upper Pelagonian nappe in addition to along the NE-dipping thrust front. North of the Peshkopie Window a SSW-NNE striking fault (Figs. 2.1b and 2.2a) downthrows the West Vardar Ophiolite to the NE against the Upper Pelagonian nappe. The NE end of this fault (Prizren-Vranica Fault (*PF*) in Fig. 2.3) is sealed by Pleistocene sediments and is interpreted as conjugate to the SPNF system, as proposed by Handy et al. 2019, their Fig. 13e. In the Hellenides, the West Vardar Ophiolite directly overlies the external nappes (Krasta-Cukali and Kruja nappes). The Krasta-Cukali nappe with its Early Jurassic pelagic strata (Robertson & Shallo, 2000; Schmid et al., 2020, Fig. 2.3) is the along-strike equivalent of the Pindos nappe in the central Hellenides, which contains ophiolites of the Pindos Basin (Shallo and Dilek 2007; Rassios and Dilek 2009; Robertson et al. 2009). This along-strike correlation has important implications for constraining transverse motion of the SPTZ, as discussed below.

Two points regarding the Dinaric-Hellenic nappe structure have direct bearing on the age of the SPTZ and SPNF: First, the widely accepted theory of a single-ocean origin for the imbricated West Vardar Ophiolite (Schmid et al. 2008, 2020; Bortolotti et al. 2013) enables us to use it as a marker for dextral offset along the SPTZ of ~75 km (Handy et al. 2019; Schmid et al. 2020). Previous paleogeographical scenarios invoking several narrow ocean basins separated by continental swells (e.g. Karamata, 2006; Robertson & Shallo, 2000) would exclude its use as a displacement marker. However, the multi-ocean hypothesis has been disproved on both structural and geochemical grounds by several publications in recent years (Carosi et al. 1996; Schmid et al. 2008, 2020; Bortolotti et al. 2013). Second, the SPNF does not cut all the units of the Dinaric nappe pile. Rather, it ends in the NE and SW, respectively, in the Drina-Ivanjica-Korab and Krasta-Cukali nappes (Fig. 2.3, inset). The SW end of the SPNF near Shkoder becomes a NW-SE trending thrust within flysch of the Krasta-Cukali nappe in the northwestern Hellenides. This thrust accommodated SW-directed, Neogene-to-Present imbrication of the older Paleogene nappe pile (Handy et al. 2019). The kinematic change from SE-directed normal faulting to SW-directed thrusting near Shkoder is therefore attributed to a Neogene clockwise rotation pole located within the Krasta-Cukali nappe (Handy et al. 2019). We return to these features below when discussing the age and amount of displacement associated with orogenic bending.

Structures and kinematics

Segments of the SPNF

The SPNF is a system of SE- to E-dipping normal faults with five segments (Figs. 2.2 and 2.3) that are kinematically related, even though they are not all continuous and of the same age: (1) The **Cukali-Tropoja Fault** bordering the Cukali- and Tropoja Domes in its footwall (labelled CD and TD in Fig. 2.2a) and extending northwest to the Plio-Pleistocene Tropoja Basin in its hanging wall near the Albanian town of Bajram Curri; (2) The **Decani Shear Zone** juxtaposing the Decani Dome in its footwall (DD in Fig. 2.2a) with the West Vardar Ophiolite in its hanging wall; (3) The **NW Kosovo Fault** running along the thrust of the Drina-Ivanjica nappe in its hanging wall and the East-Bosnian Durmitor nappe in its footwall; (4) The **Istog Fault** skirting the western and northern parts of the Western Kosovo Basin (labelled WKB in Fig. 2.2a) and juxtaposing sub-ophiolitic mélange of the West Vardar Ophiolite in its hanging wall with the Drina–Ivanjica nappe in its footwall; (5) The **Dukagjini Fault,** a subsurface fault buried beneath the Plio-Pleistocene cover of the Western Kosovo Basin and located in the hanging wall of the Decani Shear Zone, the NW Kosovo Fault and Istog Fault.

These segments have in common that the West Vardar Ophiolite forms their hanging wall. In their footwall, however, they cut progressively deeper units of the NE-dipping Dinaric nappe stack going from SW to NE. Distinguishing these fault segments is important for understanding their role on orogenic arcuation because they have different features and were active under different conditions, as described below in detail.

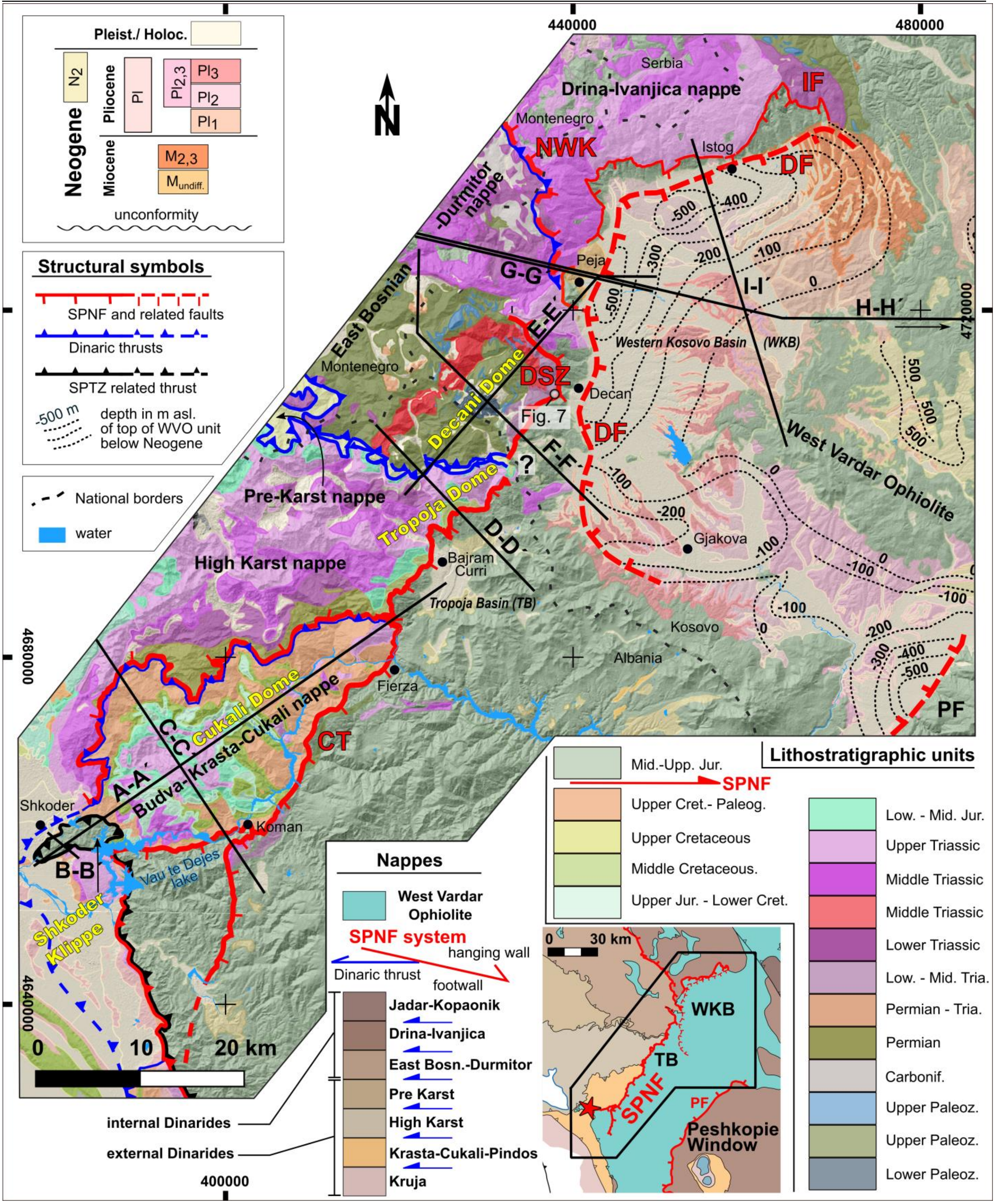

Fig. 2.3: Geological map of the Dinaric-Hellenic junction. Profiles A-A´ to I-I´ shown in Figs. 2.4, 2.6 and 2.9. Bold red letters refer to segments of the SPNF: CT = Cukali-Tropoja Fault, DSZ = Decani Shear Zone, DF = Dukagjini Fault, NWK = NW Kosovo Fault, IF = Istog Fault. Bold black letters: PF= Prizren-Vranica Fault. Inset map: TB = Tropoja Basin, WKB = Western Kosovo Basin. Red star marks vertical rotation pole of the SPNF system (Handy et al. 2019). Nappe structure after Schmid et al. (2008 & 2020). Depth to basement in the WKB taken from Tectonic Map of Kosovo 1:200.000 (Legler et al. 2006). Geology based on maps K 34-53 “Pec”, K34-65 “Kukes” (Osnovna Geološka Karta SFRJ, 1:100.000) and Geological Map of Albania 1:200,000 and 1:50,000 (Xhomo et al., 2002). CRS of map: WGS 84, UTM zone 34N, DEM based on ASTER GDEM (Abrams et al. 2020).

(1.) The **Cukali-Tropoja** Fault is best exposed along the southeastern border of the Cukali Dome (Figs. 2.3 (*CT*) and 2.4). The northern limb of the dome is bounded by a NW-dipping normal fault that is conjugate to the SPNF. The Cukali-Tropoja fault forms the SE limit of the Cukali Dome and truncates SW-directed thrusts and folds of the Krasta-Cukali and High Karst nappes within this dome (Schmid et al. 2008, 2020). The fault itself comprises a cataclastic zone up to 3 m thick that is gradational in its footwall to chlorite-sericite-bearing mylonite derived from the clay- and silt-rich shales and slates of the late Cretaceous-Eocene Krasta-Cukali flysch and Late Cretaceous marl of the High Karst nappe. This mineral assemblage is consistent with lower greenschist- to anchizonal conditions during faulting (Okrusch and Matthes 2009; Philpotts and Ague 2009). The ductile style of the post-nappe folds and the occurrence of fine-grained dynamic recrystallization in mylonitic limestone (Handy et al. 2019, their Fig. 4c) indicate that a temperature of at least 180°C prevailed in the footwall of the Cukali-Tropoja Fault prior its activity (temperature calibration of Schmid et al., 1980, 1981). Within about 100 m of the fault plane, the SE-dipping bedding and schistosity in the footwall steepen into concordance with the brittle fault plane, which is locally coated with talc, serpentine and/or calcite. Serpentine is derived exclusively from the overlying West Vardar Ophiolite and its sub-ophiolitic mélange in the hanging wall. The drag of the schistosity in the footwall units indicates top-SE motion of the hanging wall block (Handy et al. 2019, their Fig. 4b). This is consistent with the sense of shear determined from slickenfibres on fault planes dipping ~25° SE (Fig. 2.4 inset map, Groß et al., 2014, Fig. 2.5a, Handy et al., 2019, their Fig. 3).

As mentioned above, the SW end of the Cukali-Tropoja Fault roots in Paleogene flysch of the Krasta-Cukali nappe near the Vau te Dejes reservoir lake (Figs. 2.2b, 2.3 and 2.5d) near Shkoder (star in Fig. 2.2b) and continues southward as a W- to SW-directed Miocene thrust along the mountain range bordering the Peri-Adriatic foredeep basin (Figs. 2.2b and 2.3; Handy et al. 2019). This thrust is also joined by a N-S trending branch of the SPNF that cuts into the West Vardar Ophiolite close to the town of Koman (Fig. 2.3).

The NE end of the Cukali-Tropoja Fault has the Tropoja Dome (Fig. 2.4) in its footwall, skirts the Plio-Pleistocene Tropoja Basin (Fig. 2.3 and Fig. 2.5a and b) and coincides with the boundary between red shales of the sub-ophiolitic mélange and Late Cretaceous marly shale of the High Karst nappe (Fig. 2.3 and Xhomo et al., 2002). The dome plunges to the NE and is truncated by the SPNF. The northern limb of the dome shows thinned and excised middle Triassic strata, indicating that it is the site of a NE-dipping normal fault that is conjugate to the SPNF (Fig. 2.4, profile D-D´). The northeastward increase in topographic relief in the footwall along this segment, from ~1000 m (Fig. 2.4, profile A-A´) to more than 2000 m near Fierza (Fig. 2.5c), to ≥ 2500 m near Tropoja (Fig. 2.5b), reflects the contrasting morphology of platform carbonates and ophiolite units, respectively, in the foot- and hanging wall as shown in Fig. 2.5b (Handy et al. 2019, their Fig. 4a; Gemignani et al., 2022, their Fig. 4).

The vertical throw of the Cukali-Tropoja Fault increases from SW to NE along its strike (Handy et al. 2019). Using topography as a crude structural marker (elevation extracted from SRTM DEMs; Abrams et al., 2020), one can estimate a throw ranging from 0 at the vertical rotation pole near Shkoder to a minimum of ~2500 m at the Tropoja Basin (Fig. 2.2a and Fig. 2.5b). The latter was obtained from the difference in altitude of lowest and highest exposures of High Karst nappe in the footwall of the fault with respect to the originally higher West Vardar Ophiolite in the hanging wall (Grund et al. 2018). The exposures of High Karst are respectively, 200-250 m asl in the Valbona river bed (Fig. 2.5b) and 2694 m asl in the highest peak (Jezerca Peak) of the Albanian Alps. This minimum estimate is much less than the 7 km of maximum throw estimated by Handy et al. (2019) for the same locality, as obtained by comparing the altitude of the base of the West Vardar Ophiolite in the hanging wall to its base in the footwall projected from N to S into the section over several tens of km along strike.

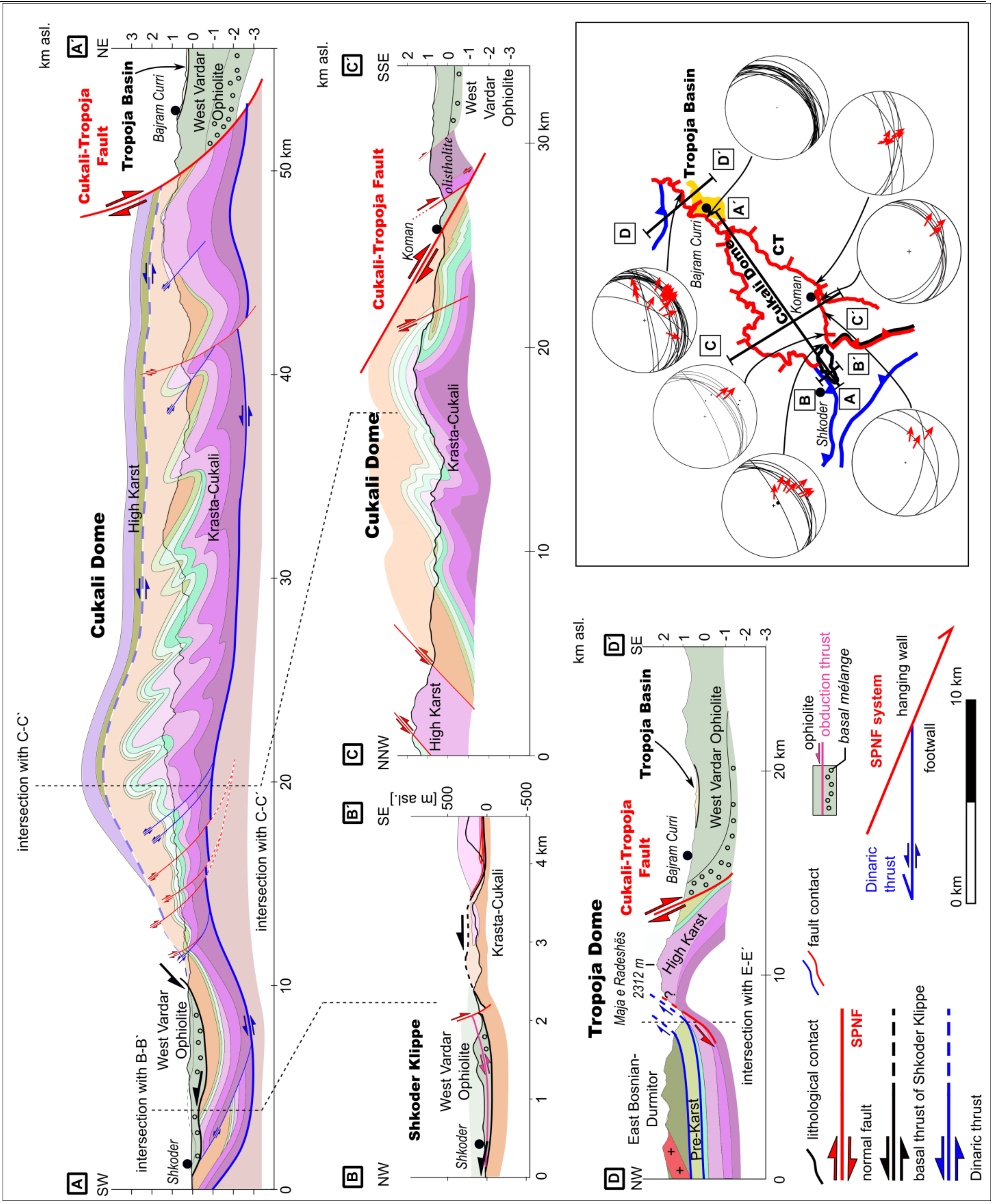

Fig. 2.4: Profiles of the Cukali-Tropoja Fault, including the Shkoder Klippe, Cukali Dome and Tropoja Dome. Location of profile traces shown in Fig. 2.3. No vertical exaggeration. Topography extracted from ASTER GDEM (Abrams et al. 2020). Lower-hemisphere equal-area projection shows orientation of fault surfaces (black lines) and striations (red arrows) with arrows indicating motion of hanging wall. Geology based on K 34-53 “Pec”, K34-65 “Kukes” (Osnovna Geološka Karta SFRJ, 1:100.000) and Geological Map of Albania 1:200,000 and 1:50,000 (Xhomo et al., 2002).

(2.) The **Decani Shear Zone** is a c. 1 km wide zone (Fig. 2.6, profile E-E´and F-F´ and Fig. 2.7) of mylonitic limestone and siliciclastic schists that dip E to ESE. Its protoliths are Mesozoic carbonates and locally breccious Triassic carbonates of the East Bosnian-Durmitor nappe and shales and slates of the sub-ophiolitic mélange and West Vardar Ophiolite, respectively, in the foot- and hanging walls (Fig. 2.7). Though this shear zone appears to be continuous along strike with the Cukali-Tropoja Fault (Fig. 2.3) to the SW, it differs from the latter in being thick, pervasively mylonitic, with only subordinate brittle deformation.

The mylonite comprises sericite-chlorite-bearing schist without biotite, and carbonates with dynamically recrystallized calcite (Fig. 2.7b – d). These features indicate temperatures between 300-350°C, typical of lower-greenschist facies conditions (Okrusch & Matthes, 2009). Temperature estimates for marble-bearing shear zones (Thassos Island, Greece) similar to the mylonitic marbles of the Decani Shear Zone indicate syntectonic temperatures of 300-350°C (Bestmann et al., 2000).

The mylonite derived from bedded limestone and shaly protoliths contains moderately E- to ESE-dipping (30-60°, Fig. 2.7- profile) shear bands on the cm, m- and multi-meter scales, as well as slickenfibres that are mostly consistent with top-down-to-the-E motion of the hanging wall. We note, however, that a few shear bands indicate top-NW shearing, a point to which we return below as possible evidence of older obduction-related thrusting at the base of the West Vardar Ophiolite.

The southern end of the Decani Shear Zone truncates the Dinaric thrust of the East Bosnian-Durmitor nappe onto the Pre-Karst nappe. As an aside, we were unable to visit the actual point of truncation at the national border (Fig. 2.3) between Kosovo and Albania due to the danger of lethal mines from the Balkan war in 1995. The shear zone forms the eastern perimeter of the Decani Dome and reaches no further than the northern limit of the dome. There, the shear zone steepens and follows the lithological contact between Paleozoic metasediments and Triassic platform carbonates within the East Bosnian-Durmitor nappe. The Decani Dome exposes pre-Mesozoic basement rocks in its core and is the site of the highest peak temperatures (≤ 400°C) in the footwall of the SPNF (Grund et al. *in prep.*). Metamorphic temperature conditions of ~400-500°C can also be obtained from similar Upper Triassic meta-limestones of the Jadar-Kopaonik nappe (Fig. 2.1b, (Sudar & Kovács, 2006)). The amplitude of the Decani Dome is greatest at its eastern end and decreases both to the N, where the mylonitic foliation of the Decani Shear Zone disappears, and to the S at its junction with the aforementioned thrust of the East Bosnian-Durmitor nappe onto the Pre-Karst nappe. These structural relations show that the Decani Dome is asymmetrical, with a steeper eastern limb that has been dragged into concordance with the mylonitic foliation of the E-dipping Decani Shear Zone (Fig. 2.6 profiles E-E’ and F-F’).

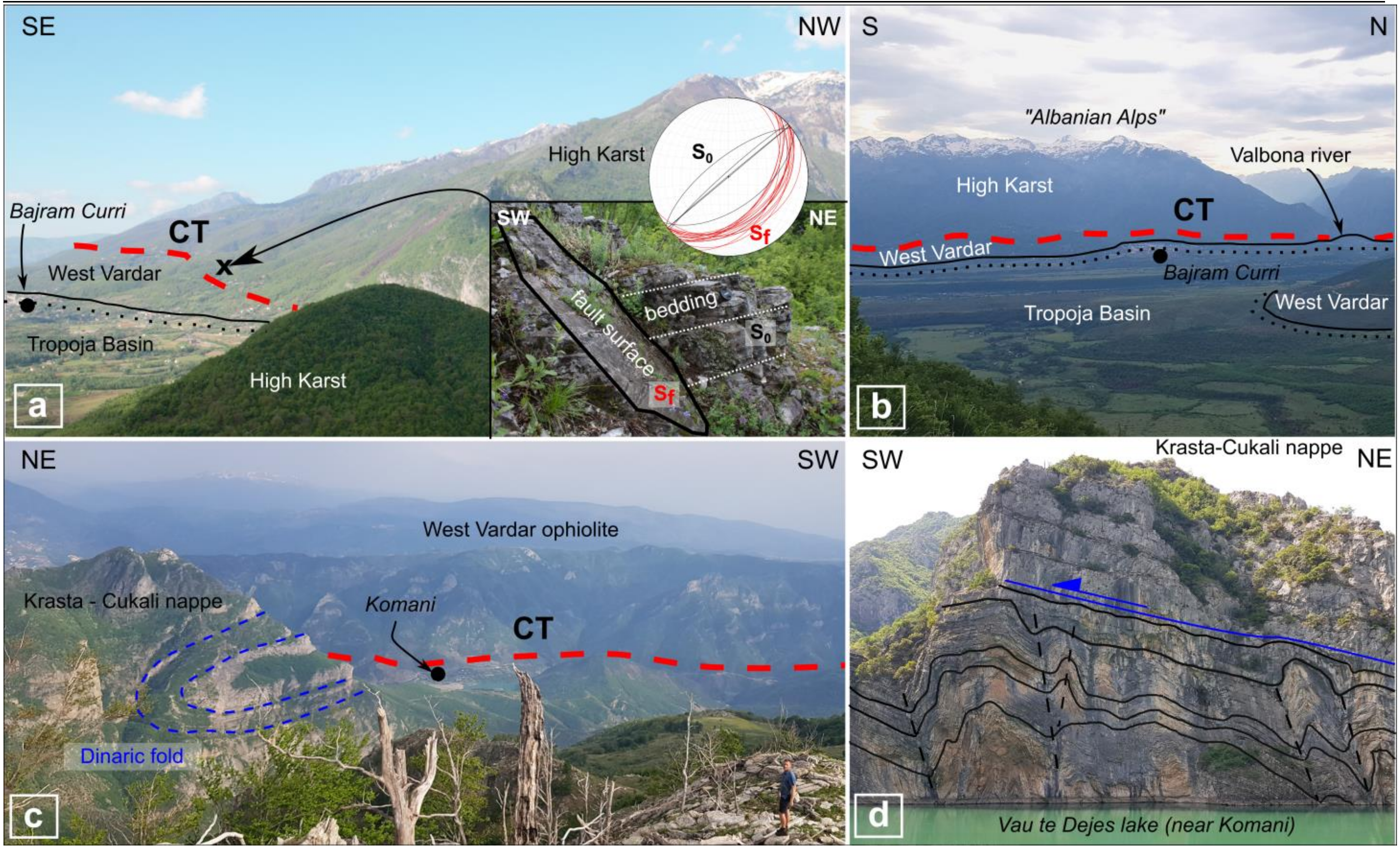

Fig. 2.5: View of the Tropoja Basin (a, b) and the Cukali Dome (c, d). Bold red dashed lines in all plates indicate trace of the Cukali-Tropoja Fault (CT) segment of the SPNF. (a) The SPNF juxtaposes the High Karst nappe (footwall) with the West Vardar Ophiolite (hanging wall) which is unconformably overlain by Plio-Pleistocene sediments of the West Kosovo Basin (line with dots). The gorge beyond the hill in the foreground is the entrance to the Valbona Valley, where Pleistocene river terraces (lower left) and Holocene carbonate breccia (at entrance to the Valbona valley) seal the SPNF fault. Lower-hemisphere equal-area projection shows orientation of bedding (S_0, black great circles) and fault surfaces (S_f, red great circles) in massive and thinly-bedded limestone of the High Karst nappe; (b) View across the Tropoja Basin (foreground) of the West Vardar Ophiolite and High Karst nappe, respectively, in the foot- and hanging wall of the Cukali-Tropoja Fault. The topographic relief across the fault measured from the basin surface to the highest peaks of the Albanian Alps is ~2500 m. Note the flat landscape with river terraces in the foreground incised in horizontal Plio-Pleistocene sediments unconformably overlying the West Vardar Ophiolite; (c) View from top of Mount Cukali showing a large SW-vergent Dinaric fold. Note person on lower right for scale; (d) Dinaric folds and thrust of Cretaceous carbonate of the Krasta-Cukali nappe at the Vau te Dejes reservoir lake near Komani (location of lake in Figs. 2.2 and 2.3).

(3.) The **NW Kosovo Fault** is located north of the Kosovarian city of Peja (Peć in Serbo-Croatian) and strikes NNW-SSE. At its southern end near Peja (Fig. 2.3), the fault is inferred from the absence of a slice of West Vardar Ophiolite exposed along strike to the north, which is interpreted to have been tectonically excised. About 20 km north of Peja, close to the Montenegro–Kosovo border (Fig. 2.3), NW-SE striking fault planes with slickensides indicate top-down-NE movement of Middle Triassic limestone of the Drina-Ivanjica nappe with respect to Lower Triassic limestone and Paleozoic basement of the East-Bosnian-Durmitor nappe (Fig. 2.2a). The southward continuation of the NW Kosovo fault is speculative due to its poor, largely inaccessible exposure in the protected, nature monument area of the Rugova Gorge (Bajraktar et al. 2010; Tahirsylaj et al. 2010) west of the Peja. It is tempting to link it via a putative system of minor faults to a large, NE-dipping normal fault just S of Peja that juxtaposes West Vardar Ophiolite in the hanging wall with Upper Triassic carbonate of the East Bosnian Durmitor nappe in its footwall (Fig. 2.3). There, the normal fault dips ~20-40° to the NE and is marked by a ~5 m thick cataclastic zone comprising blocky serpentinite. This fault disappears eastwards below Neogene sediments of the Western Kosovo Basin (Fig. 2.3), possibly connecting at depth with the Dukagjini Fault. In the absence of structural, stratigraphic markers to determine the amount of vertical throw directly, we use the vertical thickness of West Vardar Ophiolite exposed to the north along the NW Kosovo Fault between the Drina-Ivanjica and East Bosnian-Durmitor nappes (maps of Schmid et al. 2008, 2020) to estimate the amount of tectonic excision. This amounts to some 800 m**,** which we regard as a minimum for the actual amount of throw on the NW Kosovo Fault (Fig. 2.2a). Greater pre-orogenic thicknesses of the ophiolite body and/or thinning of the body during Paleogene nappe imbrication would lead to higher estimates of tectonic excision and vertical throw.

(4.) The **Istog Fault** (*Istok* in Serbo-Croatian) north of the Western Kosovo Basin strikes generally WSW-ENE and juxtaposes sub-ophiolitic mélange of the West Vardar Ophiolite in its hanging wall with severely jointed middle Triassic carbonate of the Drina–Ivanjica nappe in its footwall (Fig. 2.3, profile I-I` in Fig. 2.6). It accommodated top-SE motion **(**equal-area plots in Fig. 2.6**)** and can be followed west and north along the arcuate strike of the Western Kosovo Basin towards its NE end. There, the fault is covered by gently dipping Miocene strata and disappears beneath the Pliocene cover of the Western Kosovo Basin. The Istog Fault has a displacement of at least ~700 m along the northern part of the Western Kosovo Basin (Fig. 2.2a) based on the vertical offset of sub-ophiolitic mélange in its hanging wall and West Vardar Ophiolite in its footwall (Fig. 2.3 and Fig. 2.6, profile I-I`).

The relative position of the Istog and Dukagjini Faults along the northern part of the Western Kosovo Basin therefore closely resembles that of the NW Kosovo and Dukagjini Faults along the western margin of the same basin, except that the units juxtaposed in the foot- and hanging walls of the Istog Fault are tectonically higher within the internal Dinaric nappe pile, which comprises imbricated tectonic slices. Specifically, the West Vardar Ophiolite in the hanging wall of this fault originally overlay the Drina–Ivanjica nappe, which itself overlay the slice of West Vardar Ophiolite exposed in the hanging wall of the NW Kosovo Fault (Schmid et al 2008, 2020). About 10 km north of Peja, where the strike of the Istog Fault changes from N-S to WSW-ENE, the basinward-dipping sub-ophiolitic mélange of the West Vardar Ophiolite is unconformably overlain by Pliocene strata, constraining the age of basinwards tilting in the hanging wall of the Istog Fault to have been earlier than early Pliocene, probably late Miocene (Fig. 2.3).

(5.) The **Dukagjini Fault** is a subsurface fault that has so far only been mapped in geo-electric investigations as an offset of basement rock, taken to be the West Vardar Ophiolite beneath the Western Kosovo Basin (Appendix I: map and geo-electric resistivity cross sections, Geophysical Institute of the Jugoslavia Republic, 1978, courtesy of Sali Mulaj, Prishtina, Kosovo). The offset is substantial, amounting to ~1000 m across a horizontal distance of ~1 km (Figs. 2.3 and 2.8, Fig. 2.6 profiles E-E´, F-F´, G-G and I-I` and Fig. 2.9 profile H-H`) as shown in previous geological profiles of the basin (Knobloch et al. 2006; Legler et al. 2006; Linder and Perkuhn 2013). In our profiles, we depict the fault as a discrete surface delimiting a half-graben filled with clastics and lacustrine sediments that gradually decrease in thickness to the east away from the fault. There, the Mio-Pliocene sediments of the basin onlap onto the post-obduction Cretaceous limestone above the West Vardar Ophiolite (Figs. 2.3 and 2.9, profile H-H´). The depth to the top of the basement (West Vardar Ophiolite) is indicated in Figure 2.3 by dashed contour lines (Legler et al. 2006), revealing the crescent-like shape of the basin in map view that mimics both the arcuate trace of the Dukagjini Fault and the aforementioned segments of the SPNF exposed in its footwall (Knobloch et al., 2006; Legler et al., 2006). The deepest parts of the basin are 500 m below sea level and occur adjacent to the Dukagjini Fault, east and northeast of Peja (Figs. 2.3 and 2.10, Fig. 2.6 profiles E-E´, F-F´, G-G and I-I` and Fig. 2.9 profile H-H`). Borehole data (Elezaj 2009; Elezaj and Kodra 2012) indicate that the basin fill comprises middle to upper Miocene clastics (breccia, conglomerate, sandstone, lignite, Fig. 2.8) and lacustrine deposits (clay, lignite) that thicken towards the fault (Fig. 2.9, profile H-H’) and are unconformably overlain by Plio-Pleistocene sediment (Knobloch et al. 2006; Elezaj and Kodra 2012). The Pliocene sequences overlie the SPNF (Fig. 2.3), placing a pre-early Pliocene upper stratigraphic age limit on normal faulting along the Dukagjini Fault. These horizontally deposited sediments are exposed near Peja (Fig. 2.9, profile H-H’). We interpret tilting of late Miocene-Pliocene (?) sediments to document the latest activity of parts of the Dukagjini Fault in the Western Kosovo Basin (Fig. 2.8g).

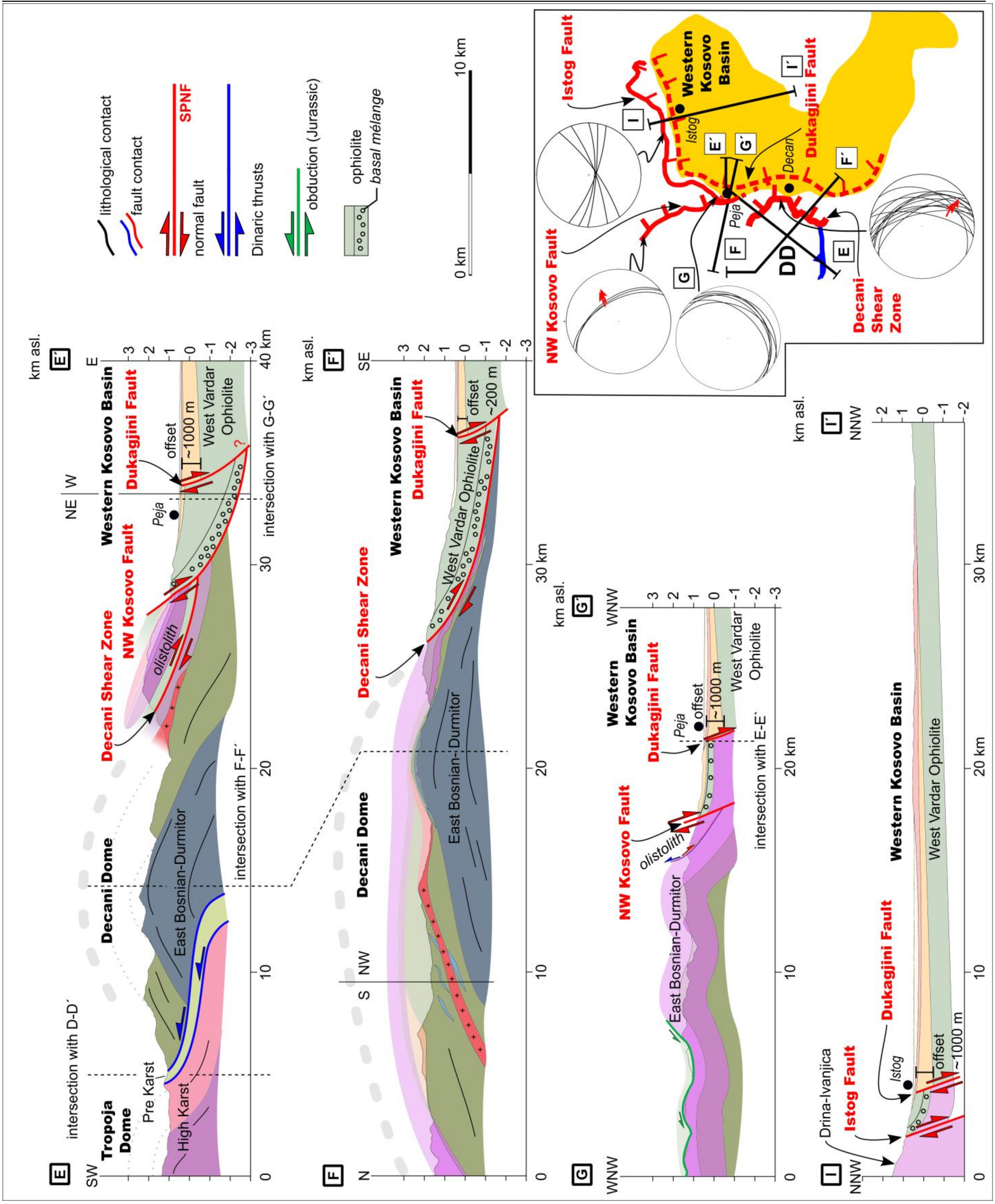

Fig. 2.6: Profiles of the Decani Shear Zone, Decani Dome, NW Kosovo Fault and Dukagjini Fault along the western and northwestern sides of the Western Kosovo Basin. Location of profile traces shown in Fig. 2.3. No vertical exaggeration. Inset map: DD = Decani Dome; Lower-hemisphere equal-area projections show orientation of fault surfaces and striations (black great circles and red arrows, respectively), with arrow heads indicating motion of the hanging wall. Topographic profiles from ASTER GDEM (Abrams et al. 2020). Geology based on K 34-53 “Pec”, K34-65 “Kukes” (Osnovna Geološka Karta SFRJ, 1:100.000) and Geological Map of Albania 1:200000 and 1:50000 (Xhomo et al., 2002).

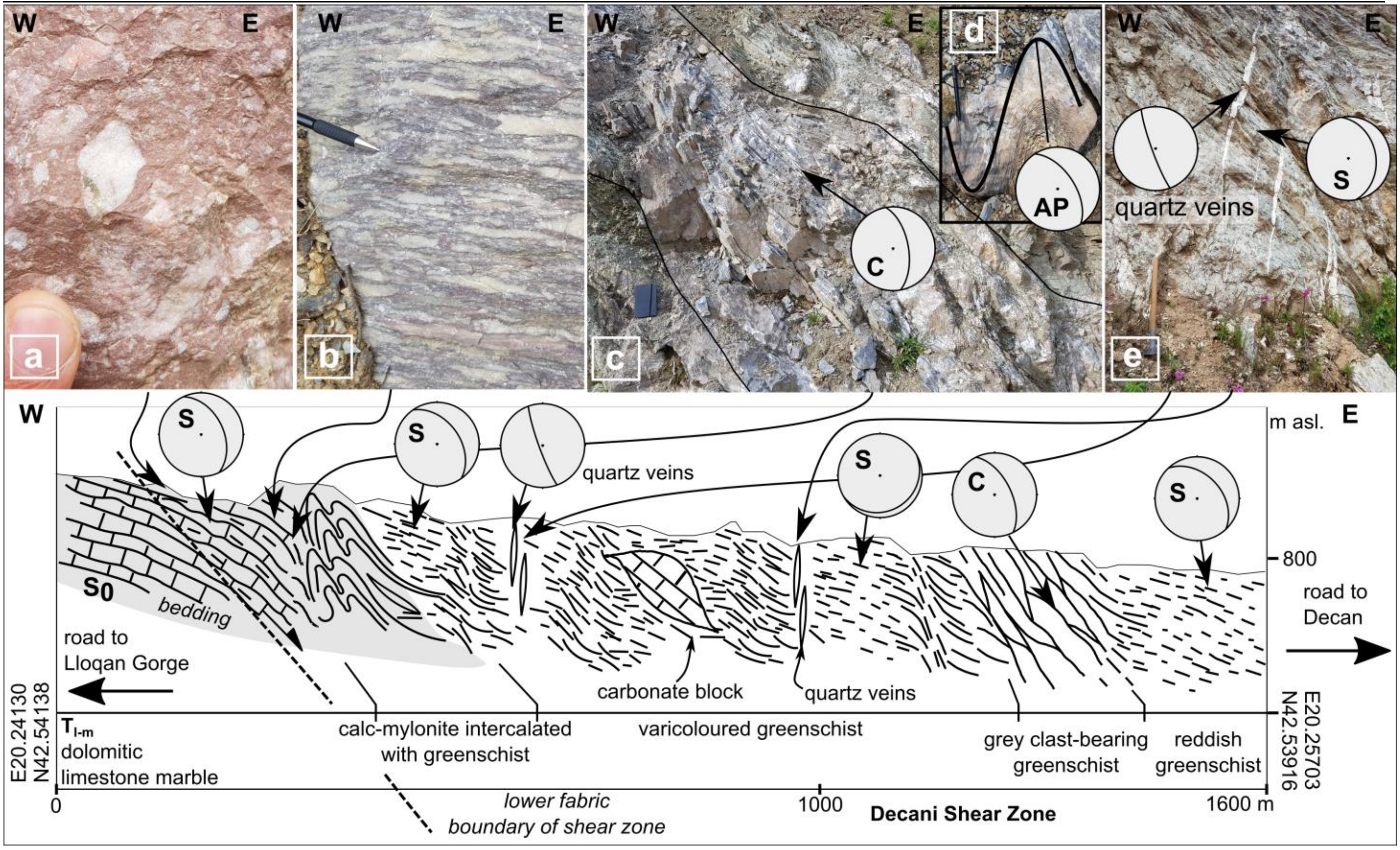

Fig. 2.7: Road cut of the Decani Shear Zone about 3 km west of the town of Decan (location in Fig. 2.3; coordinates in WGS 84 (World Geodetic System of 1984, GEM 10C/ EPSG:4326) with outcrops (a-d) across the lithological boundary between the East Bosnian-Durmitor nappe (footwall, grey) and basal mélange of the West Vardar (hanging wall, white). Dashed line on the left side of the profile marks the lower shear zone related fabric boundary of the Decani Shear Zone within the East-Bosnian-Durmitor nappe. The Decani overprint is strongest in mylonitic foliation domains marked "C", which are zones of highly non-coaxial shear. The angle between S and C foliations is consistent with downthrow of the Decani hanging wall on the E side of the section (see text). Lower-hemisphere equal-area stereo plots (Priest 1985) show orientations of foliations and en-echelon quartz veins. Field photos: (a) Brecciated lower to middle Triassic dolomitic marble of the East Bosnian-Durmitor nappe; b) Mylonitic fabric in lower to middle Triassic dolomitic marble; (c) Isoclinally folded and mylonitized lower to middle Triassic dolomitic marble intercalated with greenschist and calc-schist of the sub-ophiolitic mélange of the West Vardar Ophiolite; (d) Tight-to-similar fold in mylonitized lower to middle Triassic dolomitic marble with axial plane (AP) dipping to the NE (057/57 dip azimuth/dip); (e) En-échelon quartz-filled extensional veins (oriented 250/83, dip azimuth/dip) cut the S foliation of the shear zone and are interpreted as subordinate brittle overprint during the waning stages of top-down-E motion of the hanging wall.

The throw of ~1000 m on the Dukagjini Fault in the western part of the West Kosovo Basin near Peja (Figs. 2.3 and 2.6) is seen most clearly from the depth of the unconformity at the base of the Miocene strata interpreted from the geo-electric data (contours in Fig. 2.3 and Fig. 2.6, profiles E-E´, F-F´, G-G; Fig. 2.9, profile H-H`).

Between the Dukagjini and NW Kosovo Faults in the western part of the West Kosovo Basin, Mid-Miocene sediments overlying the West Vardar Ophiolite dip gently eastwards toward the basin, except at locations just north of Peja, where the sediments dip towards the northwest (Fig. 2.8g). These Miocene sediments lap onto the E-dipping West Vardar Ophiolite and its sub-ophiolitic mélange (Figs. 2.3 and 2.8b). The basal Miocene unconformity dips gently towards the basin (Fig. 2.6, profile E-E`). Along the northern margin of the Western Kosovo Basin and in the hanging wall of the Dukagjini Fault, middle to upper Miocene sediments are affected by S-vergent thrusts (Fig. 2.8d), indicating that the Western Kosovo Basin experienced post-late Miocene, N-S directed shortening.

The Western Kosovo Basin hosts the White Drin River sub-basin catchment (Kovaçi et al. 2015) at an altitude of ~500 m asl. This river drains to the south before flowing into the Adriatic Sea. The basin is bordered to the west and northwest by the *Albanian Alps*, which reach an average elevation of 2500 m asl. (Fig. 2.8a). A ridge some 600–1000 m high separates the Western Kosovo Basin from the much smaller Plio-Pleistocene Tropoja Basin (Fig. 2.3) at the Albanian-Kosovarian border (Gemignani et al. 2022). In the next section, we discuss the bearing these observations have on the origin of the West Kosovo Basin, as well as on the activity of the SPNF system.

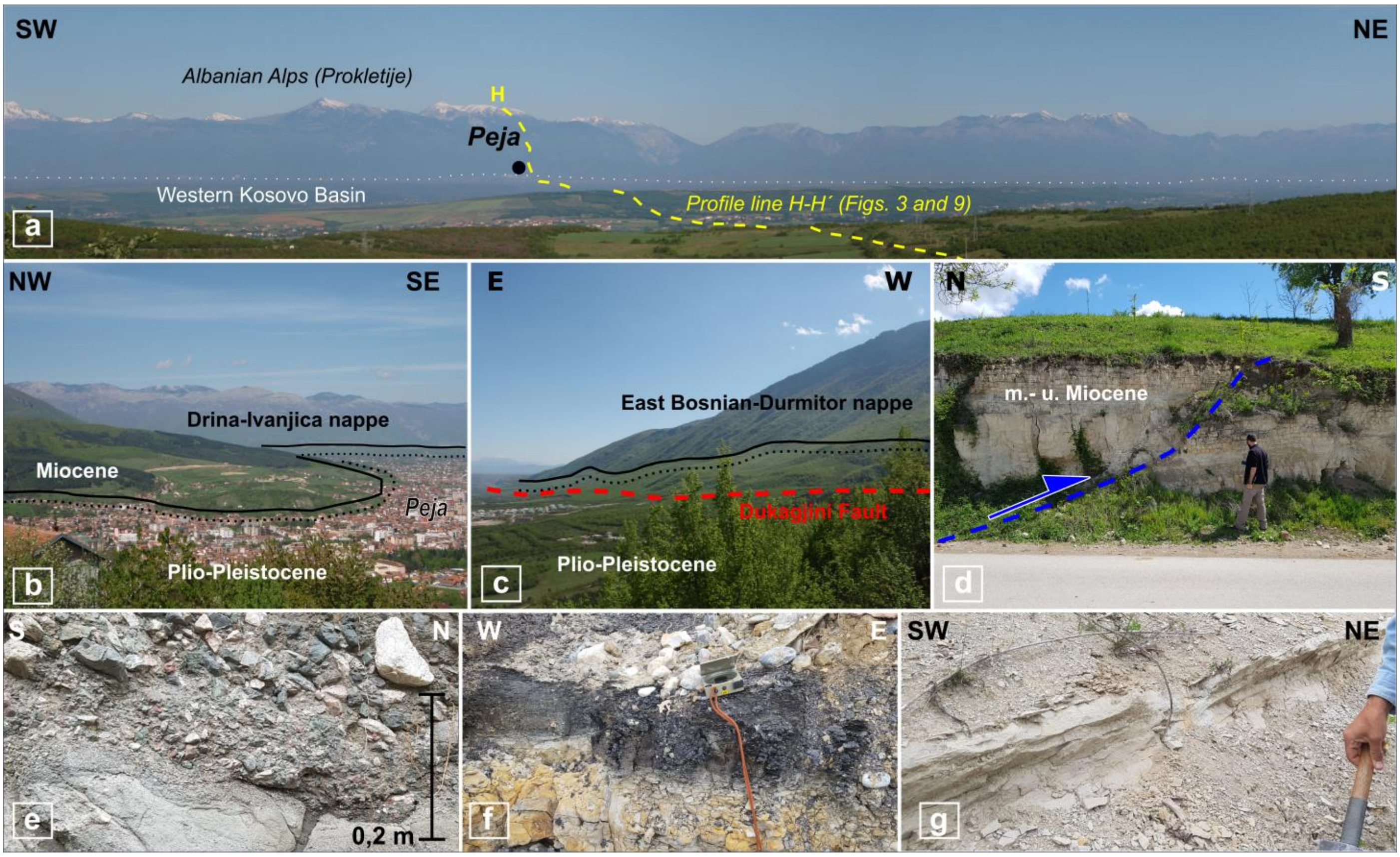

Fig. 2.8: Field impressions of the Western Kosovo Basin: (a) Flat landscape and tremendous increase in relief along the SPNF; (b) Miocene sediments and unconformably overlying Plio-Pleistocene sediments upon which the city of Peja is built. In the background, Triassic limestone of the Drina-Ivanjica nappe forming the mountain range bounding the Western Kosovo Basin to the north; (c) Plio-Pleistocene sediments south of Peja that unconformably overlie the trace of Dukagjini Fault (dashed red line); (d) Thrusts in middle to upper Miocene sediments in the northeastern part of the Western Kosovo Basin indicate south-directed shortening; (e) Poorly rounded and sorted basal conglomerate of middle Miocene age (15.97 Ma) marking the onset of rift-related sedimentation in the Western Kosovo Basin; (f) ~1 m thick layer of late Miocene lignite near Peja with calcareous-marly lacustrine sediments above and below. Bedding of lignite layers oriented 348/24 (dipdir/dip); (g) Calcareous Pliocene (?) layer within shaley marl containing freshwater mollusks. Sediments dip towards the northwest (286/38 dip azimuth/dip). Tilting of bedding is post-depositional. Note that Figs. 3 and 9 in Fig. 2.8 a refers to Figs. 2.3 and 2.9 in this thesis.

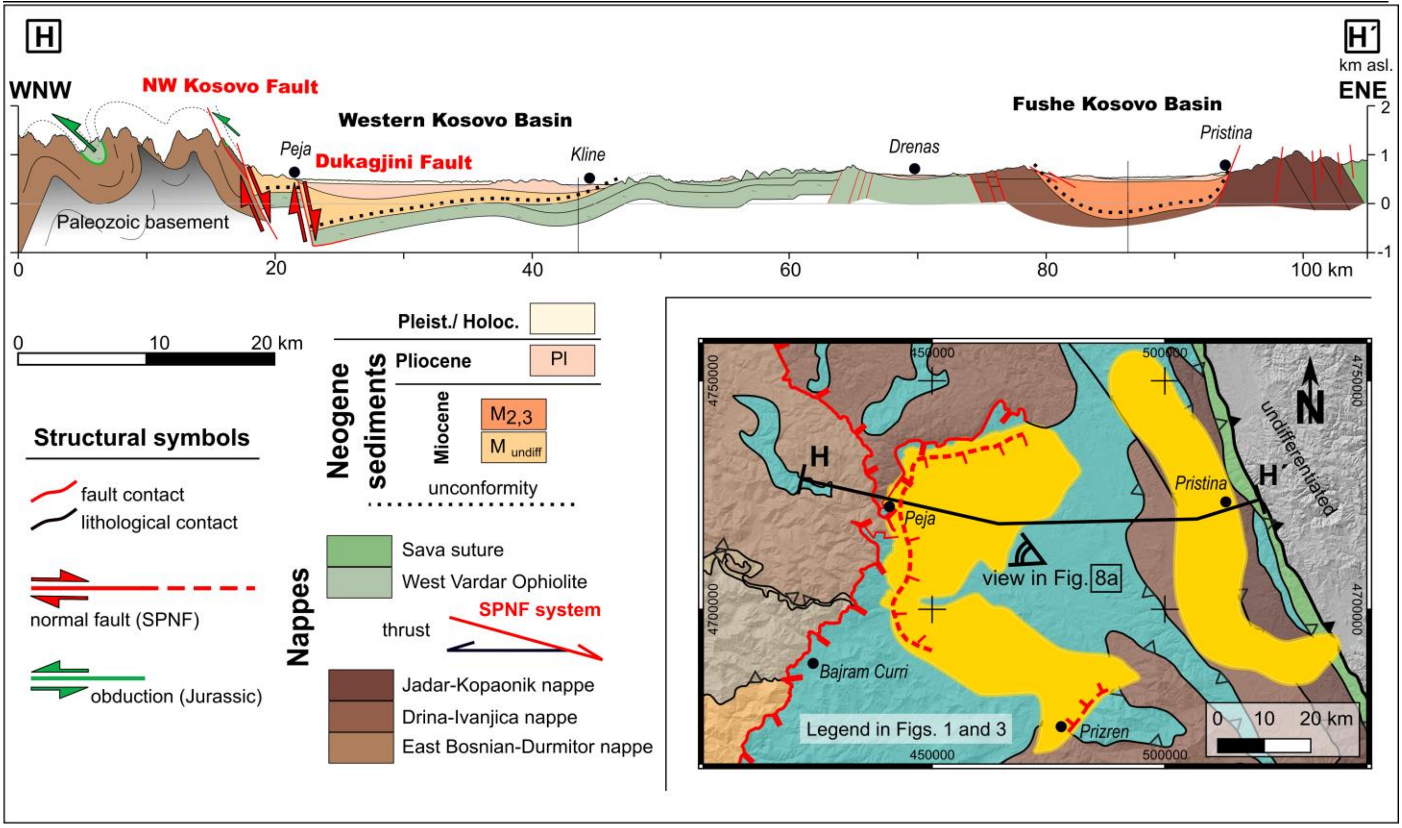

Fig. 2.9: Profile H-H' (~110 km long) across the Western Kosovo Basin and Fushe Kosovo Basin in Kosovo (western part of profile trace in Fig. 2.3). Note the asymmetric, half-graben shape of the Western Kosovo Basin and its basement of West Vardar Ophiolite. Vertical exaggeration is 3.5x. Legend for the nappes in inset map is shown in Figs. 2.1 and 2.3. Topographic profile and hillshade model extracted from ASTER GDEM (Abrams et al. 2020). Geology based on K 34-53 "Pec", K34-65 "Kukes" (Osnovna Geološka Karta SFRJ, 1:100,000) and Geological Map of Albania 1:200,000 and 1:50,000 (Xhomo et al., 2002). Structures and depth information are taken from the Tectonic Map of Kosovo 1:200,000, 2006 (Legler et al., 2006; Linder and Perkuhn, 2013). Note that Fig. 8 a in Fig. 2.9 refers to Fig. 2.8 a in this thesis.

The Shkoder Klippe

The **Shkoder Klippe** (Figs. 2.2 and 2.3) lies ~75 km to the SW of the main West Vardar Ophiolite body of the internal Dinarides, but only a few km from a comparable body of West Vardar Ophiolite directly overlying the Krasta-Cukali Nappe of the northwestern Hellenides (Xhomo et al. 2002). The klippe is thus the most external ophiolite body in the orogen and lies immediately south of the NE-SW-trending SPTZ described in the introduction. The klippe itself has a ~10 x 4 km, oval shape in map view (Fig. 2.2b). It comprises middle Jurassic West Vardar Ophiolite (Xhomo et al. 2002; Schmid et al. 2020) and its underlying mélange represents the late Jurassic obduction front onto the Adriatic margin.

Detailed mapping reveals that the obduction thrust within the klippe (marked violet in Fig. 2.2b) is truncated by a younger thrust that forms the base of the klippe and marks later, post-obduction emplacement of the klippe onto the Krasta-Cukali nappe in the footwall of the SPNF (marked black in Fig. 2.2b). This basal thrust has top-W to -SW shear-sense indicators and, together with the overlying ophiolite, is itself offset by a minor normal fault (marked red in Fig. 2.2b) that is kinematically unrelated to the SPNF. The parallelism of the subhorizontal basal thrust of the Shkoder Klippe and the foliation of the underlying Krasta-Cukali nappe preclude emplacement of the former during Dinaric nappe stacking. Simultaneous klippe emplacement and nappe stacking would have entailed a duplex structure with a structural discordance between the klippe´s basal thrust and thrusts of the underlying nappe imbricates. We do not observe such a discordance.

It is important to emphasize that this basal thrust is not the original obduction front, because the thrust contains no metamorphic sole fragments along its base and emplaced the sub-ophiolitic mélange onto Paleogene flysch of the Krasta-Cukali nappe (Fig. 2.2b and in Xhomo et al. 2002). The significance of this post-obduction thrust becomes evident when one considers that the Shkoder Klippe is located immediately to the north and west of the vertical rotation pole (Handy et al. 2019) of the SPNF system. There, normal faulting along the Cukali-Tropoja Fault did not displace the West Vardar Ophiolite. We therefore correlate the Shkoder Klippe with the large sheet of West Vardar Ophiolite overlying the Krasta-Cukali nappe to the S and E along the northwestern Hellenides. Unfortunately, the Vau te Dejes reservoir lake (Figs. 2.2b and 2.3) obscures the lateral continuity of the klippe with the main West Vardar Ophiolite sheet to the SE.

We note that the basal thrust of the Shkoder Klippe is older than the base of the West Vardar Ophiolites immediately to the south, which was overprinted by Neogene thrusting related to clockwise rotation on the SPNF (Handy et al. 2019). In *Age and kinematics of faulting, doming and basin formation* we discuss reasons supporting the idea that this basal thrust was active during dextral shearing along the SPTZ.

To summarize this chapter, the Shkoder Klippe is a relic of West Vardar Ophiolite that was emplaced to the WSW onto the external Dinaric units after stacking of the external Dinaric nappes, but before activity of the SPNF. We therefore attribute this post-obduction and post-nappe thrusting to activity of the SPTZ, which involved some 75 km of dextral strike-slip offset of the West Vardar Ophiolite front in map view. In contrast, the SPNF comprises four segments that cut progressively higher units of the Dinaric nappe stack in their footwalls going from SW to NE across the orogen. They accommodate varied amounts of vertical throw, as shown in Fig 2.2a. Most of displacement estimates are minima, but it is notable that only the longest segment (Cukali Tropoja Fault) shows an along-strike increase in throw away from the vertical rotation axis near Shkoder, as proposed by Handy et al. (2019). Further to the NE, the faults accommodate less throw and appear to be unrelated to displacement on the Dukagjini Fault bounding the Neogene Western Kosovo Basin.

Age and kinematics of faulting, doming and basin formation

Dating of the deformation described above is key to understanding the role of strike-slip and multiple normal faulting events during orogenic arcuation. In this section, we combine cross-cutting structures with biostratigraphy and existing thermochronology to constrain the kinematic history of the SPTZ and SPNF. The cross-cutting relations of the segments of the SPNF (Fig. 2.10) and timing of motions are summarized in the table in Fig. 2.11.

Shkoder-Peja Transfer (faulting) Zone (SPTZ)

The Shkoder-Peja Transfer Zone (SPTZ) offsets the front of the West Vardar Ophiolite by ~75 km and therefore post-dates Early Cretaceous obduction of the West Vardar Ophiolite onto the undeformed Adriatic passive margin (Pamić 2002; Scherreiks et al. 2014; Tremblay et al. 2015). An upper (younger) age limit on lateral motion of the SPTZ is given by the SPNF, which overprints the SPTZ and which we argue below was not active as a normal fault before late Eocene to Oligocene time, because it cuts folds and thrusts of the Dinaric nappe stack.

In the absence of structures obviously related to the SPTZ other than the map-view offset, the kinematics of the SPTZ are deduced from regional estimates of differential shortening on either side of its trace. In a map-scale kinematic reconstruction, van Hinsbergen et al. (2020) proposed a scissor-like closure of the Pindos ocean in the Hellenides, a branch of Neotethys that was the along-strike equivalent of the Krasta-Cukali basin in the Albanian Hellenides and southern Dinarides. Today, the Krasta-Cukali nappe with its pelagic Jurassic sediments (Nieuwland et al. 2001) reaches just to the NW of the SPTZ where it pinches out (Fig. 2.1b).

The question remains why a prominent fault like the SPTZ with such a large lateral offset left no discernible traces in the field, e.g., striated, NE-SW trending fault surfaces that cut across the orogen. A possible clue is that the offset of the ophiolite front marking the SPTZ reaches from the base of the internal Dinarides to the front of the Shkoder Klippe and no further, certainly not to the present orogenic front. The external Dinaric nappes (Pre-Karst, High-Karst, Krasta-Cukali, Kruja, Ionian) are Eo-Oligocene in age (Fig. 2.11 and references in figure caption). Their basal thrusts have undergone Mio-Pliocene reactivation (van Unen et al. 2019) and some are probably still active today (Bennett et al. 2008). Van Hinsbergen et al. (2020) estimate a minimum 30 km of thrusting of the High Karst nappe onto the Krasta-Cukali nappe in the last 5 Ma. This thrust in particular is therefore younger than the Eocene dextral displacement on the SPTZ. We therefore propose that it buried the trace of the SPTZ, whose SW end must be located in a part of the Krasta-Cukali nappe beneath the High Karst nappe, somewhere just to the north of the Shkoder Klippe as depicted in Figs. 2.1 and 2.3. Higher units in the Dinaric nappe stack also preserve no traces of the SPTZ, ostensibly because they were deformed or eradicated by subsequent Cukali doming and normal faulting along the SPNF. We note that dextral offset may have overlapped in time with SW-directed out-of-sequence thrusting in the Internal Dinarides, suggesting that the shortening associated with this thrusting may have accommodated the dextral offset (Fig. 2.11).

Shkoder-Peja Normal Faulting (SPNF)

The segments of the SPNF described in *Structures and kinematics* cut and therefore post-date the folded Dinaric nappe stack (Figs. 2.10a and 2.11) which had formed no later than late Eocene time according to the youngest ages of orogenic flysch below the basal thrusts of these nappes (Fig. 2.12, references in figure caption, Schmid et al. 2008). The Cukali and Decani Domes, respectively in the footwalls of the Cukali-Tropoja Fault and Decani Shear Zone, deform these folds. A brittle segment of the Cukali-Tropoja Fault cuts the NE end of the Cukali Dome (Fig. 2.4, profile A-A´, Fig. 2.10a) and the Tropoja Dome (Fig. 2.4 profile D-D´, Fig. 2.10d). Mylonitic shearing along the Decani Shear Zone facilitated extensional exhumation of the

Decani Dome as deduced from the bending of the main schistosity into the mylonitic shearing plane of the Decani Shear Zone (Figs. 2.6, profiles E-E'& F-F' and Fig. 2.7). These geometric relations suggest that doming and faulting along the SPNF were broadly coeval, with a brittle component of faulting locally outlasting doming. However, in the absence of a clearly exposed fault linking the Cukali-Tropoja Fault, NW Kosovo Fault and Decani Shear Zone to the well-dated Dukagjini Fault bordering syn-rift, mid-to-late Miocene clastics and lacustrine sediments in the West Kosovo Basin (*Structures and kinematics*), we are left with indirect kinematic and rock-mechanical arguments to constrain the age of these segments of the SPNF.

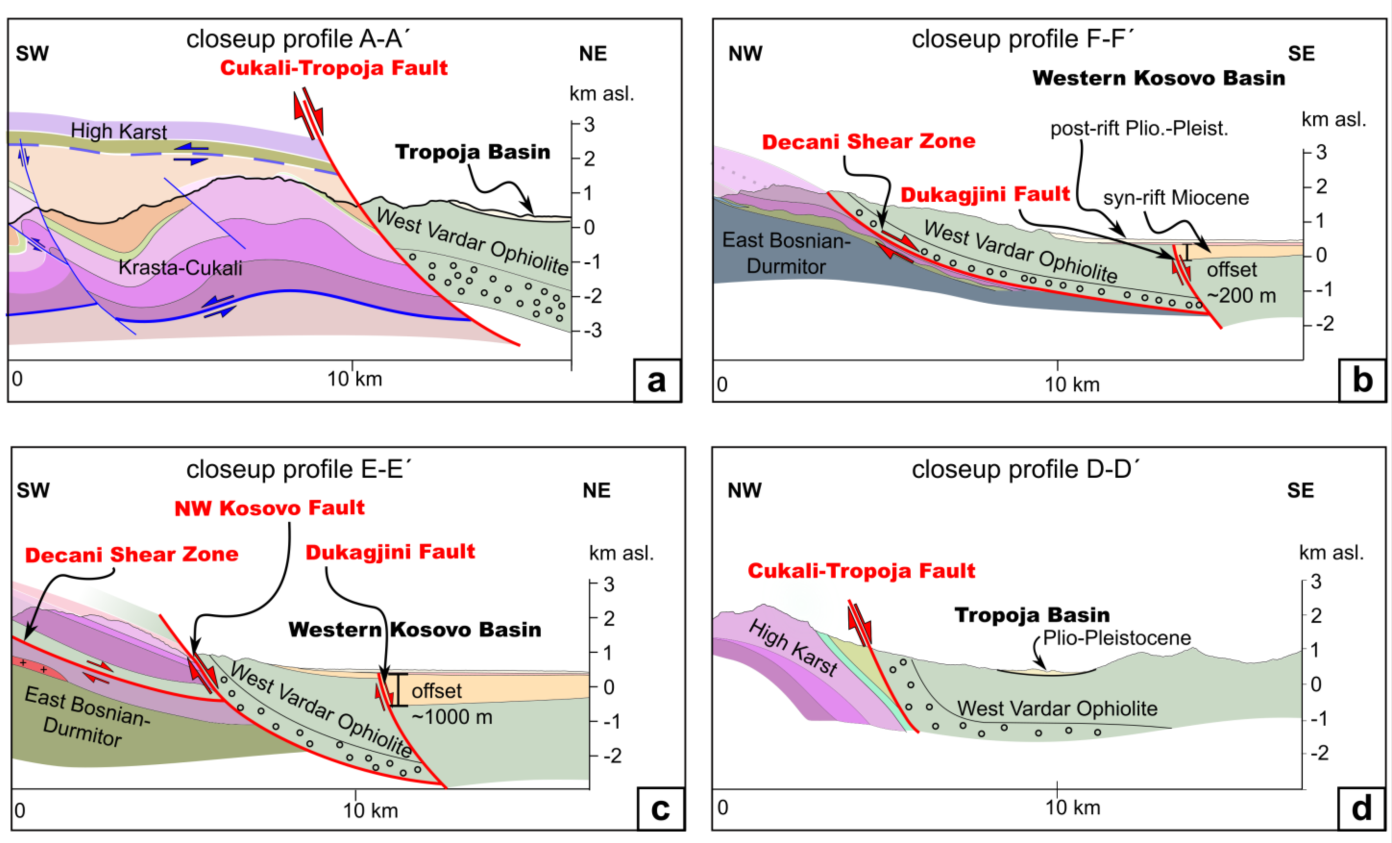

Fig. 2.10: Key parts of profiles in Figs. 2.4 and 2.6 that constrain the age of the SPNF system. Legend and traces of profiles shown in Fig. 2.3: (a) Cukali-Tropoja Fault cuts mid-Eocene to early Oligocene Dinaric thrusts and folds; (b & c) Decani Shear Zone cuts Dinaric folds and thrusts and thus has a similar younger age relative to doming and thrusting as the Cukali-Tropoja Fault. The NW Kosovo Fault cuts the Decani Shear Zone at depth and is thus younger. Both the Decani Shear Zone and NW Kosovo Fault are cut by the mid-Miocene Dukagjini Fault that borders the Western Kosovo Basin. Post-rift Plio-Pleistocene sediments seal the Dukagjini Fault and unconformably overlie syn-rift Miocene sediments; (d) Plio-Pleistocene Tropoja Basin in the hanging wall of the Cukali-Tropoja Fault seal this fault segment.

The ductile style of the post-nappe folds in the footwall of the SPNF offer a clue, because, as discussed above, these folds indicate temperatures of folding at least as high as the minimum temperature for viscous creep of calcite-rich rocks (c. 180°C, Schmid et al. 1980, 1981). This indicates that the SPNF syn- to post-dated metamorphism in its footwall. This metamorphism must be older than the Eocene ages yielded by fission track studies of apatite (annealing T of 110-60°C, Gallagher et al., 1998; Malusà & Fitzgerald, 2018) from sparce samples on either side of the Cukali-Tropoja Fault segment (Muceku et al. 2008). Taken together, the structural and metamorphic relations above suggest that the Cukali-Tropoja Fault and Decani Shear Zone were active sometime between late Paleogene (Eo-Oligocene) and early Miocene time.

The Istog (Fault) segment of the SPNF along the western and northern perimeter of the West Kosovo Basin is also inferred to have been active during this period as it cuts the Dinaric thrust contact of the Drina-Ivanjica nappe onto the East Bosnian-Durmitor nappe (Fig. 2.3). The brittle NW Kosovo fault re-activated this nappe contact as a top-E to -SE normal fault, which is consistent with a similar late Paleogene-early Miocene age range. However, it also cuts both the ENE-dipping West Vardar Ophiolite and the unconformably overlying Miocene cover in its hanging wall near the city of Peja (Figs. 2.3 and 2.6, profiles E-E`& G-G`), indicating that it accommodated post-Miocene motion as well. Combined with the WNW-ESE strike of the NW Kosovo Fault, this young re-activation age suggests that the NW Kosovo Fault truncates the Decani Shear Zone at depth (Fig. 2.10c) and possibly connects with the Dukagjni Fault beneath the Western Kosovo Basin (Figs. 2.3, 2.6, 2.9). We therefore speculate that parts of the SPNF were reactivated during opening of this basin in mid-late Miocene time. Tilted Mio-Pliocene basin fill (dipping ENE) in the footwall of the Dukagjini Fault as well as in the hanging wall of the NW Kosovo Fault near Peja (Figs. 2.8f and g) document a possible recent activity of part of the NW Kosovo Fault.

Pliocene (5.3 Ma) and younger sediments seal normal faults and mark the end of activity of the Dukagjini Fault in the Western Kosovo Basin. An absolute upper stratigraphic age limit on the SPNF comes from horizontal Pleistocene-Holocene sediments in the northwestern part of the Tropoja Basin that seal the Cukali-Tropoja Fault (Figs. 2.10d and Fig. 2.5b, (Gemignani et al. 2022)

In summary, we distinguish two phases of normal fault along the SPNF: an early phase of E-W to ESE-WNW directed extensional faulting and footwall doming that occurred sometime during Eo-Oligocene to early Miocene time, and a late phase of ESE-WSW directed extensional faulting in mid-to-late Miocene time involving syn-rift sedimentation in the hangingwall of the Dukagjini Fault and tectonic subsidence of the Western Kosovo Basin. We cannot yet ascertain whether these two phases were continuous or not. However, the local overprinting of mylonite by cataclasite along the SPNF suggests that the two phases may have been discontinuous in early-to-mid Miocene time, with the later phase locally reactivating older segments of the SPNF.

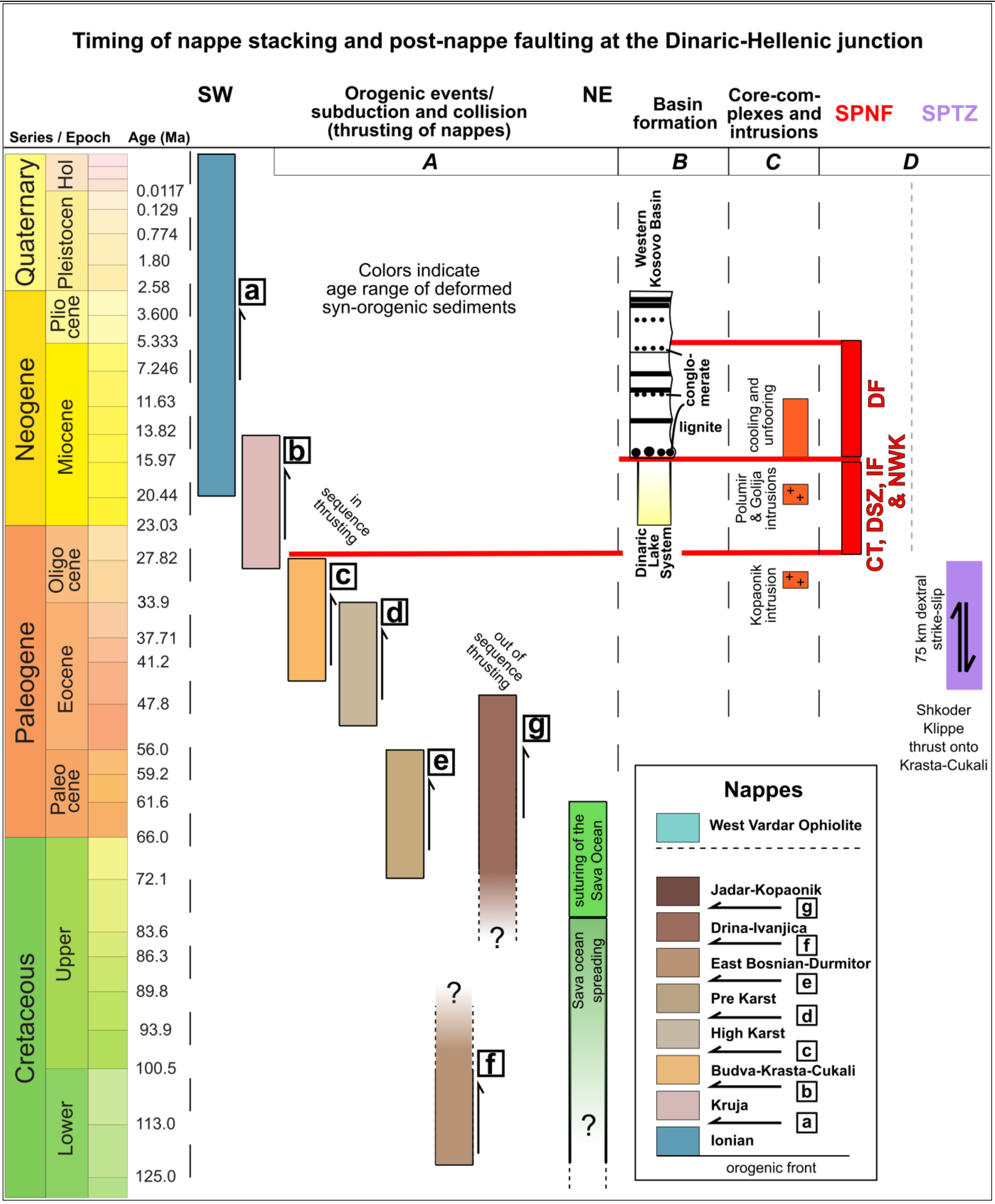

Fig. 2.11: Ages of geological events at the Dinaric-Hellenic transition: (A) Age of thrusting of Dinaric nappes, with colors indicating the age range of deformed syn-orogenic sediments in the nappes and lowercase letters indicating time when nappe was emplaced onto next lower nappe according to stratigraphic ages in footwall of basal thrusts (Cohen et al., 2021; Hinsbergen et al., 2020; Porkoláb et al., 2019; Schmid et al., 2008, 2020); (B) Sedimentation of Western Kosovo Basin (Legler et al. 2006; Elezaj and Kodra 2012) and Dinaric Lake System (van Unen et al. 2019); (C) Magmatism in the Kopaonik and Studenica core complexes (Schefer et al. 2011; Schefer 2012) and related core-complex formation and cooling; (D) Activity of segments of the SPNF and the SPTZ (Shkoder Peja Transfer Zone) as constrained by arguments in the text (Handy et al., 2019; Knobloch et al., 2006; Linder & Perkuhn, 2013). Fault segments: CT = Cukali-Tropoja Fault, DSZ = Decani Shear Zone, IF = Istog Fault, NWK = NW Kosovo Fault, DF = Dukagjini Fault. It remains a matter of speculation whether or not 1st and 2nd phases of activity of the SPNF were distinct or continuous. See text and references therein regarding age of thrust front of the West Vardar Ophiolite and the emplacement of the Shkoder Klippe.

A model for arc-parallel extension and orogenic arcuation

Figure 2.12 depicts the tectonics of the Dinaric-Hellenic mountain belt at four critical time slices in the evolution (Fig. 2.11) of the orogenic junction. In developing these maps, we used the kinematic reconstruction of van Hinsbergen et al. (2020) as a template and modified it according to the new structural, kinematic and age constraints in this paper. We thus depart from the authors` kinematic treatment of tectonic nappes as rigid bodies (e.g. Gurnis et al., 2012) that undergo translation and rotation, and instead consider primarily the motions of local orogenic structures with respect to stable Europe as constrained by the available geological and paleomagnetic criteria. Besides the SPTZ and SPNF, these structures include the orogenic front, the leading edge of the West Vardar Ophiolite and the Adria-Europe (Sava) suture.

Onset of strike-slip motion on the SPTZ

Figure 2.12a depicts the paleotectonic situation at 45 Ma, at or just before the onset of dextral shearing along the SPTZ when the Shkoder Klippe was emplaced onto the Paleogene Krasta-Cukali nappe. By that time, the orogenic front had reached the SW edge of this unit as documented by the youngest age of orogenic flysch deposited in the foredeep beneath its basal thrust (Fig. 2.11). The configuration of the leading edge of the West Vardar Ophiolite in Fig. 2.12a depends on the relative amounts of pre-Eocene (late Cretaceous?) shortening of the Dinarides and NW Hellenides (Handy et al. 2019). We have adopted a straight-line configuration parallel to the orogenic strike, but regard this geometry as speculative given the poor constraints on shortening on either side of the SPTZ (*Age and kinematics of faulting, doming and basin formation*). Nevertheless, localization of strain at this junction is possible in light of the Mesozoic facies change that already prompted (Aubouin and Dercourt 1975) to propose a transfer fault (their “transversale de Scutari-Pec”) formed during Late Triassic-Early Jurassic rifting of the Adriatic continental margin prior to the opening of the Sava Ocean branch of the Neotethyan ocean (e.g., Schmid et al. 2008). Our configuration differs from that of van Hinsbergen et al. (2020) who show a sinistral offset of some 30 km for the same time slice at 45 Ma. They arrive at this offset based on pre-late Paleogene differential shortening in the southern Dinarides (180 km comprising 30 km from 85-55 Ma (Tari 2002; Hrvatović and Pamić 2005) plus 150 km in the external Dinarides from 55-33 Ma and Hellenides (120 km for the Pelagonian and Pindos nappes in mainland Greece, e.g. Skourlis & Doutsos, 2003). If valid, this pre-Paleogene sinistral motion would necessitate an even greater amount (105 km) of subsequent dextral offset on the SPTZ to obtain the observed 75 km. This seems unwarranted in light of the poor constraints on offset and shortening, particularly in the northwestern Hellenides (van Hinsbergen et al. 2020).

Dextral shearing and clockwise arcuation

By 30 Ma (Fig. 2.12b), dextral shearing on the SPTZ was ending or had already ceased according to the age constraints discussed in the previous section and summarized in Figure 2.11. The dextral offset of part of the nappe stack between the Krasta-Cukali and Drina-Ivanjica nappes is attributed to subduction of the Pindos (ocean) Basin, a branch of Neotethys preserved in the Hellenides that is the along-strike equivalent of the pelagic Budva-Krasta-Cukali unit in the Albanian Hellenides and southern Dinarides. Evidence of this subduction in the Hellenides is preserved in Eo-Oligocene turbidites of the Meso-Hellenic Basin (Figs. 2.1 and 2.12b) which Ferrière et al.(2004) have interpreted as fore-arc deposits. Today, the Budva unit, part of the Krasta-Cukali-Pindos unit at the NW end of this nappe, reaches just to the NW of the SPTZ in Montenegro. This unit represents a tiny part of the basin that was stranded during closure. Subduction of the Budva-Krasta-Cukali-Pindos lithosphere in Paleogene time (e.g., Schmid et al. 2020) involved decreasing amounts of shortening from SE to NW along the chain (van Hinsbergen et al. 2020, their Figs. 36 and 37), necessitating a clockwise rotational pole in addition to dextral strike-slip in the vicinity of the SPTZ (green star in Fig. 2.12a). We note that the large dextral offset along the SPTZ in Figure 2.12b, which is basically constrained by today´s map view of the West Vardar Ophiolite front (Fig. 1), differs radically from the lack of any offset in the reconstruction of van Hinsbergen et al. (2020, their Fig. 36) for the same time slice at 30 Ma. This pronounced offset is attributed to an inherited structure, either an old (Paleozoic?) fault in the basement or a large transverse fault formed during early Mesozoic rifting (Aubouin and Dercourt 1975). In Figure 2.12a, a jog in the boundary between the Kruja and Krasta-Cukali units (red dashed line south of future SPTZ) of the subducting Adriatic margin is drawn to reflect an inherited transfer fault.

Oligo-Miocene magmatism and the first phase of SPNF activity

A major event at 30 Ma was the intrusion of late Paleogene-early Neogene calc-alkaline magmatites (Andrić et al., 2018; Schefer et al., 2011 and references therein) depicted in Figure 2.1 and 2.12b by the coloured domain with ages spanning 37-22 Ma and oriented oblique to the internal Dinarides, Carpatho-Balkan and Rhodopes mountains. The location of this domain at 30 Ma was obtained by backrotating it from its present location (Figs. 2.1a and 2.12) to van Hinsbergen et al. (2020)´s reconstructed position of the nappe units.

This magmatism in the upper plate of the Dinaric-Hellenic orogen has been attributed to lithospheric delamination (Schefer et al. 2011) and/or subsequent detachment (breakoff) of the Adriatic slab in response to a late Oligocene decrease in the Adria-Europe convergence rate (Handy et al. 2015). Slab detachment is a viable mechanism to explain two other striking features of the Dinaric orogen in the study area: First, the absence of Oligocene strata (Meier 2012) beneath the lower-middle Miocene unconformity in the Western Kosovo Basin (Figs. 2.6 and 2.8), which signifies pre-middle Miocene uplift and erosion. Second, the formation of latest Oligocene-Miocene metamorphic core complexes in the vicinity of the Sava suture: the Bukulja, Kopaonik, Studenica, and Jastrebac core complexes in Figs. 2.1b, 2.12b (Marović et al. 2007; Schefer et al. 2011; Stojadinovic et al. 2013, 2016; Mladenović et al. 2015; Erak et al. 2016). Both features are interpreted as a manifestation of uplift and extension of the upper plate in response to asthenospheric upwelling in the aftermath of slab detachment.

The proximity of the northeastern end of the SPNF to the Oligo-Miocene magmatic domain associated with the aforementioned core-complexes, (Figs. 2.1b, 2.11, 2.12b), suggests a causal relationship between slab detachment beneath the Dinarides and the onset of orogen-parallel extension at the Dinaric-Hellenic junction. We propose that the first phase of SPNF activity involving SE- to SSE-directed extension along the Cukali-Tropoja, Decani, NW-Kosovo and Istog Fault segments accommodated orogen-parallel stretching. We speculate that this occurred as subduction of the undetached part of the Adriatic slab beneath the Hellenic part of the orogen (Handy et al. 2019) retreated rapidly from NE to SW (Brun & Sokoutis, 2010; Burchfiel et al., 2008; Royden & Papanikolaou, 2011). Post late-Oligocene rollback subduction accompanied by stretching and calc-alkaline magmatism in the upper plate were faster in the Hellenides and Aegean region than in the Dinarides, where the slab had detached, thus reducing slab pull forces (Handy et al. 2019).

North of the SPNF, early to middle Miocene half-grabens with extensive magmatism that young from NE to SW across the internal (Matenco and Radivojević 2012) and external Dinarides (Andrić et al., 2017; van Unen et al.,2019) towards the Dinaric foreland document E-W orogen-normal extension (Fig. 2.12c). This involved significant local exhumation, for example, ~8 km in the footwall of a normal fault bounding the asymmetrical Sarajevo Basin near Sarajevo (Figs. 2.1a, 2.12d; van Unen et al., 2019). Following Matenco and Radivojević (2012), we attribute this early- to mid-Miocene extension to SW-directed delamination of the undetached part of the Adriatic slab beneath the Dinarides and/or to eastward pull of the extending Pannonian Basin to the east (Handy et al. 2019).

Second phase of SPNF activity and Miocene basin formation

The middle Miocene (Fig. 2.12c) ushered in a change in the nature of crustal stretching. Whereas the first phase of extension along the SPNF was accompanied by uplift and erosion as indicated by the lower-middle Miocene unconformity in the Western Kosovo Basin, stretching thereafter was marked by subsidence and basin filling. This basin and others like it (e.g., Burrell and Librazhd Basins, Xhomo et al. 2002; northernmost end of the Meso-Hellenic Basin, Ferrière et al. 2004, Kallanxhi & Ćorić, 2017; locations in Figs. 2.1, 2.2 and 2.12c) are bounded by normal faults, which like the subsurface Dukagjini Fault, are all located in the hanging wall of the main SPNF segments exposed at the surface. Though these older faults may have remained active under brittle conditions (cataclastic overprint described in *Structures and kinematics*), most extensional faulting from middle to late Miocene time had migrated into the hanging wall of the SPNF. Together, these normal faults accommodated coeval E-W and NW-SE extension (Handy et al. 2019). This biaxial extension has also been described in the central Southern Balkan region (central Albania and eastern Macedonia), which formed the upper plate of the retreating Hellenic orogen and subduction interface in Miocene time (Burchfiel et al. 2008). Subsequent subsidence and lacustrine deposition in Pliocene time outlasted mid-late Miocene normal faulting (*Structures and kinematics*, Fig. 2.9, profile H-H´).

Minor folds and thrusts indicative of post middle-late Miocene S-directed shortening in the Western Kosovo Basin (*Structures and kinematics*, Fig. 2.8d) corroborate fault-slip analyses indicating latest Miocene, NNE-SSW-directed shortening well to the north of the SPNF in the central Dinarides (Unen et al. 2019). The causes of this shortening are debatable. An attractive possibility is that it is related to a short-lived increase in the rate of Adria-Europe convergence in latest Miocene time. This may have induced shortening that was transmitted across the orogenic front to the thinned upper plate of the Hellenides. However, this scenario remains speculative in the absence of studies on the areal extent of late shortening structures.

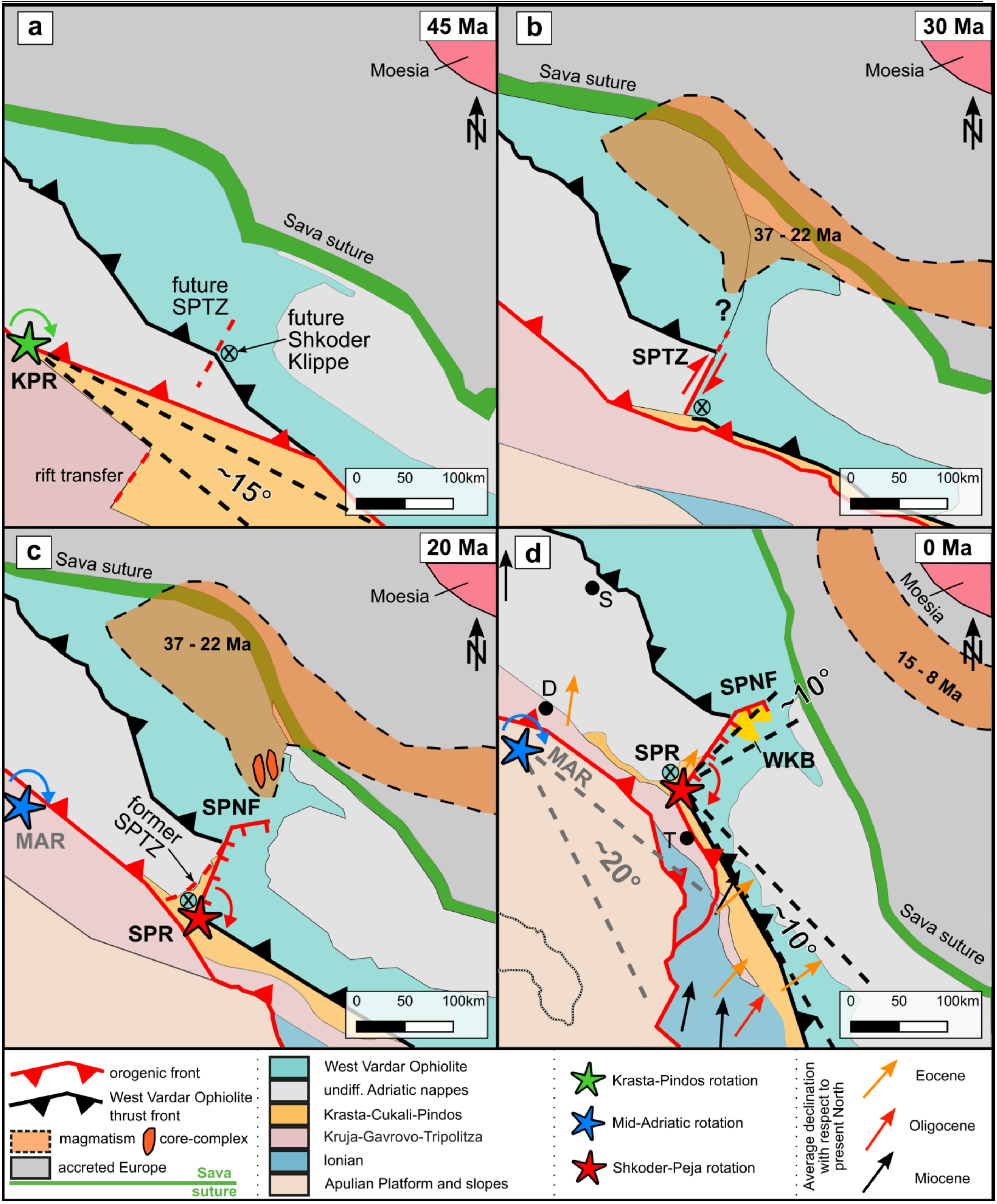
a
45 Ma
Moesia
Sava suture
future SPTZ
future Shkoder Klippe
KPR
rift transfer
~15°
0 50 100km
b
30 Ma
Moesia
Sava suture
37 - 22 Ma
?
SPTZ
0 50 100km
c
20 Ma
Sava suture
Moesia
37 - 22 Ma
SPNF
former SPTZ
MAR
SPR
0 50 100km
d
0 Ma
S
Moesia
15 - 8 Ma
D
SPNF
~10°
SPR
WKB
MAR
T
~20°
~10°
Sava suture
0 50 100km
N
orogenic front
West Vardar Ophiolite thrust front
magmatism
core-complex
accreted Europe
Sava suture
West Vardar Ophiolite
undiff. Adriatic nappes
Krasta-Cukali-Pindos
Kruja-Gavrovo-Tripolitza
Ionian
Apulian Platform and slopes
Krasta-Pindos rotation
Mid-Adriatic rotation
Shkoder-Peja rotation
Average declination with respect to present North
Eocene
Oligocene
Miocene

Fig. 2.12: Kinematic evolution of the Dinaric-Hellenic junction and associated fault structures from 45 Ma to Present: (a) At 45 Ma, onset of rollback subduction of the Krasta-Cukali-Pindos basin and ocean around a clockwise rotational axis (green star) marked KPR (Krasta-Cukali-Pindos). Rotation estimated to be ~15° (see text). Dashed red line marks the future SPTZ at the site of accretion of a proposed Mesozoic rift transfer fault (dotted red line) between the Kruja and Budva-Krasta-Cukali domains of the Adriatic margin; (b) At 30 Ma, activity of the SPTZ has just ceased after 75 km of dextral offset of the thrust front of the West Vardar Ophiolite. Magmatism, uplift and erosion affect internal units of the Dinarides. The orogenic front has reached the base of the Krasta-Cukali nappe; (c) At 20 Ma, the first phase of activity of the SPNF (27-20 Ma) is ongoing. The second phase (16 Ma-Present) is about to begin. Magmatism and extension along core complexes (orange). Extensional faulting involves a ~10° clockwise rotation of the Hellenic nappes with respect to the Dinarides around a crustal rotational axis (red star) marked SPR (Shkoder-Peja rotation pole). This entails the formation of the Western Kosovo Basin (WKB) in the hanging wall of the Dukagjini Fault. Orogenic bending of ~20° occurs about a lithospheric plate rotation pole (blue star) marked MAR (Mid-Adriatic rotation pole). The orogenic front has reached the base of the Kruja nappe; (d) Present-day situation with the SPNF separating oblique dextral collision in the SW-Dinarides from rollback subduction and clockwise rotation of the NW Hellenides. The orogenic front has reached the base of the Ionian nappe. Apulian Platform and slope deposits after Bernoulli (2001). Coloured arrows indicate average paleomagnetic declinations in variously aged sediments with respect to present north. Orange arrow = Eocene; red arrow = Oligocene; black arrow = Miocene (modified from Handy et al. 2019, their Fig. 11; de Leeuw et al., 2012; Márton et al., 2003, 2014 and references therein). Cities: T = Tirana; D = Dubrovnik; S = Sarajevo. Structures in all maps modified extensively from van Hinsbergen et al. (2020).

Arcuation of the Dinaric-Hellenic orogen, timing and amount of rotations

We now return to the questions posed in the introduction regarding activity of the SPNF and its relationship to the mechanisms of orogenic arcuation at the Dinaric-Hellenic junction. The kinematics of faulting at this junction require two vertical rotation axes. The first axis was situated at or near the SPTZ, at NE end of the Krasta-Cukali-Pindos unit (Fig. 2.12a, b) that was mostly subducted beneath the previously accreted High Karst, Pre-Karst and Pelagonian units in Eo-Oligocene time. The amount of subduction increased to the SE away from this axis, calling for clockwise rotation about this axis (Fig. 2.12b). The second axis was located at the SW end of the SPNF in Oligo-Miocene time (Fig. 2.12c), where Oligo-Miocene extension increasing from 0 along the SPNF to the NE, met coeval shortening increasing to the S along the Albanian Hellenides (*Structures and kinematics* and Handy et al. 2019). This requires clockwise rotation of units in the hanging wall of the SPNF above its basal decollement which, as shown above, must have been located within the Krasta-Cukali unit of the Paleogene Dinaric-Hellenic nappe stack.

A third, even more important rotation axis has been identified at or near the Mid-Adriatic Ridge (MAR, Figs. 2.1, 2.12 c and d) based on the progressive increase in Miocene shortening to the S, away from this axis and along the active orogenic front at the base of the Ionian nappe (Handy et al. 2019 and references therein). Following D’Agostino et al. (2008), Handy et al. (2019) inferred this to be the rotation pole for Miocene-to-recent segmentation of the Adriatic plate into counter-rotating northern (counterclockwise) and southern (clockwise) subplates, respectively named Adria sensu stricto (s.s.) and Apulia.

The rotation angles at these three vertical axes can be estimated from the amount of shortening and/or extension on the faults emanating from them. For the Eo-Oligocene axis at the northwestern end of the Krasta-Cukali-Pindos basin (Fig. 2.12a), a counterclockwise rotation of 15° is obtained from the reconstructions of the Krasta-Cukali-Pindos unit at 45 and 30 Ma. In the case of the Oligo-Miocene SPNF axis (Fig. 2.12c), a clockwise angle of <10° is obtained by resolving the combined vertical throws of the Cukali-Tropoja and Dukagjini Faults of ~ 3500 m at their NE ends onto the 30° SE-ward dip of the SPNF to obtain a horizontal extension (*Structures and kinematics*) of ~ 6 km. Of course, clockwise rotations > 10° are possible, and even likely, given the fact that all estimates of throw, and therefore also of SE-directed extension on SPNF segments to the NE of the Cukali-Tropoje segment, are minima (Fig. 2.2a). In actuality, this system of faults is expected to have accommodated much more SE-directed extension in Oligo-Miocene time.

Comparing the kinematically constrained rotations above with rotation estimates derived from paleomagnetic studies in the southern Dinarides and NW Hellenides lends insight into the timing, location and amount of orogenic arcuation. In a summary of previously published paleomagnetic data, Handy et al. (2019 and references therein, their Fig. 11) showed that the Dinaric-Hellenic orogen south of Dubrovnik (Fig. 2.1) has undergone ~50° of clockwise rotation relative to north since late Eocene-Oligocene time. This is indicated in Figure 2.12d by orange arrows for paleo-declination directions in Eocene sediments (references in caption). Even considering aggregate error in paleomagnetic calculations, the estimate 50° of rotation exceeds the observed 30° clockwise bend of the Dinaric-Hellenic junction by some 20°. Most, if not all, of this discrepancy can be attributed to the initial counterclockwise rotation of 15° associated with Eocene subduction of the Krasta-Cukali-Pindos unit, reducing the amount of post-Eocene clockwise rotation to 35° (i.e., 50°-15°). This leaves about 5° of clockwise rotation unaccounted for, an amount which can be attributed to the combined uncertainties in the paleomagnetic estimates and the kinematic reconstruction of van Hinsbergen et al. (2020) used to estimate the Krasta-Cukali-Pindos subduction.

The black paleo-declination arrows in Figure 2.12d show that since the beginning of the Neogene at 24 Ma, the Hellenic part of the orogen south of the SPNF has rotated clockwise by ~20° with respect to north and to the Dinarides. The latter have not rotated with respect to Europe since this time (de Leeuw et al. 2012). A 20° rotation is broadly consistent with the clockwise oroclinal bending angle of ~30° that was independently determined from contrasting estimates of orogen-normal Neogene shortening to the NW (10 km) and SE (100 km) of the SPNF (Handy et al. 2019).

Conclusions

The open bend in the Dinaric-Hellenic orogen coincides with an orogen-parallel change in the mode of plate convergence, from oblique collision in the Dinarides to retreating subduction and slab rollback in the Hellenides. Our investigation reveals that this 30° orogenic bend (Fig. 2.1) is marked by two kinematically and temporally distinct structures: the Eo-Oligocene Shkoder-Peja Transfer Zone (SPTZ) that effected ~75 km of dextral offset, and the late Oligo-Miocene Shkoder-Peja Normal Fault (SPNF) that accommodated orogen-parallel extension and contributed to clockwise orogenic bending. The SPTZ is overprinted by the younger SPNF, but nevertheless manifested by the anomalous position of a small klippe of West Vardar Ophiolite that was emplaced onto the Late Cretaceous-Paleogene Dinaric nappe stack just east of the current orogenic front, near the city of Shkoder (Figs. 2.2 and 2.4).

The SPNF is a composite structure with five normal fault segments (Fig. 2.3): Four of these segments make up the main branch of the SPNF and transect the orogen. They juxtapose West Vardar Ophiolite in their hanging walls with domes in their footwalls (Figs. 2.3, 2.4 and 2.6). These domes comprise folded and metamorphosed Dinaric nappes that were partly exhumed under conditions ranging from lower greenschist-facies to anchizonal conditions, during top-down-SE ductile-to-brittle shearing on the normal fault surfaces.

The amount of top-SE throw on the SPNF is poorly constrained, with estimates ranging from 0 m near Shkoder to a minimum of 2500 m to the NE (Fig. 2.2), though other segments further to the NE appear to have accommodated less (minimum of 800 m). The general increase of downthrow from SW to NE is consistent with the idea of Handy et al. (2019) that the SPNF accommodated clockwise rotation about a crustal rotation pole situated at the SW end of the fault. The fifth segment of the SPNF (the Dukagjini Fault) lies buried beneath Plio-Pleistocene sediments of the Western Kosovo Basin (WKB, Figs. 2.2 and 2.3). It offsets mid-late Miocene syn-rift clastics and lacustrine sediments by some 1000 m (Figs. 2.6, 2.9, 2.10). The Dukagjini Fault is conjugate to another subsurface normal fault (Prizren-Vranica Fault, Fig. 2.3) bordering the same Miocene syn-rift sedimentary package in the SE part of the Western Kosovo Basin (Fig. 2.3). These sediments were locally affected by minor, post-late Miocene thrusting that appears unrelated to motion on the SPNF (Fig. 2.8).

As a whole, the SPNF and its related segments accommodated E- to SE-directed extension (Figs. 2.6 and 2.7) between 27-5 Ma (Fig. 2.11). Based on overprinting structural relations in *Structures and kinematics*, we tentatively distinguish an early phase of activity on the four main fault segments transecting the orogen beginning in Oligocene time, from a later phase on the Dukagjini Fault beginning in Mid-Miocene time and ending no later than the beginning of the Pliocene (Figs. 2.3, 2.8, 2.9 and 2.11). At present, there are no criteria to determine whether these two phases were continuous, discontinuous or overlapped in time. However, Miocene extension appears to have migrated into the hanging wall of the four initial fault segments and ended along the fifth (Dukagjini Fault) segment.

The recognition of the SPTZ and SPNF as separate structures (Handy et al. 2019) differs from previous notions of the bend in the Dinaric-Hellenic orogen as the site of a single tectonic lineament, often referred to simply as the Scutari-Pec Lineament (e.g. Kissel et al., 1995; Walcott & White, 1998). Although paleomagnetic studies already pointed to this lineament as the locus of Cenozoic clockwise rotation of the northwestern Hellenides with respect to the Dinarides (e.g.,de Leeuw et al., 2012) and Europe (van Hinsbergen et al., 2005; Kissel & Speranza, 1995; Speranza et al., 1995), our field-based work provides a more differentiated view of the timing and kinematics of this rotation.

In a reconstruction of plate kinematics since 45 Ma (Fig. 2.12), we attribute the dextral offset along the SPTZ to the reactivation of an inherited Early Mesozoic rift transfer fault in the Adriatic margin (sensu Aubouin & Dercourt 1975) during Eocene accretion and subduction of the Krasta-Cukali basin and Pindos ocean. The closure of this ocean, an arm of Neotethys, involved a clockwise rotation of ~15° about a vertical axis located at or near the junction of the Dinarides and Hellenides between 45 and 30 Ma. The initiation of this rotation may have been kinematically linked to the onset of back-arc extension and slab rollback in the southern Hellenides (Aegean) at 45 Ma (Brun et al. 2016).

From 27 Ma onwards, the SPNF contributed ~10° of crustal rotation during orogen-parallel extension (Figs. 2.12c and d). It is tempting to relate the first phase of motion on the SPNF to Oligo-Miocene magmatism, crustal extension (including core complexes, Fig. 2.1) and uplift of the internal Dinarides. We speculate that these events were triggered by delamination and/or detachment of the Adriatic slab beneath the Dinarides (Schefer et al. 2011; Andrić et al. 2018). The second phase of motion on the SPNF beginning in mid-Miocene time was associated with basin subsidence (e.g., formation of the Western Kosovo Basin) and continued clockwise rotation of the Paleogene nappe stack in the NW Hellenides. Only parts of this rotation has been taken up by structures that relate to the SPNF system at the Dinaric-Hellenic junction, because the SPNF only affected the Paleogene nappe stack (Figs. 2.2 and 2.3), not the entire orogenic lithosphere (Handy et al. 2019). Most of the Miocene and younger bending of the orogen was accommodated by ~20° clockwise rotation about a vertical axis in the vicinity of the Mid-Adriatic Ridge (Figs. 2.12c and d) based on a compilation of paleomagnetic, seismological (Handy et al., 2019 and references therein) and geodetic work (D'Agostino et al. 2008).

Insight into the causes of Neogene orogenic bending come from previously published teleseismic P-wave tomography (Fig. 2.1b, Hall & Spakman, 2015) showing that the Dinarides-Hellenides junction straddles a short (150 km) relic of the previously torn Adriatic slab under the southern Dinarides, and a much longer (>400 km), ostensibly untorn part of this slab beneath the NW Hellenides (e.g., Piromallo & Morelli, 2003; Wortel & Spakman, 2000). The torque resulting from downward pull of the longer retreating part of the slab beneath the Hellenides is a compelling mechanism to explain clockwise orogenic bending and orogen-parallel extension localized at the SPNF during Neogene subduction rollback (Handy et al. 2019). The Paleogene component of bending associated with earlier closure of the Krasta-Cukali basin and Pindos ocean may have had a similar cause, even though with a shorter slab exerting downward pull.

Acknowledgments

This study was financed by German Research Foundation (DFG, grant No. Gi 825/4-1; No. Ha 21/21-1; No. Pl 534/3-1), Freie Universität Berlin and PROMOS (DAAD). Zenun Elezaj, Sali Mulaj, Philip Groß, Benjamin Schmitz, Peter Biermanns, Stefan Schmid and Kamil Ustaszewski are thanked for discussions in the field and thereafter. Sascha Zertani, Philip Groß, Lisa Kaatz and Leonardo Caprioli, Sebastian Cionoiu mapped extensively for their BSc and MSc projects and we appreciate the input from their theses in our work (Fig. 2.2b). Eline Le Breton helped us by using G-Plates to export and process van Hinbergen et al. (2002)´s model for our time slices in Fig. 2.12. Finally, we acknowledge the work of student participants in mapping classes in Albania since 2012. GIS work and graphics were designed with open-source software *QGis* and *Inkscape*.

Chapter III: Thermal record of obduction, nappe stacking and orogen-parallel extension at the Dinaric - Hellenic junction

Submitted soon in a peer-reviewed journal

Marc U. Grund[1], Jörg Giese[2], Lorenzo Gemignani[1], Mark R. Handy[1], Jan Pleuger[1], Edward Sobel[3], Sascha Zertani[4], Julian Hülscher[1], Philip Groß[5] & Hannah Pomella[6]

(1) Freie Universität Berlin, Institute of Geological Sciences, Berlin, Germany, (2) Geological Survey of Norway -NGU- Trondheim, Norway, (3) University Potsdam, Institute of Geosciences, Potsdam, Germany, (4) University of Oslo, Department of Geosciences, Oslo, Norway, (5) Heidelberg University, Earth Sciences, Heidelberg, Germany, (6) University Innsbruck, Department of Geology, Innsbruck, Austria

Abstract

We present new thermochronological constraints on the age of ophiolite obduction, Dinaric nappe stacking, orogen-parallel extension and arcuation, and basin formation at the junction of the Dinaric and Hellenic orogens. Two prominent structural domes, the Decani and Cukali Domes that exhumed the Dinaric nappe stack in the footwall of the Shkoder-Peja Normal Fault system (SPNF), mark this junction. The highest nappe comprises ophiolite of the Vardar ocean, a branch of Neotethys, which presently underlies the Neogene West Kosovo Basin in the hanging wall of the SPNF.

Peak-metamorphic temperatures of ~280°C from RSCM analysis of shales in the sub-ophiolitic mélange of this ophiolite nappe were attained during latest Jurassic-Early Cretaceous time, followed by cooling <180°C ((U/Th)-He zircon ages; ZHe) in Cretaceous (~125-100 Ma) time. Stratigraphic criteria indicate that thrusting and nappe stacking beneath the emplaced ophiolite in the Internal Dinarides initiated in Late Cretaceous time. Peak temperature contours in the nappe stack cross the thrust contacts, with a maximum temperature of ~460°C reached in the Decani Dome. There, the nappes underwent extensional mylonitic shearing and cooling from ~460°C to < 240°C (zircon fission track ages; ZFT) at ~70 Ma. Nappe stacking in the External Dinarides continued throughout Middle Eocene to Early Oligocene time according to stratigraphic criteria. Peak-temperatures in the External Dinaric nappes were lower (~180-280°C) and correspond to a burial depth of ~6-10 km. Peak-temperature contours transect both the nappe contacts and the Cukali Dome. This indicates that peak temperatures were attained after nappe stacking and Cukali doming. Cooling below ~180°C (57-43 Ma, ZHe) and ~110°C (35-21 Ma, apatite fission track ages) across the dome suggests that the Dinaric nappes cooled slowly after Early Eocene time (3.0-3.2°C/Ma). This slow cooling corresponds to an average denudation rate of 0.1-0.2 mm/yr, equivalent to removal of ~1.6–3.2 km of overburden since ~16 Ma. This age coincides broadly with the stratigraphically constrained onset of normal faulting along the Dukagjini segment of the SPNF that bounds the Western Kosovo Basin.

The thermal evolution outlined above is attributed to two pulses of doming and extension in the upper plate of the retreating Dinaric-Hellenic subduction. We speculate that the first pulse in the Late Cretaceous (80-70 Ma) occurred in the upper plate of the SW-propagating orogenic front. The second pulse occurred sometime between 32 and 16 Ma, and is attributed to rollback subduction of the Hellenic slab towards the SW.

Introduction

Paleogene to Neogene arcuation, orogen-perpendicular and orogen-parallel extension of the Dinaric-Hellenic orogen has been accommodated by extension along the Shkoder Peja Normal Fault system (SPNF) that gradually increases towards the northeast, from zero near the city of Shkoder (Albania) to a minimum of ~3.5 km near the town of Peja in Kosovo (Grund et al. *in review*). Dating the activity of the SPNF and quantifying its displacement are difficult, because marker horizons/units are missing in the foot- and hanging walls. In addition, the thermal imprint of nappe stacking and doming in the footwall of the SPNF remains enigmatic. The SPNF (Fig. 3.1) juxtaposes the highest unit of the Dinaric-Hellenic nappe stack, the West Vardar Ophiolitic nappe, with the nappes of the Adriatic margin (Schmid et al. 2008; Handy et al. 2019). The junction of the Dinarides and Hellenides (Fig. 3.1) also coincides with a change in Mesozoic facies in the nappe units (Aubouin and Dercourt 1975; Handy et al. 2019), with a change in the strike of the orogen from NW-SE to NNW-SSE (Fig. 3.1b; Schmid et al, 2020), and arching of the main drainage divide encompassing the Western Kosovo Basin (Gemignani et al., 2022). As syn-orogenic extension is often associated with crustal exhumation and denudation focused in the footwall of large normal faults (e.g., Grasemann and Mancktelow 1993; Fügenschuh et al. 1997; Schmid et al. 2013), cooling and exhumation along and across the SPNF may have led to different thermochronological evolution of its foot- and hanging walls (e.g., Ehlers 2005). Thus, the major questions addressed in this paper:

What is the timing and amount of burial, heating and cooling of the southern Dinaric fold-and-thrust belt? What is the thermal effect of post-nappe-stacking extension and orogenic arcuation? What is the timing of cooling and exhumation along/ across the SPNF and what are the geodynamic drivers (e.g. slab rollback, slab delamination?) in the Dinarides and Hellenides?

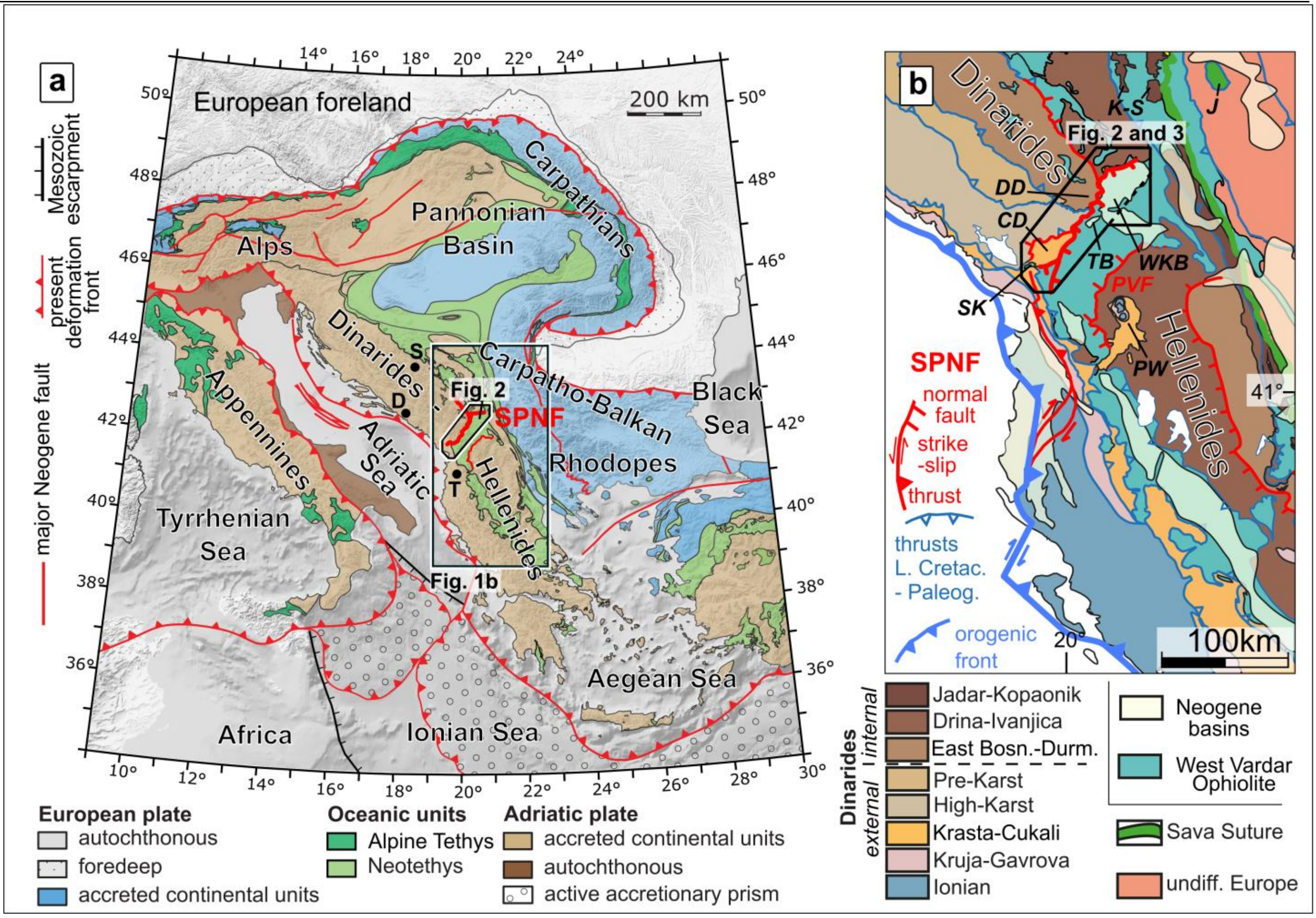

Fig. 3.1: Tectonic maps: (a) Alpine orogens of the central Mediterranean. Cities: D = Dubrovnik, S = Sarajevo, T = Tirana; (b) Dinaric-Hellenic junction with the Shkoder-Peja Normal Fault system (SPNF, thick red line) and associated structures: SK = Shkoder Klippe; CD = Cukali Dome; TB = Tropoja Basin; DD = Decani Dome; WKB = Western Kosovo Basin. K-S = Kopaonik and Studenica core-complexes with Oligo-Miocene intrusions in the southern Dinarides compiled from Schefer et al. (2011), J = Jastrebac core-complex. Nappes, Neogene basins, orogenic front, thrusts and normal faults modified from Schmid et al. (2008, 2020), Handy et al. (2019) and Grund et al. (*in review*).

Upper-crustal extension expresses in the footwalls of the SPNF by dome structures, the Cukali Dome in western- and the Decani Dome in the eastern part of the SPNF (CD and DD in Fig. 3.1b), while in parts of the hanging walls sedimentary basins are developed (Tropoja Basin and Western Kosovo Basin; Fig. 3.1b). SPNF normal faulting is characterized by anchizonal to greenschist facies ductile to brittle faulting and fault migration into the hanging wall (Grund et al. *in review*).

Considering a larger framework, rotation of ~ 30° of the Hellenides relates to post Oligocene convergence of >100 km in the northern Hellenides and <10 km in the Dinarides (Handy et al. 2019). This difference relates to changes in slab dynamics across the Dinaric-Hellenic junction, from slab delamination beneath the Dinarides to slab tearing and rollback subduction beneath the Hellenides (Bijwaard and Spakman 2000; Piromallo and Morelli 2003; Schefer et al. 2011; Handy et al. 2019; Schmid et al. 2020; van Hinsbergen et al. 2020).

Our approach to answer the questions mentioned above is to combine thermochronometry with Raman spectroscopy on carbonaceous matter (RCSM) thermometry to gain insight into the evolution of the different SPNF faulted blocks and domes and conclude on the geodynamic evolution regarding cooling and exhumation pattern during active formation and arcuation of the orogen. The goal of this study is also to constrain the regional thermal evolution, specifically the maximum metamorphic temperatures, cooling and exhumation of Adriatic nappes at the Dinaric-Hellenic junction. We discuss the thermal and temporal structural evolution of an arcuate fold-and-thrust belt (Davis et al. 1984; Poblet and Lisle 2011) with large tectonic nappes that were thrusted and imbricated in an active subduction-collision orogen. Our methods applied deal with a temperature range of ~350 – 110° C (Rahn et al. 2004, 2019; Reiners and Brandon 2006; Malusà and Fitzgerald 2018) for thermochronometry, whereas RSCM (Fig. 3.2) indicates maximum paleo-peak temperatures (Rahl et al. 2005; Boutoux et al. 2016; Lünsdorf and Lünsdorf 2016; Lünsdorf et al. 2017) of rocks. Our data indicates burial and heating to temperatures of ~180-280°C for the external Dinaric nappes and higher temperatures of ~320-460°C in the internal Dinaric nappes (Fig. 3.2). Cooling below ~240°C, partly post-dating dome formation in the internal Dinarides started at ~70 Ma and continued coeval in the entire southern Dinarides to <180°C at ~50 Ma and to <110°C at ~30 Ma. The absence of a differential cooling signal in the SPNF foot- and hanging walls relates to different timing and different thermal conditions of the SPNF segments, to small fault offsets, slow cooling and slow slip rates whereat isotherms partly equilibrated at the same rate as normal faulting and both hanging-and footwall were commonly exhumed. Cooling rates of 3.2 - 3.0°C/ Ma are referred to erosion and denudation with of 0.1-0.2 mm/yr relating to a ~1.6 – 3.2 km rock pile eroded since the Middle Miocene (16 Ma), the assumed beginning of sedimentation in the Western Kosovo Basin, whereat basin formation relates to activity of the youngest part (Dukagjini Fault) of the SPNF. Our study shows the importance of integrating structural analysis with thermochronological data to reveal the evolution of the Adriatic fold-and-thrust belts and its related fault system and extensional structures. We combined the resolution of the applied thermochronological methods with structural information to allow a considerate interpretation about orogenesis, arcuation and crustal extension along the Dinaric-Hellenic junction.

Regional Geology

Orogen evolution and tectonic units

Orogeny in the Dinarides and Hellenides started with the obduction of Neotethyan West Vardar Ophiolites onto the adjacent Adriatic margin in the Middle Jurassic to earliest Cretaceous time (Babić et al. 2002; Gawlick et al. 2008; Bortolotti et al. 2013; Scherreiks et al. 2014). Following obduction, nappes derived from the Adriatic margin were accreted to the upper European Plate, a process that is still ongoing today (Schmid et al. 2008, 2020; Jouanne et al. 2012; d'Agostino et al. 2020; Schmitz et al. 2020). The main "Dinaric" phase of thrusting took place presumably during Middle Eocene to Early Oligocene with Adria-Europe convergence (Schmid et al. 2008, 2020; van Unen et al. 2019). Our nappe terminology follows the arrangement and subdivision of tectonic units in Schmid et al. (2008, 2020).

The tectonic units (Fig. 3.1b) of the Dinarides and Hellenides are mainly derived from the passive Adriatic continental margin and are situated southwest of the Sava zone (Fig. 3.1b), the site of the Adria-Europe suture in latest Cretaceous time (Schmid et al. 2008). The internal Dinaric and Hellenic nappes (i.e. the East Bosnian-Durmitor, Drina-Ivanjica and Jadar-Kopaonik nappes in the Dinarides and the Pelagonian nappes of the Hellenides) are composite nappes each comprising a lower part derived from the former Adriatic continental margin and an upper part with obducted West Vardar Ophiolite (Schmid et al. 2008, 2020). The external Dinaric nappes (Krasta-Cukali, High Karst, Pre-Karst) contain no ophiolitic relicts and consist of mostly Mesozoic platform carbonates intercalated by deepwater basins (Channel and Horvath 1976).

The West Vardar Ophiolite (Schmid, et al., 2008), or Mirdita Ophiolite (Meço and Aliaj 2000) comprises Jurassic ophiolites that formed in a northern branch of the Neotethys Ocean (Fig. 3.1).

The ophiolite was obducted in the Late Jurassic onto the Adriatic passive continental margin (Tremblay et al. 2015, and other references cited therein; Schmid et al., 2008). The base of the ophiolites comprise a mélange, herewith called sub-ophiolitic mélange, that consists of both continental- and oceanic-derived rocks and a metamorphic sole (Carosi et al. 1996; Bortolotti et al. 2005). Overlying sediments of Late Jurassic conglomerate and breccia (termed "conglobreccia" in the Albanian maps, Xhomo et al. 2002) and Cretaceous limestone (Schmid, et al., 2008) locally cover the West Vardar Ophiolite. The units described above were stacked within NE-dipping thrusts and thrust to the NW onto the undeformed Adriatic margin (Schmid, et al., 2008). The most external ophiolite body is the Shkoder Klippe (Fig. 3.1b), a small, ~4 x 10 km oval shaped klippe of West Vardar Ophiolite which directly overlies the Krasta-Cukali Nappe. The basal thrust of the Shkoder Klippe is not the original obduction front and was active after stacking of the external Dinaric nappes but before the activity of the SPNF (Grund et al. *in review*).

Skoder-Peja Normal Fault (SPNF) system and dome structures

The SPNF is a system of SE- to E-dipping normal fault segments (Fig. 3.2; Grund et al. *in review*) running from Shkoder (Albania) to Peja (Kosovo, Fig. 3.2) and further to the NE along the western and northern limits of the Western Kosovo Basin (Figs. 3.1b and 3.2). The fault segments all have the West Vardar Ophiolite in their hanging wall and are kinematically related, even though they are not all continuous and of the same age. In their footwall, however, they cut progressively deeper units of the NE-dipping Dinaric nappe stack going from SW to NE. The SPNF has two larger anchizonal to low-grade metamorphic domes (Fig. 3.1b) in its footwall, the Cukali Dome (Fig. 3.1b; ; Handy et al. 2019, Grund et al. *in review))*, along the Cukali-Tropoja Fault (Fig. 3.2) and the Decani Dome (Fig. 3.1b) with the related Decani Shear Zone (Fig. 3.2; Grund et al. *in review*). These domes deform the Dinaric nappes and are cut by the SPNF (Grund et al. *in review*). The brittle-to-ductile Cukali-Tropoja Fault segment (Fig. 3.2), represents the western part of the SPNF and extends northwest to the Plio-Pleistocene Tropoja Basin (Fig. 3.1b) in its hanging wall near the Albanian town of Bajram Curri (Fig. 3.2). The Cukali Dome, a tectonic window, is a ~40x20 km SW-NE oriented doubly-plunging anticline, it exposes the Krasta-Cukali nappe below the High Karst nappe to the surface. The central part of the Cukali Dome contains carbonates of Late Triassic and Early Jurassic ages and hosts the eponymous 1721 m asl. high Mt. Cukali (Cvijić 1901; Louis 1927; Xhomo et al. 2002), the youngest rocks are Late Cretaceous to Paleogene flysch sediments (Xhomo et al. 2002). These youngest rocks occupy the marginal zones around the entire dome - in contrast to the older strata in the center. A SW-NE oriented normal fault limits the Cukali Dome (Figs. 3.2 and 3.3) to the north (Xhomo et al. 2002). The vertical throw of the Cukali-Tropoja Fault increases from SW to NE along its strike (Handy et al. 2019), ranging from 0 m near Shkoder to a minimum of ~2500 m adjacent to the Tropoja Basin (Grund et al. *in review,* Grund et al. 2018).

The Decani Shear Zone SPNF segment (Figs. 3.2 and 3.3) is a c. 1 km wide zone of lower-greenschist facies mylonites (syn-kinematic temperatures ~300-350°C, Grund et al. *in review)* that dips E to ESE, it represents the eastern part of the SPNF and it juxtaposes the Decani Dome in its footwall. The Decani Dome (Figs. 3.1b and 3.2), has lower Paleozoic metasediments in its center surrounded by upper Paleozoic metasediments and Mesozoic strata of the East Bosnian-Durmitor nappe. The Decani Shear Zone flanks the Decani Dome to the E-SE and reaches no further than the northern limit of the dome and has a minimum throw of ~2500 m (Grund et al. *in review*), similar to the eastern part of the Cukali-Tropoja Fault. The Dukagjini Fault (Fig. 3.2) is a subsurface fault buried beneath the Plio-Pleistocene cover of the Western Kosovo Basin. It was active from Mid-Miocene (16 Ma) to Pliocene (5.3 Ma) times, has a vertical offset of ~1000 m and is sited in the hanging wall of the Decani Shear Zone (Legler et al. 2006; Elezaj 2009; Elezaj and Kodra 2012; Grund et al. *in review*). Taking the minimum value of ~2500 m vertical offset for Decani Shear Zone in combination with the ~ 1000 m offset of the Dukagjini Fault yields to a combined minimal offset of ~ 3500 m at the eastern part of the SPNF. To independently quantify the amount of vertical offset along strike of the SPNF and to date the activity of the different SPNF segments, we investigate the thermal history of its foot- and hanging walls. We also want to evaluate the thermal imprint of the footwall domes related to fault activity and nappe stacking.

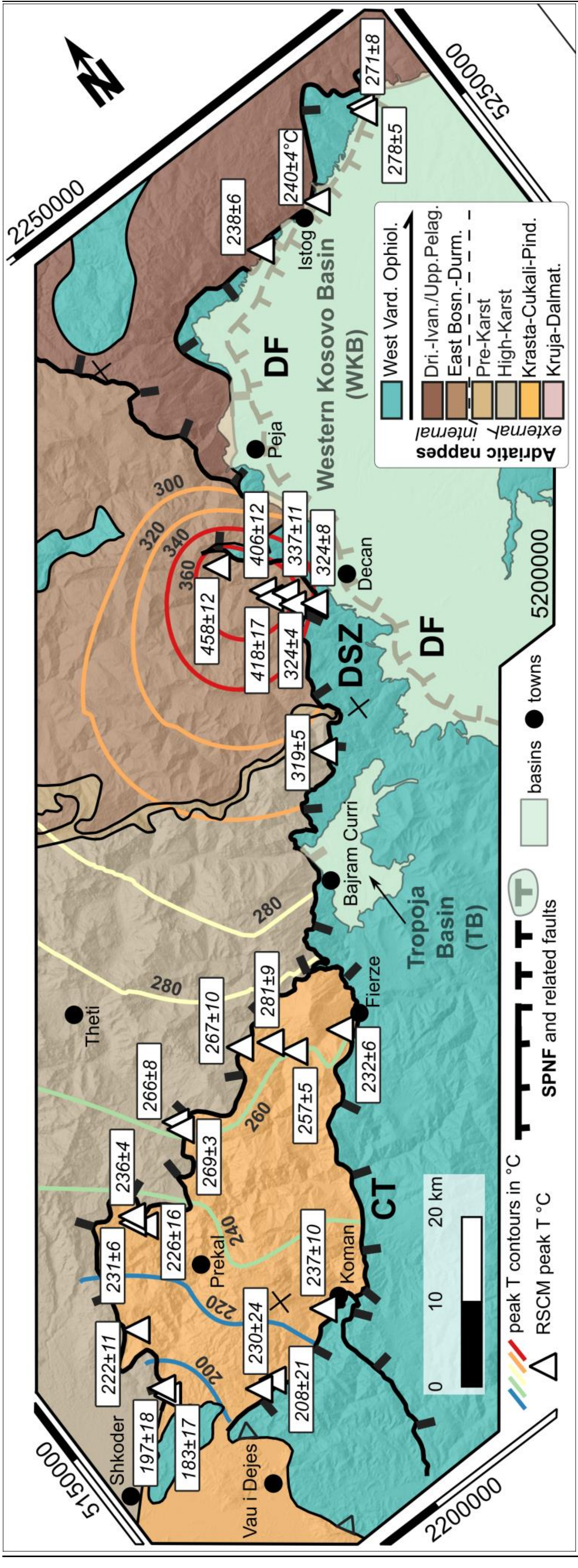

Fig. 3.2: Tectonic map of the Dinaric-Hellenic junction with nappes according to Schmid et al. 2008, 2020. Outline of this figure shown in Fig. 3.1a. Segments of the SPNF: CT = Cukali-Tropoja Fault; DSZ = Decani Shear Zone; DF = subsurface Dukagjini Fault (dashed line). White triangles mark samples used for RSCM analysis with maximum peak temperatures in °C and errors at the 95% confidence interval (Tab. 4/ Appendix II). Note that samples Al-MG_58, 59, 60 and 61 are not located on this map, but in the inset map to Fig. 3.3. Sample coordinates listed in Tab. 4/ Appendix II. Colored peak-temperature contours obtained by linear, ordinary Kriging analysis (Krige 1951) with a grid-size resolution of 2 km, performed with Smart-Map Plugin 1.0.0 in QGis 3.22.6 software. Crosses mark points of intersection of coordinates at map frame. CRS of map: WGS 84, UTM zone 34N DEM based on ASTER GDEM (Abrams et al. 2020).

Sedimentary basins at the Dinaric-Hellenic junction

The Dinaric-Hellenic junction has two Neogene sedimentary basins (Meço and Aliaj 2000; Elezaj and Kodra 2012) which are fed by the adjacent *Albanian Alps (Prokletije);* (Elezaj 2009; Elezaj and Kodra 2012; Meier 2012). The Western Kosovo Basin (Elezaj & Kodra, 2012; Knobloch et al., 2006; Linder & Perkuhn, 2013, Figs. 3.1, 3.2 and 3.3) formed as a terrestrial (Elezaj and Kodra 2012) half-graben basin in response to the activity of the Dukagjini Fault (Figs. 3.2 and 3.3; Grund et al. *in review*, Legler et al. 2006). It evolved from Mid-Miocene to Pliocene times with a change in elevation from 500 m asl. at basin level to more than 2500 m asl. in the mountain range (Gemignani et al. 2022). The Western Kosovo Basin is the largest regional sedimentary basin that is nowadays drained via the Drin River system (Marković 1990; Tahirsylaj et al. 2010; Kovaçi et al. 2015; Gemignani et al. 2022) to the Adriatic Sea. The Tropoja Basin (Figs. 3.2 and 3.3) is a small (~60 km^2 filled with Pliocene-Holocene strata) sedimentary basin (Xhomo et al. 2002; Gemignani et al. 2022). The sediments in this basin form several, incised river terraces that have developed within a morphologic depression in the hanging wall of the Cukali-Tropoja Fault (Grund et al. *in review*) floored by West Vardar Ophiolite. A steep increase in elevation (Abrams et al. 2020; Gemignani et al. 2022) from basin level to the *Albanian Alps* coincides with the structural and lithological boundary of the carbonates of the High Karst nappe with the West Vardar sub-ophiolitic mélange. Pliocene to Recent sediments cover the assumed SPNF fault trace with no tectonic displacement of these sediments (Gemignani et al. 2022). As erosion and denudation are drivers for exhumation, we want to quantify the amount of material that has been potentially removed in the source area since the begin of sedimentation in the basins. We therefore investigate the thermal history of the source area to identify the processes that led to cooling and exhumation. We evaluate erosion and denudation rates that we derive from cooling rates and compare these values to accumulated sediment thicknesses in the basins to estimate how much sediment has been eroded and accumulated and possibly already removed from the basins.

Regional thermochronology and thermometry

Existing low temperature thermochronometry shows an eastward younging trend in central and northern Albania with cooling ages in the temperature range of ~250-70° C (Muceku et al. 2006, 2008). Fastest cooling rates of about 1.2 mm/yr between 6 and 4 Ma were depicted in the Korab Pelagonian Unit in the Peshkopia Window (Muceku et al. 2006, 2008); Fig. 3.3 inset map). Ages of 57 ± 5 to 17 ± 8 Ma (2σ errors) for (U-Th)/He thermochronology on apatite (AHe) occur in northern and western Albania (external Dinaric units) and 10 ± 3 to 5 ± 2 Ma in eastern Albania (Peshkopia Window). These ages indicate more recent cooling in the East (Muceku et al. 2006). Also apatite fission track (AFT) ages from 51 ± 11 to 41 ± 11 Ma (Muceku et al., 2006) in the western part of the West Vardar Ophiolite in central and northern Albania are older than comparable ages in the East (Muceku, et al., 2006). Zircon (U-Th)/He (ZHe) ages of 101 ± 6 Ma in the northeast and 50 ± 2 to 20 ± 3 Ma in the east underline the west to east younging trend of cooling. Muceku et al. (2006, 2008) propose that the increased cooling in the internal Dinarides reflect a differential exhumation of the internal units compared to the external units with Miocene to Pliocene extension in eastern Albania. Rapid exhumation happened in the Peshkopia Window (Muceku, et al., 2008) by extensional reactivation of NE-SW trending thrusts in the Korabi zone, mostly related to Hellenic rollback subduction (Muceku et al. 2006, 2008). Schefer et al. (2011) examine the thermochronological history of the southern Dinarides in southern Serbia. The emplacement of Oligocene (Kopaonik, Drenje, Zeljin) as well as Miocene (Golija and Polumir) granitoids in the internal Dinarides (Jadar–Kopaonik–Studenica thrust sheet, Fig. 3.1b) is associated with Miocene core-complex formation and Dinaric-Hellenic back-arc extension (Schefer et al. 2011) and slab delamination. AFT and zircon fission track (ZFT) data indicate rapid cooling from above ~300°C to ~ 80°C between 16 and 10 Ma, induced by extension related exhumation of plutons that are located in the center of core complexes (Schefer et al. 2011). The central Dinarides (High Karst nappe) in Croatia, ~ 400 km NNW of the Dinaric-

Hellenic junction indicate maximum burial temperatures of ~200-270°C and show cooling between 80 and 35 Ma (Środoń et al. 2018). Summarized, there are so far only four locations near to the Dinaric-Hellenic junction that were sampled for thermochronological studies (Muceku et al. 2006, 2008) revealing three AFT ages (49 – 39 Ma), two ZFT ages (174 ± 15 and 103 ± 10 Ma) and respectively one AHe (17 ± 4 Ma) and one ZHe age (101 ± 6 Ma). Other over regional studies using geochronological constraints (Mikes et al. 2009; Porkoláb et al. 2019) from the central Dinarides refer to the timing of the Jurassic evolution of the Neotethys, predating the main Dinaric-Hellenic stages of orogeny, as well as magmatism and obduction of the West Vardar Ophiolite.

Methodology

Sampling strategy

The areas of sampling are shown in Figure 3.3, including the Shkoder Klippe located at the southwestern end of the SPNF system (Grund et al. *in review)* as well as the Cukali and Decani Domes (Fig. 3.3) and the West Vardar sub-ophiolitic mélange north of Istog (Fig. 3.2) in Kosovo. In order to identify differential cooling and to test the idea of an along-strike increase in offset proposed by Handy et al. (2019) and Grund et al. (*in review)*, we sampled profiles across and along the SPNF, with the Dinaric nappes in the footwall and the West Vardar Ophiolite in the hanging wall. To apply low-temperature thermochronology on apatite and zircon, we sampled siliciclastic or felsic magmatic lithologies in the aforementioned nappes. In total, we separated heavy minerals in 52 samples (sample size ~10 to 25 kg), yielding 13 AFT, 17 ZHe and 13 ZFT samples for analysis (Fig. 3.3). From each such sample, we made a polished thin-section for RSCM analysis, with results presented in Figure 3.2. From lithologies with few heavy minerals (e.g. mudstone, marls, fine-grained siltstones) we collected a total of 30 samples exclusively for RSCM analysis. The locations, samples and methods are listed in Figure 3.3 as well as in Appendix II: Tabs. 1, 2, 3 and 4.

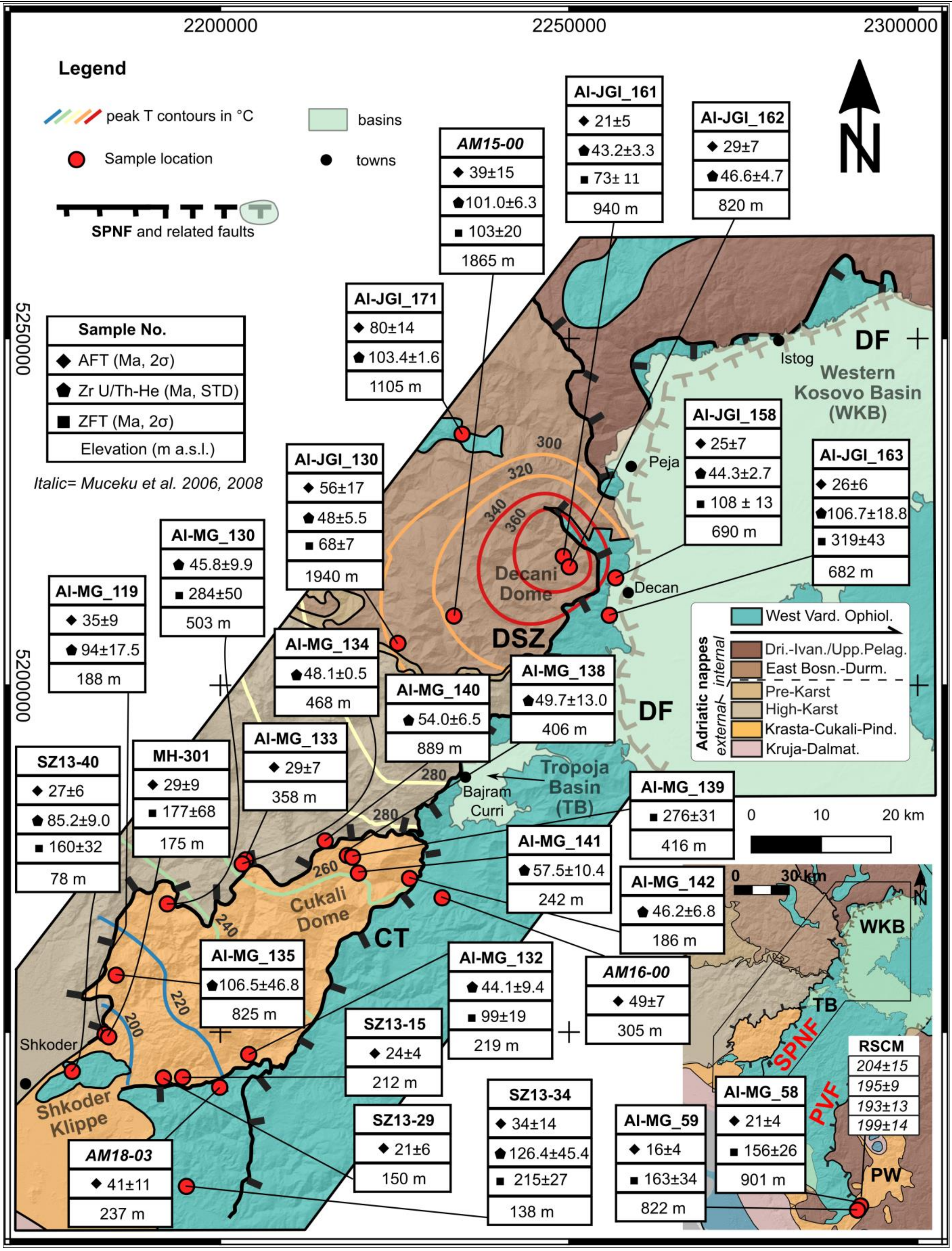

Fig. 3.3: Sample locations (red dots) and thermochronological ages at the Dinaric-Hellenic junction. Samples listed in italics are previously published ages of Muceku et al. (2006, 2008). Inset map shows locations of samples near the Peshkopie Window (PW). CT = Cukali-Tropoja Fault; DSZ = Decani Shear Zone, DF = Dukagjini Fault; WKB = Western Kosovo Basin; TB = Tropoja Basin, SPNF = Shkoder Peja Normal Fault system; PVF = Prizren-Vranica Fault. Peak T contours as in Fig. 3.2. CRS of map: WGS 84, UTM zone 34N DEM based on ASTER GDEM (Abrams et al. 2020).

Low-temperature thermochronology and thermometry

We used a multi-proxy thermochronological concept to obtain the ages of cooling to temperatures below 240-110°C, corresponding to the effective closure temperatures, T_c (Reiners and Brandon 2006) of zircon fission track (~240°C, ZFT), zircon (U–Th)/He (~180°C, ZHe), and apatite fission track (~110°C, AFT), and RSCM thermometry to determine the peak paleo-temperatures. In order to gain method-independent age data, we used two independent dating techniques, fission track dating and (U–Th)/He dating. Fission tracks in zircon and apatite anneal and thus reset their ages in a certain range of temperatures, in the partial-annealing zone (PAZ; Laslett et al. 1987), between ~110-60°C for apatite (APAZ) and ~350-240°C for zircon (ZPAZ). ZHe dating has a comparable temperature range, the partial retention zone (PRZ; ~200-160°C) where He diffuses through the crystal lattice (Reiners et al. 2002). All ages obtained with these systems are thus apparent ages, as partial annealing/retention during cooling and thus inheritance cannot be excluded. All of the applied dating techniques make use of the decay of ^{238}U in the crystal, fission track dating uses the resulting, constant formation of spontaneous fission tracks (Gallagher et al. 1998; Malusà and Fitzgerald 2018; Kohn et al. 2019) to quantify the time during which the crystal cooled through and below the T_c window. The number of fission tracks per area in a single crystal with a known uranium concentration provides thermochronological age information (e.g. Hurford and Green 1983; Malusà and Fitzgerald 2018; Hülscher et al. 2021). ZHe analyses are based on the accumulation of He from U and Th decay in the crystal lattice. Measuring ^{4}He, U and Th of the single, whole zircon crystal provides thermochronological age information about the crystal and thus the host rock (Reiners and Farley 2001; Farley 2002; Reiners et al. 2002; Reiners 2005; Reiners and Brandon 2006). Sample preparation including crushing, heavy mineral separation and sample preparation was done at the FU Berlin and at University Innsbruck. Detailed information about the lab protocol, irradiation, measuring, counting and the evaluation of the age data is attached in Appendix II.

Raman spectroscopy of carbonaceous material (RSCM) characterizes the irreversible transformation of immature organic matter to crystalline graphite, which mainly depends on temperature (Beyssac et al. 2002). RSCM is used to determine the peak-metamorphic temperature conditions of metasediments that contain organic matter (Rahl et al. 2005; Beyssac et al. 2007; Wiederkehr et al. 2011; Lünsdorf and Lünsdorf 2016; Lünsdorf et al. 2017) in a large variety of geological settings (e.g. Scharf et al. 2013b; Groß et al. 2020). Detailed descriptions of this method is given in Appendix II.

Thermal modelling

To model the 2D spatial distribution of the RSCM data (Fig. 3.2), we used the geostatistical approach of linear Ordinary Kriging (Krige 1951) analysis of the Smart-Map Plugin 1.0.0 in *QGis 3.22.6* software. We used a grid-size of 2000 m to determine peak-temperature patterns in the southern Dinarides and Hellenides (Fig. 3.2). As RSCM data is primarily available for the Dinaric nappes, we limit our approach to the Dinaric nappe stack in the footwall of the SPNF as a major structural boundary (Fig. 3.2). We emphasize that this does not mean that paleo-peak-temperature isolines were cut or displaced by the SPNF, but lacking samples of the hanging wall of the SPNF exclude modelling across this major structural boundary. We also exclude Kriging modelling in internal Dinaric nappes above the East Bosnian-Durmitor nappe because of lack of data. We performed a Monte-Carlo simulation (Raychaudhuri 2008; Harrison 2009) using the ZFT, ZHe and AFT cooling ages for cooling temperatures of <240°C to ~180°C to ~110°C to surface temperature (18±2°C) to determine cooling rates for the Dinaric- Hellenic junction.

Results

Peak temperature thermometric estimates from RCSM

We analyzed 30 samples with a peak-temperature range of ~183-458°C (Fig. 3.2 and Tab. 4, Appendix II). These temperatures are within the calibration limits of the RSCM method (160-600°C; Lünsdorf et al. (2017)) allowing us to internally compare our dataset. As our temperatures are calibrated, it also allows a comparison to temperatures from literature data, e.g. from color alteration index of deformed conodonts (Sudar and Kovács 2006) or illite–smectite palaeotemperatures (Środoń et al. 2018) in the central and southern Dinarides. The south-westernmost part of the Cukali Dome (Fig. 3.3) shows the lowest peak temperatures of ~183-230°C, whereas the northeastern part of the Cukali Dome has higher peak temperatures of ~232-281°C (Fig. 3.2). Peak-temperature contours in the Cukali Dome and in the High Karst nappe remain undisturbed by nappe contacts or the Cukali dome structure. At the northern part of the Cukali-Tropoja Fault (Fig. 3.2, Grund et al. *in review*), a sample in close vicinity to the fault yields a temperature of ~319°C (Fig. 3.2, Tab. 4, Appendix II). The samples from the Decani Shear Zone experienced peak temperatures in the range of ~324-362°C (Fig. 3.2, Tab. 4, Appendix II) whereas peak temperatures reached ~458°C in the core of the Decani Dome (Fig. 3.2). Peak temperatures in the Decani Dome form concentric peak-temperature contours (Kriging modelling, Fig. 3.2) around the perimeter of the dome. The temperature in the West Vardar sub-ophiolitic mélange north of the Western Kosovo Basin near the town of Istog (Fig. 3.2) peaked between ~234°C and ~278°C. Samples Al-MG_58, 59, 60 and 61 from the Krasta-Cukali nappe south of the Peshkopia Window yield temperatures between ~193 – 204°C (Tab. 4, Appendix II), indicated in inset map in Fig. 3.3.

Low-temperature thermochronology across the SPNF

The western sampling sites are located on a section across the Cukali-Tropoja Fault segment (Fig. 3.2) from the Krasta-Cukali and High Karst nappes in the footwall to the West Vardar Ophiolite in the hanging wall (Fig. 3.3). The samples from the western foot- and hanging walls (Cukali-Tropoja Fault) come from an elevation of 138 – 212 m asl. (Fig. 3.3, Tab. 1, 2 and 3, Appendix II). Samples from the south-westernmost part of the Cukali Dome show Cretaceous ZHe significantly older ages than the Paleocene- Middle Eocene majority of ZHe ages along the SPNF. AFT ages in the southwestern SPNF part across the Cukali-Tropoja Fault (Fig. 3.3) range from Oligo- to Early Miocene in age. Farther east, we sampled across the Decani Shear Zone (Figs. 3.2 and 3.3) from the East Bosnian-Durmitor nappe in the footwall and the West Vardar Ophiolite in the hanging wall at elevations of 682 – 940 m. Two samples of the eastern SPNF, Al-JGI_130 (1940 m asl.) and sample Al-JGI_171 (1120 m asl.) were taken at higher elevations and about 12-15 km west of the Decani Shear Zone in its footwall. AFT ages across the Decani Shear Zone are similar to the Oligo-Miocene ages across the Cukali-Tropoja Fault in the southwestern part across the SPNF. Sample Al-JGI_163 in the Decani Shear Zone hanging wall has a, related to the majority of the ZHe ages, much older Lower Cretaceous age, comparable to the ages in the south-westernmost part of the Cukali Dome. Paleozoic to Mesozoic ZFT ages are heterogeneously distributed along the SPNF except for a cluster of mid- to Late Cretaceous ages in the Decani Dome in the footwall of the Decani Shear Zone (Fig. 3.3). In addition to the samples of the Dinaric-Hellenic junction, we obtained two other AFT cooling ages (Al-MG_58; 21 ± 4 Ma and Al-MG_59; 16 ± 4 Ma) south of the Peshkopia Window (Fig. 3.3, inset map) to evaluate the robustness and comparability of data published elsewhere (e.g. Muceku et al. 2008; Schefer et al. 2011). All thermochronological ages and according sample locations are given in Figure 3.3; detailed sample information is given in Appendix II in Tab. 1, 2, 3, and 4.

Discussion

Cooling ages and provenance signals

To determine the age of Dinaric folding and thrusting and the activity of the SPNF, it is necessary to distinguish between cooling ages after partial annealing/ retention, inheritance and provenance signals from the eroded hinterland that survived orogenesis. The latter occurs if temperatures were insufficient (i.e., below the critical temperature or too short-living) to open (He retention in zircon) or to anneal (fission track dating) and therefore to fully reset the age system in the crystals (Carlson et al. 1999; Ketcham et al. 2007; Guedes et al. 2013; Malusà and Fitzgerald 2018). The former occurs if temperatures exceeded this critical temperature, e.g. during orogenic burial and heating. We note that not all AFT and ZFT samples show P(χ2) values of >5 % (Galbraith 2008, 2010), indicating that crystals belong to more than one kinetic population (e.g. provenance signal) or that the crystals are partially reset. However, the poor sample (crystal) quality makes interpretation of this statistical approach complicated. Thus, we use RSCM analysis to determine whether the peak temperature experienced by a sample was above or below the critical temperatures for partial annealing/retention in the AFT, ZHe and ZFT systems (Fig. 3.4 and chapter 3 above). Apparent cooling ages must always be younger than the depositional ages of the host rock (in the case of metasediments) or than their magmatic crystallization, but slow cooling may causes annealing during cooling which results in mixed ages, even though the samples were fully reset.

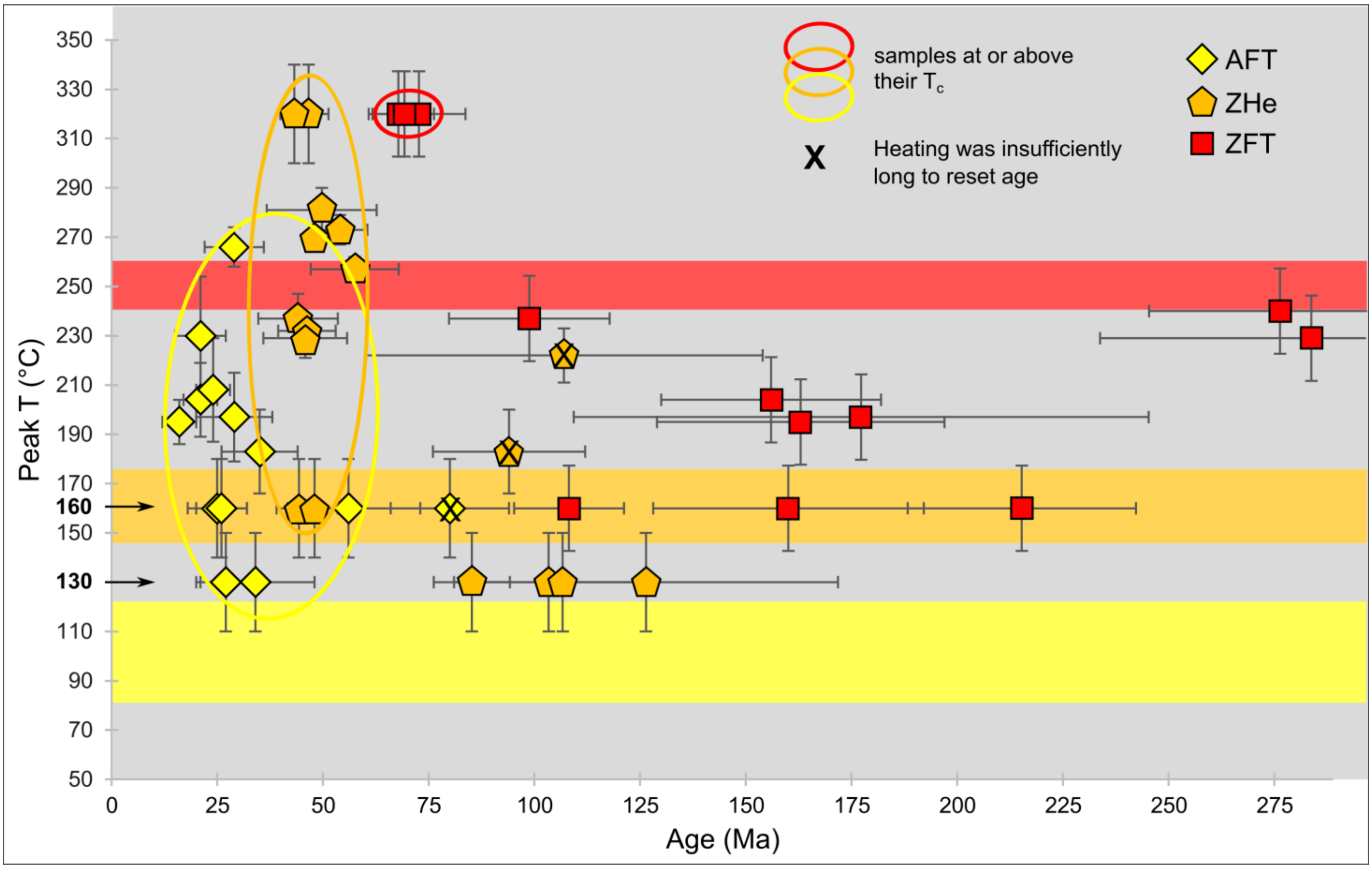

Fig. 3.4: Comparison of AFT, ZHe and ZFT ages and their effective closure temperatures, T_c (colored horizontal bars) versus peak temperature from RSCM analysis. Temperatures of samples at 130°C and 160°C (indicated by arrows) correspond to reset cooling ages from the lower-temperature related, reset thermochronological system (AFT for ZHe and ZHe for ZFT) from the same sample location. Samples that experienced $T_{peak} > T_c$ yield cooling ages (AFT), whereas those with $T_{peak} < T_c$ (ZHe ages > 60 Ma, ZFT > 75 Ma) yield inherited ages of the source rock (see text for explanation).

As all AFT ages are significantly younger than the depositional/formation ages of the host rocks, we interpret these ages as apparent cooling ages (Tab. 1, Appendix II; Figs. 3.5 and 3.6). Even during cooling, alteration and partial resetting of samples, as stated above, is possible. The large spread of single-grain ages is attributed either to crystal alteration, weathering, cracking (resulting in small countable surfaces) and heterogeneous apatite chemistry (beside from Dpar measurements as a proxy for chemistry, Tab. 1) and/or to variations in grain size and quality (due to provenance variations), paired with a relatively long time of the samples spent in the APAZ. This single-grain age spread results in relatively large 2σ errors. The distribution of the AFT cooling ages along the foot- and hanging walls of the SPNF is shown in swath profiles in Figure 3.6.

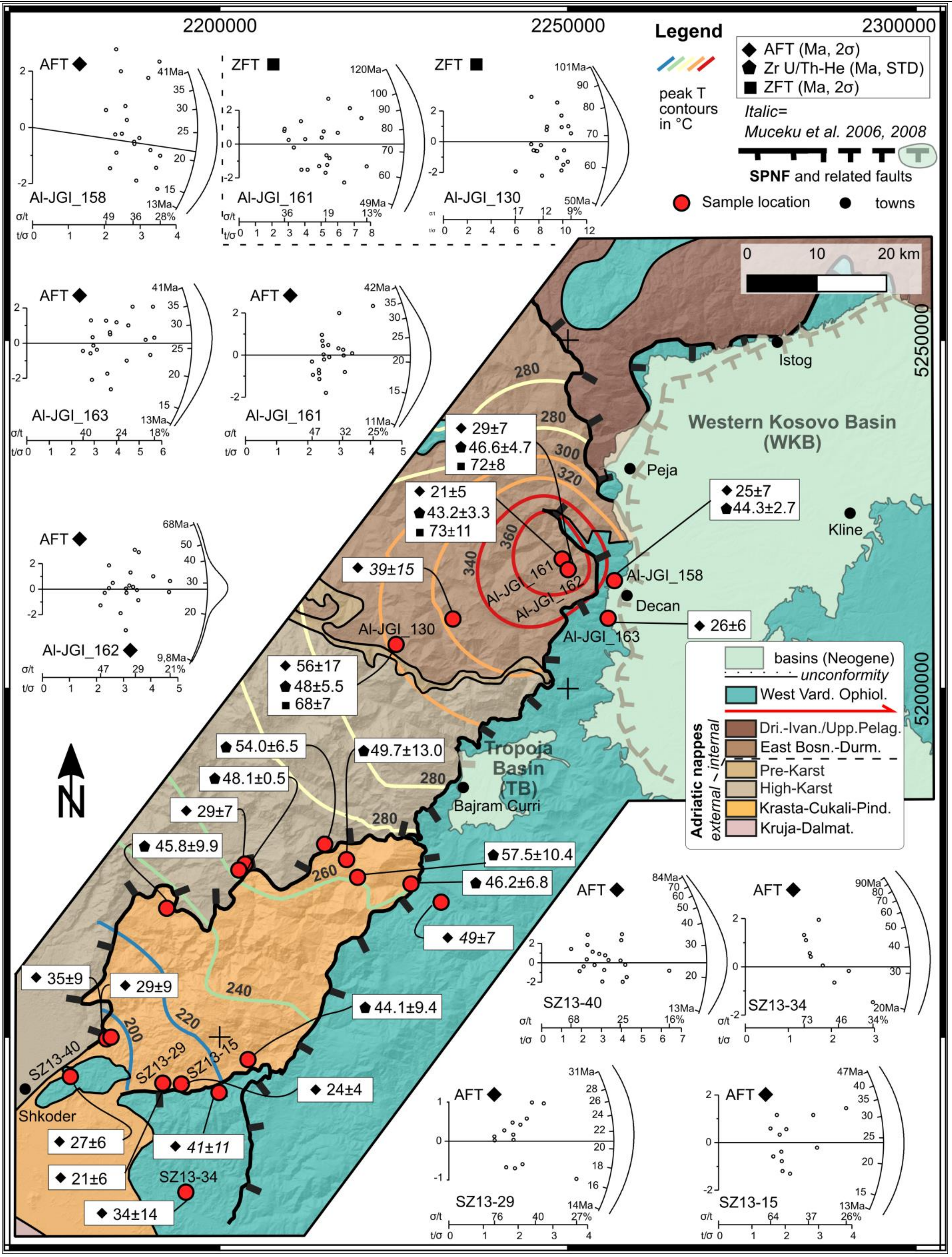

Fig. 3.5: AFT, ZHe and ZFT apparent cooling ages and radial plots of selected samples along the SPNF. The ages from the mélange underlying the West Vardar ophiolite (green) are interpreted to post-date obduction (see text for explanation). Peak T contours based on Kriging of RSCM peak temperatures shown in Fig. 3.2. Radial plots of all samples are available in Appendix II and in the supplementary material. Plots were made with RadialPlotter (Vermeesch 2009).

Samples Al-JGI_130 and Al-JGI_171 (no RSCM data available) have central AFT ages (56±17Ma and 80±14 Ma, respectively) that are older and have larger errors than the average age of other samples. These two samples were collected at elevations > 1000 m, thus an age-elevation relation cannot be excluded (Fig. 3.3). However, the small number of samples from such elevations and the large errors in their ages (including sample *AM15-00* from Muceku et al. (2006), Fig. 3.3) preclude further detailed age-altitude analysis and thus an altitude-age correction. We therefore exclude sample Al-JGI_171 (80±14 Ma) in our cooling model, as its error does not overlap with the other ages in this study. Samples Al-JGI_130 and *AM15-00* have less statistical weighting in our discussion compared to the other AFT ages.

Our ZHe data show a more complex pattern of reset (as shown in Fig. 3.5) and unreset ages. Two ZHe samples in Figure 3.3 (Al-MG_119; Al-MG_135) indicate cooling ages significantly older than the depositional ages of the host rock. However, these two samples from the SW part of the Cukali Dome (Fig. 3.1b) either never attained the T_c according to the peak-temperature contours (Fig. 3.4), or the time spent in the PAZ was too short. No peak temperature (Figs. 3.2 and 3.5) is available for samples Al-JGI_171 and Al-JGI_163, with Lower Cretaceous ZHe age, but their location in the ophiolitic mélange overlying the East Bosnian-Durmitor nappe and in the hanging wall of the SPNF hint that they were probably not sufficiently buried and heated during Dinaric thrusting. Seven ZHe ages (57-44 Ma) in the central and northeastern part of the Cukali Dome reflect ages younger than the stratigraphic/formational ages of the host rock and peak temperatures above the PRZ. Thus, these ages are interpreted as cooling ages. ZHe ages of 43-48 Ma within the Decani Dome and in the hanging wall of the Decani Shear Zone come from rocks that experienced peak temperatures of >320°C, indicating that the ages are cooling ages. We interpret only three ZFT ages (Al-JGI_130; Al-JGI_161 and Al-JGI_158) to reflect cooling ages, as only these ages are younger than the depositional/magmatic ages of the lithologies and come from areas that experienced peak temperatures greater than ~240 °C.

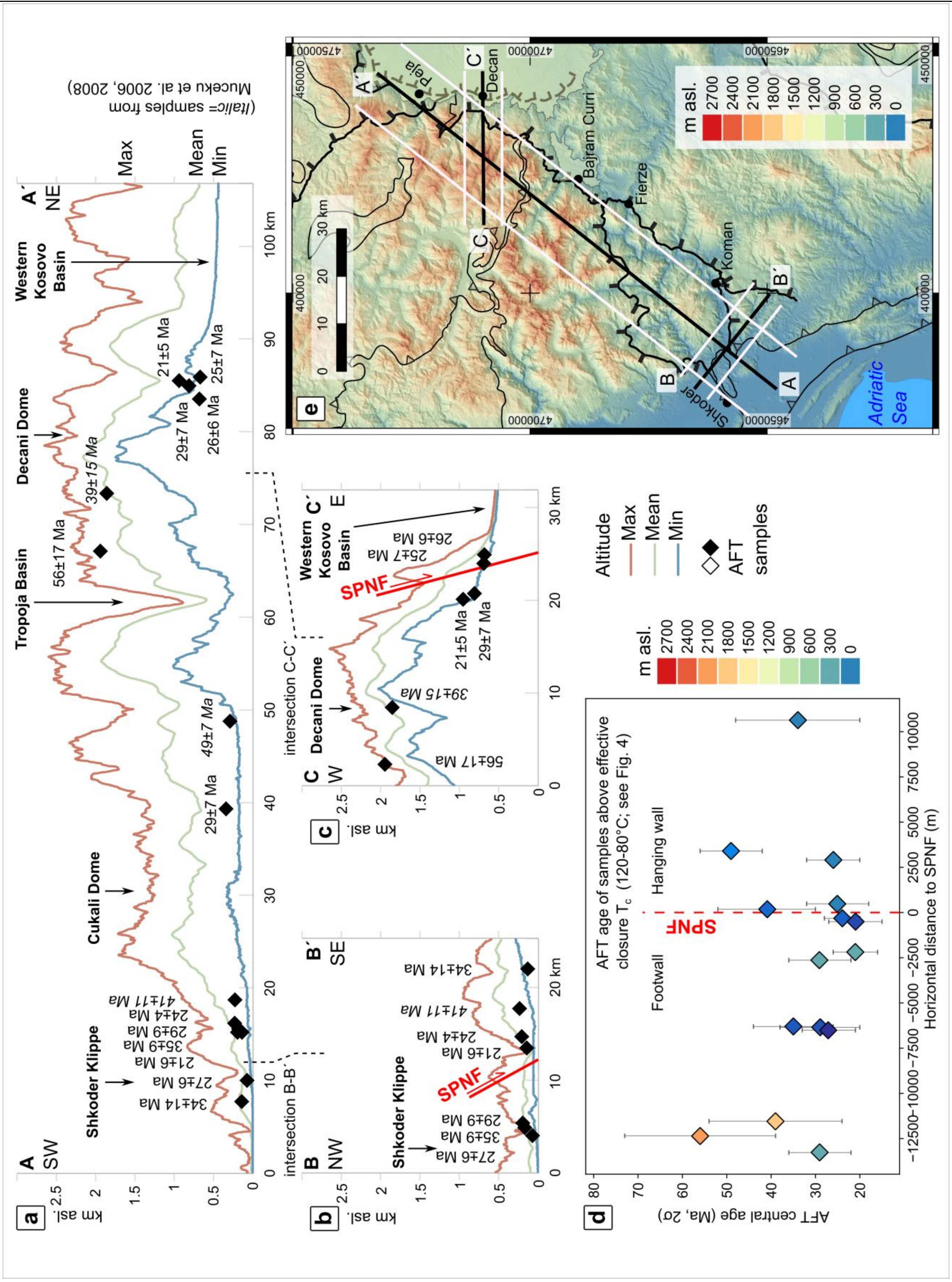

Fig. 3.6: Topography and central AFT cooling ages along and across the SPNF (traces in inset map): (a) Along the footwall of the SPNF; (b) Across the southwestern part of the SPNF including the Shkoder Klippe; (c) Across the northeastern part of the SPNF system near Decan, including the Decani Shear Zone and Decani Dome; (d) AFT ages of samples above effective closure Tc (~110°C; see Fig. 3.4) vs. their shortest horizontal distance to the SPNF. Color - sample elevation, red dashed line - SPNF fault trace. Note that there is no correlation between age, sample elevation and distance to fault trace in either the foot- or the hanging wall. Vertical axis of all swath topographic profiles is exaggerated ~10x. Swath profiles are based on ASTER GDEM (Abrams et al. 2020) and extracted with SAGA GIS 2.3.2 software. Hillshade and DEM based on ASTER GDEM (Abrams et al. 2020). CRS of map (e): WGS 84, UTM zone 34N.

Age of nappe stacking and folding

Obduction

We interpret the peak temperatures of ~234-278°C from the sub-ophiolitic mélange of the West Vardar Ophiolite in the NE part of the study area near the town of Istog (Fig. 3.2) to reflect the local conditions of late obduction-related metamorphism in the immediate footwall of the West Vardar Ophiolite. Obduction-related metamorphism in the Korabi-Pelagonian nappe in the Hellenides (equivalent to the units of the Internal Dinarides) happened in Latest Jurassic to Early Cretaceous times (148 to 130 Ma, Most 2003; Tremblay et al. 2015). This metamorphism thus pre-dates the burial metamorphism related to Dinaric nappe stacking (van Unen et al. 2019; Schmid et al. 2020), which is inferred to have occurred somewhat later in the footwall of the obduction front when the slices of Adriatic continental margin were already incorporated in the Dinaric nappe stack. Samples SZ13-40 from the Shkoder Klippe and SZ13-34 from the hanging wall of the Cukali-Tropoja Fault (Fig. 3.3) yield Cretaceous ZHe ages, similar to ZHe and ZFT ages for samples near Decan (106-103 Ma from Al-MG_171, Al-JGI_163; 108 Ma from Al-JGI 158, Fig. 3.3). We interpret these Cretaceous ages to date cooling of the West Vardar Ophiolite after its final emplacement in Late Jurassic to Early Cretaceous time (Schmid et al. 2008). This is in agreement with previously described Early Cretaceous cooling below ~240°C of the West Vardar Ophiolite located further southward in the Korabi-Pelagonian nappe (Most 2003; Tremblay et al. 2015).

Accretion, burial and folding

The peak temperature range in the footwall of the Decani Shear Zone (324 – 458°C) is attributed to latest Jurassic to Early Cretaceous burial by nappe stacking of the Internal Dinaric nappes (thrusting of the Dina-Ivanjica nappe over the East Bosnian-Durmitor nappe, Fig. 3.7a). This happened after the obduction of the West Vardar Ophiolite (Babić et al. 2002; Gawlick et al. 2008; Bortolotti et al. 2013; Scherreiks et al. 2014; Grund et al. *in review*). The depth attained by the East Bosnian-Durmitor nappe during obduction, thrusting and nappe stacking amounts to a minimum of 11-15 km for an assumed geothermal gradient of ~30°C (Cermak et al. 1996; Sudar and Kovács 2006). Similar, slightly shallower depths have been estimated for the Drina-Ivanjica nappe (9-10 km, Porkoláb et al. 2019) which overlies the East Bosnian-Durmitor nappe. K/Ar ages of 130-150 Ma for the Drina-Ivanjica nappe (Porkoláb et al. 2019) suggest that burial and peak metamorphism of the Internal Dinarides (Upper Jurassic- Lower Cretaceous metamorphism) was older than in the External Dinarides. The main phase of thrusting, nappe stacking and burial in the latter is constrained by flysch in the footwall of nappe contacts to be Eo-Oligocene (e.g., Schmid et al. 2008 and refs therein).

Peak temperatures of ~180-280°C in the external Dinaric Krasta-Cukali and High Karst nappe (Fig. 3.2) indicate a burial depth of ~6-10 km if one assumes a geothermal gradient of 30 °C/ km (Cermak et al., 1996). Similar temperature values (~200-270°C) are also reported about 400 km NNW of the Dinaric-Hellenic junction from the High Karst nappe (Środoń et al. 2018) in the central Dinarides. The thickness of the nappe stack is attributed to the Dinaric phase of thrusting and nappe stacking, which has been dated with stratigraphic criteria at Middle Eocene to Early Oligocene, ~ 45–28 Ma (Schmid et al., 2020; van Unen et al., 2019) for the emplacement of the High Karst nappe onto the Krasta-Cukali unit. The Eocene ZHe cooling ages (Fig. 3.5) are interpreted to date syn-to post orogenic cooling soon after the attainment of peak temperatures during and after Dinaric nappe stacking. Clearly, cooling of these units began after nappe stacking and has not been interrupted since.

Age of doming and cooling

Decani Dome and Decani Shear Zone

Peak metamorphic temperatures in the East Bosnian-Durmitor nappe (~458°C) were likely reached when this unit was overthrust by the Drina-Ivanjica nappe at 130-150 Ma (Porkoláb et al. 2019). The rounded shape of the peak-temperature contours (Fig. 3.2) in the Decani Dome suggests that doming post-dated the thermal peak. Top-SE normal-sense mylonitic shearing at syn-kinematic temperatures of ~300-350°C along the Decani Shear Zone (Grund et al., *in review*) occurred at peak temperatures significantly (~100-150°C) less than the peak temperatures in the dome itself. It seems reasonable to relate this doming that affected the East Bosnian-Durmitor nappe in the footwall of the Decani Shear Zone (Fig. 3.7b) to exhumation that resulted in cooling to below ~240°C at 73 – 68 Ma (apparent ZFT cooling ages, Figs. 3.3 and 3.5), some 60-80 Ma after the attainment of peak metamorphic temperatures.

If the cooling ages are valid, then Decani doming and shearing were much older than Oligo-Miocene activity of other segments of the SPNF as constrained by cross cutting relationships and stratigraphic criteria (Grund et al., *in review*). We therefore propose that at ~ 80 Ma the Decani doming and normal-sense exhumational shearing (Fig. 3.7b and f) may have occurred in a back-arc setting east of the accretion-subduction front advancing to the SW in the external parts of the Dinaric orogen (Fig. 3.7b) that were active at that time (van Hinsbergen et al. 2020; their Fig. 39). Extension in the upper plate of retreating subduction systems is well known in other central Mediterranean orogens (e.g., Faccenna et al. 1997, 2001). Initial stages of the Central Mediterranean subduction zones reach back to Upper Cretaceous at ~90-80 Ma (Faccenna et al. 2001), similar to timing of back-arc extension along the Decani Dome at ~80 Ma.

A possible later, brittle component of faulting that overprints mylonitic structures may represent reactivated parts of Decani Shear Zone (Grund et al. *in review*). Alternatively, mylonitic and brittle faulting may have been coeval and merely reflect a thermal gradient during juxtaposition of the warm footwall block with the cold hanging wall block or variations in strain-rate.

Cooling below ~ 180°C (ZHe ages, Figs. 3.5 and 3.7f) started in Early Eocene and affected the East Bosnian-Durmitor and parts of the West Vardar Ophiolite hanging wall close to the shear zone, with no evidence of reheating. This was followed by Oligocene to Early Miocene cooling below ~110°C across the Decani Shear Zone including parts of the West Vardar Ophiolite (Fig. 3.5). However, rapid cooling from above 300°C to 80°C in the Miocene (Schefer et al. 2011), as occurred in the nearby inner-Dinaric Jadar-Kopaonik nappe (K-S in Fig. 3.1b), is not evident in our dataset.

Cukali Dome

Our data show that the rocks of the Cukali Dome were buried and heated to temperatures of ~180 to 280°C after their deposition in the Early Paleogene. We note that the stratigraphic age of the youngest sediments in the nappe ranges from ~72–56 Ma (Xhomo et al. 2002), just overlapping with the oldest (~57 Ma) ZHe ages. This suggests that most of the sampled sediments were deposited somewhat earlier within the stratigraphically constrained age range of sedimentation (Maastrichtian- Early Paleocene; Xhomo et al. 2002). This certainly occurred prior to burial, heating and cooling below ~180°C. Although all seven ZHe samples from the Cukali Dome were taken from sediments of the Krasta-Cukali nappe with different depositional ages, they show similar apparent cooling ages (Fig. 3.5). Cooling to about ~110°C in Late Oligocene to Early Miocene time is indicated by AFT apparent cooling ages and most likely not interrupted by heating events, as indicated by the uniformity of Oligocene to Early Miocene cooling ages across the Cukali Dome. This cooling was similar timed in the next higher High Karst nappe, just north of the Cukali Dome with an AFT cooling age of 29±7 Ma (Fig. 3.5; Al-MG_133) across the normal fault that limits the Cukali Dome to the north (Figs. 3.2 and 3.3).

Modelled peak-temperature contours cut the nappe contacts of the external Dinaric nappes remain unaffected by Cukali Doming (Fig. 3.2). Thus, thermal modelling indicates that doming left no thermal imprint. Cooling below 180°C and 110°C, respectively, was coeval within and outside the Cukali Dome. We suggest that the peak temperatures in the Cukali Dome were reached after or during the latest stages of nappe stacking, the contours have not been disturbed by doming. Thus, doming was coeval to nappe stacking, maybe related to the different mechanical properties within the nappe stack to the north and to the south of the Cukali Dome. It is likely that doming was too small to disturb isotherms sufficiently and that the present day surface exposure (Fig. 3.7j) of the Cukali Dome relates to erosion and denudation processes.

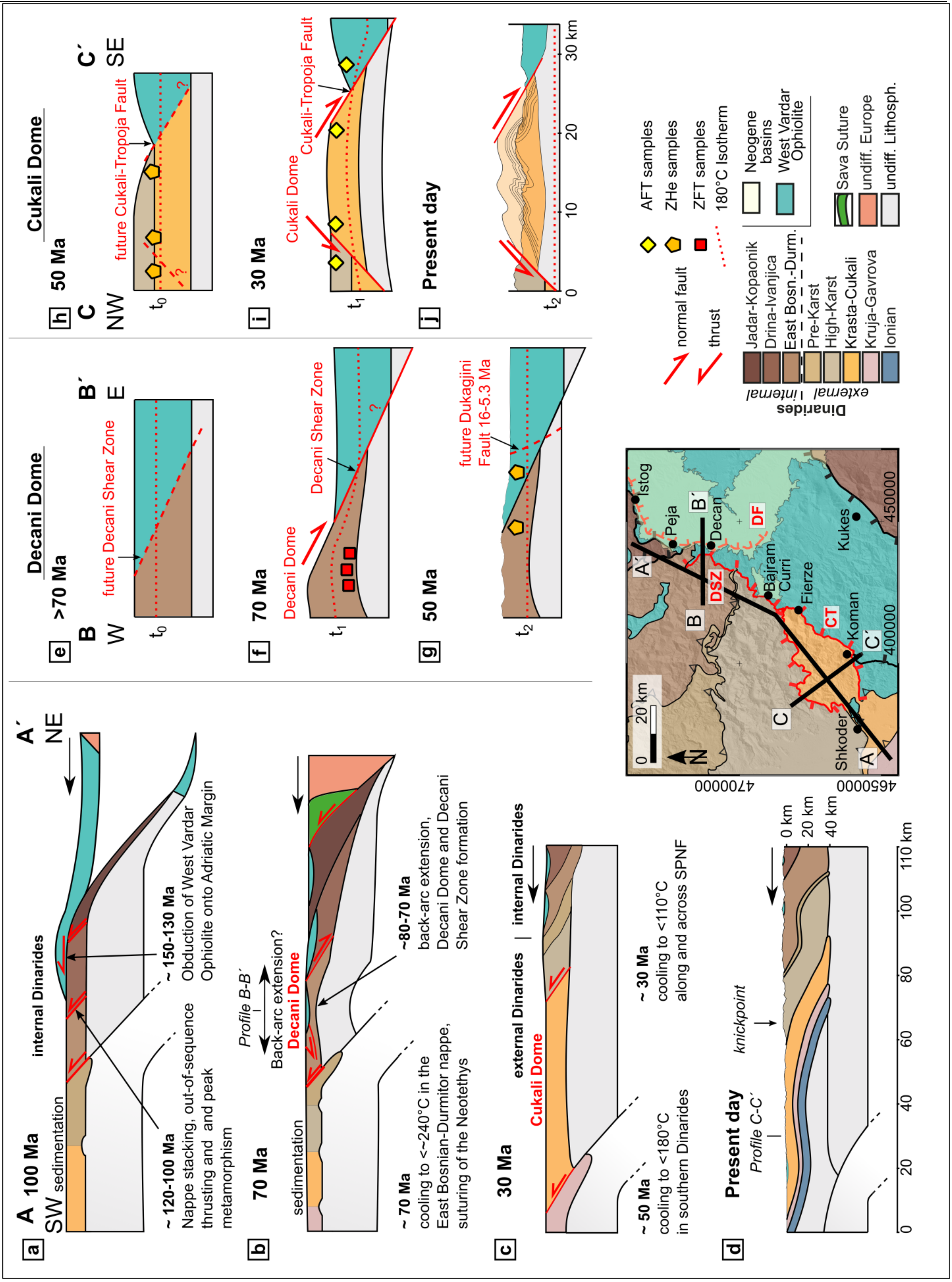
a
A 100 Ma
SW sedimentation
internal Dinarides
A´
NE
~ 120-100 Ma
Nappe stacking, out-of-sequence thrusting and and peak metamorphism
~ 150-130 Ma
Obduction of West Vardar Ophiolite onto Adriatic Margin
b
70 Ma
sedimentation
Profile B-B´
Back-arc extension?
Decani Dome
~ 70 Ma
cooling to <~240°C in the East Bosnian-Durmitor nappe, suturing of the Neotethys
~80-70 Ma
back-arc extension, Decani Dome and Decani Shear Zone formation
c
30 Ma
external Dinarides
Cukali Dome
internal Dinarides
~ 50 Ma
cooling to <180°C in southern Dinarides
~ 30 Ma
cooling to <110°C along and across SPNF
d
Present day
Profile C-C´
knickpoint
0 km
20 km
40 km
0
20
40
60
80
100
110 km
Decani Dome
e
>70 Ma
B
W
B´
E
future Decani Shear Zone
t0
?
f
70 Ma
Decani Dome
Decani Shear Zone
t1
?
g
50 Ma
future Dukagjini Fault 16-5.3 Ma
t2
Cukali Dome
h
50 Ma
C
NW
C´
SE
future Cukali-Tropoja Fault
t0
?
i
30 Ma
Cukali Dome
Cukali-Tropoja Fault
t1
j
Present day
t2
0
10
20
30 km
0
20 km
N
A
Shkoder
C
C´
Koman
CT
Fierze
Bajram Curri
DSZ
B
A´
Peja
Decani
B´
DF
Istog
Kukes
4700000
4650000
400000
450000
normal fault
thrust
AFT samples
ZHe samples
ZFT samples
180°C Isotherm
Dinarides
internal
external
Jadar-Kopaonik
Drina-Ivanjica
East Bosn.-Durm.
Pre-Karst
High-Karst
Krasta-Cukali
Kruja-Gavrova
Ionian
Neogene basins
West Vardar Ophiolite
Sava Suture
undiff. Europe
undiff. Lithosph.

Fig. 3.7: Tectonothermal reconstruction of Dinaric nappe stacking and normal faulting along the SPNF (not to scale). (a) Internal Dinarides at 100 Ma during closure of the northern branch of Neotethys and obduction of West Vardar Ophiolite onto the passive Adriatic margin. Peak-metamorphic temperatures in the Dinarides (~300 - <500°C; Sudar and Kovács 2006; Porkoláb et al. 2019, this study) are related to obduction (~150 – 130 Ma) and subsequent nappe stacking (~ 120 – 100 Ma; Porkoláb et al. 2019) in the internal Dinarides. Cretaceous cooling ZHe ages from the ophiolite indicate pre-orogenic cooling after obduction-related metamorphism; (b) Internal Dinarides at 70 Ma with syn-orogenic flysch sedimentation in the Krasta-Cukali unit and back-arc extension causing exhumation in the Decani Dome formation in the footwall of the Decani Shear Zone, a low-angle detachment fault. ZFT cooling ages indicate cooling from ~460-320°C to < 240°C at around ~70 Ma, simultaneous with Sava suturing and the beginning Adria-Europe collision; (c) Dinarides in Paleogene time (30 Ma) along A-A´ in inset. AFT and ZHe samples were buried and heated to at least ~180°C in the entire SPNF footwall. Cooling through the ~180°C and ~110°C isotherms in the external and internal Dinaric nappes; (d) Present-day cross-section of the southernmost Dinarides in the footwall of the SPNF; (e) Pre-70 Ma situation across the future Decani Shear Zone with undisturbed t_0 240°C isotherm: (f) Cooling of the footwall of the Decani Shear Zone (Decani Dome) to < 240°C by 70 Ma as indicated by ZFT cooling ages between 68-73 Ma. Note upwelling of the t_1 240°C isotherm during doming, indicated by preserved RSCM peak-temperatures; (g) Coeval cooling of the foot- and hanging walls of the Decani Shear to < 180°C (t_2 isotherm) indicated by uniform ZHe ~50 Ma cooling ages across the shear zone in profile B-B´; (h) Cooling of the external Dinaric units <180°C (t_0 isotherm) at ~50 Ma in the footwall of the Cukali-Tropoja Fault. t_0 isotherm equilibrated after Dinaric phase of thrusting and nappe stacking; (i) Slow and minor extension at around 30 Ma at the Cukali Dome possibly caused slight upwarping of isotherm t_1(110°C isotherm) but is not recorded as indicated by uniform cooling to <110°C of foot- and hanging walls; (j) Present profile across the central part of the Cukali Dome bounded by normal faults (including Cukali-Tropoja Fault). CRS of inset map: WGS 84, UTM zone 34N. Profiles not drawn to scale.

Age of the SPNF

Reset ZFT cooling ages (Fig. 3.5) are restricted to the footwall of the Decani Shear Zone and expose rocks preserving the oldest cooling ages (<240°C, 73 – 68 Ma) of the Dinaric nappe stack (Fig. 3.7). The 11 reset ZHe cooling ages along the Dinaric-Hellenic junction (57-43 Ma; Fig. 3.5) represent cooling of the rocks to below ~180°C after Dinaric nappe stacking. The ages overlap within 1σ error along and, at the Decani Shear Zone, also across the SPNF. Thus, the proposed increase in throw along the SPNF towards the east occurred prior to cooling of the footwall to temperatures below ~180°C at 57-43 Ma.

The Cukali-Tropoja segment (CT; Fig. 3.3) of the SPNF and the Decani Shear Zone (DSZ; Fig. 3.3) were active after cooling to below ~180°C as indicated by uniform ZHe cooling ages. Also, overlapping apparent AFT cooling ages across the Cukali-Tropoja Fault and the Decani Shear Zone (swath profiles in Fig. 3.6 and Fig. 3.5) preclude differential cooling and exhumation between foot- and hanging walls. This is not surprising for the SW end of the Cukali-Tropoja segment of the SPNF, where the vertical offset is only ~ 300 m at most (Handy et al. 2019) and would be insufficient to be detected as different cooling histories on either side of the fault.

On the map scale, the Cukali-Tropoja Fault cuts the southern limb of the Cukali Dome, but on the outcrop scale, the foliation in the dome is observed to bend into concordance with the macroscopic fault plane (Grund et al. *in review*). Together, these suggest that faulting syn-, but more likely, post-dated doming, but partly the foliation of the southern limb of the Cukali Dome bends towards the fault plane, whereas it is not unusual that structures, i.e. foliations are rotated into parallelism to major faults or shear zones (e.g. White et al. 1986). ZHe ages (e.g. ~46 and ~48 Ma) and AFT ages (~29 and ~35 Ma) across the NW-dipping, top-NW normal fault delimiting the northwestern limb of the Cukali Dome (Fig. 3.5) indicate cooling below the Tc (~180°C and ~110°C) of these age systems during or shortly after nappe emplacement (Grund et al. *in review*). Moreover, the similar AFT cooling ages (within error) on either side of the SPNF documents uniform cooling from 110 – 60°C of the region after motion on the SPNF had stopped or was insignificant. This constrains most throw due to normal faulting along the main segments of the SPNF to have occurred prior to and during Early Miocene time. Within error of the thermochronological systems, this means the extensional exhumation in the footwall pre- to syn-dated the stratigraphically constrained onset of Middle Miocene subsidence of the West Kosovo Basin along the Dukagjini segment of the SPNF (Figs. 3.2 and 3.3; Grund et al., *in review*).

In the northeastern part of the Cukali-Tropoja Fault with >2500m of differential offset shows surprisingly similar apparent AFT cooling ages (Oligo-Miocene) on either side of the SPNF. This holds true all along-strike of the SPNF from Shkoder to Decan (Figs. 3.3, 3.6 and 3.7).

Since our data show no discernable trend in ages along and across the SPNF, a complex scenario for faulting across the Cukali Tropoja Fault and the latest, brittle phase of the Decani Shear Zone must be concidered. Peak temperatures indicate that the West Vardar Ophiolite nappe in the SPNF hanging wall and the Dinaric nappe stack in the footwall reached temperatures greater than the APAZ. The similar ages for each system on either side of the SPNF suggest that cooling through the APAZ occurred at about the same time and rate (Fig. 3.6).

We speculate that the large spread of single-grain AFT ages reflects prolonged exposure of the samples to temperatures within the partial annealing zone (Reiners and Farley 2001). Cooling and exhumation was probably initially faster in the Decani Dome at > 240°C followed by cooling to temperatures < 240°C. We attribute the absence of discernable differential cooling across the SPNF either to normal faulting at temperatures higher than the T_c of the thermochronometers used here, or more likely, to slow and/or minor displacement on the SPNF. As our ZFT and RSCM analysis reveals only a limited number of reset ZFT ages (T above 240°C) and maximum ~460°C peak-temperatures, it is unlikely that normal faulting happened at much higher temperatures than those of our applied thermochronometers. We therefore argue that the temperature difference and displacement between the foot- and hanging walls was small enough to be undetectable by the ZHe and AFT systems.

However, the heavy mineral fertility of the sampled foot and hanging wall lithologies may also have biased our ages. Most of the Dinaric nappes in the footwall of the SPNF contain vast areas of limestone, not fertile in heavy minerals. The hanging wall contains strongly weathered ophiolites intercalated by weathered deep-sea sediments, also poor in heavy minerals. Nevertheless, our sampling strategy of sampling large amounts of material and cautious mineral separation and preparation allows robust and comparable interpretation of foot- and hanging wall thermochronometers.

Estimated cooling rates at the Dinaric-Hellenic junction

The SPNF has a relatively small amount of throw compared to other, crustal-scale normal faults (e.g., Brenner fault in the European Alps: displacement ranging from 2-20 km (Behrmann 1988; Rosenberg and Garcia 2011) up to 44-70 km (Fügenschuh et al. 1997, 2012), discussion in Fügenschuh et al. 2012 and references therein. The slip rate of the Brenner fault is stated to be a rate of 4.2±0.9 km/Myr (Wolff et al. 2020). Taking the minimum time limits for SPNF faulting between ~28 Ma and ~16 Ma (end of Dinaric thrusting and begin of Dukagjini Fault, see chapter above) with an offset of ~2500 m for the Cukali-Tropoja Fault, combined with ~1000 m offset of the Dukagjini Fault leads to ~3500 m offset, resulting in a relatively low slip rate of ~0.3 km/Myr. Considering that, the Decani Shear Zone was active even before 28 Ma and that the activity of the Dukagjini Fault continued after its onset at 16 Ma, slip rates would be even lower that ~0.3 km/ Myr. If valid, such low slip rates possibly imply that the thermochronological ages record mostly post-tectonic thermal relaxation rather than fault slip (Braun 2016; Wolff et al. 2020). However, the low slip rate calculate above is an absolute minimum value as it entails the assumption of continuous faulting during the entire period, which is unlikely. Faulting probably occurred within a shorter period.

To determine the amount and rate of thermal relaxation, we calculated cooling rates (Fig. 3.8) for the East Bosnian-Durmitor nappe since Latest Cretaceous time as well as for the Krasta-Cukali and High Karst nappes since Early Eocene time. The East Bosnian-Durmitor nappe shows cooling rates of ~ 3.2°C/Myr, cooling from <240°C to <180°C between ~70 and 50 Ma. Subsequent cooling of both the Internal and External Dinarides from <180°C to <110°C during 50 and 30 Ma occurred at a rate of ~3.0°C/Myr. Cooling from ~30 Ma to the present occurred at a rate of ~3.2 °C/Myr (<110°C to 180°C; Fig. 3.8). We assume a maximum paleo-geothermal gradient of 30°C/km, similar to the present maximum geothermal gradient (Cermak et al. 1996), and which is consistent with the average 32-30°C/km for the paleo-geothermal gradient in the central part of the External Dinarides (Środoń et al. 2018).

Presuming that cooling is related solely to exhumation, we use the long-term cooling rate of ~3.2 - 3.0°C/Myr between Eocene and Miocene times (AFT and ZHe cooling ages; Fig. 3.8) to estimate an erosion rate of 0.1-0.2 km/Ma (Reiners and Brandon (2006; their Fig. 3.4)), or ~0.1 – 0.2 mm/yr, for time spans of 30-20 Ma. This is the time span during which the samples cooled though the T_c of the different thermochronological systems (ZFT at ~70 Ma, ZHe at ~50 Ma and AFT at ~30 Ma to present day). If valid, these slow cooling rates suggest long-term erosion and denudation (e.g. Willigers et al. 2001) rather than to active tectonic settings (e.g. Ni 1989; Gemignani et al. 2018). Very active tectonic events with large fault offsets would have left any signal in the thermal signal between hanging and footwall samples. Such active tectonics happened for example in the nearby Jadar-Kopaonik nappe (Schefer et al. 2011), with tectonic unroofing and core-complex formation (K-S in Fig. 3.b) accompanied by cooling rates of 10°C/Myrs from 10 Ma to present day (Schefer et al. 2011).

As there is no significant difference in thermochronological ages, even using different and independent methods and samples, it is likely, that both foot and hanging wall are commonly exhumed. The simplest and most plausible explanation is erosion; however, some denudation was probably related to tectonics, in short time periods below the resolution of the broad time span given by our applied thermochronometers. Our calculated cooling and erosion rates are much lower, than compared tectonic exhumation related rates of 1.2 mm/yr in the Peshkopia Window (Fig. 3.9).

Based on the erosion and denudation rates of 0.1 – 0.2 km/Myr, we suggest that a ~1.6 – 3.2 km thick rock pile in the footwall of the SPNF was eroded and deposited since the Middle Miocene (16 Ma) as determined from the oldest syn-rift sediments in the Western Kosovo Basin (Elezaj and Kodra 2012). This amount of sediments is however not entirely preserved in the basin, as the Western Kosovo Basin presently drains to the Adriatic Sea, some Mio-Pliocene lake sediments (Gemignani et al. 2022) have already been eroded as evidenced by the exposure of Miocene lignite (Kopp 2016) in the basin (Elezaj 2009; Elezaj and Kodra 2012).

Erosion rates of 0.01-0.2 mm/yr reported for interglacial periods and present day drainages from other Alpine mountains (e.g. Matsuoka 2008) are comparable to the values calculated above in our study area. This is reasonable because the Dinarides were located more to the south (~30°N) at 40 - 30 Ma (Scotese 2002; Środoń et al. 2018; van Hinsbergen et al. 2020). According to Gemignani et al. (2022), changes in landscape morphology at the Dinaric-Hellenic junction reflect a combination of inherited structural relief from the SPNF and short-term climatic effects such as post-glacial melting and drainage integration. Fault activity is an indirect driver for focused erosion and sediment transport (Copley et al. 2009).

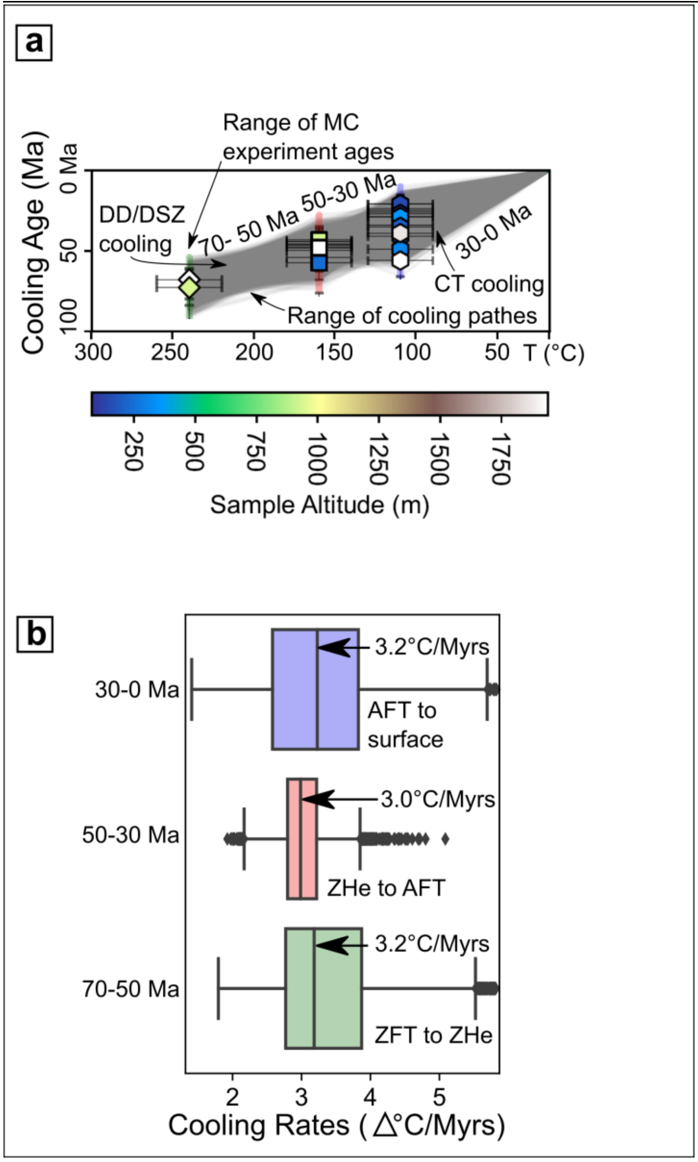

Fig. 3.8: Cooling models: (a) Cooling ages vs. temperature (°C) of the ZFT, ZHe and AFT systems. Modelling included all samples from Fig. 3.5 from SPNF foot- and hanging walls excluding inherited provenance signals. Grey shaded area indicates range of possible cooling paths from Monte Carlo (MC) experiment (Raychaudhuri 2008; Harrison 2009) with 10.000 iterations. Color indicates sample altitude. Color-swath indicates the range of MC experiment ages; (b) Cooling rates obtained from the MC experiments. Numbers are 50% confidence interval cooling rates from temperatures <240-18°C from each thermochronological system.

Peak temperatures determined with RSCM south of the Peshkopia Window (Fig. 3.3 inset map) indicate that the Krasta-Cukali nappe experienced similar temperatures (~ 200°C) as in the western part of the Cukali Dome. Early to Mid-Miocene AFT cooling ages south of the Peshkopia Window (Fig. 3.3, inset map, Fig. 3.9, Tab. 1, Appendix II) overlap with published ages from the Peshkopia Window (Fig. 3.9, (Muceku et al. 2006, 2008), and are younger than along the SPNF. We speculate that this age pattern reflects accelerated Mio-Pliocene orogen-normal extension and rapid exhumation in the upper plate of the retreating Hellenic subduction (Fig. 3.9; Wortel and Spakman 2000; Muceku et al. 2008). Our data certainly do not record rapid Oligo-Miocene uplift and exhumation of the Dinarides, as proposed in response to Dinaric slab delamination (Schefer et al. 2011; Balling et al. 2021).

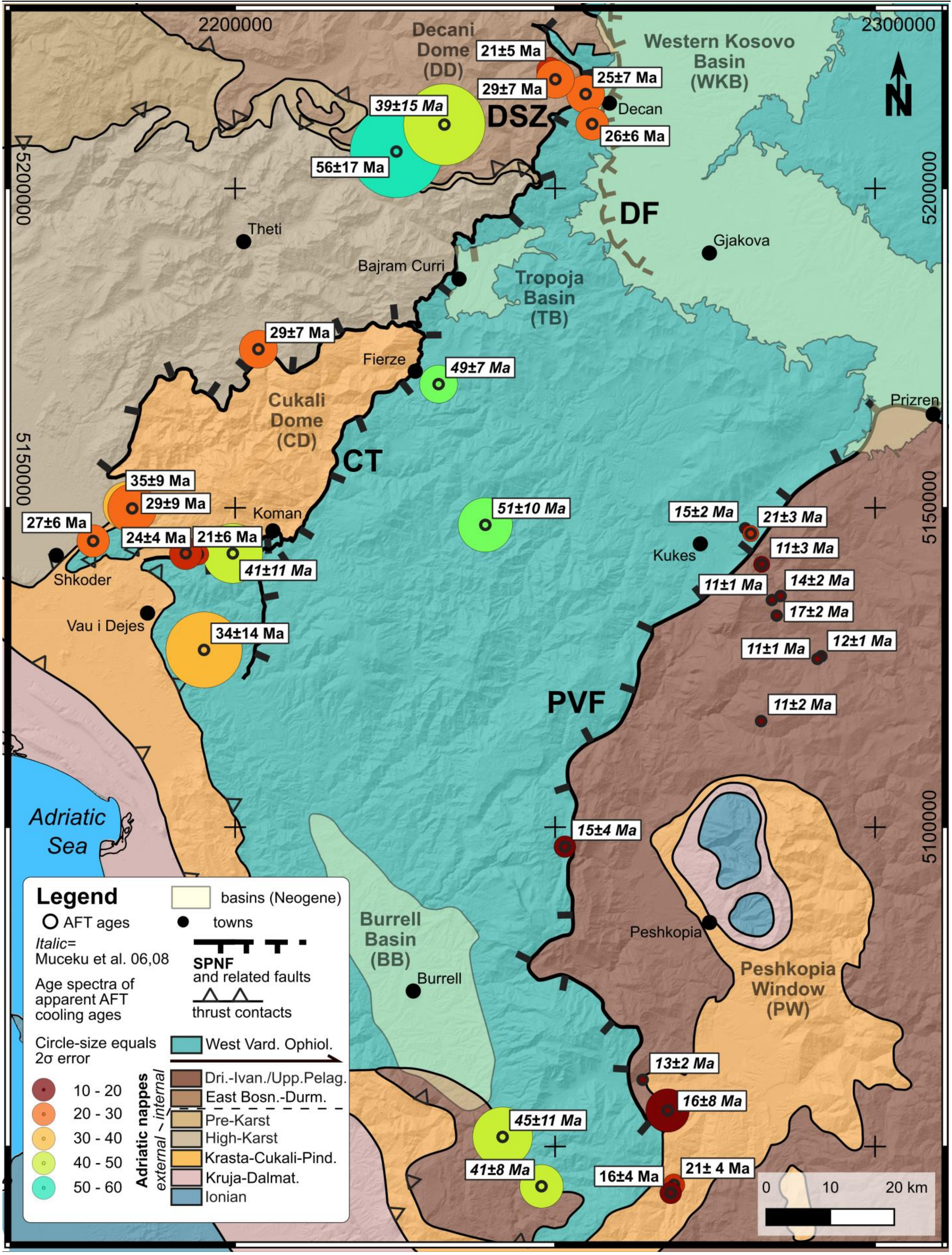

Fig. 3.9: Distribution of regional AFT cooling ages from central and northern Albania and southwestern Kosovo in this study and Muceku et al. 2006, 2008 (italic numbers). Color of circles indicates age of samples. Circle diameter indicates 2σ standard deviation. CRS of map: WGS 84, UTM zone 34N. Hillshade based on ASTER GDEM (Abrams et al. 2020).

Conclusions

The thermochronological and thermometric analysis of the Dinaric-Hellenic junction reveals peak-temperatures that relate to an early orogenic phase (ocean-continent obduction) and a later phase of collisional nappe stacking and burial. Subsequent heating was followed by cooling and exhumation, first in the Internal Dinarides (cooling to <240°C in Late Cretaceous), then affecting the External Dinarides (cooling to <180°C in Early Eocene and to <110°C in Oligo-Miocene). This cooling is partly attributed to exhumation in the footwall of the SPNF. Obduction-related metamorphism of the West Vardar Ophiolite most probably occurred in Latest Jurassic- Early Cretaceous (148 to 130 Ma) time (Most 2003; Tremblay et al. 2015), with temperatures reaching ~280°C. Obduction was followed by cooling of the ophiolite in Cretaceous time (~105-85 Ma) as indicated by ZHe ages, during or slightly after cooling of the Korabi-Pelagonian composite nappe (incorporating ophiolites) in the Hellenides. Nappe stacking and burial to 11-15 km depth and heating to peak temperatures of ~460°C in the Internal Dinarides happened after West Vardar obduction, whereas nappe stacking happened later in and the external Dinarides (Eo-Oligocene). ZFT cooling ages in the Decani Dome indicate cooling to below ~240°C during the period 73 – 68 Ma. Arcuate peak-temperature contours around the perimeter of the dome indicate that the attainment of peak-temperatures pre-dates Decani doming of the East Bosnian-Durmitor nappe in the footwall of the Decani Shear Zone. Mylonitic shearing at temperatures of ~300-350°C occurred at temperatures only slightly less than those attained in the dome itself, suggesting that doming and faulting along the Decani Shear Zone were broadly coeval. We therefore propose that at ~80 Ma the Decani doming and exhumational shearing occurred during earlier post-nappe exhumation, probably in a back-arc setting, to the east of the accretion-subduction front then active in the external parts of the Dinaric orogen.

Peak temperatures of ~180-280°C in the Krasta-Cukali and High Karst nappe (External Dinarides) indicate ~6-10 km depth during burial which can be attributed to Dinaric thrusting and nappe stacking in Middle Eocene to Early Oligocene time. Peak-temperature contours cut across nappe contacts and are unaffected by the Cukali Dome, which itself syn- to post-dates Dinaric nappe stacking. Locally, cooling below ~180°C and ~110°C, respectively, occurred simultaneously in the respective temperature window at different locations in the Cukali Dome, as evidenced by uniformly distributed ZHe and AFT ages in and beyond the dome. This indicates either that peak temperatures were attained after doming, equilibrated peak temperatures before cooling below ~180°C-110°C, or that doming was too small to disturb the peak temperature pattern.

The activity of the Cukali-Tropoja Fault, part of the SPNF, post-dates the Dinaric phase of nappe stacking (<28 Ma) as it cuts Dinaric folds and thrusts and it syn-to post-dates Cukali Doming. Although the offset of the Cukali-Tropoja Fault increases from 0 near Shkoder to >2500 m near Bajram Curri and Decan, uniform ZHe (T_c ~180°C; ~50 Ma) and AFT cooling ages (T_c ~110°C; ~30 Ma) along and across the SPNF indicate no detectable fault offset and differential cooling in foot- and hanging walls. We thus suggest that some offset along the SPNF occurred prior or during Early Miocene time, after Dinaric nappe stacking but before cooling to ~110-60°C. Prolonged exposure of the AFT samples to temperatures in their partial annealing zone indicate slow cooling, so gradual that thermal equilibration presumably happened at the same rate as normal faulting. It remains speculative that normal faulting occurred at temperatures higher than the T_c of the applied thermochronometers. The more likely explanation is that the throw on the SPNF was too small and insufficient to disturb the temperature field enough to be detectable by the thermochronological systems within their uncertainties.

In summary, we distinguish early Dinaric extension along the Decani Shear Zone with post-nappe stacking activity of the Cukali-Tropoja and Dukagjini Faults and probably reactivated brittle parts of the Decani Shear Zone. Thus, the first (1) activity of the Decan part of the SPNF relates to late Cretaceous and possibly early Paleogene extension, whereas a second phase of activity in Late Oligocene-early Miocene time, occurred along the Cukali-Tropoja segment of the SPNF. The third phase (3) relates to the Dukagjini Fault in the hanging wall of the other segments and was related to the formation of the Mid-Miocene to Pliocene Western Kosovo Basin.

Long-term cooling rates, of 3.0-3.2°C/Ma since the Late Cretaceous times for the East- Bosnian-Durmitor nappe and since the Early Eocene for the Krasta-Cukali and High Karst nappe in the footwall of the SPNF indicate slow cooling and exhumation that mostly relates to erosion and denudation with rates of 0.1-0.2 mm/yr. However, faulting along the SPNF may have enhanced exhumation and cooling over shorter periods which are beyond the resolution of our applied thermochronometers. Taking the erosion and denudation rates at face value, we estimate that ~1.6 – 3.2 km of overburden in the SPNF footwall has been eroded since the Middle Miocene (16 Ma). The Western Kosovo Basin which began to subside at 16 Ma (Elezaj 2009) would seem a likely sink for this eroded material.

We suggest that Pliocene orogen-parallel extension, slab rollback and rapid exhumation of the upper crust was focused south of the SPNF, in the area of the Peshkopia Window rather than along the Dinaric-Hellenic junction. Rapid Oligo-Miocene uplift and exhumation related to Dinaric slab delamination reported from other parts of the Internal Dinarides is not recorded in our data from the Dinaric-Hellenic junction. However, extension since Middle Miocene times relates to activity of the Dukagjini Fault and the Western Kosovo Basin formation.

Acknowledgments

We thank Stefan Schmid, Zenun Elezaj, Sali Mulaj, Benjamin Schmitz, Peter Biermanns and Kamil Ustaszewski for discussions in the field and thereafter. Thanks also go to Christoph Glotzbach for providing Durango standard apatite and Ray Donelick from Apatite.com for providing Fish Canyon Tuff standard crystals. Leonardo Caprioli assisted with mineral separation and performed the RSCM analyses in the northern part of the West Kosovo Basin. Kujtim Onuzi helped us with logistics in the field and established unvaluable links to local scientists and institutions. GIS work and graphics were designed with open-source software SAGA GIS, QGis and Inkscape, calculations and modelling was performed with Python software. This study was financed by German Research Foundation (DFG, grant No. Gi 825/4-1; No. Ha 21/21-1; No. Pl 534/3-1), Freie Universität Berlin and PROMOS (DAAD).

Chapter IV: Response of drainage pattern and basin evolution to tectonic and climatic changes along the Dinarides-Hellenides orogen

L. Gemignani[1], B. V. Mittelbach[1-2†], D. Simon[1], A. Rohrmann[1], M. U. Grund[1], A. Bernhardt[1], K. Hippe[1], J. Giese[1-3†], M. R. Handy[1]

(1) Institut für Geologische Wissenschaften, Freie Universität Berlin, Berlin, Germany, (2) Department of Earth Sciences, ETH-Zürich, Switzerland, (3) The Geological Survey of Norway (NGU), NO-7491 Trondheim, Norway, †Current Address

Published 2022 in: Front. Earth Sci. 10:821707. doi: 10.3389/feart.2022.821707
DOI: https://doi.org/*10.3389/feart.2022.821707*

Abstract

The junction of the Dinaric and Hellenic mountain belts hosts a trans-orogenic normal fault system (the Shkoder-Peja Normal Fault or SPNF) that has accommodated oroclinal bending, as well as focused basin formation and drainage of the Drin River catchment. Analysis of fluvial morphology of the Drin River system reveals higher values of river slope indices (*k*sn) and χ (Chi) between the normal faults of the SPNF and the Drin drainage divide. The drainage divide is predicted to be migrating away from the SPNF, except at the NE end of the SPNF system. Two basins analyzed in the hanging wall of the SPNF, the Western Kosovo Basin (WKB) and Tropoja Basin (TB), contain flat-lying late Pliocene-to-Holocene sedimentary rocks deposited well after the main fault activity and immediately after the LGM. These layers document an early Pleistocene transition from lacustrine to fluvial conditions that reflects a sudden change from internal to external drainage of paleo-lakes. In the TB, these layers were incised to form three generations of river terraces, interpreted to reflect episodic downstream incision during re-organization of the paleo-Drin River drainage system. ^{36}Cl-cosmogenic-nuclide depth-profile ages of the two youngest of these terraces (~12 and ~8 ka) correlate with periods of wetter climate and increased sediment transport in post-LGM time. The incision rate (~12 mm/yr) is significantly greater than reported in central and southern Albania. Thus, glacial/interglacial climatic variability, hinterland erosion and baselevel changes appear to have regulated basin filling and excavation cycles when the rivers draining the WKB and TB became part of the river network emptying into the Adriatic Sea. These dramatic morphological changes occurred long after normal faulting and clockwise rotation on the SPNF initiated in late Oligocene-Miocene time. Faulting provided a structural and erosional template upon which climate-induced erosion in Holocene time effected reorganization of the regional drainage pattern, including the formation and partial demise of lakes and basins. The arc of the main drainage divide around the SPNF deviates from the general coincidence of this divide with the NW-SE trend of the Dinaric-Hellenic mountain chain. This arc encompasses the morphological imprint left by roll-back subduction of the Adriatic slab beneath the northwestern Hellenides.

Introduction

Drainage networks in orogens are sensitive to tectonics and climatic conditions (Lavé and Avouac 2001; Whittaker et al. 2007; Whipple 2009; Wobus et al. 2010; Kirby and Whipple 2012; Whittaker 2012; Schwanghart and Scherler 2020) . These factors affect landscape morphology on the scale of continents, but the time scales on which they operate overlap on the spatial scale of orogens, faults, and individual basins (Whipple and Tucker 1999). The challenge addressed here is to distinguish spatial and temporal controls on the landscape in an active orogen with a prolonged history of oroclinal bending. We investigate the junction of the Dinaric-Hellenic mountain belt on the Balkan Peninsula, where the retreating Adriatic slab has affected lithospheric deformation from Paleocene to Holocene times (e.g. Burchfiel et al. 2008; Handy et al. 2019). We use the Neogene intramontane drainage basins of Northern Albania and Kosovo to examine the competing effects of both fossil and active fault systems, as well as transient Pliocene-Holocene climate on fluvial dynamics and landscape evolution.

Intramontane basins are either internally or externally drained depending on whether the river system draining the basin is connected with a lower base level (e.g., the sea). Thus, a change in the base level of a river in response to tectonic and/or climatic events can lead to the integration of river branches and landscape change (D'Agostino et al. 2001; Garcia-Castellanos 2006; Harkins et al. 2007; Attal et al. 2008; Geurts et al. 2018, 2020). On the other hand, numerical models have shown that river capture and integration can themselves change the local base level, producing pervasive changes in the river network geometry. Such transformations involve drainage divide migration and knickpoint mobility (e.g. Willett et al. 2014; Yang et al. 2015; Whipple et al. 2017). Several cycles of progressive basin filling and subsequent excavation characterize the spatiotemporal evolution of drainage basins. The basin gains or loses connectivity with the orogenic foreland (e.g., Aterno River in the Italian Apennines; see D'Agostino et al. 2001; Geurts et al. 2018). In either case, the fluvial system exerts a first-order control on the position and magnitude of sedimentary supply within the basin (Whittaker et al. 2007) which can be used to infer patterns of hinterland erosion (Braun et al. 2018; Gemignani et al. 2018).

The tectonics of the Dinaric-Hellenic mountain belt running along the eastern side of the Adriatic Sea (Fig. 4.1a) accommodated Late Cenozoic shortening related to northwestward advance of the Adriatic Plate relative to Eurasia, and the southwestward retreat of the subducting Adriatic slab beneath the Hellenides (e.g. Jolivet and Brun 2010; black arrows in Fig 4.1b). Slab rollback induced distributed extension of the upper plate of this subduction (Royden 1996) which has affected crustal structure, landscape, and drainage patterns from the Southern Balkans to the Aegean and Adriatic regions since the Late Paleocene to Present (e.g. Burchfiel et al. 2008). The rate of rollback subduction has increased to ~10 mm/yr since the Late Miocene (Jolivet and Brun 2010).

The junction of the Dinaric and Hellenic belts is an excellent place to study the competing effects of tectonics and climate on the fluvial network. This junction is the site of an oroclinal bend of some 20° (Fig. 4.1) that coincides with an orogen-parallel transition in mantle structure from a detached shallow segment of the Adriatic slab beneath the Dinarides to a long attached segment of the same slab to the south beneath the Hellenides (high Vp domains in blue in Fig. 4.1b, Wortel and Spakman 2000; Piromallo and Morelli 2003; Handy et al. 2019). This junction coincides with a system of faults, most prominent among them the Shkoder-Peja Normal Fault (SPNF, Fig. 4.1a), that cut across the orogen (Burchfiel et al. 2008; Schmid et al. 2008; Handy et al. 2019). Paleomagnetic studies indicate that bending started in Paleogene time, but increased markedly in Neogene time (Speranza et al. 1995; Kissel et al. 1995; Muceku et al. 2008). The bend in the orogen coincides with Cenozoic intramontane basins and an anomalous drainage pattern, including arcuation of the main drainage divide (MDD, dashed blue line in Fig. 4.1), that cuts to the northeast across the orogen (Fig. 4.1).

The Drin River at the Dinaric-Hellenic junction in northern Albania (Fig. 4.1) originates at the Ohrid Lake where it is called the Black Drin (Fig. 4.1a), then runs to the NW for ~150 km parallel to the strike of the orogen before joining its northern branch, the White Drin, near the town of Kukes (Fig. 4.1a). From there, the river cuts down through the West Vardar Ophiolite in a graben between conjugate normal faults of the SPNF system (thick red lines in Fig. 4.1a). The Drin empties into the Adriatic Sea near the city of Shkoder (Fig. 4.1a).

The present-day boundary between active orogenic shortening and extension defined in geodetic studies (Jouanne et al. 2012; D'Agostino et al. 2020) is referred to here as the shortening-extension transition (SET), signified by a dashed yellow line in Figure 4.1a. The SET trends across the nappe boundaries and also runs discordantly to the main drainage divide (blue dashed line in Fig. 4.1a). The drainage divide is deflected to the NE around the SPNF and its related faults.

Two basins in the hanging wall of the SPNF, the Western Kosovo Basin and Tropoja Basin, contain middle Miocene-Pliocene and Plio-Pleistocene clastic and freshwater sediments, respectively (Fig. 4.1a; Meço and Aliaj 2000). These basins are interpreted to have formed during clockwise rotation of the Hellenic part of the orogen with respect to the Dinaric segment (Handy et al. 2019). We note that some Neogene normal faults and basins also strike parallel to the orogen (e.g., basins labelled BB and KB in Fig. 4.1a) and form asymmetric half-grabens in the hanging wall of former Dinaric thrusts (Dumurdzanov et al. 2005; Burchfiel et al. 2008; Andrić et al. 2017; Handy et al. 2019). The Neogene age of the graben fill coincides with thermochronometric constraints on the age of cooling and exhumation in the footwall of such orogen-parallel normal faults from ~23 Ma until to ~4 Ma (Muceku et al. 2008).

In this paper, we investigate tectonic and climatic processes affecting the evolution of river drainage at the Dinaric-Hellenic junction. Following an introduction to the geology and morphology of the basins and their catchments at this junction, we provide descriptions of the stratigraphy and river terraces carved into the Tropoja Basin. This is followed by an outline of the methods used to characterize and date the landscape on scales ranging from this basin to the entire orogenic bend. A description of the basin stratigraphy and its river terraces carved into this basin is followed by a presentation of new ^{36}Cl exposure ages of these terraces. A morphometric analysis of the regional drainage network at the orogenic junction then lays the foundation for a discussion of how the river channel network has responded to tectonic uplift, erosion, and climate since Pliocene time. We conclude with a conceptual model for the Pliocene-to-Present evolution of basins at the Dinaric-Hellenic junction. It is found that the Neogene fault system that accommodated oroclinal bending and Hellenic slab rollback is the main factor controlling morphology on the orogenic scale. Faulting and footwall uplift increased rocks´ erodibility through fracturing and hill-slope degradation, whereas terrace incision and drainage integration through river capture events after the Last Glacial Maximum (LGM) regulated basin infilling on the scale of individual basins.

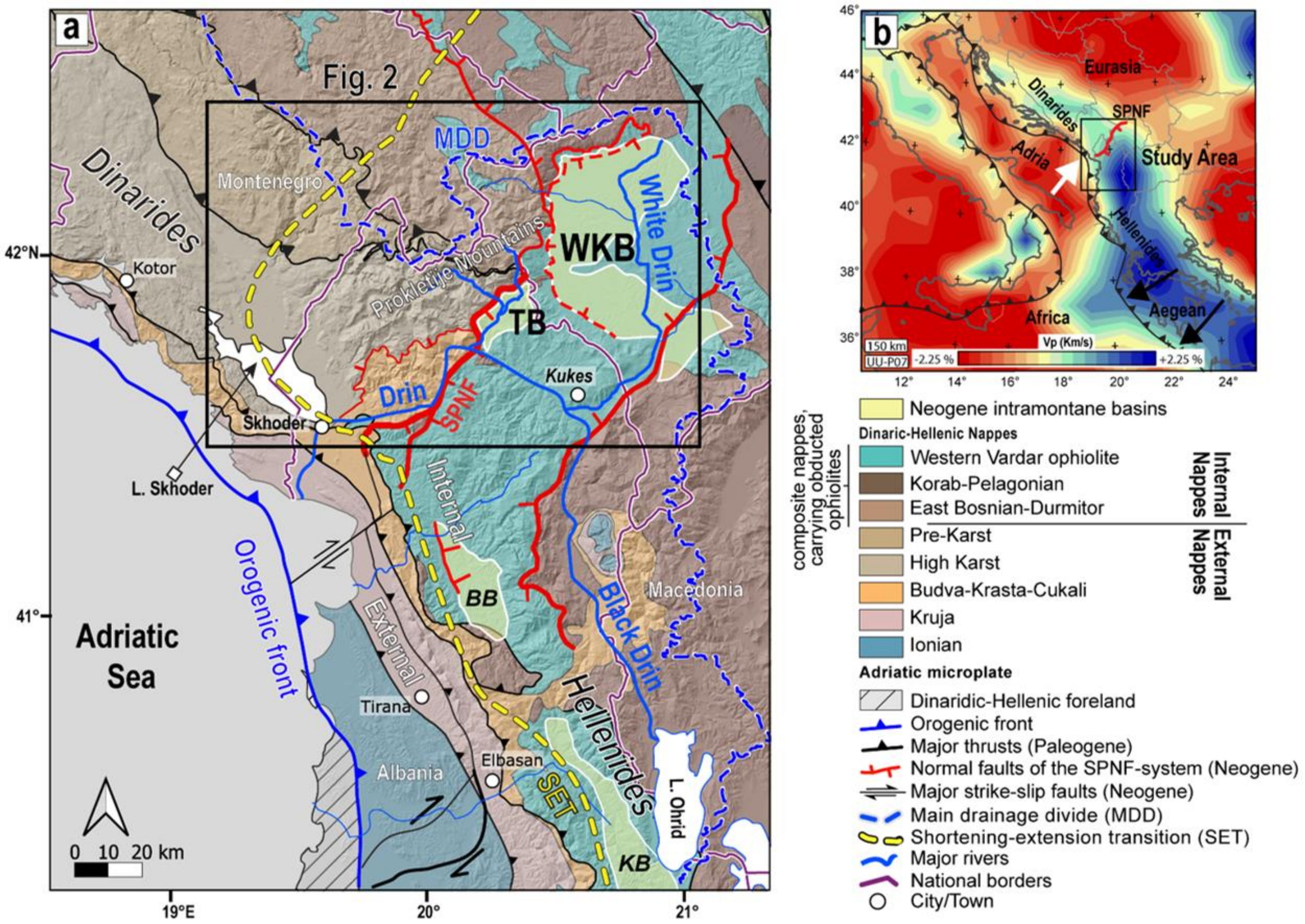

Fig. 4.1: Overview maps: (a) Tectonic map of the junction between the southern Dinarides and northwestern Hellenides. Faults and main nappe units are modified after Schmid et al. (2020). Blue lines - branches of the Drin River. Thick dashed yellow line – present-day transition from ongoing shortening to ongoing extension (SET) after Jouanne et al. (2012). Thick dashed blue line – main drainage-divide (MDD). Outlined box indicates the area of Figure 4.2. TB - Tropoja Basin, WKB - Western Kosovo Basin, SPNF - Shkoder-Peja Normal Fault, BB - Burrel Basin, KB - Korça Basin. Shaded relief based on SRTM-1 arc-second DEM (Farr et al. 2007; NASA JPL 2013); (b) Map of teleseismic P-wave anomalies at 150 km depth of the southeastern Mediterranean area. P-wave tomography is from Hall and Spakman (2015, their UU-P07 model). White arrow – motion of Adria relative to Eurasia. Black arrows - motion of the Hellenic orogenic front with respect to Eurasia since ~ 15 Ma due to retreat of the Adriatic slab beneath the Hellenides.

Geology of the study area

Tectonic setting

The Neogene tectonics of the Dinarides-Hellenides is characterized by NE-SW shortening (e.g. Cavazza et al. 2004) due to the northward motion of the Adriatic plate with respect to Europe (Fig. 4.1).

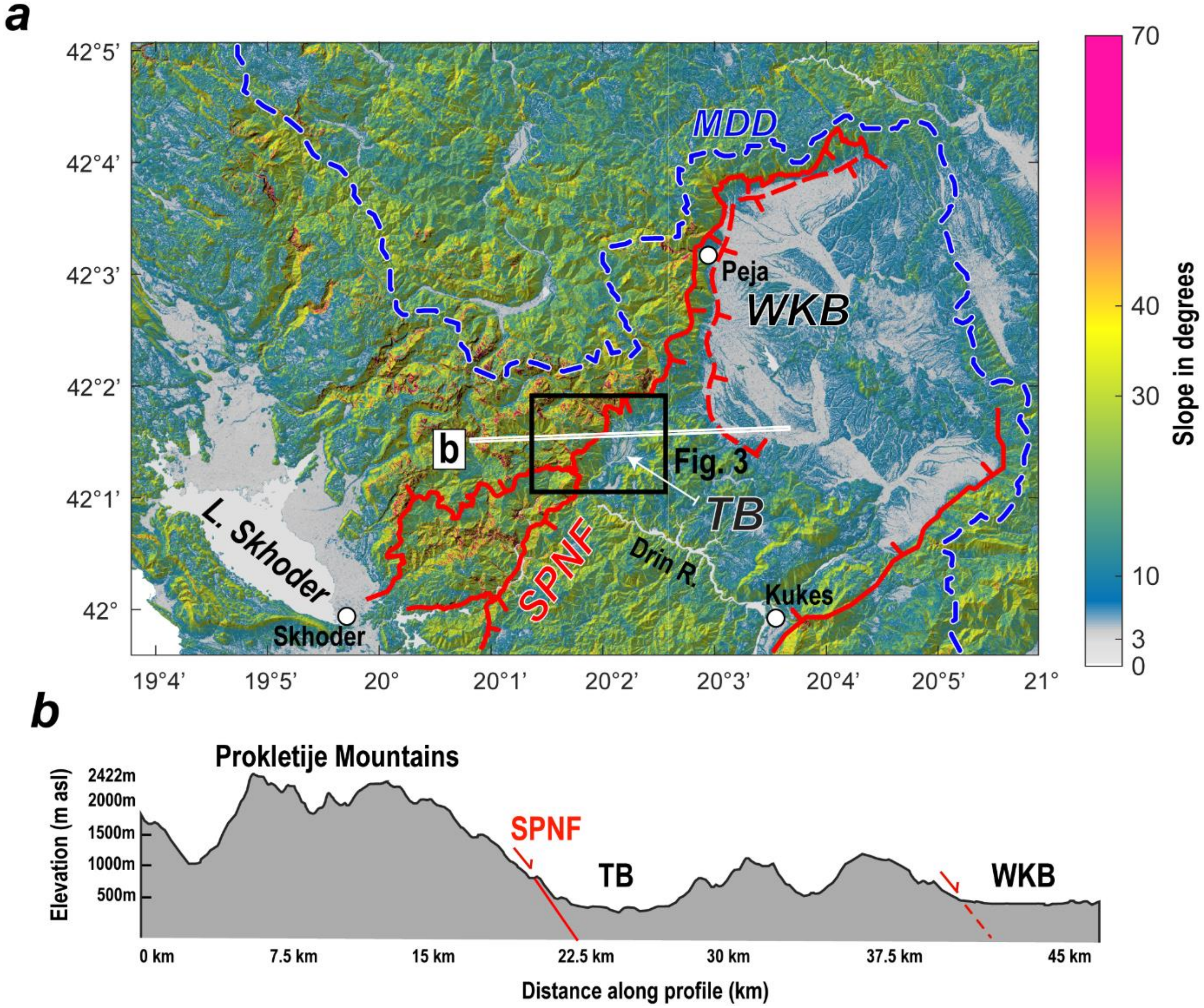

Fig. 4.2: Topography of the Dinaric-Hellenic junction: (a) Shaded slope map with major normal faults of the SPNF system marked as thick red line (surface exposure) and dashed red line (subsurface exposure). Blue dashed line - main drainage-divide (MDD). The slope analysis is based on SRTM-1 arc-second DEM (Farr et al. 2007; NASA JPL 2013); (b) Topographic cross-section along the trace in (a) includes the SPNF (solid red line) and related subsurface normal fault (dashed red line) bordering the Tropoja Basin (TB) and Western Kosovo Basin (WKB), respectively.

The Western Kosovo Basin and Tropoja Basin are both located in the hanging wall of the main normal fault of the SPNF system (Fig. 4.2). The stratigraphy of the Western Kosovo Basin is indicative of several cycles of internal drainage (e.g. Elezaj and Kodra 2012). The Black Drin River (Fig. 4.1) traverses crust that underwent Mio-Pliocene exhumation and E-W extension (Muceku et al. 2008), as well as subsidence that included the deposition and preservation of Pliocene lake sediments (Lindhorst et al. 2015).

The SPNF and related faults coincide with a significant jump in elevation and slope angles (Fig. 4.2). The maximum relief of ~2500m occurs in the vicinity of the Tropoja and Western Kosovo Basins, where the Proketlije Mountains with peaks of ~ 2700m are juxtaposed with the flat basins at only 200-350 masl (Fig. 4.2b). At the northern limit of the Western Kosovo Basin the relief decreases to ~1000m.

The Topoja Basin is filled with ~ 400 m of Pliocene-Holocene sedimentary rock (Fig. 4.4, Meço and Aliaj 2000; Gjani and Dilek 2010; Pashko and Aliaj 2020). Three rivers (Valbona, Gashit and Bushtrices, Fig. 4.3) carved the basin fill and generated three terraces (Figs. 4.3, 4.4). We sampled the lower and intermediate terraces for terrestrial cosmogenic nuclide (TCN) dating (yellow stars in Figs. 4.3a, b). The Valbona Valley hosts the principal river of the same name that drains the Topoja Basin. This uppermost part of this valley contains a niche rock glacier shielded by the topography of the Albanian Alps (Prokletije Mountains, Fig. 4.2), a ~3 km high mountain range (Kuhlemann et al. 2009). The striking relief of the Albanian Alps has been interpreted to reflect differences in the erodibility of the rocks on either side of the SPNF, as well as possible activity of this fault (Handy et al. 2019). The Pliocene-Holocene fill of the Tropoja Basin unconformably overlies the West Vardar Ophiolites in the hanging wall of the SPNF (Fig. 4.4).

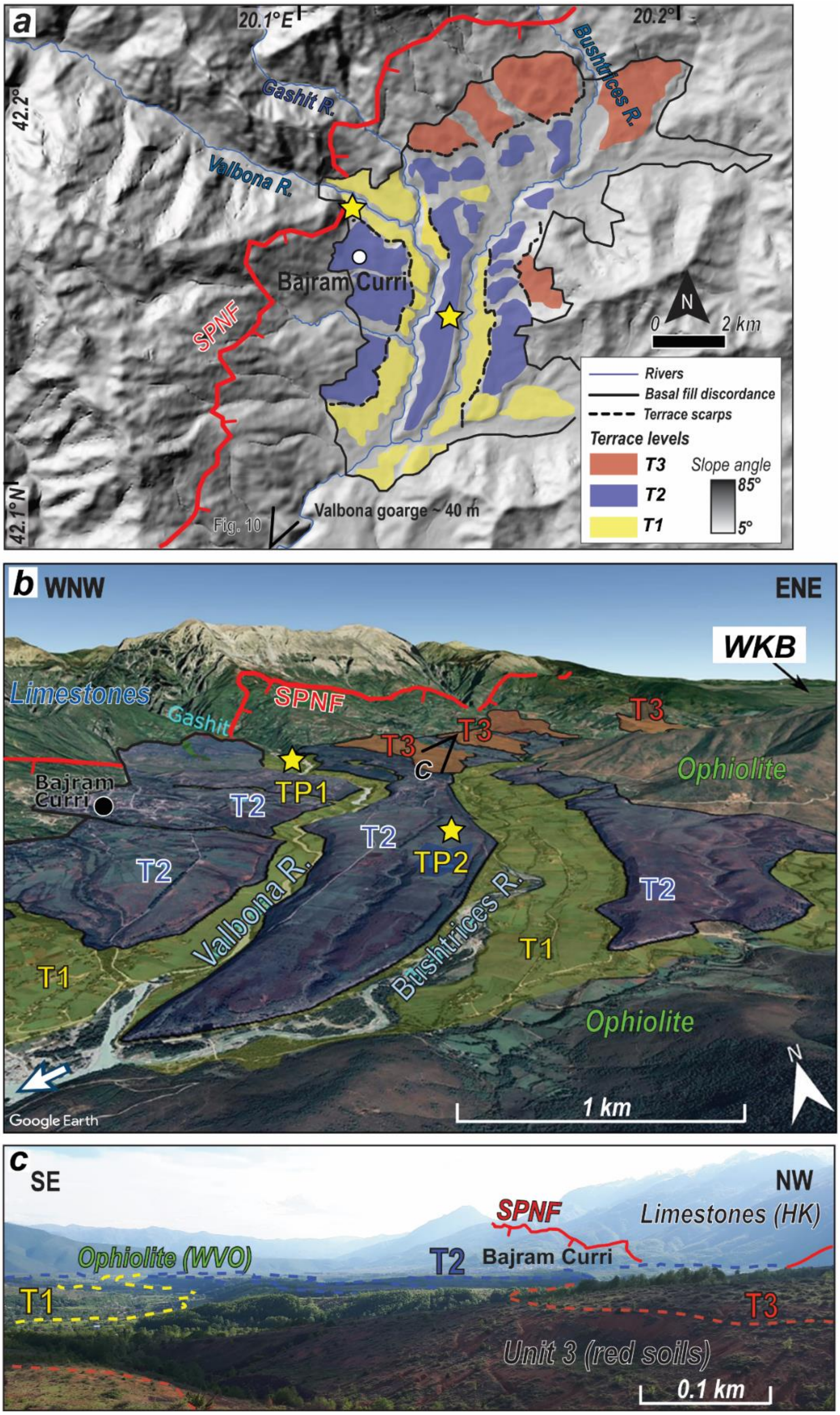

Fig. 4.3: Overview of fluvial terraces and abandoned river channels documenting episodic incision of the Tropoja Basin (TB) sediments: (a) Map with DEM hill shading and location of fluvial terraces. Terraces are numbered from youngest to oldest levels, T1 to T3. Thick red line - trace of the SPNF; Blue - present-day rivers in the TB; (b) Satellite image from Google Earth of the Tropoja Basin showing terrace surfaces coloured according to relative age. Imagery from Google Earth™, 42°.18‘N, 20°06‘E, 7/01/2021. Yellow stars - location of ^{36}Cl depth profiles; (c) Pleistocene-Holocene fluvial terraces. Note hummocky “terra rossa” (red soils) of Unit 3 (foreground) and the high relief of the Albanian Alps (background right) in the footwall of the SPNF. WVO - Western Vardar Ophiolite; HK - High Karst Nappe.

Tropoja Basin stratigraphy and river terraces

The Tropoja Basin contains three lithostratigraphic units with subhorizontal bedding (units 1-3 in Fig. 4.4; Pashko and Aliaj 2020). The bottom unit (Unit 1) is up to ~25 - 75 m thick and unconformably overlies the West Vardar Ophiolite. This unit contains layers of marls intercalated with medium- and coarse-grained sandstone (Figs. 4c, 5c). It has been dated as Late Pliocene using mollusk aggregations, pollen, and intercalated diatom-rich layers of marls (Gjani and Dilek 2010; Pashko and Aliaj 2020). We interpret this unit as a lacustrine deposit in a paleo-intramontane lake. At the Valbona River outlet, this unit onlaps the sub-ophiolitic mélange of the West Vardar Ophiolite and the Triassic limestone and Cretaceous flysch of the High Karst nappe (Figs. 4.4a, b). The strata locally dip some 20° to the NW, i.e., towards the SPNF (Fig. 4.5c). The very local nature of this dip and the lack of an increased layer thickness toward the SPNF precludes any fault-related rotation of the layers in the hanging wall of the SPNF. Instead, we attribute these unusual strata orientations to gravity sliding.

The intermediate unit (unit 2) is up to ~150 m thick and unconformably overlies unit 1 (Fig. 4.4b). Unit 2 comprises clast-supported conglomerate with a sand-clay matrix and local coal seams (Figs. 4.4c, 4.5d). Coarse sandstone layers and light-grey carbonaceous conglomerates contain tractional sedimentary structures. We interpreted unit 2 as a fluvial conglomerate of Late Pleistocene-Holocene age (Pashko and Aliaj 2020). Layers of unit 2 seal the SPNF at the outlet of Valbona (Fig. 4.4a), indicating that little or no normal faulting has occurred since their deposition.

Unit 3 some 30-50 m thick occurs along the northern and the southeastern margins of the Tropoja Basin (Fig. 4.4a) and comprises lithologies ranging from reddish conglomerates, sandstones and redshales of presumably Holocene age (Fig. 4.5a). Some of its units have been weathered red. Red soils form by the autogenic dissolution of carbonate and the possible addition of allochthonous aeolian sands commonly described in the Balkans as Terra Rossa (e.g. Muhs et al. 2010).

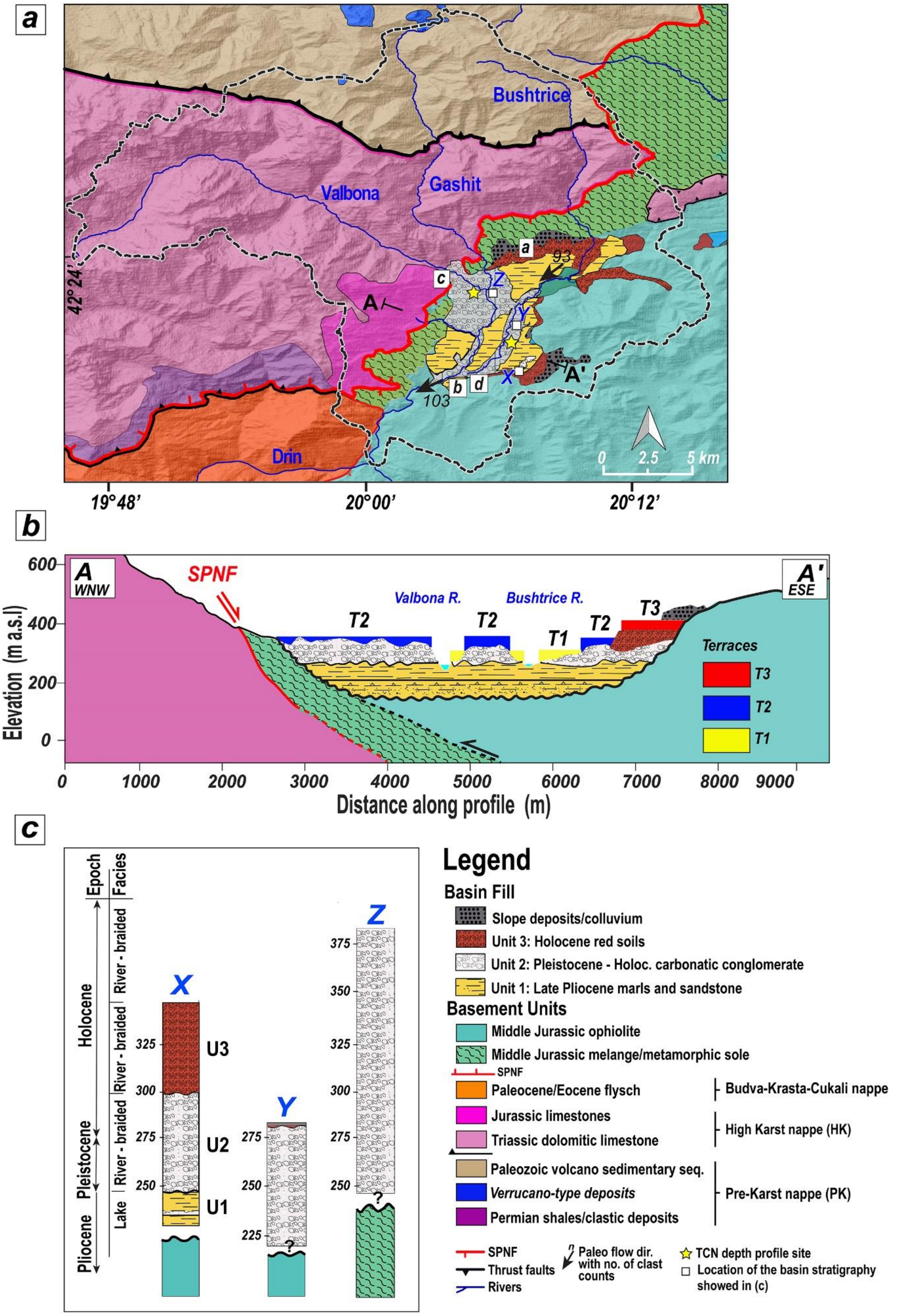

Fig. 4.4: Tectonic map and stratigraphy of the Tropoja Basin: (a) Lithostratigraphic map of the study area. The black dashed line represents the drainage area of the basin catchment at the confluence with the Drin River. Trace of the geologic profile A-A' shown in (b). Major rivers are shown in blue. The terraces in (b) have the same colour as in Fig. 4.3. Labels a-d are locations of pictures in Fig. 4.5; (b) Cross-section of the basin with bedrock, basin fill and fluvial terraces; (c) Stratigraphic columns at three locations X, Y, Z shown in (a).

The bedding of all units is generally sub-horizontal with local variations due to gravity sliding. Measured dip and dip-directions of the clast imbricates in bedding of the carbonaceous conglomerate of unit 2 indicate river paleocurrent directions (dotted lines of Fig. 4.5d). After correction, the paleocurrent transport direction is south- to southwest-directed (azimuth 120°, black arrows in Fig. 4.4a and Appendix III/Supplementary Fig. S5).

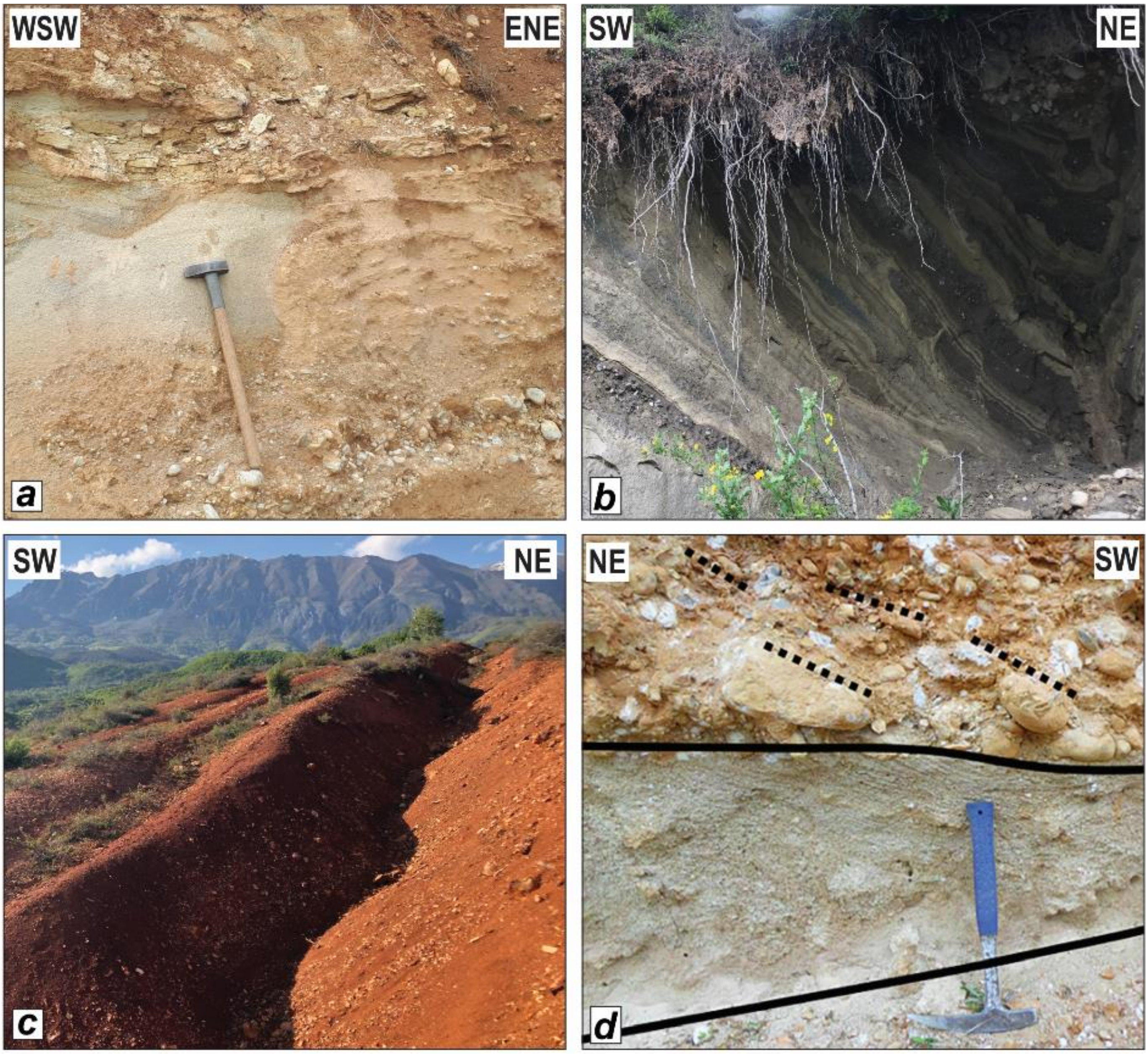

Fig. 4.5: Lithologies of the Tropoja Basin: (a) Unit 1: Grey marl and conglomeratic layers. The hammer is ~ 55 cm long; (b) Unit 1: grey marl and intercalated sandstone with bedding locally tilted to the NW; (c) Unit 3: Red beds (Terra Rossa) at the northern margin of the basin with layers of round pebbles; (d) Unit 2: Carbonate-rich conglomerate with inclined bedding overlying carbonaceous sandstone between black lines. Length of hammer ~33 cm. Locations of pictures labelled a-d in Fig. 4.4a.

Materials and Methods

^{36}Cl depth profile dating

Terraces T1 and T2 in the Tropoja Basin were sampled for cosmogenic ^{36}Cl dating (Gosse and Philips 2001; Ivy-Ochs et al. 2009) in two freshly excavated vertical terrace profiles, labelled TP1 and TP2 (yellow stars in Fig. 4.3). TP1 is in the lowest terrace T1 at 283 m asl (Table 4.1) that incised unit 2 (Fig. 4.4b) along the Valbona River. A total of six samples (500g each) of conglomerate comprising carbonate components and calcite cement were collected at equal vertical intervals between depths of 50 and 250 cm. Samples were not collected near the surface to avoid disturbances of the depth profile by bio- or cryoturbation (e.g. Schaller et al. 2009). In sampling, care was taken to select well-rounded pebbles to ensure fluvial provenance and common pre-depositional history (Appendix III/ Supplementary Information - Table S1). TP2 was sampled at 286 m asl in a freshly dug trench on terrace T2 on carbonate conglomerates of unit 2 (Table 4.1) following the same sampling procedure.

^{36}Cl dating was performed by the isotope dilution method (Ivy-Ochs et al. 2004, 2009). The samples were leached twice with 2 M HNO_3 for 24 hrs to remove meteoritic chlorine and an aliquot of ~ 10 g was separated for main and trace element analysis. The remaining sample material was dissolved with pure HNO_3 and spiked with 3.6 g of a ^{35}Cl carrier. Chlorine was precipitated as AgCl by adding $AgNO_3$ to the sample and then dissolved again in an NH_3 solution to remove sulfur as a precipitated $BaSO_4$ (Ivy-Ochs et al., 2004). Accelerator Mass Spectroscopy (AMS) analysis was performed at the Laboratory for Ion Beam Physics (LIP) at the ETH-Zurich following the procedure described by Christl et al. (2013). In addition to AMS measurements, we measured main and trace elements to correct the ^{36}Cl production rate (Appendix III/ Supplementary Information- Table S2).

We computed the depth profile age using Monte Carlo simulations in Mathcad (see Mair et al. (2019)). Information about the inherited amount of ^{36}Cl before exposure and the age of exposure was obtained from ^{36}Cl concentration patterns for each depth profile (Hidy et al. 2010; Mair et al. 2019). The model was designed to compute depth-profiles of cosmogenic nuclide for a series of user input parameters. In the Monte Carlo routine, we accounted for the topographic shielding effect and inheritance of ^{36}Cl. The input parameters required by the algorithm and the values used are summarized in Appendix III/ Supplementary Information in Table S3.

Topographic and fluvial analysis

We analyzed the river landscape at the Dinaric-Hellenic junction with two morphological measures: k_{sn} , the channel steepness index, as shown in Figures 4.7a and 4.9a (Flint 1974; Snyder et al. 2000; Kirby and Whipple 2001) and χ (Chi), which we use as a proxy for fluvial-morphological stability in eroding and uplifting systems (Perron and Royden 2013; Willett et al. 2014), as shown in Figure 4.9b.

The channel steepness index, k_{sn} is a dimensionless parameter defined as:

$$k_{sn} = S/A^{-\theta} \qquad \text{Eq. (1)}$$

where S is the local river gradient (taken to be positive in the downstream direction), A is upstream drainage area, and θ_{ref} is a reference concavity index (Wobus et al. 2006). Stated simply, k_{sn} tells us how much the channel steepness deviates from a reference concavity that is corrected for differences in drainage area. Faulting or lithological boundaries can cause steepness to deviate from θ_{ref}, such that the k_{sn} values will increase on the uplifting block and/or on the side of the fault with the more erosion-resistant bedrock. The higher the uplift rate and/or the more erosion-resistant the bedrock, the higher the k_{sn}-value and the greater the deviation from the reference concavity, θ_{ref}.

χ (Chi) has dimensions of length (m) and is defined:

$$\chi = \int_{xb}^{x} \left(\frac{A_0}{A(X')}\right)^{\theta} dx' \qquad \text{Eq. (2)}$$

where A_0 is an arbitrary scaling area and the integration to obtain χ is performed from a base level at xb to a location x upstream along the river channel. In our applications of χ below, the difference in χ values between river channels can be interpreted as an indicator for divide instability, provided that the uplift rate, climate, and rock erodibility are equal and that there are no major transients in river profiles (Willett et al. 2014). The river with the lower overall χ value has greater erosive potential than does the river with the higher overall χ value. χ maps like Figure 4.9b help visualize the direction that unstable drainage divides are expected to migrate (see Discussion).

In the *Discussion*, we use k_{sn} and χ maps (Fig. 4.9) to assess how faulting, lithology, post-LGM climate and base level change have affected fluvial morphology at the scale of the Dinaric-Hellenic junction. The two parameters, k_{sn} and χ, are complimentary because k_{sn} is more sensitive to short-wavelength perturbations in the river profile, whereas χ better detects changes in regional steady state in the fluvial system, with the changes referring to a shift from an older steady-state condition to the current steady-state condition. A steady-state condition in the morphological sense refers to a combination of variables (base level, climate, lithology, uplift rate, bedrock characteristics) that are assumed to be invariant in time and space over the area considered.

k_{sn} and χ were extracted from a digital elevation model (DEM) at 30 m (1 arcsec) resolution (Shuttle Radar Topography Mission, SRTM; Farr et al. 2007; NASA JPL 2013). The analysis itself was performed using the MATLAB software package TopoToolbox version 2 (Schwanghart and Scherler 2014, 2017). The stream network was obtained from the DEM using the D8 flow direction algorithm. Watersheds with an area of ≤10 km^2 (e.g., streams created by spring meltwater) were disregarded in order to avoid artefacts at the low resolution of the DEM (30m). We calculated the reference concavity (θ) using a Bayesian optimization of θ with the *mnoptim* function described in TopoToolbox (Schwanghart and Scherler, 2017). A reference value of $\theta_{ref} = 0.423$ was used for the part of the Dinaric-Hellenic orogen in Figures 4.7, 4.9 and 4.10.

Knickpoints are defined as points or zones (knickzones) of abrupt change in the slope of rivers (e.g., Whipple and Tucker 1999; Kirby and Whipple 2012). Knickpoints can be identified either in plots of elevation vs horizontal distance constructed from DEMs (e.g., Fig. 4.8c) or in plots of elevation vs χ (e.g., Figs. 7b). Elevation-distance plots are easier to grasp at first glance, but the advantage of elevation vs χ plots is that knickzones appear as morphological deviations from a steady-state river profile (Perron and Royden 2013; Neely et al. 2017). We identified knickpoints with a preprocessing routine described in Schwanghart and Scherler (2017).

For the Drin River analysis in Figure 4.8, we used a tolerance value of 124 m calculated as the difference between filled and incised channels with a minimum uphill area of 15000 pixels (= 13.5 km2). This high tolerance value allowed us to identify knickzones in a large catchment area (e.g., Figs. 8c, 10). Knickpoints in the much smaller Tropoja Basin catchment were calculated with a lower tolerance value of 60 m. Anthropogenic knickpoints, for example, dams along the Drin, were not considered in any of the analyses.

Results

Terrace exposure ages from the ^{36}Cl depth profiles

The two sampled terrace profiles, TP1 and TP2, show an exponential decrease of ^{36}Cl concentration with depth (Figs. 6a, b) that allows us to estimate the erosion/incision rates (e.g., Gosse and Klein 2015). Probability Density Plots (PDPs) showing frequency vs age have right-skewed distribution curves (Fig. 4.6c). We chose the modal value instead of the mean as the best-fit exposure ages of ~8.2 ka and ~12.3 ka for terraces T1 and T2, respectively (dotted grey lines in Fig. 4.6c, Table 4.1). The ages overlap within error. The age errors are mainly due to uncertainties related to the neutron capture production rate.

Table. 4.1: Results of the ^{36}Cl Cosmogenic Nuclide Analysis

Profile	*Level*	*Lat.*	*Long.*	*Alt. m asl*	*EARL***	*Mean*	*Median*	*Mode*	*Lowest χ^2*	*Max*	*Min*
TP1*	T1	42.38 N	20.08 E	283	12	10.4 ka	9.7 ka	**8.2 ka**	17.3 ka	35.1 ka	3.7 ka
TP2*	T2	42.36 N	20.10 E	286	56	14.5 ka	13.9 ka	**12.3 ka**	15.5 ka	40.2 ka	5.8 ka
Incision rate (mm/yr)						10.7	10.4	**11.7**	24.4	8.6	20.9

*Labelled as TP1-N, TP2-S in the Appendix III/ Supplementary Informations

**EARL: Elevation above present-day river level (m)

The interested reader is referred to section 1.4 of the Appendix III/ Supplementary Information for a description of the method used to calculate river incision rates. We compared the minimum, maximum, and modal ages, which resulted in a best-fit incision rate of 11.7 mm/yr (Table 4.1). This value is assumed as the best approximation of the fluvial incision rate of the Valbona River into the Tropoja Basin sediments during the Late-Pleistocene to Holocene time.

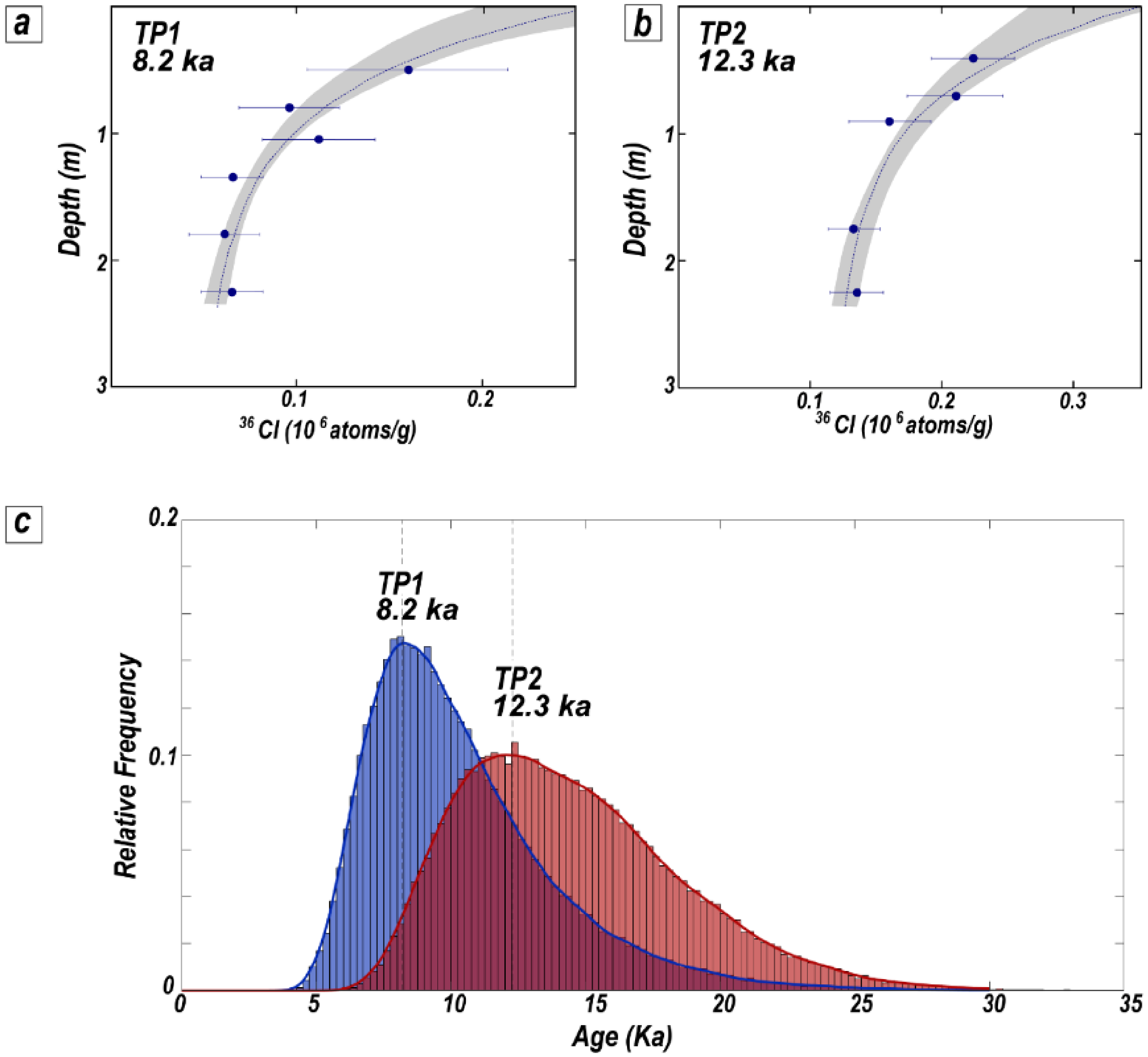

Fig. 4.6: ^{36}Cl nuclide concentration vs profile depth for the two sample profiles TP1 (a) and TP2 (b) Profile locations shown as yellow stars in Fig. 4.3a. - spaces. Symbols in (a) and (b): black lines - error bars, grey areas - solution space from Monte-Carlo simulations, dashed curved lines - best-fit age, (c) Probability Density Plots (PDPs) and histograms (n = 10^6) of the two depth profiles showing exposure ages for terraces T1 and T2. Symbols for (c): grey dotted line - mode of the asymmetric right-skewed (nonnon-Gaussian) distributions.

Results of the geomorphic analysis

Most of the 80 knickpoints in the Tropoja Basin (Fig. 4.7) do not coincide directly with significant lithological contacts along the SPNF, e.g., between the High Karst (HK) carbonates and the more erodible Cretaceous flysch and ophiolitic mélange (Fig. 4.7a; Appendix III/ Supplementary Fig. S3). They also do not cluster along the SPNF itself (Fig. 4.7a). This suggests either that they have migrated upstream since the most recent activity of the fault or that they reflect reconfiguration of rivers within the drainage system and the establishment of a new steady state. Yet another possibility is that they reflect a fall in the base-level of the entire system (e.g., lowering of the Adriatic Sea).

A striking feature of the knickpoints in the Tropoja Basin is that about half of them cluster at two distinct intervals in the elevation vs χ plot with respect to the basin outlet (Figs 7b, c). The outlet is taken to be the confluence of the river draining the basin with the main trunk of the Drin River (solid square in Fig. 4.7a). These clusters are colored pink (1st cluster) and yellow (2nd cluster) in the longitudinal profiles and kernel distribution in Figure 4.7b, c. Many of them coincide with changes in k_{sn} values, as shown by the colours along the streams in Figure 4.7a. The other knickpoints (white dots) are scattered across the drainage. We discuss scenarios for their origins in the Landscape morphology, terraces and climate.

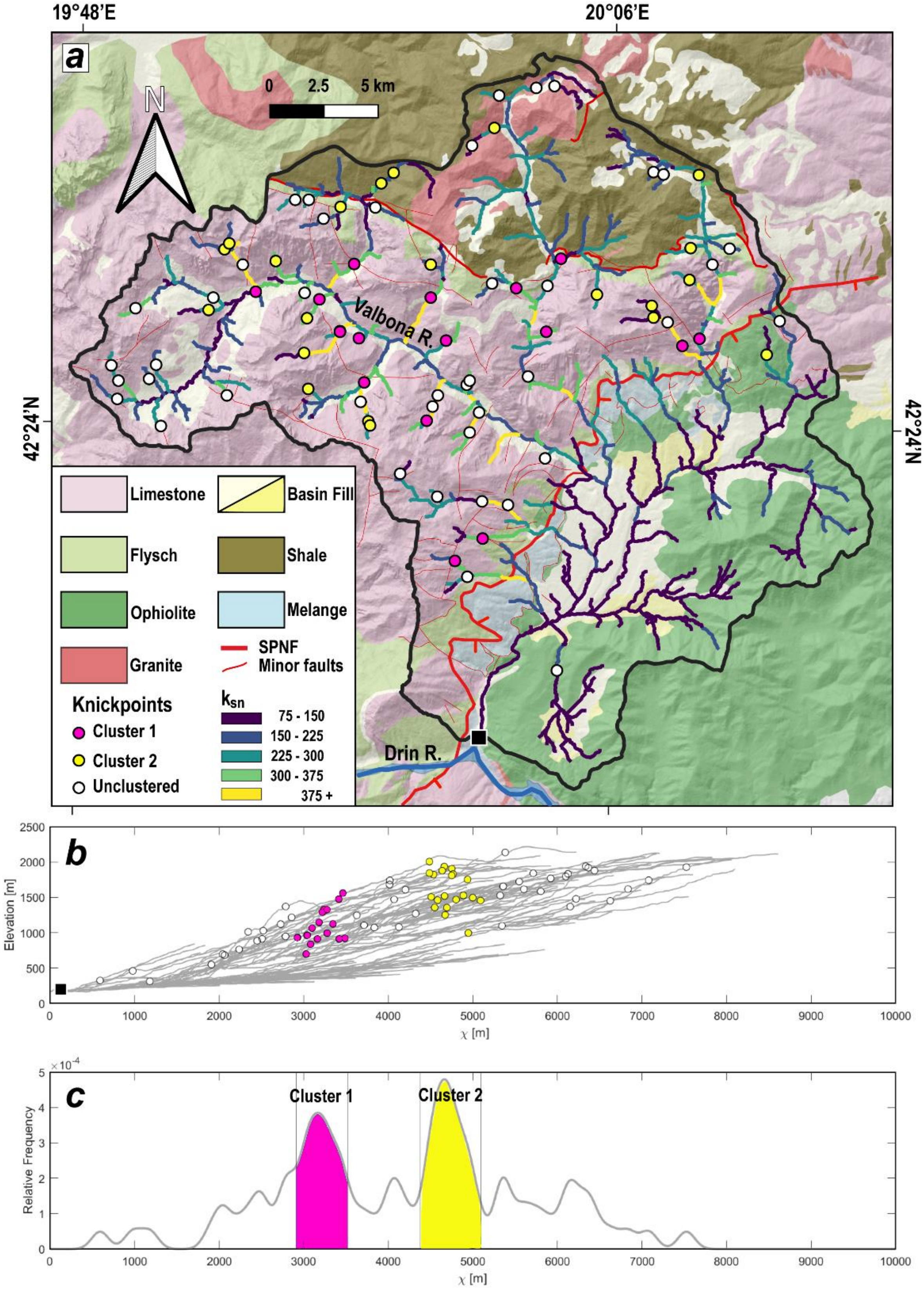

Fig. 4.7: Morphometric analysis of the rivers in the Tropoja Basin catchment: (a) Map of normalised channel steepness index (ksn) of the upstream-drainage area of the Tropoja Basin from the base level indicated as a square in (a); (b) χ -normalised longitudinal profiles of the stream network in the Tropoja Basin. The base level is for the plot is taken to be the confluence of Valbona and Drin Rivers (square in (a)). Circles indicate knickpoints colored according to the peaks in the Kernel density distribution (c); (c) Knickpoints are grouped in two clusters using the computed significant peaks in the Kernel density function (100 m width). Lithologies in (a) are from Xhomo et al. (2002). The base level for the analysis is the confluence of Valbona and Drin Rivers (square in (a)).

To compare the fluvial metrics of the Tropoja Basin catchment with the regional drainage network, we identified a total of 114 knickpoints in the entire Drin River drainage basin, starting from the Drin River outlet (taken here to be the base level, Fig. 4.8a) to elevations between ~ 190 and 1850 m asl (Fig. 4.8b). These are coloured red and blue depending on their location with respect to the line marked SET for the transition from orogen-normal shortening to extension. We note that the knickpoints in the Drin drainage system in Figure 4.8a include six points in the Tropoja Basin catchment (labelled TB in Figs. 4.8a and 4.8c).

Overall, channel slopes are much steeper along the Adriatic coastal mountain range where shortening is ongoing than in the high-relief Dinaric hinterland where the orogen is actively extending. There, the horizontal displacement rates range from 1.5-4 mm/yr normal to the strike of the orogen (Figs. 4.8b and c, D'Agostino et al. 2020). The knickpoints identified in the coastal range (red dots in Fig. 4.8c) are much more closely spaced than in the hinterland (blue dots in Fig. 4.8c). Most knickpoints occur where rivers flow from the high relief of the carbonate rocks forming the Dinaric nappes (Fig. 4.1) to alluvial plains underlain by Neogene sediments (Figs. 4.8a, b). These are located 80 to 200 km upstream of the Drin outlet and are interpreted as paleo-lakes, as labelled in Figure 4.8c and discussed in the next chapter.

Two features of the distribution of blue knickpoints stand out in the channel profiles in Figure 4.8c: (1) At distances of ≥ 90 km from the Drin outlet, a gap in slope between 1000 and 1300 m asl separates a group of points above 1300 m asl from the rest of the points below. This gap corresponds generally with a flat segment of the Drin River trunk at 300-400m asl that is labelled paleo-lake in Figure 4.8c; (2) At distances closer to the Drin outlet (< 90 km), the blue knickpoints occur at a broad range of elevations between 300 and 1400 m. The relationship of the knickpoints and their elevation to paleo-lakes is discussed below in section *Regional drainage pattern and its controls*.

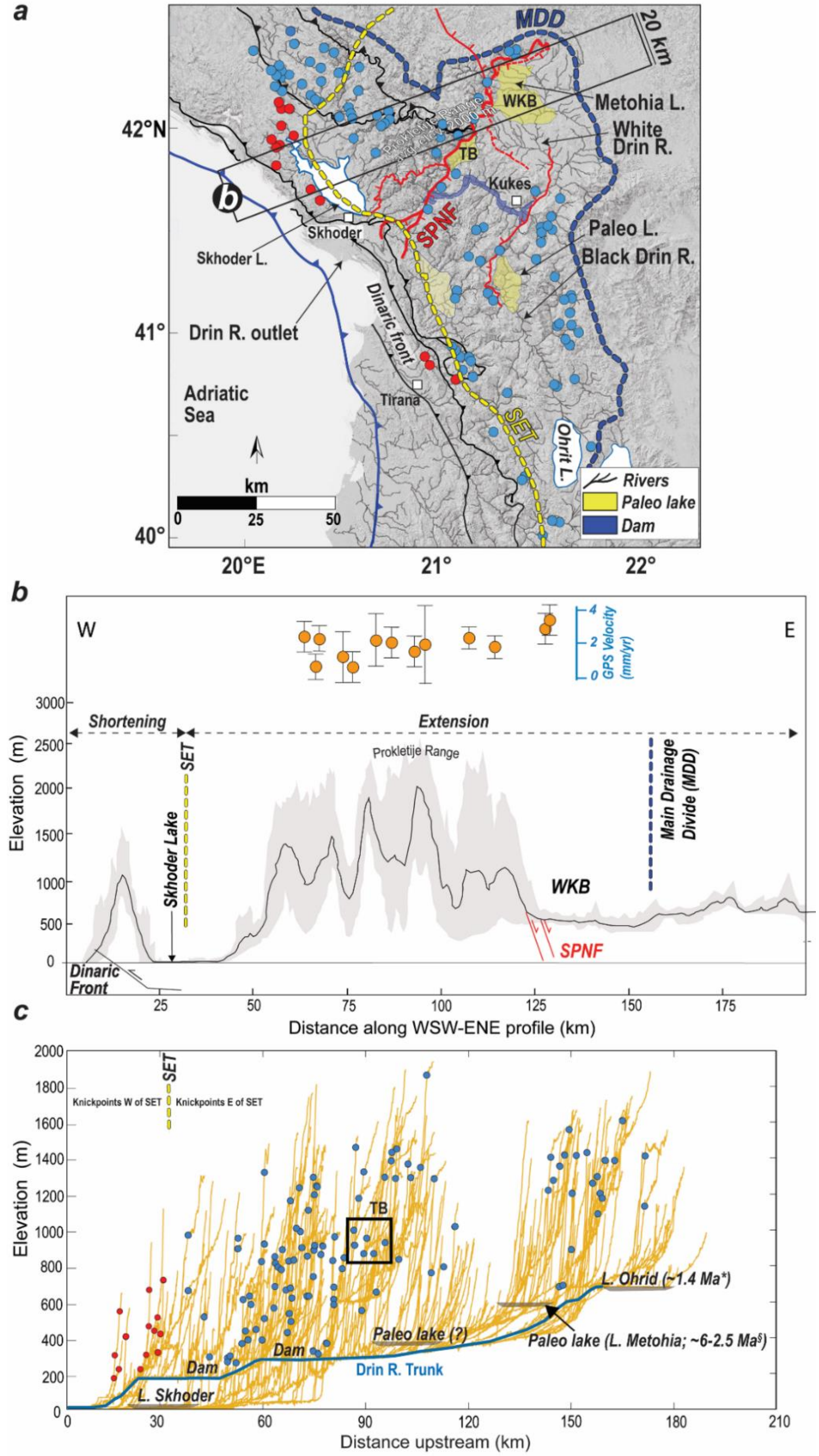

Fig. 4.8: Distribution of knickpoints and relief (defined as the difference between the min and max elevations) at the Dinarides-Hellenides junction: (a) Hillshade map based on SRTM-1 arc-second DEM (Farr et al. 2007; NASA JPL 2013); Additional elements are river streams (black lines), the trace of the shortening-extension transition (SET - yellow dashed line), main drainage divide (MDD - blue dashed line). Knickpoints to the west and east of the SET are colored, respectively, red and blue. The base-level is the outlet of the Drin River into the Adriatic Sea as labelled in (a); (b) 20-km wide swath profile with maximum and minimum elevations at upper and lower boundaries of the grey area, respectively. The mean elevation is represented as a solid black line. Faults - normal (red) and thrust (black). GPS velocities given in mm/yr (orange dots) with their relative errors as a vertical line. GPS data in (b) are from D'Agostino et al. (2020); (c) Longitudinal river profiles and locations of knickpoints identified in (a), 0 km on the x-axis is the Drin River outlet, the reference level used in the calculation of knickpoints. Paleo-lakes are indicated as grey polygons. Age estimates of Lake Orhid (~1.4 Ma–to-Present) taken from Wagner et al. (2019) and of the paleo-Metohia Lake in the Western Kosovo Basin (WKB) from Neubauer et al. (2015).

The k_{sn} and χ-maps in Figure 4.9 for the entire fluvial network of the Dinaric-Hellenic junction show that the footwall of the SPNF and its related faults coincide with of the highest values of both parameters. Here, it is important to note again that the SPNF juxtaposes contrasting lithologies, from limestone rocks of the Dinaric nappes in its footwall to ophiolite and sub-ophiolitic mélange of the West Vardar Ophiolites in its hanging wall (see Appendix III/ Supplementary Fig. S1). Lower k_{sn} values characterize the graben between the conjugate normal faults of the SPNF system, as well as the Adriatic coast, west of the SET (blue colors in Fig. 4.9a).

Bright colors in Figure 4.9b, c, and d indicate four areas parts of the river network that are not in steady-state and where drainage divide mobility is highest: (1) the northern and eastern borders of the Drin catchment along the SPNF system towards the hinterland; (2) along the White Drin in the north; and (3) along the Black Drin in the east, as well as (4) in the vicinity of the Ohrid Lake. The northwestern part of the Drin catchment seems also to be in a transient state as indicated by the stark contrast of χ-values on either side of the drainage divide (Fig. 4.9b, c).

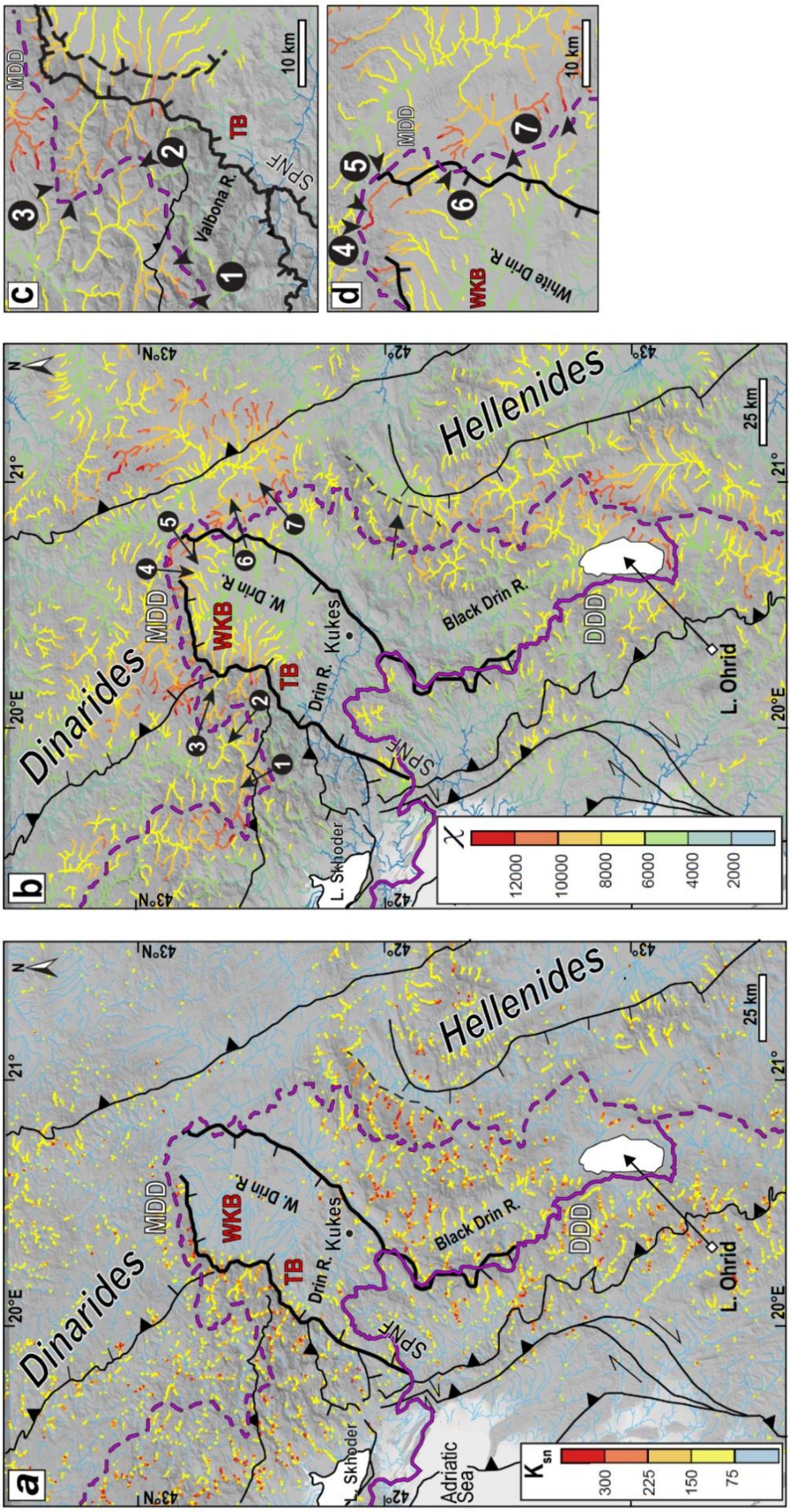

Fig. 4.9: Stream metrics for the Dinaric-Hellenic junction, including the MDD – main drainage divide (purple dashed line), the DDD – Drin drainage divide (thin purple line) and main faults (thin black lines), including the SPNF (thick black line): (a) Map of river steepness index, k_{sn}; (b) χ-map showing the degree of adjustment to current steady-state conditions using the Adriatic Sea as a base level. Note the contrast in k_{sn} and χ values across the MDD, which partly coincides with the DDD, and in the footwall of the main normal fault of the SPNF; (c-d) Close-ups of the drainage divide areas located in the footwall of the SPNF system showing the influence of the fault on patterns of χ values. Arrows indicate the interpreted direction of the drainage divide. TB = Tropoja Basin; WKB = Western Kosovo Basin. Shaded relief based on SRTM-1 arc-second DEM (Farr et al. 2007; NASA JPL 2013).

Discussion

The overarching question posed when interpreting our data is: How are patterns of deposition and erosion linked on different scales? To answer this, we begin with the regional scale of the Drin River catchment, then progress to the smaller scale of the Tropoja Basin, where the record of sedimentation and fluvial incision is best preserved and can be assessed in the context of faulting, climatic variation, stream-capture and autogenic factors, e.g., events that occurred within the basin.

Regional drainage pattern and its controls

Several important points emerge from the river stream metrics at the scales of the Tropoja Basin (Fig. 4.7) and the Dinaric-Hellenic junction (Figs. 8, 9, and 10). On the orogenic scale, we observe that both k_{sn} and χ-values are higher in the footwall of the main normal faults making up the SPNF system (thick black lines in Fig. 4.9). These high values indicate that the fluvial network is still adjusting to rock uplift and variable erosion along and across the SPNF system. This is particularly evident by the jump in k_{sn} values along an E-W trending segment of the SPNF forming the northern border of the Western Kosovo Basin (Fig. 4.9a). This may indicate ongoing activity of that part of the fault. Another potentially active fault scarp can be identified in the k_{sn} map in the hanging wall of the large low-angle normal fault located just east of the main drainage divide (dashed black line in Fig. 4.9a, from Dumurdjanov et al. (2020). Alternatively, the difference in k_{sn} values between the carbonate-rich bed channels (High Karst and Pre-Karst units) and the ophiolitic, silico-clastic and metamorphic bed channels (West Vardar Ophiolites and associated nappes; Figs. 4.1, 4.9a, and Appendix III) can be regulated by water runoff, infiltration, and chemical dissolution processes in the carbonate-rich bedrock (e.g., Central Apennines, Tucker et al. (2011). Chemical dissolution of carbonates and water infiltration can lower the bed of the channel, altering the channel's steepness that, in turn, increases the time response to external forcing, steepening the topography in the karst areas (e.g. Ott et al. 2019).

A further striking feature is that the χ values are generally highest in the narrow domain between the SPNF and the main drainage divide (MDD in Figs. 4.9b, and close-ups c, d). This suggests that this domain is not in equilibrium with the current steady-state conditions. We note that these locally high χ values occur against a background of heightened χ values across the entire Dinaric-Hellenic chain, indicating substantial migration of fluvial divides on the scale of the orogen. This is especially evident at the White Drin outlet into the Western Kosovo Basin (arrows in Fig. 4.9b). Interestingly, the Western Kosovo and Tropoja basins both show very low k_{sn} values and low-moderate χ values (Figs. 4.9a, b), in keeping with the observation that they are relatively flat, uplifted domains with little ongoing erosion (see white areas in the slope map, Fig. 4.2a).

Following Willett et al. (2014), we interpret the asymmetry of χ values on either side of the main drainage divide and the SPNF in Figure 4.9b to indicate that in most places, the divide is migrating away from the fault (black arrows in Fig. 4.9b). Only at the N and NE end of the SPNF do the χ values indicate that the divide is migrating to the SW, i.e., into the graben between the two normal faults (Figs. 4.9c, d).

The confluence of tributary channels delineates the trunk of the Drin River (Fig. 4.8b) and defines flat river segments on its way to the current outlet at the Adriatic Sea (Fig. 4.8c). These segments partly coincide with Plio-Pleistocene deposits like those found at Lake Ohrid (Fig. 4.8a). We therefore interpret these flat segments as paleo-lakes in the sense of Whittaker and Boulton (2012), (Figs. 4.8a, c). A good example of such a paleo-lake is Lake Metohia, which occupied part of the Western Kosovo Basin during Pliocene to Early Pleistocene time (Neubauer et al., 2015; location in Fig. 4.8a). These paleo-lakes probably formed prior to river-capture events, as proposed below in Regional drainage pattern and its controls.

There are no discontinuities in stream profiles and river metrics across the transition from active extension to shortening (SET in Figs. 4.8c and 4.9a), indicating either that this transition is not sharp or that the rate of river incision is high with respect to the current strain-rate of the crust. Along the Adriatic coast where thrusting and shortening are ongoing (Figs. 4.1, 4.8a), the streams have steep sides and clustered knickpoints (red dots in Fig. 4.8c). This is interpreted to reflect the ongoing adjustment of the streams to tectonically induced uplift.

Knickzones away from the Adriatic coast and situated east of the SET within 90 km of the Drin outlet at elevations from 300 to 1400 m asl (Fig. 4.8c and section *Topographic and fluvial analysis*) probably reflect various older events. It is tempting to attribute the lowest ones between ~ 200 and 400 m to base-level fall during the lowering of the Adriatic Sea by some 120 m during the LGM (Pirazzoli 1991; Lambeck and Purcell 2005). However, points above 400 m asl may well be older. Some of the knickpoints may be related to downcutting in the immediate aftermath of Messinian drainage of the Mediterranean Sea (Garcia-Castellanos and Villaseñor 2011). However, most of the rivers adjoining the N-S directed Black Drin River may have not drained in the Adriatic Sea at that time as they were part of an internally drained systems (see *Discussion*). Others may reflect one or more episodes of regional uplift associated with extension in the upper plate of the retreating and delaminating Adriatic slab (e.g., Matenco and Radivojević 2012; van Unen et al. 2019).

The gap in knickpoints identified in Figure 4.8b further away from the Drin outlet and within the Dinaric hinterland at elevations between 1200 and 1600 m asl is enigmatic insomuch as it coincides with the lateral extent of a flat segment of the Drin River trunk (Fig. 4.8c and section *Material and Methods*). One explanation is that this gap may be an artifact of projecting river channels in the high Albanian Alps far to the north (e.g., north of the Western Kosovo Basin) into the same section as the Drin River trunk. Rivers with these high-altitude knickpoints only join the Drin River after traversing the mountains from north to south, perpendicular to the plane of section in Figure 4.8c. Alternatively, these high slope knickpoints formed during normal faulting along segments of the SPNF along the northern limit of the Western Kosovo Basin (Figs. 2a, 9a and discussion above); these knickpoints have since migrated into the footwall of the SPNF.

Landscape morphology, terraces and climate

Today, we see that the Tropoja Basin is adjusted to the current steady-state conditions (Fig. 4.9 a and b), as indicated by low χ values from the outlet of the Adriatic Sea to the Tropoja Basin and within the Drin River up to the vicinity of the town of Kukes. Large parts of the Western Kosovo Basin and the Black Drin River are not adjusted to the current steady-state conditions (high χ-values in Fig. 4.9b) with respect to the current base-level represented by the Adriatic Sea.

We focus our analysis on the Tropoja Basin as is gives us the opportunity to relate incision events and knickpoint migration to dated terrace levels. This in turn provides a potential age for catchment-wide reorganization events. To do this, we first identify mobile knickpoints, defined as knickpoints that migrate upstream due to a downstream perturbation (e.g., base-level fall, Crosby and Whipple 2006). Assuming that the confluence of the tributary streams and the Drin River trunk (the base-level reference, $\chi = 0$ in the χ-plots of Figs. 4.7 and 4.10) were stationary while the knickpoints migrated upstream, we computed knickpoints scaled to an upstream drainage area (e.g., Crosby and Whipple 2006; Berlin and Anderson 2007; Marrucci et al. 2018; Schwanghart and Scherler 2020). In catchments with uniform erodibility and precipitation, the knickpoint migration celerity (V) scales with tributary drainage area (A):

$$V = C\,A^{p} \qquad \text{Eq. (3)}$$

where C and p are constants fitted to the data (Crosby and Whipple 2006). The drainage area (A) is integrated over the river distance to produce variable χ and points with the same contributing drainage area in the river network plot at the same value of χ. As the propagation velocity of the signal is proportional to the upstream drainage area, each knickpoint propagating upstream from the basin outlet (black square in Fig. 4.7a) has a similar value of χ. The 71 knickpoints in Figure 4.10 are interpreted to reflect pulses of change in steady-state conditions that are migrating upstream. Local base-level changes in the fluvial system due to regional uplift or sea-level change can trigger discrete waves of fluvial incision that cause knickpoints to propagate upstream (e.g. Wobus et al. 2006; Berlin and Anderson 2007; Kirby and Whipple 2012; Schwanghart and Scherler 2020). During this process, rivers can add new channels to their fluvial network (Stokes et al. 2002).

During the LGM the regional base level of the Drin was the Adriatic Sea at ~ 120 m below present-day sea level (Pirazzoli 1991). However, from ~21 ka, sea level began rising in the Mediterranean Sea to its present level (Lambeck and Bard 2000). This sea-level rise was not linear, but fluctuated, with two major changes in the rate of sea level rise at ~12 and ~8 ka. At these times, sea-level rise in the Mediterranean slowed significantly for several thousands of years before accelerating again. Interestingly, these periods coincide with the times of formation of T1 and T2 terraces in the Tropoja Basin (Fig. 4.6). Unfortunately, no age exists for the oldest terrace level T3, that however must be older than 12 ka and likely is related to the lowest sea level during the LGM.

We propose that a new steady-state condition was established each time the sea-level rose significantly, thus creating an incision event or knickpoint that migrated upstream to adjust the river network to the new base level. These knickpoints are seen throughout the catchment of the Drin River (Fig. 4.10, yellow and pink dots). The youngest incision event and related knickpoints (2nd generation, pink knickpoints) are related to the adjustment to the current steady-state condition and present base level of the Adriatic Sea. Based on the age of the terrace T1, we interpret this incision event to be younger than 8 ka. Today, we infer from the low χ values in the footwall of the SPNF in the Tropoja Basin (Fig. 4.9b, c) that the wave of incision passed through the basin and reached the hanging wall of the SPNF as indicated by the high χ values there (clusters of pink and yellow colored knickpoints in Figs. 4.7a and 4.7b, respectively). On their way upstream, the migration of the knickpoints was significantly slowed because faulting along the SPNF juxtaposed erosion-resistant limestones of the High Karst Nappe with more erodible marls and shales in the sub-ophiolitic mélange of the West Vardar Ophiolite. This is also reflected by the higher values of k_{sn} in the limestone units of the High Karst nappe (HK in Figs. 4.1 and 4.3c; Appendix III/ Supplementary S3) and other Dinaric nappes (Fig. 4.9a). We speculate that an older pulse of incision and corresponding knickpoints (yellow dots and cluster in Fig. 4.7) was related to an increase in the rate of sea-level rise between 8-12 ka, resulting in a renewed change in base level (Fig. 4.10, 1st generation knickpoints, yellow dots). This 1st generation of knickpoints is still visible in the upper reaches of the Valbona and Drin Rivers, indicating that these rivers have not yet adjusted to the current steady-state conditions (Fig. 4.10). The incision age is again bracketed by our terraces T1 and T2 to have occurred sometime between 8 and 12 ka.

The numerous knickpoints in the Tropoja Basin that did not form a χ cluster (white dots in Figure 4.7a, b) cannot be attributed to any major geological features (lithological boundaries, faults) or downstream changes in drainage. They may reflect minor local structures, for example, joints in the karstified limestones making up the High Karst nappe.

We tentatively correlate the age of terrace T3 with the lowest base-level during the LGM. However, we were unable to date this terrace and its age and origin remain speculative.

Climate is a factor that can control the river network as expressed by river metrics (e.g. Wobus et al. 2006; Kirby and Whipple 2012). At the Dinaric-Hellenic junction and surrounding area, paleo-environmental multi-proxy data show a climate characterized by seasonally variable precipitation since the Plio-Pleistocene (Lacey et al. 2016; Wagner et al. 2019) with a slight increase in summer precipitation during the Younger Dryas cold event (~ 12.3 ka) and the temperate periods (Bordon et al. 2009). Alternating glacial and interglacial periods have a clear impact at the local scale of individual drainage systems, with increasing or decreasing sedimentation rates that may have occurred independently of tectonic activity along the SPNF system (e.g., terrace aggradation vs terrace incision; (Pazzaglia 2013). This is evident in the stratigraphy of the Tropoja Basin, where lacustrine sediments were covered by coarse-grained fan-type clastics long after tectonic activity on the SPNF ceased (Fig. 4.4 and in Discussion).

Fluvial terraces contain information about climatic fluctuations (Tucker and Slingerland 1997; Macklin et al. 2002; Pazzaglia 2013). The onset of humid-air circulation during glacial-interglacial cycles in the Mediterranean region led to a transient climate after ~1.36 Ma (Lake Ohrid climatic proxies, Wagner et al. 2019) linked with increased sedimentation rates (i.e., Ohrid Lake Fig. 4.1; (Macklin et al. 2002; Carcaillet et al. 2009; Vogel et al. 2010b; Wagner et al. 2012). Despite the significant error of our ^{36}Cl ages (Fig. 4.5; e.g. Hidy et al. 2010), the modal ages of ~12 ka and ~8 ka, respectively, from the intermediate and lowest terraces in the Tropoja Basin (TP1 and TP2 in Fig. 4.3) both fall within post-LGM time (Hughes 2007). Late-Pleistocene glaciation (Würmian phase) in the highest elevation of the Prokletije mountains (Albanian Alps) is documented by moraines that occur down to ~1000 m asl (Milivojević et al. 2008; Hughes 2009 – see also in Appendix III/ Supplementary Information - Fig. S3). Melting of cirque-type glaciers leading to more intense precipitation at these latitudes began after the Younger Dryas at ~12 ka (Wagner et al. 2019), followed abruptly by a short (~10^2 yrs) regional cold phase at 8.2 ka (Alley and Ágústsdóttir 2005) when the climate was locally drier. These periods correspond with an overall increase in erosion during cooler phases in the northern hemisphere during the Cenozoic (Herman et al. 2013). We infer that these climatic events also affected the upper reaches of the rivers, increasing sediment supply to the Tropoja Basin through the fluvial river network. This increased sediment supply together with the decreasing rate of sea-level rise were conducive for the formation of terraces in the Tropoja Basin. The terrace morphologies (Fig. 4.3) indicate that T1 occurs within an entrenched channel, whereas T2, and possibly T3, marks the inset of a broad alluvial plain sediment formed by a braided river system (unit 2 and planar morphology in Figs. 4.3, 4.4 and Appendix III/ Fig. S5). The interpretation that T2 was incised after the inset of braided river system is consistent with the idea that the river had reached its transport capacity for sediments. Immediately after abandoning terrace level T2, the Valbona River started to cut down, forming an entrenched channel in T1. River entrenchment can reduce lateral river migration, leading to bank collapse (Malatesta et al. 2017). In turn, limited lateral mobility of the river increases vertical incision. Thus, the onset of river entrenchment can initiate a positive feedback that leads to yet more incision due to the concentration of stream power within a narrower bed (Malatesta et al. 2017). We propose that T1 may have resulted from bank erosion. Another factor to consider for the formation of the terraces in the Tropoja Basin is potential for landslides and damming of the Valbona River. Meltwater and increased runoff, possibly combined with earthquakes (e.g. Muço 1995; Muço et al. 2012), would be expected to trigger slope instability in the form of landslides and debris flows that suddenly entered the drainage system (Stock and Dietrich 2006; Marc et al. 2015). The 6.4 M_w 2019 Dursi event or 7 M_w 1905 Skhodra earthquake (Caporali et al. 2020; D'Agostino et al. 2020) are only two recent examples of active seismicity at the Dinaric-Hellenic junction. We speculate that at the outlet of the Tropoja Basin, the Valbona River may have been dammed landslides that fill a narrow gorge of ~ 40m depth (e.g. Jaupaj et al. 2017; speculative dashed white lines in Figure 4.10a). Episodic damming could have aided or led to the creation of the terraces visible in the Tropoja Basin.

In comparing our estimated incision rates for the Tropoja Basin (Table 4.1) with the ^{10}Be-based incision rates for central and southern Albanian river terraces during the LGM and post-LGM periods, we find that the latter (~1.4 mm/yr, e.g., for Osum River terraces T7 and T8; Carcaillet et al. 2009) are ten times lower than the ~12 mm/yr that obtained here for the ~12 - 8 ka interval between terraces T2 and T1 (Table 4.1). This difference can be explained either by greater precipitation in northern Albania or by the migration of the knickzone through the Tropoja Basin. We rule out the former explanation because there is no evidence for a significant difference in the amount of precipitation in northern and southern Albania since the LGM (Wagner et al., 2019). The more likely explanation is therefore that the high incision rate in the Tropoja Basin marks the passage of the incision wave related to the 1st generation of knickpoints (yellow dots in Figs. 4.7 and 4.10) still found in the upper reaches of the Valbona River.

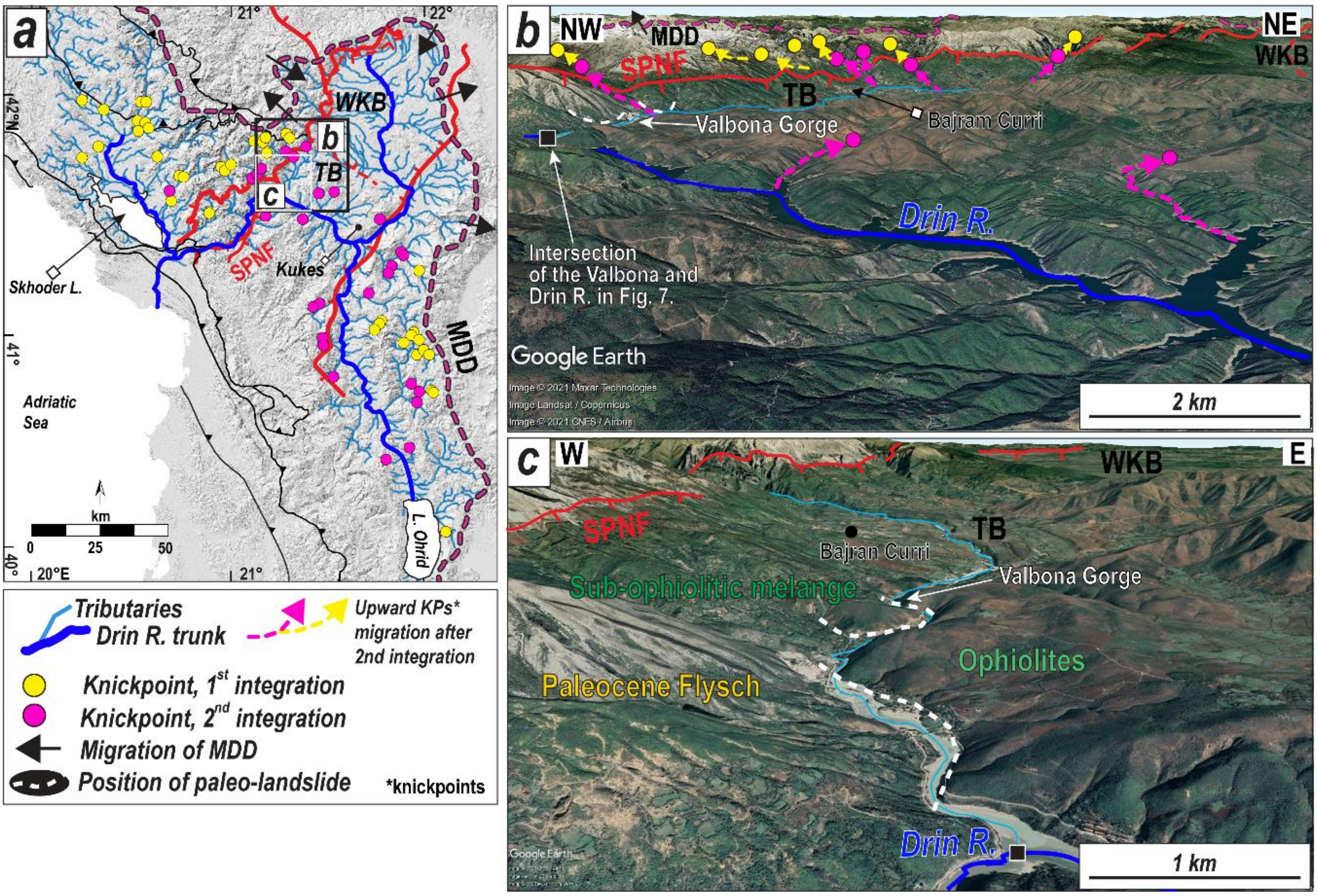

Fig. 4.10: Knickpoints along rivers in the Drin catchment: (a) Two knickpoint generations as a function of distance from the Drin River trunk (blue stream): 1st generation – yellow dots, 2nd generation - pink dots, as in Fig. 4.7. Youngest knickpoints coloured red in Fig. 4.8 are not shown here. Black arrows indicate the predicted migration direction of the main drainage divide (MDD) as shown in Fig. 4.9b; (b) Bird's-eye view of the two generations of knickpoints in the vicinity of the Tropoja Basin (TB). Pink arrows – migration direction of 2nd generation of knickpoints; Yellow arrows - upstream migration direction of 1st knickpoint generation followed by 2nd integration of the Drin River (see text for explanation); (c) Bird's-eye view of the Valbona gorge and intersection with the Drin River trunk. Dashed white lines indicate the traces of the potential position of paleo-landslide damming the Valbona River outlet. These are based on a qualitative analysis from Google earth and from the landslide inventory map of Albania (Jaupaj et al., 2017). Images from Google Earth™, 42°.13‘N, 20°11‘E, 7/22/2021.

To summarize this chapter, the combination of ^{36}Cl ages of the fluvial terraces and geomorphic metric analysis show that river incision and sedimentation after the LGM was episodic in the region. Prior to that, in the Early Pleistocene, a change from an internally to an externally drained system for the Drin River must have occurred as widespread lake sediments and relict topographic features mimicking former lake geometries are found. A tectonically controlled difference in base-level along the SPNF initially led to the formation of internally drained basins and lakes in the internal Dinarides which, like the Western Kosovo Basin and Tropoja Basin, lasted until Pliocene-to-Early Pleistocene time (Aliaj 2006; Neubauer et al. 2015; Pashko and Aliaj 2020). Most of these basins no longer exist and evidence of their former presence is preserved as the flattened parts of river profiles draining from the hinterland to the Adriatic Sea (Fig. 4.8c). Since Pliocene - Early Pleistocene time, drainage integration involving over-spilling of lakes and possibly also, in the case of the Topoja Basin, episodic breaching of dams would have resulted in regional drainage integration during the formation of the current Drin River. In the next section, we address the implications of potential drainage integration and shifts in drainage divides with respect to the Cenozoic faulting across Dinaric-Hellenic junction.

Model for post-Miocene evolution of landscape at the Dinaric-Hellenic Junction

In the preceding chapters, we have documented how Cenozoic normal faults acted as a template upon which the last ice age substantially modified the landscape in this domain of tectonic bending at the Dinaric-Hellenic junction. Here, we present a conceptual model of how the post-Miocene rivers and lakes evolved in this structurally complex area (Fig. 4.11). Three stages of landscape formation are discerned that account for the salient stratigraphic, palynological and fluvial features of the area (Fig. 4.11).

During stage 1 (Late Pliocene, Fig. 4.11a), two intramontane fresh-water lakes filled parts of the Western Kosovo Basin and Tropoja Basin (Meço and Aliaj 2000; Aliaj et al. 2001; Neubauer et al. 2015; Pashko and Aliaj 2020). By this stage, most if not all normal faulting along the SPNF had ceased, as indicated by basal Pliocene sediments that seal the subsurface branch of the SPNF beneath the Western Kosovo Basin (the Dukagjini Fault, Meço and Aliaj, 2000) and sub horizontal orientation of Plio-Pleistocene sediments in the Tropoja Basin (Fig. 4.4b). The basins were internally drained (endorheic) at this stage, as supported by the evidence for quiet lacustrine sedimentation (marls in unit 1 of the Tropoja Basin, Figs. 4.4, 4.5), the lack of any traces of fluvial down cutting and the absence of fluvial deposits downstream of the basins that, if present, would indicate basin drainage. The main drainage divide during stage 1 is therefore inferred to have been located to the WSW of the Western Kosovo Basin and Tropoja Basin, as drawn in Figure 4.11a. The base level for this paleo-drainage system is assumed to have been towards the SE, possibly into the Aegean Sea, but evidence is scarce.

We estimate an approximate accumulation rate of 0.1-0.2 mm/yr for stage 1 based on the 200-300 m thickness of Pliocene Late-Pleistocene lacustrine sediments in the southwestern part of the Western Kosovo Basin (Elezaj 2009). These sedimentation rates are comparable with mean sedimentation rates in Lake Ohrid (Fig. 4.1) of ~ 0.3-0.5 mm/yr since the Early-Pleistocene (Lindhorst et al. 2015). Based on this first-order estimate, the basin subsidence during stage 1 would have been higher than the sedimentation rate in the basin as evidenced by the deposition of lake sediments of the basal unit 1 and by the Lake Ohrid evidence for under filled conditions since the Pliocene (Vogel et al. 2010a; Lindhorst et al. 2015).

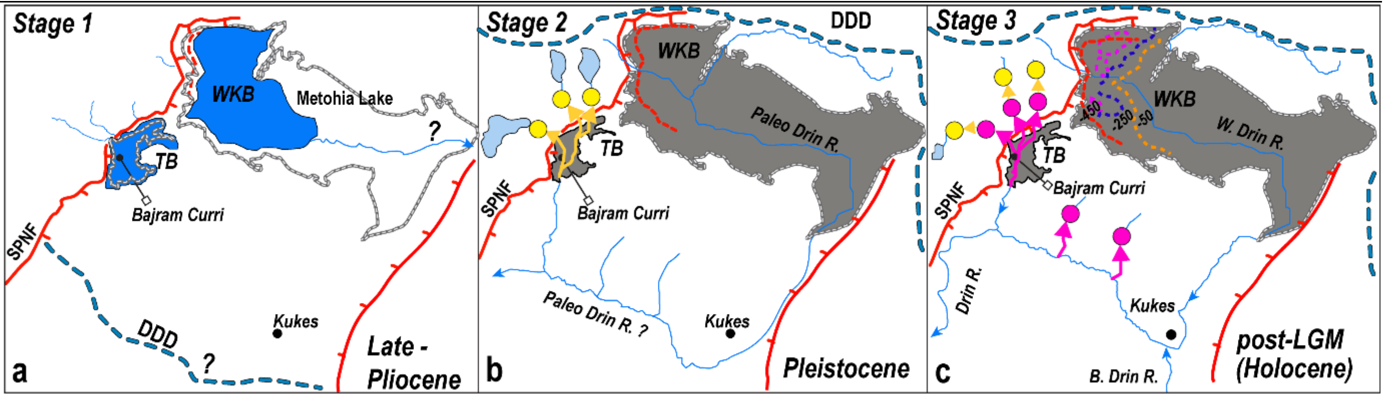

Fig. 4.11: Post-Miocene evolution of drainage in the vicinity of the Tropoja Basin (TB) and Western Kosovo Basin (WKB) at the Dinaric-Hellenic junction. Sketches are not to scale: (a) Stage 1 (Late Pliocene): the TB and WKB are two internally drained intramontane lakes; Stage 2 (Pleistocene): First river integration and transition from internally drained (endorheic) to externally drained (exorheic) basins. Upstream migration of 1st knickpoint generation at the outlet of the TB to the Paleo-Drin (yellow arrows); Stage 3 (Post-LGM, Holocene): Incision of the Drin River due to dramatically increased erosional capacity through downstream river capture (see text for details). Knickpoints propagate upstream from the trunk into the tributary basins in the footwall of the SPNF. 1st generation (yellow dots) migrates upstream from the trunk (Drin) after the second integration event. Symbols: Blue lines - river network, thick grey lines and grey polygons - present-day extent of the TB and WKB, thick red lines - normal faults of the SPNF system, light blue polygons - cirque glaciers in the Albanian Alps of northern Albania, pink arrows – migration of 2nd knickpoint generation. Dotted colored lines in stage 3 of the WKB represent present-day isopachs of the base of Miocene-Pliocene sediments (based on the Tectonic Map of Kosovo, 1:200000, Legler et al. 2006).

Stage 2 (Pleistocene) was presaged in the Tropoja Basin by the deposition of sandstone in Unit 1 and the unconformable deposition of grey conglomerates of unit 2 (Fig. 4.4b). This unconformity at the base of unit 2 documents erosion under fluvial conditions in the Tropoja Basin that ushered in stage 2 (Fig. 4.11b). We attribute this marked change from lacustrine to highly erosive fluvial conditions to basin drainage and river integration downstream of the basins. Similar transitions have been found to develop in fault-bounded extensional basins where fluvial sediments make up the highest part of the stratigraphy (e.g., Central Italian Apennines: Geurts et al. 2018, 2020 and references therein). River integration occur when basins and lakes overflow, spilling their water downstream and inducing top-down erosion in intramontane basins in the internal part of orogens (Geurts et al. 2018). In the Tropoja Basin, overspilling of the Late Pliocene lake towards the end of stage 1 (Fig. 4.11a) may have been augmented by melting of niche glaciers (Hughes 2009) in the upper Valbona Valley, producing an increase of sediment and water supply.

The main drainage divide is depicted in Figure 4.11 to have migrated upstream toward the internal part of the orogen between stages 1 and 2, thus reflecting the motion of headward erosion in response to river integration and capture of former lake areas. Stage 3 (Post LGM - Holocene) was characterized by at least three pulses of river incision with related knickpoint migration (Fig. 4.11c) and potential further drainage integration/capture within the regional river network. This stage corresponds to episodic fluvial downcutting and terracing in the Tropoja Basin. Overall, the changes in the rate of base-level rise from the LGM to the present controlled knickpoint formation and propagation upstream. This was modulated by late and/or post-LGM climatic fluctuations, as described in *Results*. The coincidence of the two fluvial terraces in the Tropoja Basin dated at ~ 12 and ~ 8 ka with the two-knickpoints in the tributary valleys of this basin (Fig. 4.9a) suggests that two knickpoint generations migrated upstream following significant base-level changes during stage 3 (Fig. 4.11). We infer that by stage 2, most of the basins were already externally drained (exorheic). This includes some, if not all, of the paleo-lakes whose former existence in the internal Dinarides is recorded in the flat parts of river profiles (Fig. 4.8c).

Conclusions

In this paper, we show that the landscape at the Dinaric-Hellenic junction has undergone dramatic changes long after the cessation of the main Neogene activity of the normal faults of the SPNF that transect the mountain range. In particular, the most recent ice age enhanced depositional and erosional events in its aftermath used the Cenozoic normal faults as a template for a strong morphological imprint. The first-order modification of the landscape during Pleistocene to Holocene time is perhaps best exemplified by the arcuate shape of the present drainage divide around the SPNF at the junction of Dinaric and Hellenic segments of the mountain belt. This fault and its related extensional structures exerted a strong control on the localization of Pleistocene to Holocene precipitation, erosion and deposition, including the reorganization of fluvial drainage patterns leading to the formation and partial demise of lakes and basins.

Regarded at the scale of individual basins, the landscape reflects a subtle feedback between tectonic and climate-induced processes. Differential erosion fostered by the fault-induced juxtaposition of lithologies with contrasting erodibilities and possibly triggered by seismicity set the stage. But it was climatic variation, especially glaciation and subsequent melting, that increased erosion rates and changed the erosional base-level, facilitating a switch from internal to external drainage of lakes and basins into the Drin River. Our data show that river integration increased after the Last Glacial Maximum (LGM) when the Drin River drainage expanded its upstream drainage area, leading to a top-down incision of the river system.

Overall, our data supports the idea that rollback subduction in the Hellenides and associated extension, both parallel- and normal to the orogen, affect landscape formation. This happened because crustal extension accommodating slab steepening and bending were sufficient to localize faulting and induce basin subsidence. Normal faults like the SPNF control erodibility and provide river paths that focus erosion and sediment transport (e.g., Copley et al. 2009). Pliocene E-W orogen-normal extension is reflected by the present-day trace of the Black Drin, which runs parallel to the strike of the Dinaric thrusts, before cutting down to the Adriatic Sea parallel to the SPNF. Thus, slab dynamics in conjunction with post-LGM erosion at the Dinaric-Hellenic junction have exerted a first-order control on the geometry of the drainage patterns.

Acknowledgements

We thank Naki Akçar (University Bern), Jan Pleuger (FU Berlin), Eline Le Breton (FU Berlin), Dirk Scherler (GFZ/FU Berlin) and Kujtim Onuzi (Univ. Tirana) for engaging discussions during the course of our work. Lab work was assisted by Philipp Hoelzmann and Frank Kutz (both FU Berlin, major element compositions), Jessica A. Stammeier (ICP-MS trace element composition analysis), C. Vockenhuber (^{36}Cl research, support of MSc students at the Ion Beam Physics (Physics-LIP), Zurich), Olivia Steinemann-Kronig (support with terrestrial cosmogenic nuclides lab work). The funding for our research came from German Science Foundation in the form of Grants Gi 825/4-1 and Ha 2403/21-1, respectively, to co-authors JG and MH. This grant also supported the work of the first author, as well as the MSc work of co-authors DS and BM, and the PhD of MG. The TCN ages were made possible by a grant from RADIATE (Grant Agreement No. 19001937) to the first author for analyses conducted by BM. Finally, we acknowledge the remarks of the associated editor Gang Rao and two anonymous reviewers.

Chapter V: Conclusions

Our thermochronologic ages and structural information date back to the early phase of the formation of the Dinaric and Hellenic nappes at the time of the obduction of the West Vardar ophiolite onto the passive Adriatic continental margin. This early phase was followed by nappe stacking and extension, which is still detectable today in the Internal Dinaric nappes, followed by nappe stacking that covered the entire Dinarides and extension along the Dinaric-Hellenic junction. The structural overprinting of this initial situation and the arcuation of the Dinaric-Hellenic orogen is due to the later Shkoder Peja Transfer Zone (SPTZ) and the multiphase activity of the Shkoder Peja Normal Fault system (SPNF), which are considered in chronological order in this conclusion. The most recent history of the geomorphological evolution of the Dinaric-Hellenic junction, which considers primarily the post-active phase of the SPNF, forms the final part of this conclusion.

Subsequent heating in the Internal Dinarides was followed by cooling and exhumation (<240°C in Late Cretaceous) and later in the External Dinarides (cooling to <180°C in Early Eocene and to <110°C in Oligo-Miocene). Obduction-related metamorphism of the West Vardar Ophiolite occurred in Latest Jurassic- Early Cretaceous (148 to 130 Ma) time (Most 2003; Tremblay et al. 2015), with temperatures reaching ~280°C. Obduction was followed by cooling of the ophiolite in Cretaceous time (~105-85 Ma) as indicated by ZHe ages. Nappe stacking and burial to 11-15 km depth and heating to peak temperatures of ~460°C in the Internal Dinarides happened after West Vardar obduction, whereas nappe stacking happened later (Eo-Oligocene) in the External Dinarides. ZFT cooling ages in the Decani Dome indicate cooling to below ~240°C during the period of 73 – 68 Ma. Arcuate peak-temperature contours around the perimeter of the Decani Dome indicate that the attainment of peak-temperatures pre-dates Decani doming of the East Bosnian-Durmitor nappe in the footwall of the Decani Shear Zone. Mylonitic shearing happened at temperatures of ~300-350°C, doming and faulting along the Decani Shear Zone were broadly coeval. At ~80 Ma the Decani doming and exhumational shearing occurred during earlier post-nappe exhumation, probably in a back-arc setting, to the east of the accretion-subduction front then active in the external parts of the Dinaric orogen. Peak temperatures of ~180-280°C in the external Dinaric Krasta-Cukali and High Karst nappes indicate ~6-10 km depth during burial which can be attributed to Dinaric thrusting and nappe stacking since Middle Eocene to Early Oligocene time. Peak-temperature contours cut across nappe contacts and are unaffected by the Cukali Dome, which itself syn- to post-dates Dinaric nappe stacking. Locally, cooling below ~180°C and ~110°C, respectively, occurred simultaneously in the respective temperature window at different locations in the Cukali Dome, as evidenced by uniformly distributed ZHe and AFT ages in and beyond the dome. This indicates either that peak temperatures were attained after doming, equilibrated peak temperatures before cooling below ~180°C-110°C, or that doming was too small to disturb the peak temperature pattern.

At the same time that nappe stacking, maximum temperatures and subsequent cooling occur in the External Dinarides, an orogen-parallel change in the nature of plate convergence occurs farther west at the active subduction zone, leading from oblique collision in the Dinarides to retreating subduction and plate retreat in the Hellenides. The ~75 km dextral offset of the front of the West Vardar Ophiolite along the SPTZ can be attributed to the reactivation of an inherited Early Mesozoic rift transfer fault in the Adriatic margin (sensu Aubouin & Dercourt 1975) during Eocene accretion and subduction of the Krasta-Cukali basin and Pindos ocean. This involved a clockwise rotation of ~15° about a vertical axis located at or near the junction of the Dinarides and Hellenides between 45 and 30 Ma, probably kinematically linked to the onset of back-arc extension and slab rollback in the southern Aegean Hellenides at 45 Ma (Brun et al. 2016). From 27 Ma onwards, the SPNF contributed ~10° of crustal rotation during orogen-parallel extension, whereas most of the Miocene and younger bending of the orogen was accommodated by ~20° clockwise rotation about a vertical axis in the vicinity of the Mid-Adriatic Ridge. The recognition of the SPTZ and SPNF as separate structures differs from previous notions of the bend in the Dinaric-Hellenic orogen as the site of a single tectonic lineament, our field-based work provides a more differentiated view of the timing and kinematics of this rotation.

Along with rotation, orogen-parallel extension began along the SPNF, which is a composite structure with five normal fault segments, four of these segments make up the main branch of the SPNF and transect the orogen. They juxtapose West Vardar Ophiolite in their hanging walls with domes in their footwalls. These domes comprise folded and metamorphosed Dinaric nappes that were partly exhumed under conditions ranging from lower greenschist-facies to anchizonal conditions, during top-down-SE ductile-to-brittle shearing on the normal fault surfaces. Although extension along the Decani Shear Zone, as stated above has the same orientation as the main part of the other segments of the SPNF, the early, mylonitic phase at 80 Ma is temporally distinct from the main active phase of the SPNF. Nevertheless, the Decani Shear Zone is part of the SPNF because it offsets the same units/nappes and the activity of the brittle, post-mylonitic component of the Decani Shear Zone coincides with that of the other main segments. The amount of top-SE throw on the SPNF is poorly constrained, with estimates ranging from 0 m near Shkoder to a minimum of ~2500 m to the NE. The general increase of downthrow from SW to NE is consistent with the idea of Handy et al. (2019) that the SPNF accommodated clockwise rotation about a crustal rotation pole situated at the SW end of the fault. The activity of the Cukali-Tropoja Fault, the western part of the SPNF, post-dates (<28 Ma) the Dinaric phase of nappe stacking as it cuts Dinaric folds and thrusts and it syn-to post-dates Cukali Doming. Although the offset of the Cukali-Tropoja Fault increases from 0 near Shkoder to >2500 m near Bajram Curri and Decan, uniform ZHe (T_c ~180°C; ~50 Ma) and AFT cooling ages (T_c ~110°C; ~30 Ma) along and across the SPNF (Cukali-Tropoja Fault and Decani Shear Zone segments) indicate no detectable fault offset and differential cooling in foot- and hanging walls. We thus suggest that some offset along the SPNF occurred prior or during Early Miocene time, after Dinaric nappe stacking but before cooling to ~110-60°C. Prolonged exposure of the AFT samples to temperatures in their partial annealing zone indicate slow cooling, so gradual that thermal equilibration presumably happened at the same rate as normal faulting. The throw on the SPNF was most likely too small and insufficient to disturb the temperature field enough to be detectable by the thermochronological systems within their uncertainties. The fifth segment of the SPNF, the Dukagjini Fault, lies buried beneath Plio-Pleistocene sediments of the Western Kosovo Basin. It offsets mid-late Miocene syn-rift clastics and lacustrine sediments by some 1000 m and is conjugate to the subsurface Prizren-Vranica Fault bordering the same Miocene syn-rift sedimentary package in the SE part of the Western Kosovo Basin. The activity of the Dukagjini Fault ended no later than the beginning of the Pliocene. At present, there are no criteria to determine whether the SPNF phases were continuous, discontinuous or overlapped in time. However, Miocene extension appears to have migrated into the hanging wall of the four initial fault segments and ended along the Dukagjini Fault segment.

In summary, we distinguish early Dinaric extension along the Decani Shear Zone with post-nappe stacking activity of the Cukali-Tropoja and Dukagjini Faults and probably reactivated brittle parts of the Decani Shear Zone. Thus, the first (1) activity of the Decan part of the SPNF relates to late Cretaceous and possibly early Paleogene extension, whereas a second phase of activity in Late Oligocene-early Miocene time, occurred along the Cukali-Tropoja segment of the SPNF. The third phase (3) relates to the Dukagjini Fault in the hanging wall of the other segments and was related to the formation of the Mid-Miocene to Pliocene Western Kosovo Basin.

Based on our newly acquired thermochronologic data and on the fact that there is no differential offset in cooling across the SPNF, we were able to calculate cooling rates for the southernmost Dinarides. The thermochronologic ages of each system provide cooling ages through which the rock sample cooled through a known temperature field, from which we calculate cooling rates. From these cooling rates, we infer the geologic process most likely associated with these rates. Long-term cooling rates, of 3.0-3.2°C/Ma since the Late Cretaceous times for the East- Bosnian-Durmitor nappe and since the Early Eocene for the Krasta-Cukali and High Karst nappe in the footwall of the SPNF indicate slow cooling and exhumation that mostly relates to erosion and denudation with rates of 0.1-0.2 mm/yr. However, we are looking at relatively long timescales geologically, and shorter, e.g. tectonically driven events (SPNF activity) accelerating cooling, are possible within the time frames considered. Taking the erosion and denudation rates at face value, we estimate that ~1.6 – 3.2 km of overburden in the SPNF footwall has been eroded since the Middle Miocene (16 Ma). The Western Kosovo Basin which began to subside at ~16 Ma (Elezaj 2009) would seem a likely sink for this eroded material.

The causes of the Neogene orogenic bending are provided by previously published teleseismic P-wave tomographies (Fig. 2.1b, Hall & Spakman, 2015), which show that the Dinarides-Hellenides junction is a short (150 km) relict of the previously rifted Adriatic plate beneath the southern Dinarides and a much longer (>400 km), apparently untorn part of this plate beneath the NW Hellenides (e.g., Piromallo & Morelli, 2003; Wortel & Spakman, 2000). The torque resulting from the downward pull of the longer, retreating part of the plate beneath the Hellenides is a required mechanism to explain the clockwise orogenic bending and orogen-parallel extension localized during the Neogene subduction rollback at the SPNF (previously explained by Handy et al. 2019, among others). We suggest that Pliocene orogen-parallel extension, plate rollback, and rapid upper crustal exhumation were concentrated south of the SPNF, in the area of the Peshkopia Window, rather than along the Dinarian-Hellenic junction. The rapid Oligo-Miocene uplift and exhumation associated with the detachment of the Dinaric plate reported from other parts of the Internal Dinarides is not recorded in our data from the Dinaric-Hellenic junction. This suggests that there is a transition zone along the Dinaric-Hellenic junction where the opposing forces of the Dinaric and Hellenic slabs balance each other, and therefore produce a more moderate exhumation and cooling pattern. However, the extension since the middle Miocene is related to the activity of the Dukagjini fault and the formation of the Western Kosovo Basin.

Although the aforementioned processes of extension along the SPNF and orogenic bending occurred mainly in the Paleogene and Neogene and are due to profound structural changes in lithospheric dynamics, preserved evidence of the earlier tectonic history is found in the present-day geomorphology along the Dinaric-Hellenic junction. In particular, the recent glacial period with its increased depositional and erosional events used the Cenozoic faults as a template for strong morphological imprinting. Landscape change during the Pleistocene to Holocene is evidenced by the arcuate shape of the present-day watershed around the SPNF at the Dinaric-Hellenic junction. Stretching along the SPNF exerted a strong influence on the localization of Pleistocene to Holocene erosion and deposition, which also led to the reorganization of fluvial drainage patterns, the formation of lakes and sedimentary basins. Looking at individual basins, the landscape reflects a subtle feedback between tectonic and climatic processes. This is based on differential erosion, which was favored by the encounter of lithologies with different erodibility and possibly triggered by seismic activity. However, it was primarily climatic changes (glaciation and melt) that increased erosion rates and altered erosion levels, enabling a shift from internal to external drainage of lakes and basins in the Drin. Our data show that river integration increased after the LGM as the Drin increased its upstream drainage basin, resulting in a top-down incision of the river system. Normal faults such as the SPNF control erodibility and form flow paths that focus erosion and sediment transport. Pliocene orogenic normal extension in an east-west direction is reflected in the present-day trace of the Black Drin, which parallels the strike of the Dinaric thrusts before draining into the Adriatic Sea parallel to the SPNF. Thus, plate dynamics and the resulting upper-crustal extensional structures such as the SPNF, in conjunction with post-LGM erosion at the Dinaric-Hellenic junction, primarily influenced the geometry of drainage patterns and the present-day geomorphology of the Dinaric-Hellenic junction.

Chapter VI: Outlook

The data and interpretation of this dissertation have raised new scientific issues and ideas that may be worth considering as a focus for future research projects. Below we address some of them ideas of interest for research in the Balkans, particularly with respect to the feedback of the upper lithosphere to deeper changes in subduction zones and mantle processes, as well as the response of the expression of geomorphology to these processes. Proposals for new research projects can contribute to further understanding of regional geology, as well as be applied to other settings with laterally changing conditions along colliding and subducting continental lithosphere, and thus be applied transregionally.

- The Prizren-Vranica Fault (*PF* in Fig. 2.3) is a conjugate fault to the Dukagjini Fault, delimiting the Western Kosovo Basin to the SE. This fault is shown on the Tectonic Map of Kosovo (e.g. Legler et al. 2006), and the sediment thickness is also increasing towards the fault, similar to the Dukagjini Fault in the northwestern part of the Western Kosovo Basin. Therefore, a similar temporal activity of the two faults can be assumed. It could be possible that due to different morphological conditions (e.g., outcrops along riverbeds), the Prizren-Vranica Fault is outcropped at the surface, and thus a direct observation of this fault and inferences about deformation conditions are possible. An analysis of the exposed fault and its relation to the Dukagjini Fault would also contribute to the understanding of the tectonic formation conditions of the Western Kosovo Basin.
- The relationship of the Oligo-Miocene SPNF to the Dukagjini Fault is so far only supported by the projection of surface measurements to depth, and derived constructed geological profiles. Geophysical surveys (reflection seismology, geoelectric measurements) from the sedimentary basins (Tropoja and Western Kosovo Basin) into the footwall (Albanian Alps) could help to map the subsurface structural setting and thus allow direct conclusions on the relationship of the different fault branches. The strongly varying geophysical properties of the basin sediments, as well as the lithologies from the footwall and hanging wall, should make it possible to represent them with the help of geophysical methods.
- The poor accessibility and remoteness in the *Albanian Alps* has made further investigation and sampling in Cukali Dome and beyond in the High Karst nappe impossible in the context of this thesis. However, the fault that borders Cukali Dome to the NW (Fig. 3.3), and strikes SW-NE, is the counterpart of the Cukali-Tropoja Fault to the north of Cukali Dome. The orientation of this fault, as well as the units it offsets, are similar to that of the Cukali-Tropoja Fault. Direct mapping of this fault, as well as small-scale thermochronologic profiling across this fault in lithologies that may contain more heavy minerals (Permian conglomerates in the High Karst nappe), could contribute to the understanding and relationship of this fault to the Cukali-Tropoja Fault and the formation of the Cukali Dome. However, this would require a field campaign lasting several weeks with appropriate self-sufficient supplies and equipment, and vehicles with appropriate off-road capabilities.
- Pliocene orogen-parallel extension does not occur along the SPNF, as interpreted by us, but in the area of the Peshkopia Window, as suggested by other authors. The Prizren-Vranica Fault (PVF in Fig. 3.9) represents the conjugate fault system for large parts of the Oligo-Miocene Cukali-Tropoja Fault, which forms a large-scale horst and graben structure with the West Vardar Ophiolite in the graben (Fig. 3.9). The relationship of the two apparently different ages but kinematically related structures could help in understanding the formation of this horst and graben structure. Were the faults created contemporaneously? Was there a concurrent active phase of these faults? Why is younger cooling and exhumation pronounced just across the Prizren-Vranica Fault, and not along the SPNF?

- The Okshtunit Dome (location approximately at the sampling points of Al-MG_58 and Al-MG_59 in Figure 3.3.) northeast of the Mesohellenic Librazhd Basin forms a similarly oriented but much smaller dome structure as the Cukali Dome and is composed of similar Mesozoic deep-sea sediments. In addition, RSCM peak temperatures are similar to those in the Cukali Dome and therefore indicate that nappes in the Dinarides and Hellenides, which are separated by approximately 80 km, reached similar burial depths. Our thermochronological results show that the cooling and exhumation of this structure is slightly older than in the Peshkopia Window, and partially overlaps with the ages from the Cukali Dome. However, the normal faults bounding the dome truncates the Prizren-Vranica Fault, and therefore must be younger than this structure. The following questions therefore arise: Did nappe stacking in the Dinarides and Hellenides occur, at least in parts, simultaneously and with similar burial depths? How does the dextral offset along the SPTZ fit into this concept, and shouldn't the Hellenides have been much further east with respect to the External Dinarides before this offset? Is there a previously unknown orogenic normal extensional component that enabled the exhumation of the Okshtunit and the Cukali Dome? What is the relationship to the two domes of the kinematically related SPNF and PVF?

References

Abrams M, Crippen R, Fujisada H (2020) ASTER Global Digital Elevation Model (GDEM) and ASTER Global Water Body Dataset (ASTWBD). Remote Sens 12:1–12. https://doi.org/10.3390/rs12071156

Alfimov V, Ivy-Ochs S (2009) How well do we understand production of 36Cl in limestone and dolomite? Quat Geochronol 4:462–474. https://doi.org/10.1016/j.quageo.2009.08.005

Aliaj S (2006) The Albanian Orogen: Convergence Zone Between Eurasia and the Adria Microplate. Adria Microplate GPS Geod Tectonics Hazards 133–149. https://doi.org/10.1007/1-4020-4235-3_09

Aliaj S, Baldassarre G, Shkupi D (2001) Quaternary subsidence zones in Albania: Some case studies. Bull Eng Geol Environ 59:313–318. https://doi.org/10.1007/s100640000063

Alley RB, Ágústsdóttir AM (2005) The 8k event: Cause and consequences of a major Holocene abrupt climate change. Quat Sci Rev 24:1123–1149. https://doi.org/10.1016/j.quascirev.2004.12.004

Andrić N, Sant K, Matenco L, et al (2017) The link between tectonics and sedimentation in asymmetric extensional basins: Inferences from the study of the Sarajevo-Zenica Basin. Mar Pet Geol 83:305–332. https://doi.org/10.1016/j.marpetgeo.2017.02.024

Andrić N, Vogt K, Matenco L, et al (2018) Variability of orogenic magmatism during Mediterranean-style continental collisions: A numerical modelling approach. Gondwana Res 56:119–134. https://doi.org/10.1016/j.gr.2017.12.007

Aoya M, Kouketsu Y, Endo S, et al (2010) Extending the applicability of the Raman carbonaceous-material geothermometer using data from contact metamorphic rocks. J Metamorph Geol 28:895–914. https://doi.org/10.1111/j.1525-1314.2010.00896.x

Attal M, Tucker GE, Whittaker AC, et al (2008) Modelling fluvial incision and transient landscape evolution: Influence of dynamic Channel adjustment. J Geophys Res Earth Surf 113:1–16. https://doi.org/10.1029/2007JF000893

Aubouin J, Dercourt J (1975) Les transversales dinariques derivent-elles de paleofailles transformantes ? CR Acad Sc Paris 281:347–350

Babić L;, Hochuli PA;, Zupanic J (2002) The Jurassic ophiolitic mélange in the NE Dinarides : dating, internal structure and geotectonic implications. Eclogae geol Helv 95:263–275. https://doi.org/10.5169/seals-168959

Bajraktar F, Pruthi V, Hajdari R, et al (2010) History of Geoheritage Conservation in Kosovo. Schriftenr der Dtsch Gesellschaft für Geowissenschaften 66:107–107. https://doi.org/10.1127/sdgg/66/2010/107

Balling P, Grützner C, Tomljenović B, et al (2021) Post-collisional mantle delamination in the Dinarides implied from staircases of Oligo-Miocene uplifted marine terraces. Sci Rep 11:1–11. https://doi.org/10.1038/s41598-021-81561-5

Behrmann JH (1988) Crustal-scale extension in a convergent orogen : the Sterzing-Steinach mylomte zone in the Eastern Alps. Geodin Acta 2:63–73. https://doi.org/10.1080/09853111.1988.11105157

Bennett RA, Hreinsdóttir S, Buble G, et al (2008) Eocene to present subduction of southern Adria mantle lithosphere beneath the Dinarides. Geology 36:3–6. https://doi.org/10.1130/G24136A.1

Berlin MM, Anderson RS (2007) Modeling of knickpoint retreat on the Roan Plateau, western Colorado. J Geophys Res Earth Surf 112:1–16. https://doi.org/10.1029/2006JF000553

Bestmann M, Kunze K, Matthews A (2000) Evolution of a calcite marble shear zone complex on Thassos Island, Greece: Microstructural and textural fabrics and their kinematic significance. J Struct Geol 22:1789–1807. https://doi.org/10.1016/S0191-8141(00)00112-7

Beyssac O, Goffé B, Chopin C, Rouzaud JN (2002) Raman spectra of carbonaceous material in metasediments: A new geothermometer. J Metamorph Geol 20:859–871. https://doi.org/10.1046/j.1525-1314.2002.00408.x

Beyssac O, Simoes M, Avouac JP, et al (2007) Late Cenozoic metamorphic evolution and exhumation of Taiwan. Tectonics 26:. https://doi.org/10.1029/2006TC002064

Bijwaard H, Spakman W (2000) Non-linear global P-wave tomography by iterated linearized inversion. Geophys J Int 141:71–82

Bordon A, Peyron O, Lézine AM, et al (2009) Pollen-inferred Late-Glacial and Holocene climate in southern Balkans (Lake Maliq). Quat Int 200:19–30. https://doi.org/10.1016/j.quaint.2008.05.014

Borojević Šoštarić S, Palinkaš AL, Neubauer F, et al (2014) The origin and age of the metamorphic sole from the Rogozna Mts., Western Vardar Belt: New evidence for the one-ocean model for the Balkan ophiolites. Lithos 192–195:39–55. https://doi.org/10.1016/j.lithos.2014.01.011

Bortolotti V, Chiari M, Kodra A, et al (2004) New evidences for Triassic morb magmatism in the Northern Mirdita Zone ophiolites (Albania). Ofioliti 29:247–250. https://doi.org/10.4454/ofioliti.v29i2.217

Bortolotti V, Chiari M, Marroni M, et al (2013) Geodynamic evolution of ophiolites from Albania and Greece (Dinaric-Hellenic belt): One, two, or more oceanic basins? Int J Earth Sci 102:783–811. https://doi.org/10.1007/s00531-012-0835-7

Bortolotti V, Marroni M, Pandolfi L, Principi G (2005) Mesozoic to tertiary tectonic history of the Mirdita ophiolites, northern Albania. In: Island Arc. pp 471–493

Boutoux A, Bellahsen N, Nanni U, et al (2016) Thermal and structural evolution of the external Western Alps: Insights from (U–Th–Sm)/He thermochronology and RSCM thermometry in the Aiguilles Rouges/Mont Blanc massifs. Tectonophysics 683:109–123. https://doi.org/10.1016/j.tecto.2016.06.010

Braun J (2016) Strong imprint of past orogenic events on the thermochronological record. Tectonophysics 683:325–332. https://doi.org/10.1016/j.tecto.2016.05.046

Braun J, Gemignani L, Van Der Beek P (2018) Extracting information on the spatial variability in erosion rate stored in detrital cooling age distributions in river sands. Earth Surf Dyn 6:257–270. https://doi.org/10.5194/esurf-6-257-2018

Brun JP, Faccenna C, Gueydan F, et al (2016) The two-stage Aegean extension, from localized to distributed, a result of slab rollback acceleration. Can J Earth Sci 53:1142–1157. https://doi.org/10.1139/cjes-2015-0203

Brun JP, Sokoutis D (2010) 45 m.y. of Aegean crust and mantle flow driven by trench retreat. Geology 38:815–818. https://doi.org/10.1130/G30950.1

Burchfiel BC, Nakov R, Dumurdzanov N, et al (2008) Evolution and dynamics of the Cenozoic tectonics of the South Balkan extensional system. Geosphere 4:919–938. https://doi.org/10.1130/GES00169.1

Caporali A, Floris M, Chen X, et al (2020) The november 2019 seismic sequence in albania: Geodetic constraints and fault interaction. Remote Sens 12:1–10. https://doi.org/10.3390/rs12050846

Carcaillet J, Mugnier JL, Koçi R, Jouanne F (2009) Uplift and active tectonics of southern Albania inferred from incision of alluvial terraces. Quat Res 71:465–476. https://doi.org/10.1016/j.yqres.2009.01.002

Carlson WD, Donelick RA, Ketcham RA (1999) Variability of apatite fission-track annealing kinetics: I. Experimental results. Am Mineral 84:1213–1223. https://doi.org/10.2138/am-1999-0901

Carosi R, Cortesogno L, Gaggero L, Marroni M (1996) Geological and petrological features of the metamorphic sole from the Mirdita nappe, northern Albania. Ofioliti 21:21–40

Cavazza W, Roure F, Spakman W, et al (2004) The Mediterranean Region from Crust to Mantle. Springer Berlin Heidelberg

Cermak V, Kresl M, Kucerova L, et al (1996) Heat Flow in Albania. Geothermics 25:91–102. https://doi.org/0375--6505(95)00036--4

Channel JET, Horvath F (1976) The African-Adriatic promotory as a palaeogeographical premise for Alpine orogeny and plate movements in the Carpatho-Balkan region. Tectonophysics 35:71–101. https://doi.org/doi:10.1016/0040-1951(76)90030-5

Chiarabba C, De Gori P, Speranza F (2009) Deep geometry and rheology of an orogenic wedge developing above a continental subduction zone: Seismological evidence from the northern-central Apennines (Italy). Lithosphere 1:95–104. https://doi.org/10.1130/L34.1

Christl M, Vockenhuber C, Kubik PW, et al (2013) The ETH Zurich AMS facilities: Performance parameters and reference materials. Nucl Instruments Methods Phys Res Sect B Beam Interact with Mater Atoms 294:29–38. https://doi.org/10.1016/j.nimb.2012.03.004

Çiner A, Stepišnik U, Sarıkaya MA, et al (2019) Last Glacial Maximum and Younger Dryas piedmont glaciations in Blidinje, the Dinaric Mountains (Bosnia and Herzegovina): insights from 36Cl cosmogenic dating. Mediterr Geosci Rev 1:25–43. https://doi.org/10.1007/s42990-019-0003-4

Claude A, Akçar N, Ivy-Ochs S, et al (2019) Changes in landscape evolution patterns in the northern Swiss Alpine Foreland during the mid-Pleistocene revolution. Bull Geol Soc Am 131:2056–2078. https://doi.org/10.1130/B31880.1

Cohen KM, Finney SC, Gibbard PL, Fan JX (2021) International Chronostratigraphic Chart. ICS Int Chronostratigr Chart 199–204

Copley A, Boait F, Hollingsworth J, et al (2009) Subparallel thrust and normal faulting in Albania and the roles of gravitational potential energy and rheology contrasts in mountain belts. J Geophys Res Solid Earth 114:1–12. https://doi.org/10.1029/2008JB005931

Crosby BT, Whipple KX (2006) Knickpoint initiation and distribution within fluvial networks: 236 waterfalls in the Waipaoa River, North Island, New Zealand. Geomorphology 82:16–38. https://doi.org/10.1016/j.geomorph.2005.08.023

Cvijić J (1901) Die dinarisch-albanesische Scharung. Sitzungsberichte der Kais Akad der Wissenschaften, Wien

D’Agostino N, Avallone A, Cheloni D, et al (2008) Active tectonics of the Adriatic region from GPS and earthquake slip vectors. J Geophys Res Solid Earth 113:1–19. https://doi.org/10.1029/2008JB005860

D’Agostino N, Jackson JA, Dramis F, Funiciello R (2001) Interactions between mantle upwelling, drainage evolution and active normal faulting: An example from the Central Appennines (Italy). Geophys J Int 147:475–497. https://doi.org/10.1046/j.1365-246X.2001.00539.x

D’Agostino N, Métois M, Koci R, et al (2020) Active crustal deformation and rotations in the southwestern Balkans from continuous GPS measurements. Earth Planet Sci Lett 539:. https://doi.org/10.1016/j.epsl.2020.116246

Davis D, Suppe J, Dahlen FA (1984) Mechanics of Fold-and-Thrust Belts and Accretionary Wedges. J Geophys Res 88:10087–10101. https://doi.org/10.1029/JB089iB12p10087

de Leeuw A, Mandic O, Krijgsman W, et al (2012) Paleomagnetic and geochronologic constraints on the geodynamic evolution of the Central Dinarides. Tectonophysics 530–531:286–298. https://doi.org/10.1016/j.tecto.2012.01.004

Dewey JF (1988) Extensional collapse of orogens. Tectonics 7:1123–1139. https://doi.org/10.1029/TC007i006p01123

Dewey JF, Bird JM (1970) Mountain Belts and the New Global Tectonics. J Geophys Res 75:2625–2647

Dimitrijević MD (1997) Geology of Yugoslavia, Geological. Geological Institute GEMINI Special Publication

Dimo-Lahitte A, Monie P, Vergely P (2001) Metamorphic soles from the Albanian ophiolites: Petrology, 40Ar/39Ar geochronlogogy, and geodynamic evolution. Tectonics 20:78–96

Dumitru TA (1993) A new computer-automated microscope stage system for fission-track analysis. Int J Radiat Appl Instrumentation Part 21:575–580. https://doi.org/10.1016/1359-0189(93)90198-I

Dumurdjanov N, Milutinovic Z, Salic R (2020) Seismotectonic model backing the PSHA and seismic zoning of Republic of Macedonia for National Annex to MKS EN 1998-1:2012 Eurocode 8. J Seismol 24:319–341. https://doi.org/10.1007/s10950-020-09912-9

Dumurdzanov N, Serafimovski T, Clark Burchfiel B (2005) Cenozoic tectonics of Macedonia and its relation to the South Balkan extensional regime. Geosphere 1:1–22. https://doi.org/10.1130/GES00006.1

Dunkl I (2002) Trackkey: A windows program for calculation and graphical presentation of fission track data. Comput Geosci 28:3–12. https://doi.org/10.1016/S0098-3004(01)00024-3

Dunne J, Elmore D, Muzikar P (1999) Scaling factors for the rates of production of cosmogenic nuclides for geometric shielding and attenuation at depth on sloped surfaces. Geomorphology 27:3–11

Ehlers TA (2005) Crustal Thermal Processes and the Interpretation of Thermochronometer Data. Rev Mineral Geochemistry 58:315–350. https://doi.org/10.2138/rmg.2005.58.12

Elezaj Z (2009) Cenozoic molasse basins in Kosovo and their geodynamic evolution. Muzeul Olteniei Craiova Oltenia Stud şi Comunicări Ştiinţele Naturii 25:343–350

Elezaj Z, Kodra A (2012) Geology of Kosova, 1. Tekst Universitar, Pristina

Erak D, Matenco L, Toljić M, et al (2016) From nappe stacking to extensional detachments at the contact between the Carpathians and Dinarides – The Jastrebac Mountains of Central Serbia. Tectonophysics 710–711:162–183. https://doi.org/10.1016/j.tecto.2016.12.022

Faccenna C, Becker TW, Lucente FP, et al (2001) History of subduction and back-arc extension in the central Mediterranean. Geophys J Int 145:809–820. https://doi.org/10.1046/j.0956-540X.2001.01435.x

Faccenna C, Mattei M, Funiciello R, Jolivet L (1997) Styles of back-arc extension in the Central Mediterranean. Terra Nov 9:126–130. https://doi.org/10.1046/j.1365-3121.1997.d01-12.x

Farley KA (2002) (U-Th)/He dating: Techniques, calibrations, and applications. Rev Mineral Geochemistry 47:. https://doi.org/10.2138/rmg.2002.47.18

Farr TG, Rosen PA, Caro E, et al (2007) The shuttle radar topography mission. Rev Geophys 45:65–77. https://doi.org/10.1029/2005RG000183

Ferriere J, Baumgartner PO, Chanier F (2016) The Maliac Ocean: the origin of the Tethyan Hellenic ophiolites. Int J Earth Sci 105:1941–1963. https://doi.org/10.1007/s00531-016-1303-6

Ferrière J, Reynaud J-Y, Pavlopoulos A, et al (2004) Geologic evolution and geodynamic controls of the Tertiary intramontane piggyback Meso-Hellenic basin, Greece. Bull la Soc Geol Fr 175:361–381. https://doi.org/10.2113/175.4.361

Flint JJ (1974) Stream gradient as a function of order, magnitude, and discharge. Water Resour Res 10:. https://doi.org/https://doi.org/10.1029/WR010i005p00969

Fügenschuh B, Mancktelow NS, Schmid SS (2012) Comment on Rosenberg and Garcia: Estimating displacement along the Brenner Fault and orogen-parallel extension in the Eastern Alps, Int J Earth Sci

(Geol Rundsch) (2011) 100:1129-1145. Int J Earth Sci 101:1451–1455. https://doi.org/10.1007/s00531-011-0725-4

Fügenschuh B, Seward D, Mancktelow N (1997) Exhumation in a convergent orogen: the western Tauern window. Terra Nov 9:213–217. https://doi.org/10.1046/j.1365-3121.1997.d01-33.x

Galbraith R (2008) Statistical models for mixed ages. Nucl Tracks Radiat Meas 21:600. https://doi.org/10.1016/1359-0189(93)90234-z

Galbraith R (2010) Statistics for LA-ICP-MS based fission track dating. 12th Int Conf Thermochronology, Glas UK, 16–20 August 2010 175

Galbraith RF, Laslett GM (1993) Statistical models for mixed fission track ages. Int J Radiat Appl Instrumentation Part 21:459–470. https://doi.org/10.1016/1359-0189(93)90185-C

Galetto A, Georgieva V, García VH, et al (2021) Cretaceous and Eocene Rapid Cooling Phases in the Southern Andes (36°–37°S): Insights From Low-Temperature Thermochronology, U-Pb Geochronology, and Inverse Thermal Modeling From Domuyo Area, Argentina. Tectonics 40:1–30. https://doi.org/10.1029/2020TC006415

Gallagher K, Brown R, Johnson C (1998) Fission track analysis and its applications to geological problems. Annu Rev Earth Planet Sci 26:519–572. https://doi.org/10.1146/annurev.earth.26.1.519

Garcia-Castellanos D (2006) Long-term evolution of tectonic lakes: Climatic controls on the development of internally drained basins. Spec Pap Geol Soc Am 398:283–294. https://doi.org/10.1130/2006.2398(17)

Garcia-Castellanos D, Villaseñor A (2011) Messinian salinity crisis regulated by competing tectonics and erosion at the Gibraltar arc. Nature 480:359–363. https://doi.org/10.1038/nature10651

Gawlick HJ, Frisch W, Hoxha L, et al (2008) Mirdita Zone ophiolites and associated sediments in Albania reveal Neotethys Ocean origin. Int J Earth Sci 97:865–881. https://doi.org/10.1007/s00531-007-0193-z

Gemignani L, Mittelbach B V., Simon D, et al (2022) Response of Drainage Pattern and Basin Evolution to Tectonic and Climatic Changes Along the Dinarides-Hellenides Orogen. Front Earth Sci 10:1–21. https://doi.org/10.3389/feart.2022.821707

Gemignani L, van der Beek PA, Braun J, et al (2018) Downstream evolution of the thermochronologic age signal in the Brahmaputra catchment (eastern Himalaya): Implications for the detrital record of erosion. Earth Planet Sci Lett 499:48–61. https://doi.org/10.1016/j.epsl.2018.07.019

“Geozavod”- OOUR Geoloski Institut Beograd 1966-1977- Socijalisticka Federativna Republika Jugoslavija Osnovna Geološka Karta SFRJ, 1:100.000

Geurts AH, Cowie PA, Duclaux G, et al (2018) Drainage integration and sediment dispersal in active continental rifts: A numerical modelling study of the central Italian Apennines. Basin Res 30:965–989. https://doi.org/10.1111/bre.12289

Geurts AH, Whittaker AC, Gawthorpe RL, Cowie PA (2020) Transient landscape and stratigraphic responses to drainage integration in the actively extending central Italian Apennines. Geomorphology 353:107013. https://doi.org/10.1016/j.geomorph.2019.107013

Gjani E, Dilek Y (2010) Palynostratigraphy, paleoecology and paleoclimatology of tertiary molasse basins and the peri-adriatic depression in albania and paleogeographic implications. Tecton Crossroads Evol Orogens Eurasia-Africa-Arabia, Ankara, Turkey 90

Gleadow AJW (1981) Fission-track dating methods: What are the real alternatives? Nucl Tracks 5:3–14. https://doi.org/10.1016/0191-278X(81)90021-4

Gosse J, Klein J (2015) Terrestrial cosmogenic nuclide dating. Encycl Earth Sci Ser 799–812. https://doi.org/10.1007/978-94-007-6326-5_148-1

Gosse JC, Philips FM (2001) Terrestrial in situ cosmogenic nuclides: theory and application. Quat Sci Rev 20:1475–1560

Grasemann B, Mancktelow NS (1993) Two-dimensional thermal modelling of normal faulting: the Simplon Fault Zone, Central Alps, Switzerland. Tectonophysics 225:155–165. https://doi.org/10.1016/0040-1951(93)90277-Q

Grenerczy G, Sella G, Stein S, Kenyeres A (2005) Tectonic implications of the GPS velocity field in the northern Adriatic region. Geophys Res Lett 32:1–4. https://doi.org/10.1029/2005GL022947

Groß P, Pleuger J, Handy MR, et al (2020) Evolving temperature field in a fossil subduction channel during the transition from subduction to collision (Tauern Window, Eastern Alps). J Metamorph Geol 39:247–269. https://doi.org/10.1111/jmg.12572

Groß P, Zertani S, Cionoiu S, et al (2014) A new 1 : 10,000 geological map of the Skutari-Pec Fault and surroundings , northern Albania – evidence of orogen-parallel extension. CBGA Tirana 2014

Grund MU, Giese J, Gemignani L, et al (*in review*) Faulting, basin formation and orogenic arcuation at the Dinaric - Hellenic junction (northern Albania and Kosovo). Int J Earth Sci - Rev XXX:XXX

Grund MU, Giese J, Gemignani L, et al (*in prep.*) Thermal record of obduction, nappe stacking and orogen-parallel extension at the Dinaric - Hellenic junction. Int J Earth Sci - prep XXX:XXX

Grund MU, Giese J, Handy MR, Onuzi K (2018) Geological map (1 :10 000) of the Shkoder-Peja Normal Fault in its central segment near Bajram Curri (northern Albania) – evidence for distributed normal faulting and extension. TSK 2018 Conf Abstr. https://doi.org/10.1016/j.tecto.2012.06.008

Guedes S, Moreira PAFP, Devanathan R, et al (2013) Improved zircon fission-track annealing model based on reevaluation of annealing data. Phys Chem Miner 40:93–106. https://doi.org/10.1007/s00269-012-0550-8

Gurnis M, Turner M, Zahirovic S, et al (2012) Plate tectonic reconstructions with continuously closing plates. Comput Geosci 38:35–42. https://doi.org/10.1016/j.cageo.2011.04.014

Haas J, Jovanović D, Görög Á, et al (2019) Upper Triassic–Middle Jurassic resedimented toe-of-slope and hemipelagic basin deposits in the Dinaridic Ophiolite Belt, Zlatar Mountain, SW Serbia. Facies 65:1–29. https://doi.org/10.1007/s10347-019-0566-3

Halamić J, Gorican S, Slovenec D, Kolar-Jurkovsek T (1999) A middle jurassic radiolarite-clastic succession from the medvednica Mt. (NW Croatia). Geol Croat 52:29–57. https://doi.org/10.4154/GC.1999.03

Hall R, Spakman W (2015) Mantle structure and tectonic history of SE Asia. Tectonophysics 658:14–45. https://doi.org/10.1016/j.tecto.2015.07.003

Handy MR, Giese J, Schmid SM, et al (2019) Coupled crust-mantle response to slab tearing, bending and rollback along the Dinaride-Hellenide orogen. Tectonics 2803–2828. https://doi.org/10.1029/2019TC005524

Handy MR, Ustaszewski K, Kissling E (2015) Reconstructing the Alps–Carpathians–Dinarides as a key to understanding switches in subduction polarity, slab gaps and surface motion. Int J Earth Sci 104:1–26. https://doi.org/10.1007/s00531-014-1060-3

Harkins N, Kirby E, Heimsath A, et al (2007) Transient fluvial incision in the headwaters of the Yellow River, northeastern Tibet, China. J Geophys Res Earth Surf 112:1–21. https://doi.org/10.1029/2006JF000570

Harrison RL (2009) Introduction to Monte Carlo simulation. AIP Conf Proc 1204:17–21. https://doi.org/10.1063/1.3295638

Herman F, Seward D, Valla PG, et al (2013) Worldwide acceleration of mountain erosion under a cooling climate. Nature 504:423–426. https://doi.org/10.1038/nature12877

Hidy AJ, Gosse JC, Pederson JL, et al (2010) A geologically constrained Monte Carlo approach to modeling exposure ages from profiles of cosmogenic nuclides: An example from Lees Ferry, Arizona. Geochemistry, Geophys Geosystems 11:. https://doi.org/10.1029/2010GC003084

Hollenstein C, Müller MD, Geiger A, Kahle HG (2008) Crustal motion and deformation in Greece from a decade of GPS measurements, 1993-2003. Tectonophysics 449:17–40. https://doi.org/10.1016/j.tecto.2007.12.006

Hrvatović H, Pamić J (2005) Principal thrust-nappe structures of the Dinarides. Acta Geol Hungarica 48:133–151. https://doi.org/10.1556/ageol.48.2005.2.4

Hughes PD (2007) Recent behaviour of the Debeli Namet glacier, Durmitor, Montenegro. Earth Surf Process Landforms 32:613–628. https://doi.org/10.1002/esp.1537

Hughes PD (2009) Twenty-first Century Glaciers and Climate in the Prokletije Mountains, Albania. Arctic, Antarct Alp Res 41:455–459. https://doi.org/10.1657/1938-4246-41.4.455

Hülscher J, Sobel ER, Verwater V, et al (2021) Detrital apatite geochemistry and thermochronology from the Oligocene/Miocene Alpine foreland record the early exhumation of the Tauern Window. Basin Res 33:3021–3044. https://doi.org/10.1111/bre.12593

Hurford AJ, Green PF (1983) The zeta age calibration of fission-track dating. Isot Geosci 1:285–317. https://doi.org/10.1016/S0009-2541(83)80026-6

Hurford AJ, Hammerschmidt K (1985) 40Ar39Ar and K/Ar dating of the bishop and fish canyon tuffs: Calibration ages for fission-track dating standards. Chem Geol Isot Geosci Sect 58:23–32. https://doi.org/10.1016/0168-9622(85)90024-7

Ivy-Ochs S, Poschinger A v., Synal HA, Maisch M (2009) Surface exposure dating of the Flims landslide, Graubünden, Switzerland. Geomorphology 103:104–112. https://doi.org/10.1016/j.geomorph.2007.10.024

Ivy-Ochs S, Synal HA, Roth C, Schaller M (2004) Initial results from isotope dilution for Cl and 36Cl measurements at the PSI/ETH Zurich AMS facility. Nucl Instruments Methods Phys Res Sect B Beam Interact with Mater Atoms 223–224:623–627. https://doi.org/https://doi.org/10.1016/j.nimb.2004.04.115

Jaupaj O, Lamaj M, Kulici H, et al (2017) Landslide Inventory Map of Albania. In: Advancing Culture of Living with Landslides. Springer International Publishing, pp 39–44

Jolivet L, Brun JP (2010) Cenozoic geodynamic evolution of the Aegean. Int J Earth Sci 99:109–138. https://doi.org/10.1007/s00531-008-0366-4

Jouanne F, Mugnier JL, Koci R, et al (2012) GPS constraints on current tectonics of Albania. Tectonophysics 554–557:50–62. https://doi.org/10.1016/j.tecto.2012.06.008

Kahle HG, Cocard M, Peter Y, et al (2000) GPS-derived strain rate field within the boundary zones of the Eurasian, African, and Arabian Plates. J Geophys Res Solid Earth 105:23353–23370. https://doi.org/10.1029/2000jb900238

Kallanxhi M-E, Ćorić S (2017) Calcareous nannofossils from Oligocene-middle Miocene sediments from Albanian-Thessalian Basin (Albania): biostratigraphy and paleoecological implications. Ina 16 Athens, Greece, Conf Pap 91

Karamata S (2006) The geological development of the Balkan Peninsula related to the approach, collision and compression of Gondwanan and Eurasian units. Geol Soc Spec Publ 260:155–178. https://doi.org/10.1144/GSL.SP.2006.260.01.07

Ketcham RA, Carter A, Donelick RA, et al (2007) Improved modeling of fission-track annealing in apatite. Am Mineral 92:799–810. https://doi.org/10.2138/am.2007.2281

Kirby E, Whipple K (2001) Quantifying differential rock-uplift rates via stream profile analysis. Geology 29:415–418. https://doi.org/https://doi.org/10.1130/0091-7613(2001)029<0415:QDRURV>2.0.CO;2

Kirby E, Whipple KX (2012) Expression of active tectonics in erosional landscapes. J Struct Geol 44:54–75. https://doi.org/10.1016/j.jsg.2012.07.009

Kissel C, Speranza F, Milicevic V (1995) Paleomagnetism of external southern and central Dinarides and northern Albanides: Implications for the Cenozoic activity of the Scutari-Pec Transverse Zone. J Geophys Res Solid Earth 100:14999–15007. https://doi.org/10.1029/95jb01243

Knobloch A, Legler C, Stanek KP, Dickmayer E (2006) Geological Map of Kosovo, 1:200,000. ICMM Kosova, Prishtina

Kohn B, Chung L, Gleadow A (2019) Fission-Track Analysis: Field Collection, Sample Preparation and Data Acquisition. Springer International Publishing

Kopp OC (2016) Lignite. Encycl. Br. Access Date August 24, 2021

Kovaçi S, Prenga D, Ifti M (2015) Analysis of distributions and dynamics for water side inflows in the Drin River basin , Albania. Int J Eng Tech Res ISSN 2321-0869 03:156–161

Krige DG (1951) A STATISTICAL APPROACH TO SOME, BASIC MINE VALUATION PROBLEMS ON THE WITWATERSRAND. J Chem Metall Min Soc South Africa 52:119–139

Kuhlemann J, Milivojevic M, Krumrei I, Kubik PW (2009) Last glaciation of the Šara Range (Balkan peninsula): Increasing dryness from the LGM to the Holocene. Austrian J Earth Sci 102:146–158

Lacey JH, Leng MJ, Francke A, et al (2016) Northern Mediterranean climate since the Middle Pleistocene: A 637 ka stable isotope record from Lake Ohrid (Albania/Macedonia). Biogeosciences 13:1801–1820. https://doi.org/10.5194/bg-13-1801-2016

Lacombe O, Mouthereau F (2002) Basement-involved shortening and deep detachment tectonics in forelands of orogens: Insights from recent collision belts (Taiwan, Western Alps, Pyrenees). Tectonics 21:12-1-12–22. https://doi.org/10.1029/2001TC901018

Lal D (1991) Cosmic ray labeling of erosion surfaces: in situ nuclide production rates and erosion models: Earth and Planetary Science Letters. Earth Planet Sci Lett 104:424–439

Lambeck K, Bard E (2000) Sea-level change along the French Mediterranean coast for the past 30000 years. Earth Planet Sci Lett 175:203–222. https://doi.org/10.1016/s0012-821x(99)00289-7

Lambeck K, Purcell A (2005) Sea-level change in the Mediterranean Sea since the LGM: Model predictions for tectonically stable areas. Quat Sci Rev 24:1969–1988. https://doi.org/10.1016/j.quascirev.2004.06.025

Laslett GM, Green PF, Duddy IR, Gleadow AJW (1987) Thermal annealing of fission tracks in apatite 2. A quantitative analysis. Chem Geol Isot Geosci Sect 65:1–13. https://doi.org/10.1016/0168-9622(87)90057-1

Lavé J, Avouac JP (2001) Fluvial incision and tectonic uplift across the Himalayas of central Nepal. J Geophys Res 106:26561–26591. https://doi.org/10.1029/2001jb000359

Legler C, Stanek KP, Dickmayer E, Knobloch A (2006) Tectonic Map of Kosovo, 1:200,000. ICMM Kosova, Prishtina

Li J, Mitra S (2017) Geometry and evolution of fold-thrust structures at the boundaries between frictional and ductile detachments. Mar Pet Geol 85:16–34. https://doi.org/10.1016/j.marpetgeo.2017.04.011

Liati A, Gebauer D, Fanning CM (2004) The age of ophiolitic rocks of the Hellenides (Vourinos, Pindos, Crete): First U-Pb ion microprobe (SHRIMP) zircon ages. Chem Geol 207:171–188. https://doi.org/10.1016/j.chemgeo.2004.02.010

Linder N, Perkuhn R (2013) Carbon Capture and Storage (CCS) in Kosovo. Fichtner Min Environ World Bank Rep

Lindhorst K, Krastel S, Reicherter K, et al (2015) Sedimentary and tectonic evolution of Lake Ohrid (Macedonia/Albania). Basin Res 27:84–101. https://doi.org/10.1111/bre.12063

Louis H (1927) Albanien: Eine Landeskunde, vornehmlich auf Grund eigener Reisen. Geographische Abhandlungen- Verlag von J. Engelhorns Nachfolgern in Stuttgart, Berlin/Stuttgart

Lugović B, Slovenec D, Schuster R, et al (2015) Petrology, geochemistry and tectono-magmatic affinity of gabbroic olistoliths from the ophiolite mélange in the NW Dinaric-Vardar ophiolite zone (Mts. Kalnik and Ivanščica, North Croatia). Geol Croat 68:25–49. https://doi.org/10.4154/gc.2015.03

Lünsdorf NK, Dunkl I, Schmidt BC, et al (2014) Towards a Higher Comparability of Geothermometric Data obtained by Raman Spectroscopy of Carbonaceous Material. Part I: Evaluation of Biasing Factors. Geostand Geoanalytical Res 38:73–94. https://doi.org/10.1111/j.1751-908X.2013.12011.x

Lünsdorf NK, Dunkl I, Schmidt BC, et al (2017) Towards a Higher Comparability of Geothermometric Data Obtained by Raman Spectroscopy of Carbonaceous Material. Part 2: A Revised Geothermometer. Geostand Geoanalytical Res 41:593–612. https://doi.org/10.1111/ggr.12178

Lünsdorf NK, Lünsdorf JO (2016) Evaluating Raman spectra of carbonaceous matter by automated, iterative curve-fitting. Int J Coal Geol 160–161:51–62. https://doi.org/10.1016/j.coal.2016.04.008

Macklin MG, Fuller IC, Lewin J, et al (2002) Correlation of fluvial sequences in the Mediterranean basin over the last 200 ka and their relationship to climate change. Quat Sci Rev 21:1633–1641. https://doi.org/10.1016/S0277-3791(01)00147-0

Mair D, Lechmann A, Yesilyurt S, et al (2019) Fast long-term denudation rate of steep alpine headwalls inferred from cosmogenic 36Cl depth profiles. Sci Rep 9:1–15. https://doi.org/10.1038/s41598-019-46969-0

Malatesta LC, Prancevic JP, Avouac JP (2017) Autogenic entrenchment patterns and terraces due to coupling with lateral erosion in incising alluvial channels. J Geophys Res Earth Surf 122:335–355. https://doi.org/10.1002/2015JF003797

Malinverno A, Ryan WBF (1986) Extension in the Tyrrhenian Sea and shortening in the Apennines as result of arc migration driven by sinking of the lithosphere. Tectonics 5:227–245

Malo M, Tremblay A, Kirkwood D, Cousineau P (1995) Along-strike Acadian structural variations in the Quebec Appalachians : Consequence of a collision along an irregular margin. 14:1327–1338. https://doi.org/https://doi.org/10.1029/95TC01449

Malusà MG, Fitzgerald PG (2018) Fission-Track Thermochronology and its Application to Geology (Springer Textbooks in Earth Sciences, Geography and Environment), 1st ed. Springer International Publishing

Marc O, Hovius N, Meunier P, et al (2015) Transient changes of landslide rates after earthquakes. Geology 43:883–886. https://doi.org/10.1130/G36961.1

Marković JĐ (1990) Enciklopedijski geografski leksikon Jugoslavije, (serbian). Sarajevo : Svjetlost

Marović M, Djoković I, Toljić M, et al (2007) Extensional unroofing of the Veliki Jastrebac dome (Serbia). Geol Anal Balk poluostrva - Ann Geol la Penins Balk 21–27. https://doi.org/10.2298/gabp0701021m

Marrero SM, Phillips FM, Caffee MW, Gosse JC (2016) CRONUS-Earth cosmogenic 36Cl calibration.

Quat Geochronol 31:199–219. https://doi.org/10.1016/j.quageo.2015.10.002

Marrucci M, Zeilinger G, Ribolini A, Schwanghart W (2018) Origin of knickpoints in an alpine context subject to different perturbing factors, stura valley, maritime alps (North-Western Italy). Geosci 8:. https://doi.org/10.3390/geosciences8120443

Marshak S (1988) Kinematics of orocline and arc formation in thin-skinned orogens. Tectonics 7:73–86

Márton E, Ćosović V, Moro A (2014) New stepping stones, Dugi otok and Vis islands, in the systematic paleomagnetic study of the Adriatic region and their significance in evaluations of existing tectonic models. Tectonophysics 611:141–154. https://doi.org/10.1016/j.tecto.2013.11.016

Márton E, Drobne K, Ćosović V, Moro A (2003) Palaeomagnetic evidence for Tertiary counterclockwise rotation of Adria. Tectonophysics 377:143–156. https://doi.org/10.1016/j.tecto.2003.08.022

Matenco L, Radivojević D (2012) On the formation and evolution of the Pannonian Basin: Constraints derived from the structure of the junction area between the Carpathians and Dinarides. Tectonics 31:1–31. https://doi.org/10.1029/2012TC003206

Matsuoka N (2008) Frost weathering and rockwall erosion in the southeastern Swiss Alps: Long-term (1994-2006) observations. Geomorphology 99:353–368. https://doi.org/10.1016/j.geomorph.2007.11.013

McDowell FW, Keizer RP (1977) Timing of mid-Tertiary volcanism in the Sierra Madre Occidental between Durango City and Mazatlan, Mexico. Bull Geol Soc Am 88:1479–1487. https://doi.org/10.1130/0016-7606(1977)88<1479:TOMVIT>2.0.CO;2

Meço S, Aliaj S (2000) Geology of Albania. Gebrueder Borntraeger. Berlin. Stuttgart.

Meier J (2012) Die geologische Entwicklung des Prizren-Pejë-Beckens -The geological development of the Prizren-Pejë Basin. Zeitschrift für Geol Wissenschaften Berlin 40:

Mikes T, Baresel B, Kronz A, et al (2009) Jurassic granitoid magmatism in the Dinaride Neotethys: Geochronological constraints from detrital minerals. Terra Nov 21:495–506. https://doi.org/10.1111/j.1365-3121.2009.00907.x

Milivojević M, Menković L, Ćalić J (2008) Pleistocene glacial relief of the central part of Mt. Prokletije (Albanian Alps). Quat Int 190:112–122. https://doi.org/10.1016/j.quaint.2008.04.006

Mittelbach B V (2020) Using Cosmogenic Nuclides to constrain the Age and Origin of a Fluvial Terrace Sequence in the Tropoja Basin, NE Albania. MSc thesis, Freie Universität Berlin

Mladenović A, Trivić B, Cvetković V (2015) How tectonics controlled post-collisional magmatism within the Dinarides: Inferences based on study of tectono-magmatic events in the Kopaonik Mts. (Southern Serbia). Tectonophysics 646:36–49. https://doi.org/10.1016/j.tecto.2015.02.001

Molnar P, Lyon-Caen H (1988) Some simple physical aspects of the support, structure, and evolution of mountain belts. Spec Pap Geol Soc Am 218:179–207. https://doi.org/10.1130/SPE218-p179

Most T (2003) Geodynamic evolution of the Eastern Pelagonian Zone in north-western Greece and the Republic of Macedonia. Implications from U/Pb, Rb/Sr, K/Ar, 40 Ar/ 39 Ar geochronology and fission track thermochronology. Diss Geowissenschaftliche Fak der Eberhardt-Karls-Universität Tübingen

Muceku B, Mascle GH, Tashko A (2006) First results of fission-track thermochronology in the Albanides. Geol Soc London, Spec Publ 260:539–556. https://doi.org/10.1144/gsl.sp.2006.260.01.23

Muceku B, Van Der Beek P, Bernet M, et al (2008) Thermochronological evidence for Mio-Pliocene late orogenic extension in the north-eastern Albanides (Albania). Terra Nov 20:180–187. https://doi.org/10.1111/j.1365-3121.2008.00803.x

Muço B (1995) The seasonality of Albanian earthquakes and cross-correlation with rainfall. Phys Earth Planet Inter 88:285–291. https://doi.org/10.1016/0031-9201(94)02988-N

Muço B, Alexiev G, Aliaj S, et al (2012) Geohazards assessment and mapping of some Balkan countries

Muhs DR, Budahn J, Avila A, et al (2010) The role of African dust in the formation of Quaternary soils on Mallorca, Spain and implications for the genesis of Red Mediterranean soils. Quat Sci Rev 29:2518–2543. https://doi.org/10.1016/j.quascirev.2010.04.013

NASA JPL (2013) NASA Shuttle Radar Topography Mission Global 1 arc second [Data set]. NASA EOSDIS Land Processes DAAC. NASA EOSDIS L Process DAAC. https://doi.org/10.5067/MEaSUREs/SRTM/SRTMGL1.003

Neely AB, Bookhagen B, Burbank DW (2017) An automated knickzone selection algorithm (KZ-Picker) to analyze transient landscapes: Calibration and validation. J Geophys Res Earth Surf 122:1236–1261. https://doi.org/10.1002/2017JF004250

Neubauer TA, Harzhauser M, Georgopoulou E, et al (2015) Tectonics, climate, and the rise and demise of continental aquatic species richness hotspots. Proc Natl Acad Sci U S A 112:11478–11483. https://doi.org/10.1073/pnas.1503992112

Ni JF (1989) Active tectonics of the Himalaya. Proc Indian Acad Sci - Earth Planet Sci 98:71–89. https://doi.org/10.1007/BF02880377

Nieuwland DA, Oudmayer BC, Valbona U (2001) The tectonic development of Albania: Explanation and prediction of structural styles. Mar Pet Geol 18:161–177. https://doi.org/10.1016/S0264-8172(00)00043-X

Okrusch M, Matthes S (2009) Mineralogie: Eine Einführung in die spezielle Mineralogie, Petrologie und Lagerstättenkunde, 8th edn. Springer Berlin Heidelberg

Ott RF, Gallen SF, Wegmann KW, et al (2019) Pleistocene terrace formation, Quaternary rock uplift rates and geodynamics of the Hellenic Subduction Zone revealed from dating of paleoshorelines on Crete, Greece. Earth Planet Sci Lett 525:115757. https://doi.org/10.1016/j.epsl.2019.115757

Ozsvárt P, Dosztály L, Migiros G, et al (2012) New radiolarian biostratigraphic age constraints on Middle Triassic basalts and radiolarites from the Inner Hellenides (Northern Pindos and Othris Mountains, Northern Greece) and their implications for the geodynamic evolution of the early Mesozoic Neotet. Int J Earth Sci 101:1487–1501. https://doi.org/10.1007/s00531-010-0628-9

Pamić J (2002) The Sava-Vardar zone of the Dinarides and Hellenides versus the Vardar Ocean. Eclogae Geol Helv 95:99–114

Pashko P, Aliaj S (2020) Stratigraphy and tectonic evolution of Late Miocene - Quaternary Basins in Eastern Albania: A Review. Bull Geol Soc Greece 56:317. https://doi.org/10.12681/bgsg.22064

Pazzaglia FJ (2013) River Terraces. Treatise of Geomorphology. Elsevier

Pearce D, Rondenay S, Sachpazi M, et al (2012) Seismic investigation of the transition from continental to oceanic subduction along the western Hellenic Subduction Zone. J Geophys Res Solid Earth 117:1–18. https://doi.org/10.1029/2011JB009023

Perron JT, Royden L (2013) An integral approach to bedrock river profile analysis. Earth Surf Process Landforms 38:570–576. https://doi.org/10.1002/esp.3302

Phillips FM, Zreda MG, Benson L V., et al (1996a) Chronology for fluctuations in late Pleistocene Sierra Nevada glaciers and lakes. Science (80-) 274:749–751. https://doi.org/10.1126/science.274.5288.749

Phillips FM, Zreda MG, Flinsch MR, et al (1996b) A reevaluation of cosmogenic 36Cl production rates in terrestrial rocks. Geophys Res Abstr 23:949–952

Phillips FM, Zreda MG, Smith SS, et al (1991) Age and geomorphic history of Meteor Crater, Arizona, from cosmogenic 36Cl and 14C in rock varnish. Geochim Cosmochim Acta 55:2695–2698. https://doi.org/10.1016/0016-7037(91)90387-K

Philpotts R, Ague JJ (2009) Principles of Igneous and Metamorphic Petrology, 2nd edn. University Press, Cambridge

Pirazzoli PA (1991) World Atlas of Holocene Sea-Level Changes, 1st edn. Elsevier Oceanography Series

Piromallo C, Morelli A (2003) P wave tomography of the mantle under the Alpine-Mediterranean area. J Geophys Res Solid Earth 108:1–23. https://doi.org/10.1029/2002jb001757

Plunder A, Thieulot C, Van Hinsbergen DJJ (2018) The effect of obliquity on temperature in subduction zones: insights from 3-D numerical modeling. Solid Earth 9:759–776. https://doi.org/10.5194/se-9-759-2018

Poblet J, Lisle RJ (2011) Kinematic evolution and structural styles of fold-and-thrust belts. Geol Soc Spec Publ 349:1–24. https://doi.org/10.1144/SP349.1

Porkoláb K, Kövér S, Benkó Z, et al (2019) Structural and geochronological constraints from the Drina-Ivanjica thrust sheet (Western Serbia): implications for the Cretaceous–Paleogene tectonics of the Internal Dinarides. Swiss J Geosci 112:217–234. https://doi.org/10.1007/s00015-018-0327-2

Priest SD (1985) Hemispherical projection methods in rock mechanics. George Allen & Unwin, London

Rahl JM, Anderson KM, Brandon MT, Fassoulas C (2005) Raman spectroscopic carbonaceous material thermometry of low-grade metamorphic rocks: Calibration and application to tectonic exhumation in Crete, Greece. Earth Planet Sci Lett 240:339–354. https://doi.org/10.1016/j.epsl.2005.09.055

Rahn M, Wang H, Dunkl I (2019) A natural long-term annealing experiment for the zircon fission track system in the Songpan-Garzê flysch, China. Terra Nov 31:295–305. https://doi.org/10.1111/ter.12399

Rahn MK, Brandon MT, Batt G, Garver J (2004) A zero-damage model for fission-track annealing in zircon. Am Mineral 89:473–484

Rassios AE, Dilek Y (2009) Rotational deformation in the Jurassic Mesohellenic ophiolites, Greece, and its tectonic significance. Lithos 108:207–223. https://doi.org/10.1016/j.lithos.2008.09.005

Ratschbacher L, Frisch W, Linzer H -G, Merle O (1991) Lateral extrusion in the eastern Alps, Part 2: Structural analysis. Tectonics 10:257–271. https://doi.org/10.1029/90TC02623

Raychaudhuri S (2008) Introduction to Monte Carlo simulation. Proc 2008 Winter Simul Conf 91–100. https://doi.org/doi:10.1109/wsc.2008.4736059

Reiners PW (2005) Zircon (U-TH)/He thermochronometry. Rev Mineral Geochemistry 58:151–179. https://doi.org/10.2138/rmg.2005.58.6

Reiners PW, Brandon MT (2006) Using thermochronology to understand orogenic erosion. Annu Rev Earth Planet Sci 34:419–466. https://doi.org/10.1146/annurev.earth.34.031405.125202

Reiners PW, Farley KA (2001) Influence of crystal size on apatite (U-Th)/He thermochronology: An example from the Bighorn Mountains, Wyoming. Earth Planet Sci Lett 188:413–420. https://doi.org/10.1016/S0012-821X(01)00341-7

Reiners PW, Farley KA, Hickes HJ (2002) He diffusion and (U-Th)/He thermochronometry of zircon: Initial results from Fish Canyon Tuff and Gold Butte. Tectonophysics 349:297–308. https://doi.org/10.1016/S0040-1951(02)00058-6

Robert X, Van Der Beek P, Braun J, et al (2011) Control of detachment geometry on lateral variations in exhumation rates in the Himalaya: Insights from low-temperature thermochronology and numerical modeling. J Geophys Res Solid Earth 116:1–22. https://doi.org/10.1029/2010JB007893

Robertson A, Karamata S, Šarić K (2009) Overview of ophiolites and related units in the Late Palaeozoic-Early Cenozoic magmatic and tectonic development of Tethys in the northern part of the Balkan region. Lithos 108:1–36. https://doi.org/10.1016/j.lithos.2008.09.007

Robertson A, Shallo M (2000) Mesozoic-Tertiary tectonic evolution of Albania in its regional Eastern Mediterranean context. Tectonophysics 316:197–254. https://doi.org/10.1016/S0040-1951(99)00262-0

Rosenbaum G (2014) Geodynamics of oroclinal bending: Insights from the Mediterranean. J Geodyn 82:5–15. https://doi.org/10.1016/j.jog.2014.05.002

Rosenbaum G, Lister GS (2004) Formation of arcuate orogenic belts in the western Mediterranean region. Spec Pap Geol Soc Am 383:41–56. https://doi.org/10.1130/0-8137-2383-3(2004)383[41:FOAOBI]2.0.CO;2

Rosenberg CL, Garcia S (2011) Estimating displacement along the Brenner Fault and orogen-parallel extension in the Eastern Alps. Int J Earth Sci 100:1129–1145. https://doi.org/10.1007/s00531-011-0645-3

Rossetti F, Faccenna C, Jolivet L, et al (1999) Syn- versus post-orogenic extension: The case study of Giglio Island (Northern Tyrrhenian Sea, Italy). Tectonophysics 304:71–93. https://doi.org/10.1016/S0040-1951(98)00304-7

Royden L (1996) Coupling and decoupling of crust and mantle in convergent orogens: Implications for strain partitioning in the crust. J Geophys Res 101:17679–17705. https://doi.org/10.1029/96JB00951

Royden L, Burchfiel BC (1989) Are systematic variations in thrust belt style related to plate boundary processes? (the Western Alps versus the Carpathians). Tectonics 8:51–61

Royden LH, Papanikolaou DJ (2011) Slab segmentation and late Cenozoic disruption of the Hellenic arc. Geochemistry, Geophys Geosystems 12:. https://doi.org/10.1029/2010GC003280

Schaller M, Ehlers TA, Blum JD, Kallenberg MA (2009) Quantifying glacial moraine age, denudation, and soil mixing with cosmogenic nuclide depth profiles. J Geophys Res Earth Surf 114:1–18. https://doi.org/10.1029/2007JF000921

Scharf A, Handy MR, Favaro S, et al (2013a) Modes of orogen-parallel stretching and extensional exhumation in response to microplate indentation and roll-back subduction (Tauern Window, Eastern Alps). Int J Earth Sci 102:1627–1654. https://doi.org/10.1007/s00531-013-0894-4

Scharf A, Handy MR, Ziemann MA, Schmid SM (2013b) Peak-temperature patterns of polyphase metamorphism resulting from accretion, subduction and collision (eastern tauern window, european alps) - a study with raman microspectroscopy on carbonaceous material (RSCM). J Metamorph Geol 31:863–880. https://doi.org/10.1111/jmg.12048

Schefer S (2012) Tectono-metamorphic and magmatic evolution of the Internal Dinarides (Kopaonik area , southern Serbia) and its significance for the geodynamic evolution of the Balkan Peninsula. Inauguraldissertation. Universität Basel

Schefer S, Cvetković V, Fügenschuh B, et al (2011) Cenozoic granitoids in the Dinarides of southern Serbia: Age of intrusion, isotope geochemistry, exhumation history and significance for the geodynamic evolution of the Balkan Peninsula. Int J Earth Sci 100:1181–1206. https://doi.org/10.1007/s00531-010-0599-x

Scherreiks R, Meléndez G, BouDagher-Fadel M, et al (2014) Stratigraphy and tectonics of a time-transgressive ophiolite obduction onto the eastern margin of the Pelagonian platform from Late Bathonian until Valanginian time, exemplified in northern Evvoia, Greece. Int J Earth Sci 103:2191–2216. https://doi.org/10.1007/s00531-014-1036-3

Schmid SM, Bernoulli D, Fügenschuh B, et al (2008) The Alpine-Carpathian-Dinaridic orogenic system: Correlation and evolution of tectonic units. Swiss J Geosci 101:139–183. https://doi.org/10.1007/s00015-008-1247-3

Schmid SM, Casey M, Starkey J (1981) The microfabric of calcite tectonites from the Helvetic Nappes (Swiss Alps). Geol Soc Spec Publ 9:151–158. https://doi.org/10.1144/GSL.SP.1981.009.01.13

Schmid SM, Fügenschuh B, Kounov A, et al (2020) Tectonic units of the Alpine collision zone between Eastern Alps and western Turkey. Gondwana Res 78:308–374. https://doi.org/10.1016/j.gr.2019.07.005

Schmid SM, Paterson MS, Boland JN (1980) High temperature flow and dynamic recrystallization in carrara marble. Tectonophysics 65:245–280. https://doi.org/10.1016/0040-1951(80)90077-3

Schmid SM, Scharf A, Handy MR, Rosenberg CL (2013) The Tauern Window (Eastern Alps, Austria): A new tectonic map, with cross-sections and a tectonometamorphic synthesis. Swiss J Geosci 106:1–32. https://doi.org/10.1007/s00015-013-0123-y

Schmitz B, Biermanns P, Hinsch R, et al (2020) Ongoing shortening in the Dinarides fold-and-thrust belt: A new structural model of the 1979 (Mw 7.1) Montenegro earthquake epicentral region. J Struct Geol 141:. https://doi.org/10.1016/j.jsg.2020.104192

Schwanghart W, Scherler D (2020) Divide mobility controls knickpoint migration on the Roan Plateau (Colorado, USA). Geology 48:698–702. https://doi.org/10.1130/G47054.1

Schwanghart W, Scherler D (2014) Short Communication: TopoToolbox 2 – MATLAB-based software for topographic analysis and modeling in Earth surface sciences. Earth Surf Dynam 2:1–7. https://doi.org/https://doi.org/10.5194/esurf-2-1-2014

Schwanghart W, Scherler D (2017) Bumps in river profiles: uncertainty assessment and smoothing using quantile regression techniques. Earth Surf Dynam 5:821–839. https://doi.org/https://doi.org/10.5194/esurf-5-821-2017

Scotese CR (2002) Paleomap Project. www.scotese.com

Sekine S, Hirose H, Obara K (2010) Along-strike variations in short-term slow slip events in the southwest Japan subduction zone. J Geophys Res Solid Earth 115:. https://doi.org/10.1029/2008JB006059

Shallo M, Dilek Y (2007) Development of the ideas on the origin of Albanian ophiolites. In: Special Paper 373: Ophiolite concept and the evolution of geological thought. Geological Society of America, pp 351–363

Sharma P, Bourgeois M, Elmore D, et al (2000) PRIME lab AMS performance, upgrades and research applications. Nucl Instruments Methods Phys Res Sect B Beam Interact with Mater Atoms 172:112–123. https://doi.org/10.1016/S0168-583X(00)00132-4

Simon D (2021) The structural and sedimentological evolution of the Tropoja Basin in northeastern Albania. MSc thesis, Freie Universität Berlin

Skourlis K, Doutsos T (2003) The Pindos Fold-and-thrust belt (Greece): Inversion kinematics of a passive continental margin. Int J Earth Sci 92:891–903. https://doi.org/10.1007/s00531-003-0365-4

Snyder NP, Whipple KX, Tucker GE, Merritts DJ (2000) Landscape response to tectonic forcing: Digital elevation model analysis of stream profiles in the Mendocino triple junction region, northern California. Geol Soc Am Bull 112:1250–1263. https://doi.org/10.1130/0016-7606(2000)112<1250:lrttfd>2.3.co;2

Sobel ER, Seward D (2010) Influence of etching conditions on apatite fission-track etch pit diameter. Chem Geol 271:59–69. https://doi.org/10.1016/j.chemgeo.2009.12.012

Speranza F, Islami I, Kissel C, Hyseni A (1995) Paleomagnetic evidence for Cenozoic clockwise rotation of the external Albanides. Earth Planet Sci Lett 129:121–134. https://doi.org/10.1016/0012-821X(94)00231-M

Spikings RA, Winkler W, Seward D, Handler R (2001) Along-strike variations in the thermal and tectonic response of the continental Ecuadorian Andes to the collision with heterogeneous oceanic crust. Earth Planet Sci Lett 186:57–73. https://doi.org/10.1016/S0012-821X(01)00225-4

Środoń J, Anczkiewicz AA, Dunkl I, et al (2018) Thermal history of the central part of the Karst Dinarides, Croatia: Combined application of clay mineralogy and low-T thermochronology. Tectonophysics 744:155–176. https://doi.org/10.1016/j.tecto.2018.06.016

Stock JD, Dietrich WE (2006) Erosion of steepland valleys by debris flows. Bull Geol Soc Am 118:1125–1148. https://doi.org/10.1130/B25902.1

Stojadinovic U, Matenco L, Andriessen P, et al (2016) Structure and provenance of Late Cretaceous–Miocene sediments located near the NE Dinarides margin: Inferences from kinematics of orogenic building and subsequent extensional collapse. Tectonophysics 710–711:184–204. https://doi.org/10.1016/j.tecto.2016.12.021

Stojadinovic U, Matenco L, Andriessen PAM, et al (2013) The balance between orogenic building and subsequent extension during the tertiary evolution of the NE dinarides: Constraints from low-temperature thermochronology. Glob Planet Change 103:19–38. https://doi.org/10.1016/j.gloplacha.2012.08.004

Stokes M, Mather AE, Harvey AM (2002) Quantification of river-capture-induced base-level changes and landscape development, Sorbas Basin, SE Spain. Geol Soc Spec Publ 191:23–35. https://doi.org/10.1144/GSL.SP.2002.191.01.03

Stone JO (2000) Air pressure and cosmogenic isotope production. J Geophys Res 105:753–759

Sudar M, Kovács S (2006) Metamorphosed and ductilely deformed conodonts from Triassic limestones situated beneath ophiolite complexes: Kopaonik Mountain (Serbia) and Bükk Mountains (NE Hungary) - A preliminary comparison. Geol Carpathica 57:157–176

Sudar MN, Gawlick HJ, Lein R, et al (2013) Depositional environment, age and facies of the Middle Triassic Bulog and rid formations in the Inner Dinarides (Zlatibor Mountain, SW Serbia): Evidence for the Anisian break-up of the Neotethys Ocean. Neues Jahrb fur Geol und Palaontologie - Abhandlungen 269:291–320. https://doi.org/10.1127/0077-7749/2013/0352

Tahirsylaj S, Kastrati B, Hasan H, Sopi F (2010) Hydro Geographical Elements of Bistrica E Pejes River. BALWOIS 2010 - Ohrid, Repub Maced 25:1–4

Tapponnier P, Peltzer G, Armijo R (1986) On the mechanics of the collision between India and Asia. Collis Tectonics, Geol Soc Spec Publ 19:115–157

Tari V (2002) Evolution of the northern and western Dinarides: a tectonostratigraphic approach. Stephan Mueller Spec Publ Ser 1:223–236. https://doi.org/10.5194/smsps-1-223-2002

Tremblay A, Meshi A, Deschamps T, et al (2015) The Vardar zone as a suture for the Mirdita ophiolites, Albania: Constraints from the structural analysis of the Korabi-Pelagonia zone. Tectonics 34:352–375. https://doi.org/10.1002/2014TC003807

Tucker GE, McCoy SW, Whittaker AC, et al (2011) Geomorphic significance of postglacial bedrock scarps on normal-fault footwalls. J Geophys Res Earth Surf 116:1–14. https://doi.org/10.1029/2010JF001861

Tucker GE, Slingerland R (1997) Drainage basin responses to climate change. Water Resour Res 33:2031–2047

van Hinsbergen DJJ, Langereis CG, Meulenkamp JE (2005) Revision of the timing, magnitude and distribution of Neogene rotations in the western Aegean region. Tectonophysics 396:1–34.

https://doi.org/10.1016/j.tecto.2004.10.001

van Hinsbergen DJJ, Torsvik TH, Schmid SM, et al (2020) Orogenic architecture of the Mediterranean region and kinematic reconstruction of its tectonic evolution since the Triassic. Gondwana Res 81:79–229. https://doi.org/10.1016/j.gr.2019.07.009

van Unen M, Matenco L, Nader FH, et al (2019) Kinematics of Foreland-Vergent Crustal Accretion: Inferences From the Dinarides Evolution. Tectonics 38:49–76. https://doi.org/10.1029/2018TC005066

Vermeesch P (2009) RadialPlotter: A Java application for fission track, luminescence and other radial plots. Radiat Meas 44:409–410. https://doi.org/10.1016/j.radmeas.2009.05.003

Vermeesch P (2018) IsoplotR: A free and open toolbox for geochronology. Geosci Front 9:1479–1493. https://doi.org/10.1016/j.gsf.2018.04.001

Vignaroli G, Faccenna C, Jolivet L, et al (2009) Reply to the comment by G. Capponi et al. on “Subduction polarity reversal at the junction between the Western Alps and the Northern Apennines, Italy”, by G. Vignaroli et al. (Tectonophysics, 2008, 450, 34-50). Tectonophysics 465:227–231. https://doi.org/10.1016/j.tecto.2008.11.007

Vignaroli G, Faccenna C, Jolivet L, et al (2008) Subduction polarity reversal at the junction between the Western Alps and the Northern Apennines, Italy. Tectonophysics 450:34–50. https://doi.org/10.1016/j.tecto.2007.12.012

Vishnevskaya VS, Djeric N, Zakariadze GS (2009) New data on Mesozoic Radiolaria of Serbia and Bosnia, and implications for the age and evolution of oceanic volcanic rocks in the Central and Northern Balkans. Lithos 108:72–105. https://doi.org/10.1016/j.lithos.2008.10.015

Vogel H, Wagner B, Zanchetta G, et al (2010a) A paleoclimate record with tephrochronological age control for the last glacial-interglacial cycle from Lake Ohrid, Albania and Macedonia. J Paleolimnol 44:295–310. https://doi.org/10.1007/s10933-009-9404-x

Vogel H, Wessels M, Albrecht C, et al (2010b) Spatial variability of recent sedimentation in Lake Ohrid (Albania/Macedonia). Biogeosciences 7:3333–3342. https://doi.org/10.5194/bg-7-3333-2010

von Nopcsa DBF (1905) Zur Geologie von Nordalbanien. Jahrb der Kais Geol Reichsanstalt 55:85–152

Wagner B, Aufgebauer A, Vogel H, et al (2012) Late Pleistocene and Holocene contourite drift in Lake Prespa (Albania/F.Y.R. of Macedonia/Greece). Quat Int 274:112–121. https://doi.org/10.1016/j.quaint.2012.02.016

Wagner B, Vogel H, Francke A, et al (2019) Mediterranean winter rainfall in phase with African monsoons during the past 1.36 million years. Nature 573:256–260. https://doi.org/10.1038/s41586-019-1529-0

Walcott CR, White SH (1998) Constraints on the kinematics of post-orogenic extension imposed by stretching lineations in the Aegean region. Tectonophysics 298:155–175. https://doi.org/10.1016/S0040-1951(98)00182-6

Wegener A (2001) Translation of: Die Entstehung der Kontinente. J Geodyn 32:29–63

Wegener A (1912) Die Entstehung der Kontinente. Geol Rundschau 3:276–292. https://doi.org/10.1007/BF02202896

Whipple KX (2009) The influence of climate on the tectonic evolution of mountain belts. Nat Geosci 2:97–104. https://doi.org/10.1038/ngeo413

Whipple KX, Forte AM, DiBiase RA, et al (2017) Timescales of landscape response to divide migration and drainage capture: Implications for the role of divide mobility in landscape evolution. J Geophys Res Earth Surf 122:248–273. https://doi.org/10.1002/2016JF003973

Whipple KX, Tucker GE (1999) Dynamics of the stream-power river incision model: Implications for height limits of mountain ranges, landscape response timescales, and research needs. J Geophys Res 104:17661–17674

White SH, Bretan PG, Rutter EH (1986) Fault-zone reactivation: kinematics and mechanisms. Philos Trans - R Soc London, Ser A 317:81–97. https://doi.org/10.1098/rsta.1986.0026

Whittaker AC (2012) How do landscapes record tectonics and climate? Lithosphere 4:160–164. https://doi.org/10.1130/RF.L003.1

Whittaker AC, Boulton SJ (2012) Tectonic and climatic controls on knickpoint retreat rates and landscape response times. J Geophys Res 117:1–19. https://doi.org/10.1029/2011JF002157

Whittaker AC, Cowie PA, Attal M, et al (2007) Contrasting transient and steady-state rivers crossing active normal faults: New field observations from the central apennines, Italy. Basin Res 19:529–556. https://doi.org/10.1111/j.1365-2117.2007.00337.x

Wiederkehr M, Bousquet R, Ziemann MA, et al (2011) 3-D assessment of peak-metamorphic conditions by Raman spectroscopy of carbonaceous material: An example from the margin of the Lepontine dome (Swiss Central Alps)

Willett SD, McCoy SW, Taylor Perron J, et al (2014) Dynamic reorganization of River Basins. Science (80-) 343:. https://doi.org/10.1126/science.1248765

Willigers BJA, Krogstad EJ, Wijbrans JR (2001) Comparison of thermochronometers in a slowly cooled granulite terrain: Nagssugtoqidian Orogen, West Greenland. J Petrol 42:1729–1749. https://doi.org/10.1093/petrology/42.9.1729

Wobus C, Whipple KX, Kirby E, et al (2006) Tectonics from topography: Procedures, promise, and pitfalls. Spec Pap Geol Soc Am 398:55–74. https://doi.org/10.1130/2006.2398(04)

Wobus CW, Tucker GE, Anderson RS (2010) Does climate change create distinctive patterns of landscape incision? J Geophys Res Earth Surf 115:1–12. https://doi.org/10.1029/2009JF001562

Wolff R, Hetzel R, Dunkl I, et al (2020) Fast cooling of normal-fault footwalls: Rapid fault slip or thermal relaxation? Geology 48:333–337. https://doi.org/10.1130/G46940.1

Wortel MJR, Spakman W (2000) Subduction and slab detachment in the Mediterranean-Carpathian region. Sci Compass Rev 290:1910–1917. https://doi.org/10.1126/science.290.5498.1910

Xhomo A, Kodra A, Dimo-Lahitte A, Shallo M (2002) Geological Map of Albania 1:200.000 - North. Repub Albania, Minist Ind Energy, Polytech Univ Tirana

Yabe S, Ide S, Yoshioka S (2014) Along-strike variations in temperature and tectonic tremor activity along the Hikurangi subduction zone, New Zealand. Earth, Planets Sp 66:1–15. https://doi.org/10.1186/s40623-014-0142-6

Yang R, Willett SD, Goren L (2015) In situ low-relief landscape formation as a result of river network disruption. Nature 520:. https://doi.org/10.1038/nature14354

Table of figures

Appendix I

This appendix refers to Chapter II: “Faulting, basin formation and orogenic arcuation at the Dinaric - Hellenic junction (northern Albania and Kosovo)”

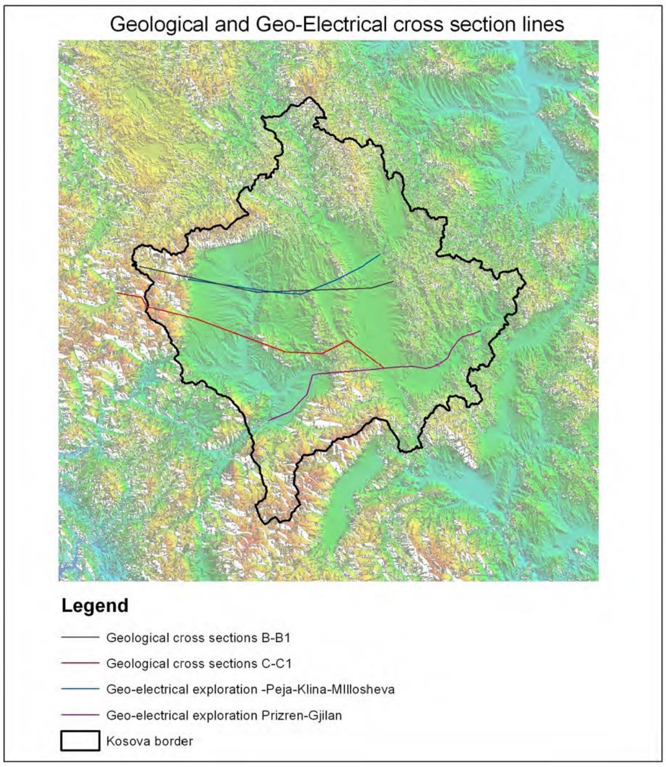

Fig. 1/Appendix I: Locations of geo-electric resistivity investigations in Kosovo from: Carbon Capture and Storage (CCS) Capacity Building in Kosovo- World Bank Report 2013 (Linder and Perkuhn 2013).

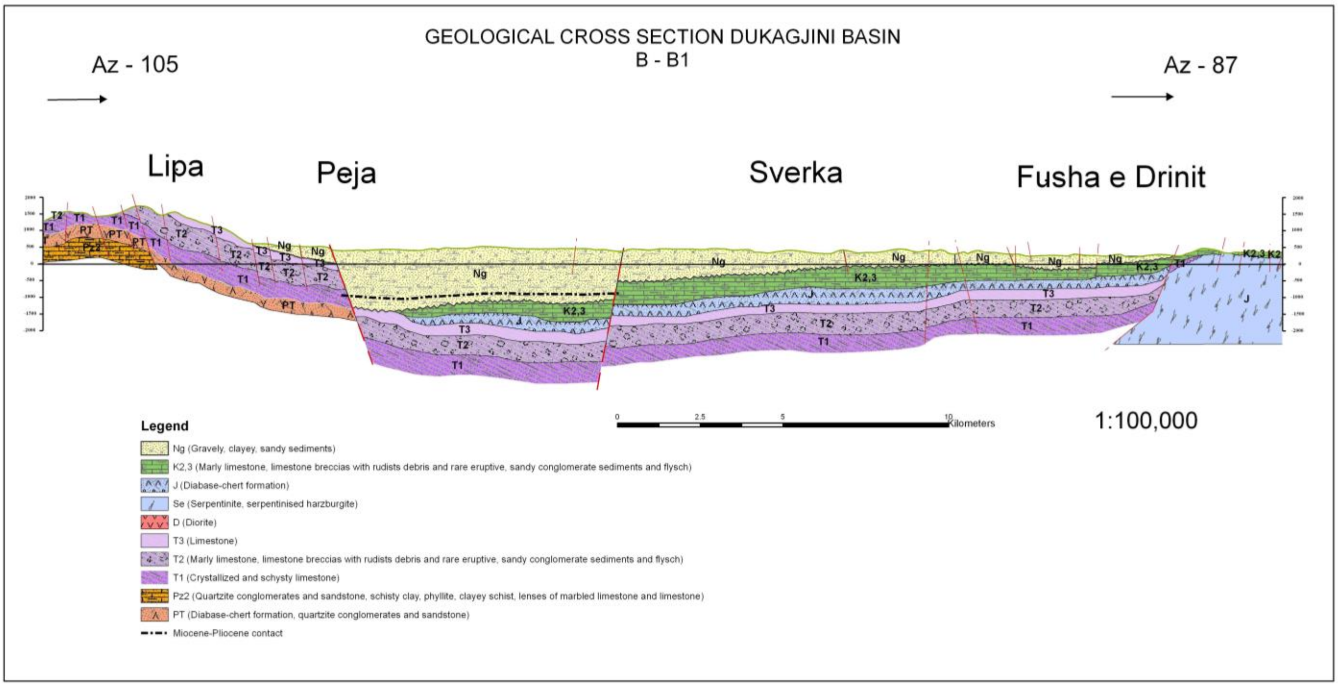

Fig. 2/Appendix I: Interpretation of the geological situation based on geo-electric investigations. Raw data and further data is available on the enclosed digital data medium in file: Appendix I.

Appendix II

This appendix refers to Chapter III: “Thermal record of obduction, nappe stacking and orogen-parallel extension at the Dinaric - Hellenic junction”

Methods and Analytics

Apatite fission track analyses

Concentrates of apatite were mounted on glass plates with epoxy resin, exposed, grinded, polished and etched with 5.5 M HNO_3 at 21±0.5 °C for 20 s (Carlson et al. 1999; Sobel and Seward 2010) to reveal the spontaneous tracks. AFT dating followed the external detector method introduced by Gleadow, 1981 and the zeta-calibration approach (Hurford & Green, 1983; mean zeta factor in Appendix II: Tab. 1,). Durango apatite with a reference age of 31.4 ± 0.5 Ma (Hurford and Hammerschmidt 1985) and Fish Canyon Tuff (apatite) with an age of 27.9 ± 0.5 Ma (McDowell and Keizer 1977) were used as age standards for the zeta calibration. CN5 and IRMM 540R were used as dosimeter glass for neutron flux monitoring during sample irradiation at Garching (Technical University of Munich, Germany) and Oregon State University (TRIGA Mark II Pulsing Research Reactor, Appendix II: Tab. 1,). Induced tracks in external detector muscovite were etched in 40% HF for 45 min at 20°C at the University of Innsbruck and at University of Potsdam after irradiation. The density of the spontaneous and induced tracks of the individual apatites were analyzed at the Freie Universität Berlin with an ZEISS AXIOPLAN 2© imaging microscope at a magnification of 1250 x equipped with a computer-driven micrometer stage using FTStage 4.04 Software (Dumitru 1993). Due to the low quality and small grain sizes of apatite in the samples, it was not possible to measure sufficient track-lengths in any of the AFT samples. AFT central ages and diagrams were produced with RadialPlotter (Vermeesch 2009). All ages are given with ±2ϭ error (Galbraith and Laslett 1993) and were calculated with the IUGS recommended approach of Hurford & Green, 1983. The results are given in Appendix II in Tab. 1, the according sample locations and information are given in Fig. 3.3. All ages are reported as central ages with their corresponding 2ϭ errors.

(U–Th)/He zircon analyses

Zircons for helium dating were handpicked from heavy mineral concentrates that were processed following the protocol of Kohn et al. (2019) at the Freie Universität Berlin and University of Innsbruck. Mineral selection, packing and dating of the zircons was done at the University of Potsdam. For each sample location, five suitably crystals with grain diameters >60-90 µm and without fractures were selected under a binocular microscope. The total length, prism length, and width were measured from two different sides to account for He loss by calculating the alpha-ejection correction following Farley (2002). Afterwards, each zircon was packed in a niobium (Nb) foil tube. He extraction was performed using an alphachron quadrupole mass spectrometer at Universität Potsdam. Parent nuclide contents of degassed zircons were measured by ICP-MS at the GFZ-Potsdam. Full analytical details are available in Galetto et al. (2021). Single grains with large analytical errors, low or very high uranium contents or alpha decay crystal damage were excluded from the data set. Pooled central ages (RadialPlotter; Vermeesch 2009) were calculated from the resulting single-grain ages of the individual samples. Radial plots of the pooled central ZHe ages are available in the enclosed digital data medium in folder Appendix II/Radial plots/ZHe. ZHe age uncertainties are given in 1ϭ standard deviation (Appenix II, Tab. 2).

Zircon fission track analyses

After separation, zircon crystals were mounted in PFA® Teflon. Revelation of fossil tracks was achieved by etching polished zircon mounts for 3-8 h in a NaOH–KOH eutectic melt at 235°C. Samples were analysed using the external detector method (Gleadow 1981). Induced tracks in a muscovite external detector were etched in 40% HF for 45 min at 20°C after irradiation of zircon at Oregon State University TRIGA Mark II Pulsing Research Reactor. Neutron flux was monitored using CN1 (for zircon) dosimeter glass. Ages were calculated using the zeta calibration (Appendix II, Tab. 3) method of Hurford & Green (1983). Fish Canyon Tuff zircon with an age of 27.9 ± 0.5 Ma (McDowell and Keizer 1977) was used as age standard for the zeta calibration. The measurements were carried out at University Innsbruck using a Zeiss Axio Imager A1 microscope equipped with an AUTOSCAN® stage. The ages were calculated using TRACKKEY software, version 4.2.g (Dunkl 2002). All results are given in Appendix II, Tab. 3, the according sample locations and information are given in Figure 3.3. All ages are reported as central ages with their corresponding 2σ errors.

RCSM method and analytical techniques

The total amount of 30 samples for RSCM were sampled across and along strike the SPNF system, from both foot- and hanging walls. The analytical results are given in Appendix II, Tab. 4, the according sample locations and information are given in Fig. 3.2. All samples (Appendix II, Tab.4) were prepared at Freie Universität Berlin as polished 30 µm standard thin-sections on a glass plate. Raman spectroscopy was performed at Freie Universität Berlin with a “Horiba ISA Dilor Labram” micro-confocal Raman spectrometer with 300mm focal length and a "Horiba Synapse" CCD-detector. The attached laser is a green solid-state 532 nm laser.

The measured raman spectra of carbonaceous matter (CM) were processed with the IFORS-software (Lünsdorf et al. 2017; Linux version downloaded in late August 2021). It provides an automated spectrum fitting approach that helps to limit operator bias (Lünsdorf et al. 2014). It also includes a calibration that allows to use the degree of crystallisation of CM (STA-parameter in IFORS), as determined via Raman spectroscopy, as a geothermometer.

Curve-fitting with IFORS was performed in the spectral range between 800-1900 cm^{-1}. We used a Hanning-window filter as baseline correction. All fitted peaks outside of the CM-band region, i.e. below 1100 cm^{-1} and above 1700 cm^{-1}, were excluded in the calculation of the STA-parameter, as well as several other peaks inside of this interval that originate from minerals other than CM. From the remaining CM-peaks, the STA-parameter was calculated for the spectral range between 1100-1700 cm^{-1}. The entire fitting procedure was consistently applied to all acquired spectra of CM. All further details concerning the curve-fitting procedure can be obtained from the configuration file of the IFORS-software that is included on the enclosed digital data medium in the file: IFORS software: config_kosovo_v20220322.cfg.

After STA-parameters were calculated for each fitted spectrum, they were translated to a temperature value with the built-in calibration by (Lünsdorf et al. 2017). This geothermometer is calibrated in the temperature range of roughly 160-600 °C (i.e. an STA-range of ca. 20-240). Some samples yielded a temperature spectrum that partly overlapped with the lower bound of this calibration range. In such cases, spectra with corresponding temperatures below ca. 140 °C were excluded from further analysis. In all analysed samples, this issue affected at maximum ca. 20% of the measured CM grains. In such very low-grade samples, this approach systematically biases the sample average temperature so that it is shifted to somewhat higher values, thus the obtained sample mean temperature must be interpreted as a maximum estimate. Additionally, we manually excluded clear outliers (e.g., very high-grade detrital graphite) and spectra where the peak-fitting procedure failed (e.g., poor spectrum quality, extreme fluorescence, spurious peaks, intense non-CM peaks in the CM-band region) from further analysis.The remaining spectra result in a temperature range for each sample (below in Appendix II- RSCM temperature spectra results). The temperature variability in each individual sample is further visualized as a kernel density estimate (KDE; below in Appendix II). Sample average temperatures were calculated as the mean, with its uncertainty given by the 95% confidence interval (CI) of the mean. The absolute uncertainty of the method is estimated in the order of ~30 °C (Aoya et al. 2010).

Tables

	Sample number	Location [Lat./Long.] WGS 84 Geographic	Alt. (m)	Lithology	Tectonic Unit	Num. gr.	Roh D x10^5 cm^-2	Roh S x10^5 cm^-2	Roh I x10^5 cm^-2	U conc. [ppm]	P (X^2)[%]	Central (Ma)	Error (2σ)	Dpar (µm)	Observer	ζ (1 σ err)
1	**Al-JGI_130**	N42.48985/ E19.98927	1940	granitic gneiss	East Bosnian Durmitor	20	13,83152	3,332	11,215	11,92	97,27	56	17	1,47	MG-1	265±18
2	**Al-JGI_158**	N42.48958/ E19.98927	690	sandstone	West Vardar Ophiolite	20	13,89138	2,337	19,911	19,9	52,01	25	7	1,5	MG-1	265±18
3	**Al-JGI_161**	N42.57384/ E20.20514	940	qz-fsp-gneiss	East Bosnian Durmitor	20	14,01109	2,006	17,438	18,67	19,33	21	5	1,5	MG-1	265±18
4	**Al-JGI_162**	N42.56498/ E20.21244	820	gneiss	East Bosnian Durmitor	20	13,96121	2,719	18,115	18,07	44,07	29	7	1,72	MG-1	265±18
5	**Al-JGI_163**	N42.51857/ E20.26402	682	sandstone	West Vardar Ophiolite	20	13,99114	4,697	33,329	33,38	32,4	26	6	1,57	MG-1	265±18
6	**MH-301**	N42.11702/ E19.61246	175	sandstone	Krasta Cukali	16	9,82546	3.970	21.867	26,46	99,27	29	9	1,81	SZ	326±23
7	**SZ13-15**	N42.06928/ E19.71068	212	sandstone	Krasta Cukali	13	9,32990	3.820	24.161	34,07	58,38	24	4	2,43	SZ	326±23
8	**SZ13-29**	N42.07025/ E19.69359	150	sandstone	Krasta Cukali	14	9,13167	3.435	24.471	30,94	97,4	21	6	1,66	SZ	326±23
9	**SZ13-34**	N41.96899/ E19.71925	138	sandstone	West Vardar Ophiolite	9	8,70219	3.398	14.933	21,07	22,5	34	14	2,04	SZ	326±23
10	**SZ13-40**	N42.08323/ E19.56363	78	sandstone	West Vardar Ophiolite	20	10,254	2.611	18.347	224,88	45,51	27	6	1,63	MG-2	331±12
11	**Al-MG_133**	N42.28382/ E19.79555	358	sandstone	High Karst Unit	15	6,80167	1,829	7.212	13,62	5,33	29	7	1,59	MG-2	331±12
12	**Al-MG_119**	N42.11642/ E19.61235	188	sandstone	Krasta Cukali	14	7,0782	3,687	14.587	25,15	59,34	35	9	1,99	MG-2	331±12
13	**Al-JGI_171**	N42.69458/ E20.07684	1105	sands./breccia	East Bosnian D./WVO	19	7,44689	7,369	11,435	19,9	32,51	80	14	2,88	MG-2	331±12
14	**Al-MG_58**	N41.40515/ E20.37890	905	sandstone	Cukali/Okshtunit Unuit	22	7,26255	2,451	14,835	26,17	28,24	21	4	1,94	MG-2	331±12
15	**Al-MG_59**	N41.39656/ E20.37436	822	sandstone	Cukali/Okshtunit Unuit	21	7,81559	1,235	10,292	16,2	23,86	16	4	2,16	MG-2	331±12

Tab. 1: Results of apatite fission track analysis. A digital table format and the radial plots (below) are also available on the enclosed digital data medium in folder: Appendix II/ Tables- Radial Plots.

	Sample number	zircon crystal	Location [Lat./Long.] WGS 84 Geographic	Alt. (m)	Lithology	Tectonic Unit	tetragonal prism width	U (ppm)	Th (ppm)	147Sm (ppm)	[U]e	Th/ 238U	4He (nmol/g)	mass (ug)	Ft	corrected age, Ma	2s analytic err., Ma	central age: IsoplotR, Ma+STDerr	no. crystals
1	**Al-MG_119**	Al-MG_119_z1	N42.11642/ E19.61235	188	sandstone	Krasta-Cukali	81,2	112,5	45,3	0,6	123,1	0,42	56,2	9,20	0,79	106,1	1,4	**94±17.5 Ma**	3
		Al-MG_119_z3	N42.11642/ E19.61235	188	sandstone	Krasta-Cukali	96,2	74,9	37,6	0,1	83,7	0,52	27,3	10,93	0,80	74,9	1,0		
		Al-MG_119_z4	N42.11642/ E19.61235	188	sandstone	Krasta-Cukali	88,7	183,6	76,7	0,6	201,6	0,43	88,0	4,79	0,77	104,5	0,9		
2	**Al-MG_130**	Al-MG_130_z2	N42.24147/ E19.69465	503	sandstone-arenite	Krasta-Cukali	69,4	368,5	245,0	2,2	426,1	0,69	63,1	2,31	0,71	38,6	0,5	**45.8±9.9 Ma**	4
		Al-MG_130_z3	N42.24147/ E19.69465	503	sandstone-arenite	Krasta-Cukali	62,2	384,1	123,2	3,8	413,0	0,33	84,6	1,65	0,68	55,5	0,7		
		Al-MG_130_z4	N42.24147/ E19.69465	503	sandstone-arenite	Krasta-Cukali	80,5	385,7	119,8	1,7	413,9	0,32	92,7	3,97	0,75	54,9	0,5		
		Al-MG_130_z5	N42.24147/ E19.69465	503	sandstone-arenite	Krasta-Cukali	61,1	166,0	223,0	2,0	218,4	1,39	29,7	1,64	0,67	37,3	0,3		
3	**Al-MG_132**	Al-MG_132_z2	N42.09645/ E19.79940	219	sandstone-shale	Krasta-Cukali	60,2	319,7	112,9	0,8	346,3	0,36	61,7	1,98	0,69	47,9	0,5	**44.1±9.4 Ma**	3
		Al-MG_132_z3	N42.09645/ E19.79940	219	sandstone-shale	Krasta-Cukali	62,4	192,5	340,4	1,1	272,5	1,83	53,0	1,92	0,69	52,3	0,6		
		Al-MG_132_z4	N42.09645/ E19.79940	219	sandstone-shale	Krasta-Cukali	60,0	88,8	76,4	0,6	106,8	0,89	13,1	1,41	0,66	34,2	0,6		
4	**Al-MG_134**	Al-MG_134_z1	N42.27673/ E19.79492	468	coarse sandstone	Krasta-Cukali	64,9	89,5	42,0	0,3	99,3	0,48	18,3	2,49	0,71	47,7	0,3	**48.1±0.5 Ma**	2
		Al-MG_134_z5	N42.27673/ E19.79492	468	coarse sandstone	Krasta-Cukali	74,2	107,6	69,8	0,5	124,0	0,67	23,8	3,12	0,73	48,5	0,4		
5	**Al-MG_135**	Al-MG_135_z1	N42.17282/ E19.62861	825	sandstone-arenite	Krasta-Cukali	100,0	89,1	75,0	0,7	106,7	0,87	30,6	6,27	0,79	66,9	0,5	**106.5±46.8 Ma**	4
		Al-MG_135_z3	N42.17282/ E19.62861	825	sandstone-arenite	Krasta-Cukali	65,8	506,6	214,7	2,3	557,0	0,44	205,3	2,94	0,71	94,8	1,5		
		Al-MG_135_z4	N42.17282/ E19.62861	825	sandstone-arenite	Krasta-Cukali	77,7	135,1	159,4	0,8	172,5	1,22	79,3	3,25	0,74	114,3	1,3		
		Al-MG_135_z5	N42.17282/ E19.62861	825	sandstone-arenite	Krasta-Cukali	71,2	95,8	124,3	0,6	125,0	1,34	86,2	2,37	0,71	177,2	1,3		
6	**Al-MG_138**	Al-MG_138_z1	N42.28805/ E19.92656	406	sandstone-shale	Krasta-Cukali	64,9	205,4	177,9	0,6	247,2	0,90	67,0	3,01	0,72	69,6	0,7	**49.7±13.0 Ma**	4
		Al-MG_138_z2	N42.28805/ E19.92656	406	sandstone-shale	Krasta-Cukali	66,1	202,6	124,9	0,6	232,0	0,64	38,3	2,21	0,71	43,2	0,9		
		Al-MG_138_z3	N42.28805/ E19.92656	406	sandstone-shale	Krasta-Cukali	60,6	266,4	48,9	0,3	277,8	0,19	52,9	2,75	0,72	49,1	0,4		
		Al-MG_138_z5	N42.28805/ E19.92656	406	sandstone-shale	Krasta-Cukali	66,2	233,8	126,5	0,3	263,5	0,56	41,1	2,07	0,70	41,3	0,2		
7	**Al-MG_140**	Al-MG_140_z1	N42.29969/ E19.89779	889	sandstone-breccia	Krasta-Cukali	121,8	205,4	20,3	0,1	210,2	0,10	58,3	12,39	0,83	61,7	0,3	**54.0±6.5 Ma**	4
		Al-MG_140_z2	N42.29969/ E19.89779	889	sandstone-breccia	Krasta-Cukali	103,9	126,1	85,6	0,3	146,2	0,70	35,4	8,34	0,81	55,2	0,4		
		Al-MG_140_z3	N42.29969/ E19.89779	889	sandstone-breccia	Krasta-Cukali	62,5	353,3	223,7	1,6	405,9	0,65	70,5	2,60	0,70	45,9	0,6		
		Al-MG_140_z5	N42.29969/ E19.89779	889	sandstone-breccia	Krasta-Cukali	76,9	293,5	250,4	2,4	352,4	0,88	78,5	4,52	0,75	54,5	0,5		
8	**Al-MG_141**	Al-MG_141_z2	N42.27113/ E19.94078	242	coarse sandstone	Krasta-Cukali	71,2	129,2	62,0	0,4	143,8	0,50	27,0	3,98	0,74	46,7	0,6	**57.5±10.4 Ma**	4
		Al-MG_141_z3	N42.27113/ E19.94078	242	coarse sandstone	Krasta-Cukali	80,5	210,3	185,0	0,7	253,7	0,91	60,1	3,69	0,75	58,6	0,7		
		Al-MG_141_z4	N42.27113/ E19.94078	242	coarse sandstone	Krasta-Cukali	60,0	199,2	102,7	0,8	223,3	0,53	63,5	3,73	0,73	71,8	0,7		
		Al-MG_141_z5	N42.27113/ E19.94078	242	coarse sandstone	Krasta-Cukali	65,1	294,0	309,0	1,5	366,6	1,09	75,8	1,90	0,69	55,7	0,4		
9	**Al-MG_142**	Al-MG_142-z1	N42.26481/ E20.00972	186	silt- sandstone	Krasta-Cukali	82,9	247,1	45,2	0,5	257,7	0,19	60,4	6,17	0,78	55,6	0,3	**46.2±6.8 Ma**	5
		Al-MG_142-z2	N42.26481/ E20.00972	186	silt- sandstone	Krasta-Cukali	72,6	159,1	82,3	1,0	178,5	0,53	36,7	3,13	0,73	51,8	0,5		
		Al-MG_142-z3	N42.26481/ E20.00972	186	silt- sandstone	Krasta-Cukali	67,4	216,9	87,9	0,3	237,5	0,42	38,2	3,42	0,74	40,3	0,3		
		Al-MG_142-z4	N42.26481/ E20.00972	186	silt- sandstone	Krasta-Cukali	60,5	288,1	96,3	0,8	310,8	0,35	48,6	2,75	0,71	41,0	0,5		
		Al-MG_142-z5	N42.26481/ E20.00972	186	silt- sandstone	Krasta-Cukali	63,2	300,9	94,7	0,2	323,2	0,33	54,9	2,11	0,71	44,5	0,6		
10	**Al-JGI_171**	Al-JGI_171_z1	N42.69458/ E20.07684	1105	sandstone-breccia	East Bosnian Durmitor	65,0	203,1	238,4	3,8	259,1	1,21	100,7	2,10	0,70	102,4	1,2	**103.4±1.6 Ma**	2
		Al-JGI_171_z3	N42.69458/ E20.07684	1105	sandstone-breccia	East Bosnian Durmitor	105,2	410,2	250,7	2,1	469,1	0,63	217,0	11,15	0,81	104,6	1,4		
11	**SZ13-40**	SZ13-40_z2	N42.08323/ E19.56363	78	sandstone	West Vardar ophiolite	60,5	255,6	151,5	1,0	291,2	0,61	104,0	2,08	0,70	94,2	1,1	**85.2±9.0Ma**	4
		SZ13-40_z3	N42.08323/ E19.56363	78	sandstone	West Vardar ophiolite	60,2	98,9	70,6	0,6	115,5	0,74	34,7	2,67	0,69	79,7	0,7		
		SZ13-40_z4	N42.08323/ E19.56363	78	sandstone	West Vardar ophiolite	66,2	180,6	126,3	1,1	210,3	0,72	61,4	2,44	0,71	76,1	1,1		
		SZ13-40_z5	N42.08323/ E19.56363	78	sandstone	West Vardar ophiolite	62,0	313,4	172,9	0,6	354,1	0,57	128,1	3,05	0,72	92,3	0,6		
12	**SZ13-34**	SZ13-34_z1	N41.96899/ E19.71925	138	sandstone	West Vardar ophiolite	61,2	199,0	96,9	0,3	221,7	0,50	158,7	2,52	0,71	183,4	1,9	**126.4±45.4 Ma**	3
		SZ13-34_z3	N41.96899/ E19.71925	138	sandstone	West Vardar ophiolite	68,0	62,2	90,0	0,6	83,4	1,49	34,0	3,97	0,73	103,1	1,7		
		SZ13-34_z4	N41.96899/ E19.71925	138	sandstone	West Vardar ophiolite	88,4	58,0	51,3	0,1	70,1	0,91	31,7	5,89	0,78	106,8	0,9		
13	**Al-JGI_163**	Al-JGI_163_z1	N42.51857/ E20.26402	682	sandstone	West Vardar ophiolite	71,8	332,6	196,7	0,8	378,8	0,61	206,7	3,94	0,74	134,3	1,1	**106.7±18.8 Ma**	4
		Al-JGI_163_z3	N42.51857/ E20.26402	682	sandstone	West Vardar ophiolite	91,0	409,3	332,0	1,4	487,3	0,84	213,0	4,98	0,77	104,2	0,9		
		Al-JGI_163_z4	N42.51857/ E20.26402	682	sandstone	West Vardar ophiolite	80,8	568,4	315,1	1,1	642,4	0,57	237,3	4,27	0,76	89,7	0,7		
		Al-JGI_163_z5	N42.51857/ E20.26402	682	sandstone	West Vardar ophiolite	76,0	385,3	287,2	0,3	452,8	0,77	189,4	3,96	0,74	103,5	1,1		
14	**Al-JGI_158**	Al-JGI_158_z1	N42.48958/ E19.98927	690	sandstone	West Vardar ophiolite	85,7	282,0	346,0	0,4	363,3	1,27	68,3	4,56	0,76	45,7	0,3	**44.3±2.7 Ma**	5
		Al-JGI_158_z2	N42.48958/ E19.98927	690	sandstone	West Vardar ophiolite	97,6	349,8	154,6	0,4	386,1	0,46	78,8	10,20	0,81	46,5	0,5		
		Al-JGI_158_z3	N42.48958/ E19.98927	690	sandstone	West Vardar ophiolite	81,9	279,0	332,1	0,9	357,1	1,23	59,6	3,01	0,74	41,9	0,3		
		Al-JGI_158_z4	N42.48958/ E19.98927	690	sandstone	West Vardar ophiolite	100,8	280,2	402,3	0,9	374,7	1,48	74,4	5,83	0,78	46,8	0,3		
		Al-JGI_158_z5	N42.48958/ E19.98927	690	sandstone	West Vardar ophiolite	90,1	456,8	275,6	0,7	521,6	0,62	89,3	4,84	0,77	41,1	0,3		
15	**Al-JGI_162**	Al-JGI_162_z1	N42.56498/ E20.21244	820	gneiss	East Bosnian Durmitor	68,2	266,7	71,1	0,1	283,4	0,28	55,2	2,71	0,72	50,2	0,8	**46.6±4.7 Ma**	5
		Al-JGI_162_z2	N42.56498/ E20.21244	820	gneiss	East Bosnian Durmitor	60,0	218,3	47,7	0,6	229,5	0,23	39,4	2,09	0,69	46,2	0,6		
		Al-JGI_162_z3	N42.56498/ E20.21244	820	gneiss	East Bosnian Durmitor	68,0	174,5	186,3	0,6	218,3	1,10	45,5	3,52	0,73	52,6	0,3		
		Al-JGI_162_z4	N42.56498/ E20.21244	820	gneiss	East Bosnian Durmitor	78,8	84,1	47,9	0,3	95,4	0,59	17,3	4,98	0,76	44,1	0,6		
		Al-JGI_162_z5	N42.56498/ E20.21244	820	gneiss	East Bosnian Durmitor	93,0	108,0	19,9	0,2	112,7	0,19	19,5	5,77	0,78	40,7	0,4		
16	**Al-JGI_161**	Al-JGI_161_z1	N42.57384/ E20.20514	940	qz-fsp-gneiss	East Bosnian Durmitor	86,1	60,5	26,4	0,2	66,7	0,45	13,0	5,12	0,77	47,0	0,4	**43.2±3.3 Ma**	4
		Al-JGI_161_z2	N42.57384/ E20.20514	940	qz-fsp-gneiss	East Bosnian Durmitor	60,3	173,8	158,4	1,1	211,0	0,94	34,5	2,05	0,68	44,3	0,4		
		Al-JGI_161_z4	N42.57384/ E20.20514	940	qz-fsp-gneiss	East Bosnian Durmitor	63,1	139,3	170,9	0,7	179,5	1,27	30,0	3,04	0,70	43,9	0,3		
		Al-JGI_161_z5	N42.57384/ E20.20514	940	qz-fsp-gneiss	East Bosnian Durmitor	93,7	134,8	75,1	0,7	152,5	0,58	24,6	6,22	0,78	38,1	0,2		
17	**Al-JGI_130**	Al-JGI_130_z1	N42.48985/ E19.98927	1940	granitic gneiss	East Bosnian Durmitor	83,6	159,5	62,7	0,5	174,2	0,41	39,1	5,91	0,78	53,4	0,7	**48.0±5.5 Ma**	4
		Al-JGI_130_z2	N42.48985/ E19.98927	1940	granitic gneiss	East Bosnian Durmitor	87,5	208,1	41,5	0,1	217,9	0,21	48,4	5,82	0,78	52,7	0,6		
		Al-JGI_130_z4	N42.48985/ E19.98927	1940	granitic gneiss	East Bosnian Durmitor	83,2	276,0	102,4	0,4	300,0	0,38	54,0	4,80	0,76	43,5	0,5		
		Al-JGI_130_z5	N42.48985/ E19.98927	1940	granitic gneiss	East Bosnian Durmitor	72,3	153,1	92,6	0,6	174,9	0,62	30,1	3,35	0,73	43,4	0,5		

Tab. 2: Results of (U/Th) He analysis in zircon. All zircon crystals have two terminations. A digital table format and the radial plots are available on the enclosed digital data medium in folder: Appendix II/ Tables- Radial plots. Radial plots on digital data medium were created with IsoplotR (Vermeesch 2018).

Apatite	Sample number	Num. gr.	Roh D x10^5 cm^-2	Roh S x10^5 cm^-2	Roh I x10^5 cm^-2	P (X^2)[%]	Central (Ma)	Error (2σ)	Observer	ζ (1 σ err)
1	**Al-JGI_130**	20	4,943	0,596	0,383	0,28	67,8	6,3	HP	178±6
2	**MH-301**	13	4,890	1,106	0,236	0,00	177,3	75,0	HP	178±6
3	**SZ13-34**	10	4,922	1,238	0,247	0,70	215,3	52,0	HP	178±6
4	**SZ13-40**	12	4,862	1,177	0,298	0,00	160,1	34,2	HP	178±6
5	**Al-MG_59**	13	4,924	1,183	0,328	0,00	153,8	29,1	HP	178±6
6	**Al-MG_58**	16	4,867	1,108	0,339	0,00	138,4	18,76	HP	178±6
7	**Al-MG_132**	16	4,871	1,034	0,447	0,00	98,8	19,1	HP	178±6
8	**Al-MG_130**	19	4,887	1,255	0,186	0,23	283,8	50,3	HP	178±6
9	**Al-MG_139**	20	4,876	1,382	0,212	42,30	276,4	30,8	HP	178±6
10	**Al-MG_161**	21	4,857	0,390	0,229	0,99	72,7	10,8	HP	178±6
11	**Al-JGI_158**	23	4,915	1,366	0,493	0,00	108,2	12,6	HP	178±6
12	**Al-MG_162**	24	4,906	0,449	0,264	0,18	71,8	8,4	HP	178±6

Tab. 3: Results of zircon fission track analysis. A digital table format and the radial plots (below) are also available on the enclosed digital data medium in folder: Appendix II/ Tables- Radial plots.

No.	sample name	No of spectra	Location [Lat./Long.] WGS 84 Geographic	Elevation (m asl.)	lithology	Tectonic nappe	t in °C		t error		
1	**Al-MG_119**	25	N42.11642/ E19.61235	188	sandstone	Budva-Krasta-Cukali	**183**	±	17	°	C
2	**Al-MG_60**	24	N41.39382/ E20.37427	851	shale	Okshtunit Window	**193**	±	13	°	C
3	**Al-MG_59-1**	26	N41.39677/ E20.37456	822	shale	Okshtunit Window	**195**	±	9	°	C
4	**MH-301**	28	N42.11702/ E19.61246	175	sandstone	Budva-Krasta-Cukali	**197**	±	18	°	C
5	**Al-MG_61**	28	N41.38589/ E20.38323	890	silt-shale	Okshtunit Window	**199**	±	14	°	C
6	**Al-MG_58-1**	28	N41.40511/ E20.37890	905	dark shale	Okshtunit Window	**204**	±	15	°	C
7	**SZ13-15**	20	N42.06928/ E19.71068	212	sandstone	Budva-Krasta-Cukali	**208**	±	21	°	C
8	**Al-MG_135**	29	N42.17282/ E19.62861	825	arenite/sandstone	Budva-Krasta-Cukali	**222**	±	11	°	C
9	**Al-MG_129**	23	N42.23398/ E19.70287	405	arenite/sandstone	Budva-Krasta-Cukali	**226**	±	16	°	C
10	**SZ13-29**	24	N42.07025/ E19.69359	150	sandstone	Budva-Krasta-Cukali	**230**	±	24	°	C
11	**Al-MG_130**	25	N42.24147/ E19.69465	503	fine sandstone/shale	Budva-Krasta-Cukali	**231**	±	6	°	C
12	**Al-MG_142**	24	N42.26481/ E20.00972	186	arenite/sandstone	Budva-Krasta-Cukali	**232**	±	6	°	C
13	**Al-MG_131**	28	N42.24579/ E19.69814	685	arenite/sandstone	Budva-Krasta-Cukali	**233**	±	7	°	C
14	**Al-MG_132**	28	N42.09645/ E19.79940	219	sandstone/shale	Budva-Krasta-Cukali	**237**	±	10	°	C
15	**LC-K-39**	29	N42.78524/ E20.42936	730	marble/fine schist	West Vardar Ophiolite	**238**	±	6	°	C
16	**LC-K-47**	27	N42.78809/ E20.48317	520	radiolarite	West Vardar Ophiolite	**240**	±	4	°	C
17	**Al-MG_141**	30	N42.27113/ E19.94078	242	coarse sandstone/conglomerate	Budva-Krasta-Cukali	**257**	±	5	°	C
18	**Al-MG_133**	30	N42.28382/ E19.79555	358	arenite/sandstone	High Karst	**266**	±	8	°	C
19	**Al-MG_140**	30	N42.29969/ E19.89779	889	conglomerate	High Karst	**267**	±	10	°	C
20	**Al-MG_134**	30	N42.27673/ E19.79492	468	coarse sandstone	High Karst	**269**	±	3	°	C
21	**Al-MG_164**	28	N42.82652/ E20.60570	728	siliciclastic sandstone	West Vardar Ophiolite	**271**	±	8	°	C
22	**MG-K-164**	30	N42.82652/ E20.60570	728	siliciclastic sandstone	West Vardar Ophiolite	**278**	±	5	°	C
23	**Al-MG_138**	29	N42.28805/ E19.92656	406	fine sandstone/shale	Budva-Krasta-Cukali	**281**	±	9	°	C
24	**AB17-4-c-p**	15	N42.44412/ E20.15902	1080	calc-mylonite	High Karst	**319**	±	5	°	C
25	**Al-MG_194**	13	N42.54007/ E20.24484	825	mylonitic marble	East Bosnian-Durmitor	**324**	±	8	°	C
26	**Al-MG_195**	28	N42.54056/ E20.24405	874	marble/fine schist	East Bosnian-Durmitor	**324**	±	4	°	C
27	**Al-MG_196**	28	N42.54048/ E20.24676	852	greenschist	West Vardar Ophiolite	**337**	±	11	°	C
28	**Al-JGI_162**	26	N42.56498/ E20.21244	820	orthogneiss	East Bosnian-Durmitor	**406**	±	12	°	C
29	**Al-MG_231**	24	N42.55795/ E20.22843	775	silvery-green white mica schist	East Bosnian-Durmitor	**418**	±	17	°	C
30	**Al-MG_234**	27	N42.60988/ E20.18817	1598	orthogneiss	East Bosnian-Durmitor	**458**	±	12	°	C

Tab. 4: Results RSCM peak temperature analysis. A digital table format and Raman temperature results (below) are also available on the enclosed digital data medium in folder: Appendix II/ Tables-RSCM data.

Radial Plots -Zircon fission track data -radial plots- created with RadialPlotter 9.5 (Vermeesch 2009)

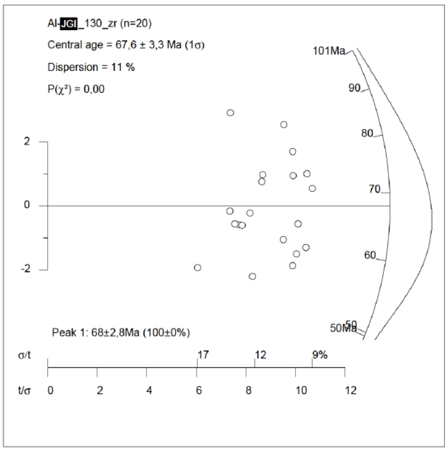

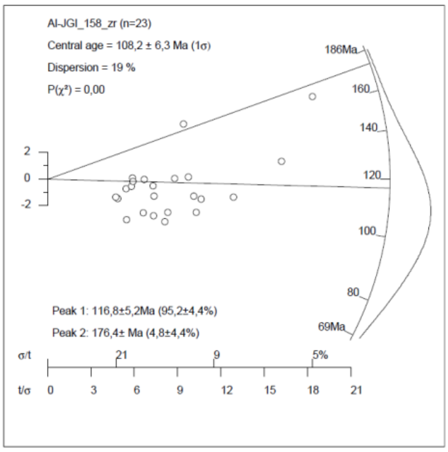

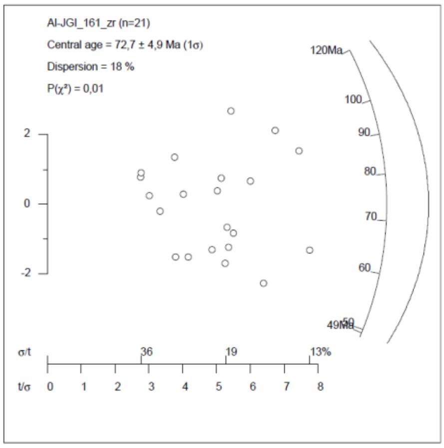

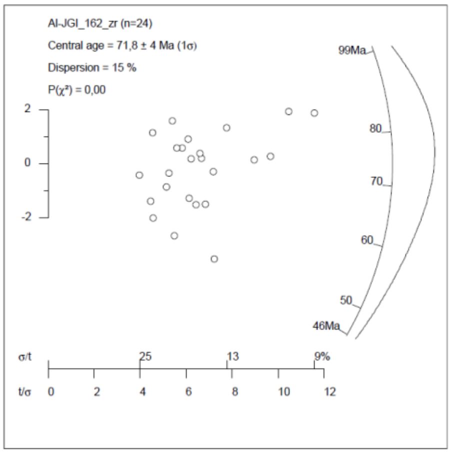

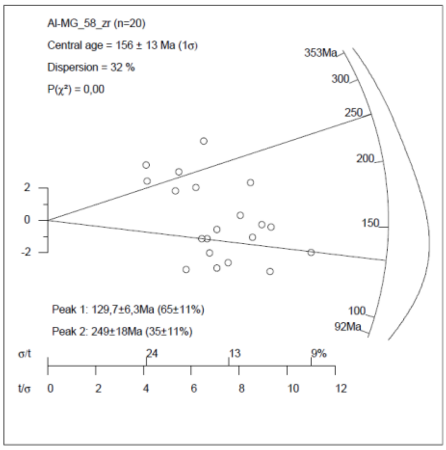

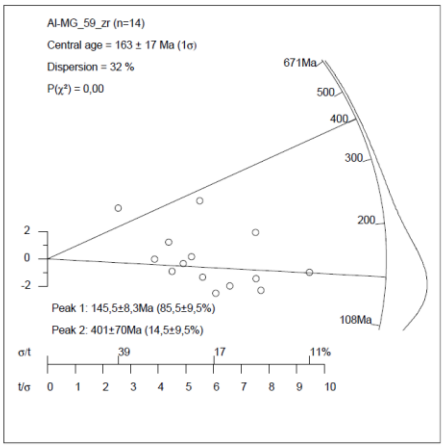

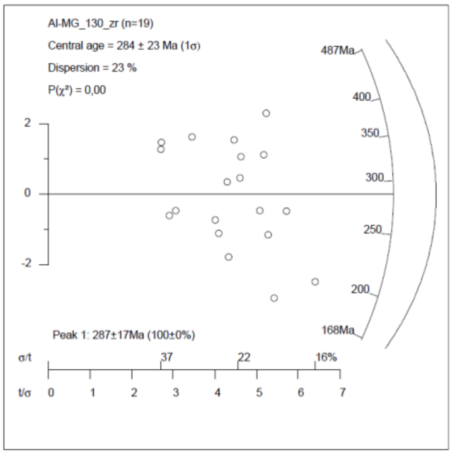

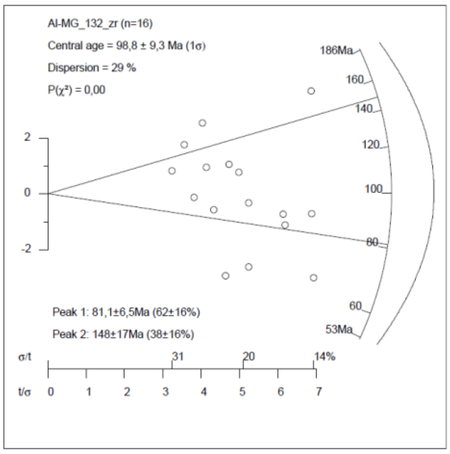

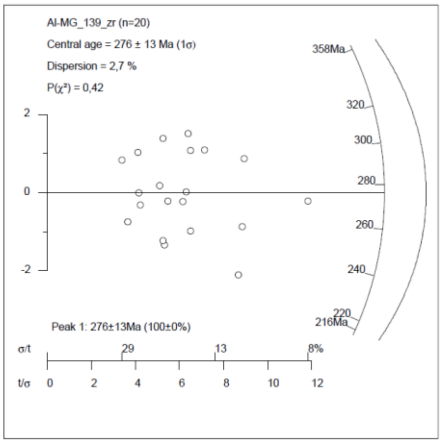

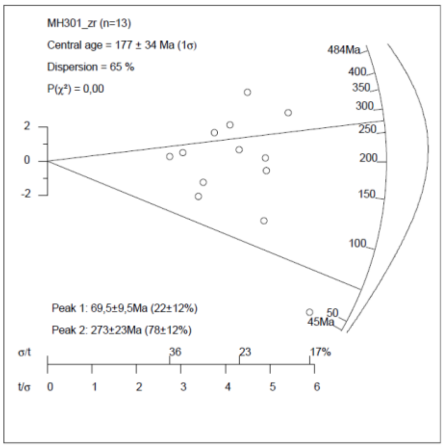

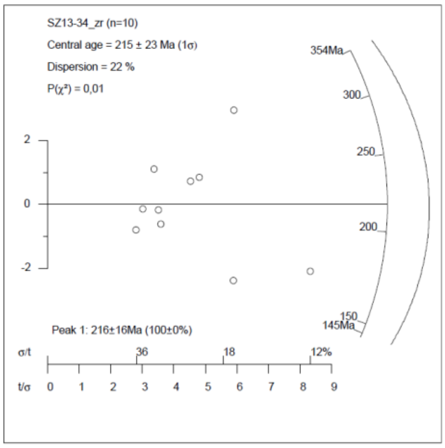

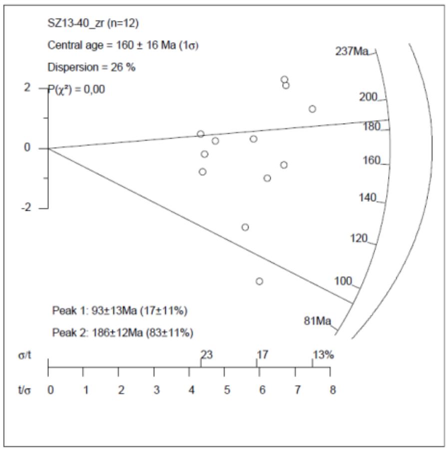

Radial Plots -Apatite fission track data -radial plots- created with RadialPlotter 9.5 (Vermeesch 2009)

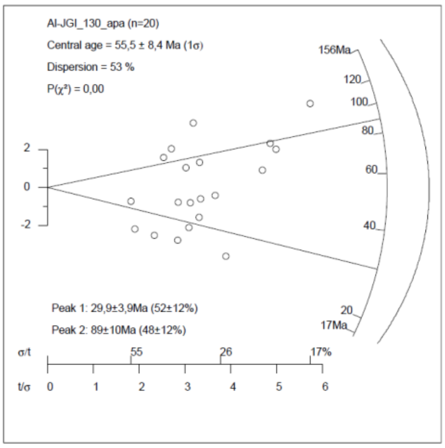

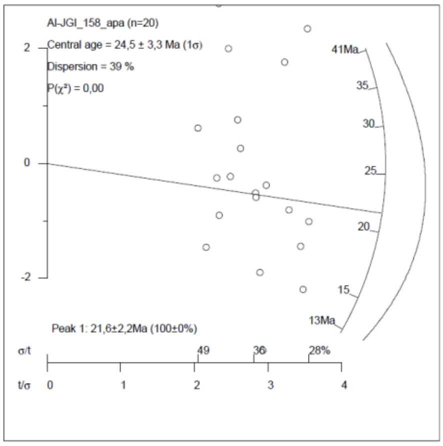

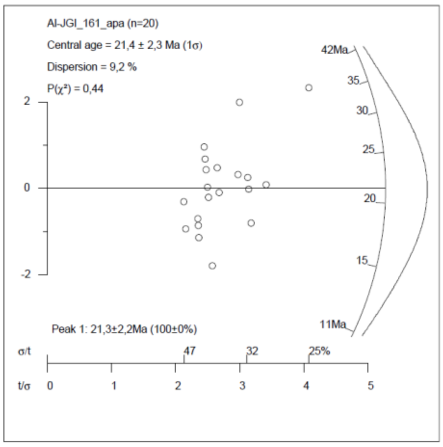

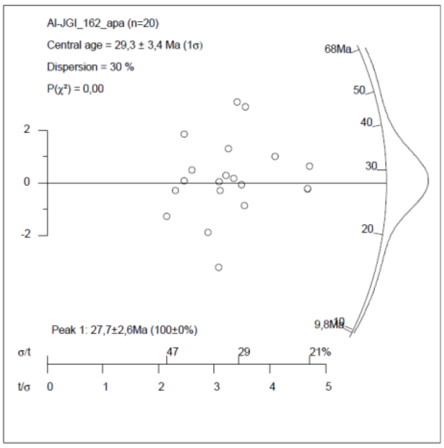

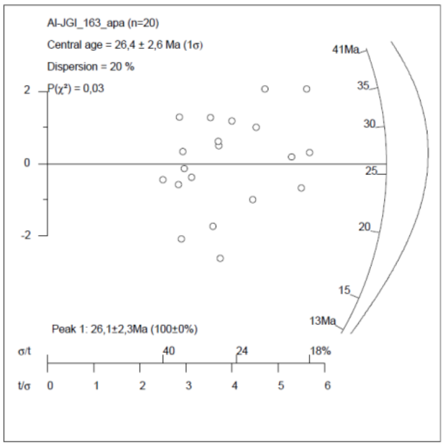

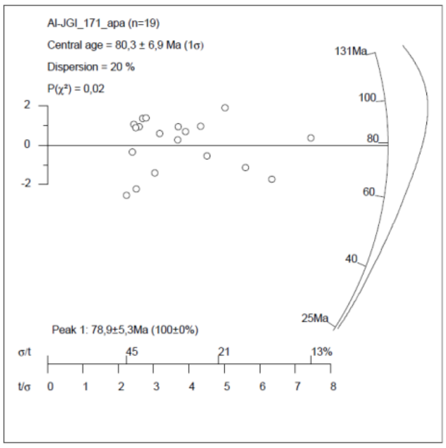

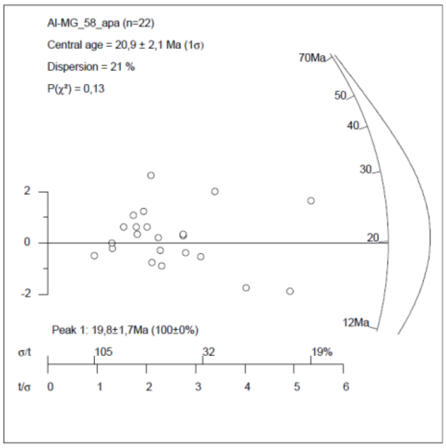

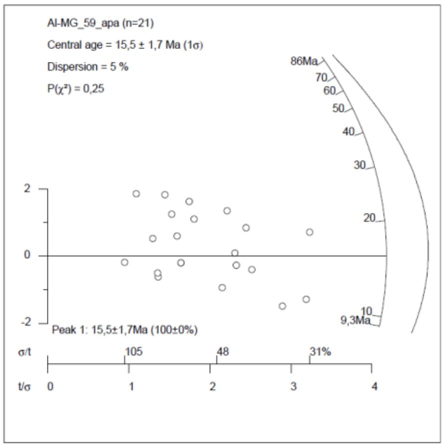

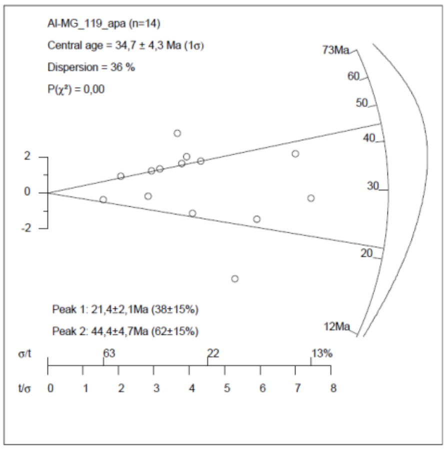

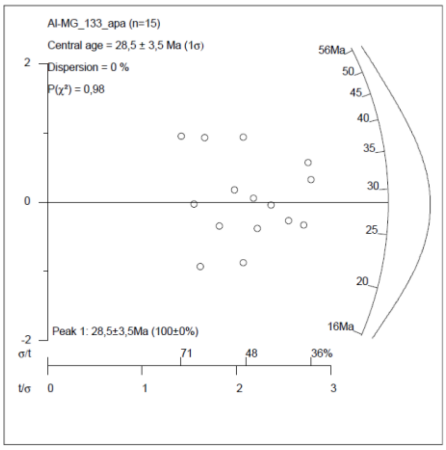

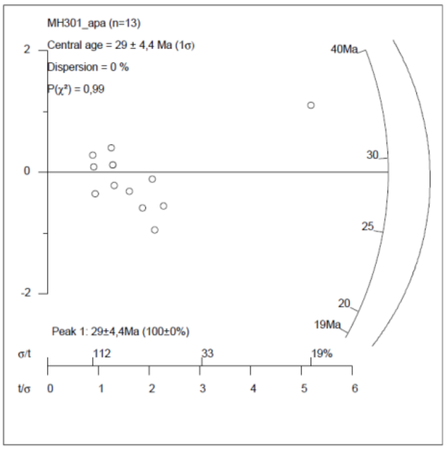

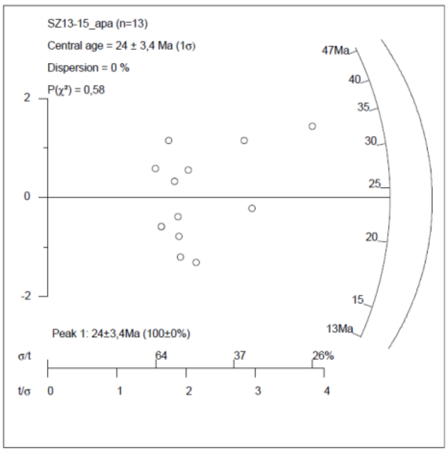

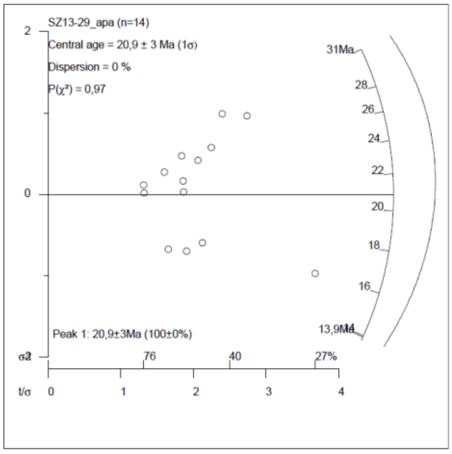

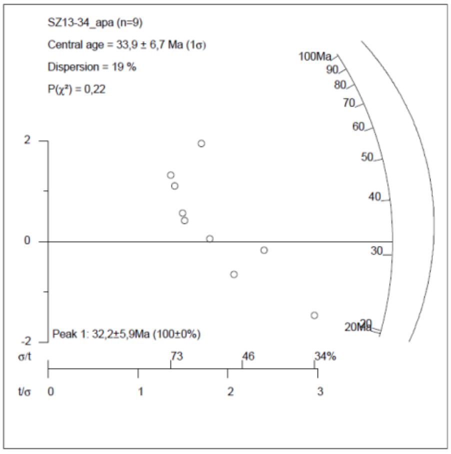

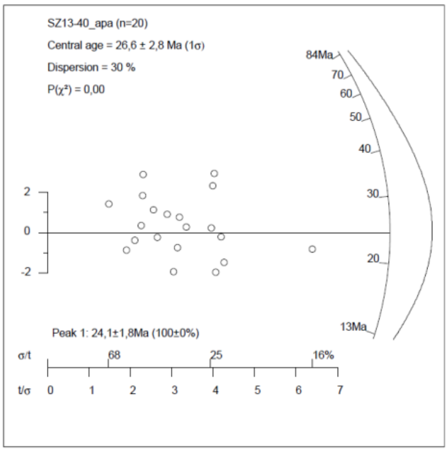

RSCM temperature spectra results and kernel density estimate (KDE) – available in digital format in the enclosed digital data medium in folder: Appendix II/RSCM data

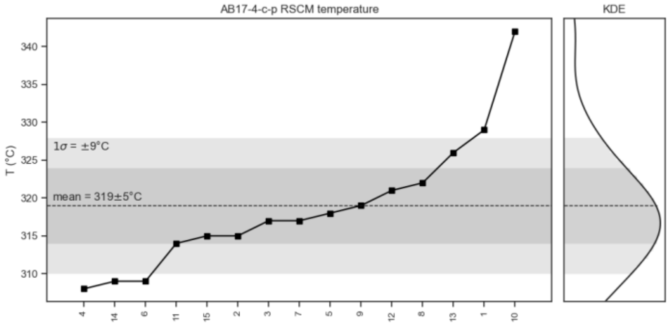

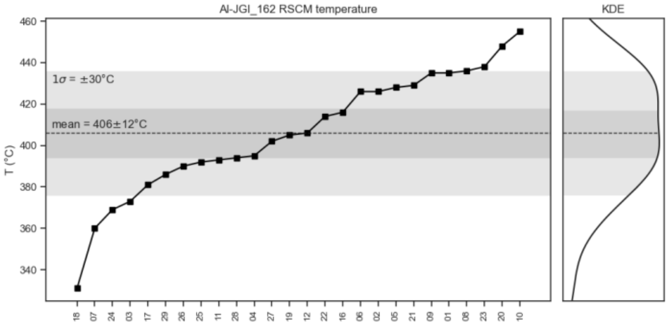

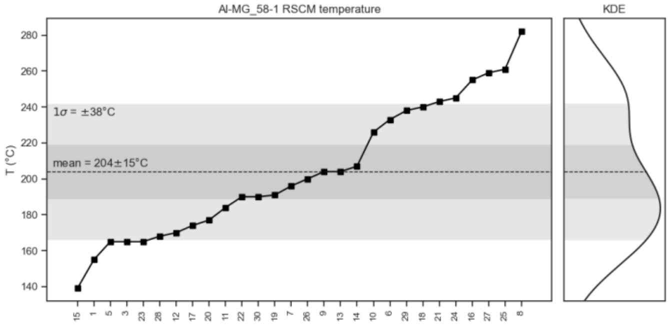

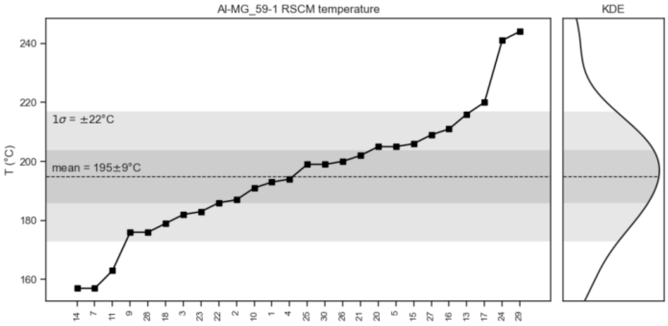

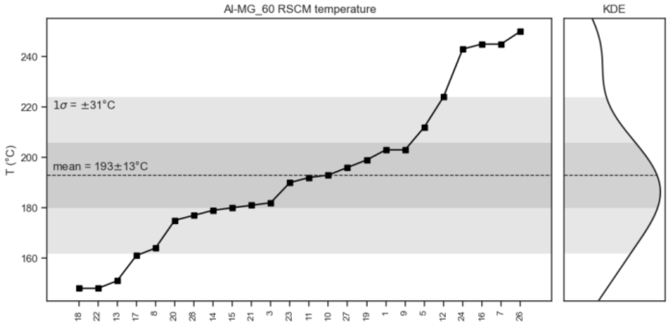

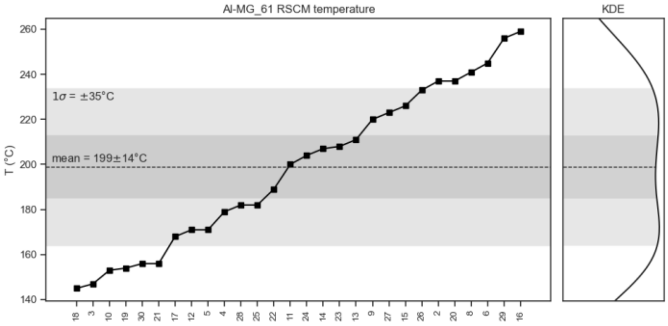

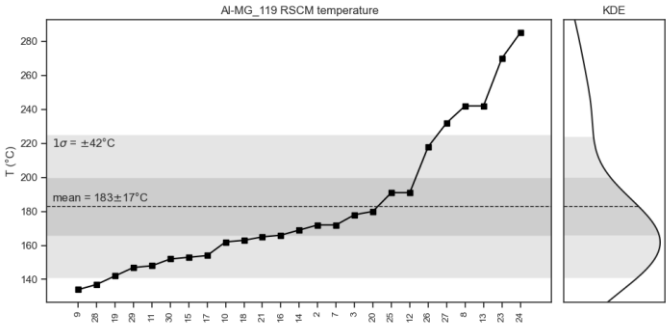
AI-MG_119 RSCM temperature
KDE
T (°C)
1σ = ±42°C
mean = 183±17°C
140
160
180
200
220
240
260
280

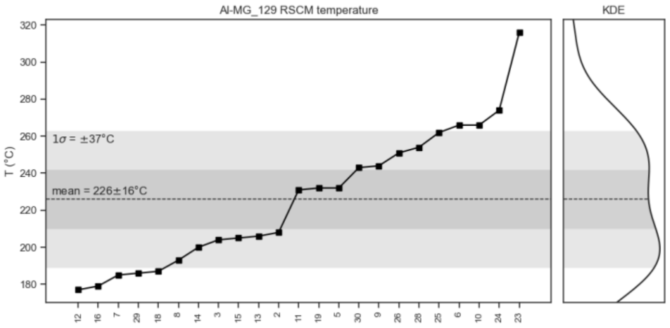
AI-MG_129 RSCM temperature
KDE
T (°C)
1σ = ±37°C
mean = 226±16°C
180
200
220
240
260
280
300
320

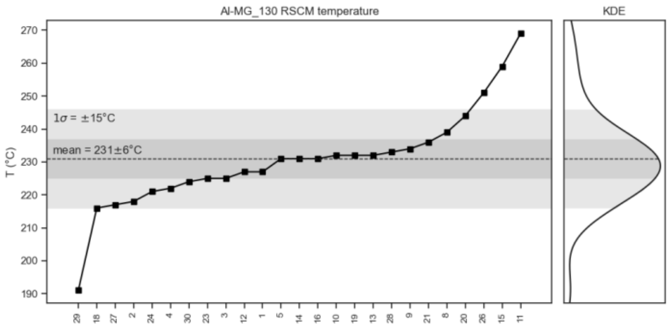
AI-MG_130 RSCM temperature
KDE
T (°C)
1σ = ±15°C
mean = 231±6°C
190
200
210
220
230
240
250
260
270

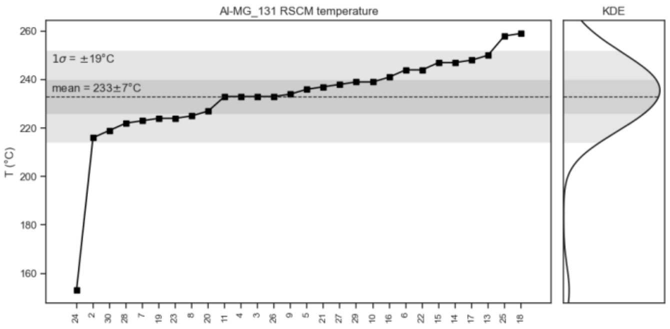
AI-MG_131 RSCM temperature
KDE
T (°C)
1σ = ±19°C
mean = 233±7°C
160
180
200
220
240
260

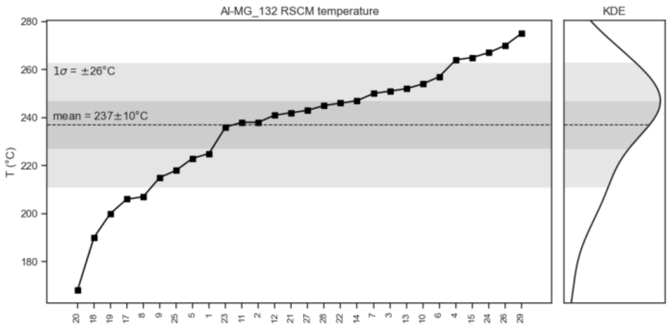
AI-MG_132 RSCM temperature
KDE
T (°C)
1σ = ±26°C
mean = 237±10°C
180
200
220
240
260
280

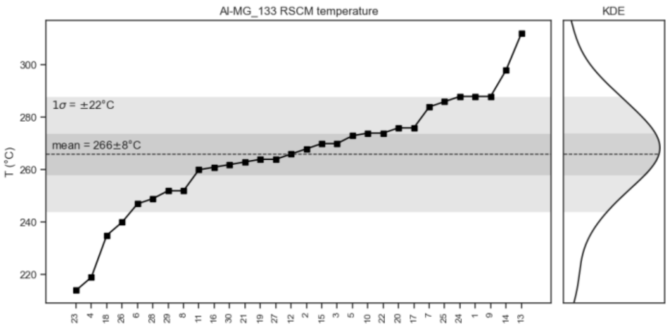
AI-MG_133 RSCM temperature
KDE
T (°C)
1σ = ±22°C
mean = 266±8°C
220
240
260
280
300

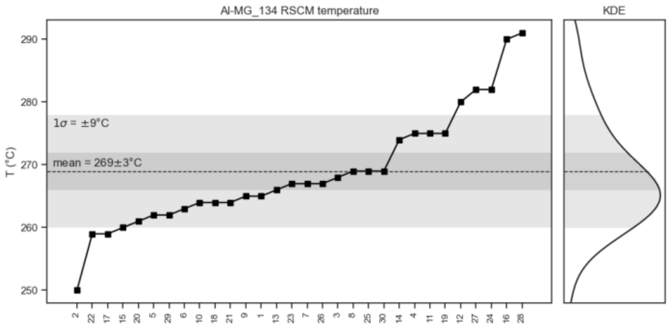
AI-MG_134 RSCM temperature
KDE
T (°C)
1σ = ±9°C
mean = 269±3°C
250
260
270
280
290

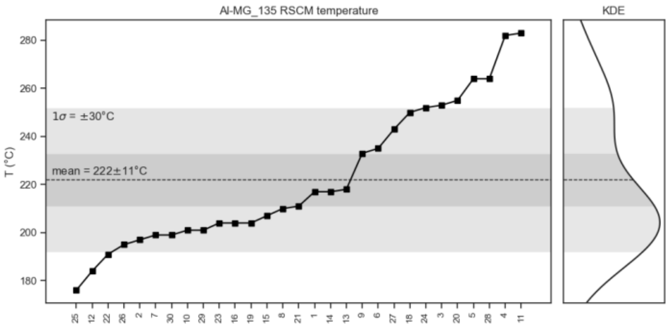
AI-MG_135 RSCM temperature
KDE
T (°C)
1σ = ±30°C
mean = 222±11°C
180
200
220
240
260
280

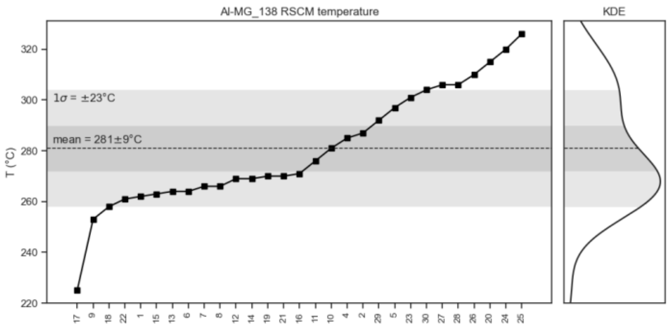
AI-MG_138 RSCM temperature
KDE
T (°C)
1σ = ±23°C
mean = 281±9°C
220
240
260
280
300
320

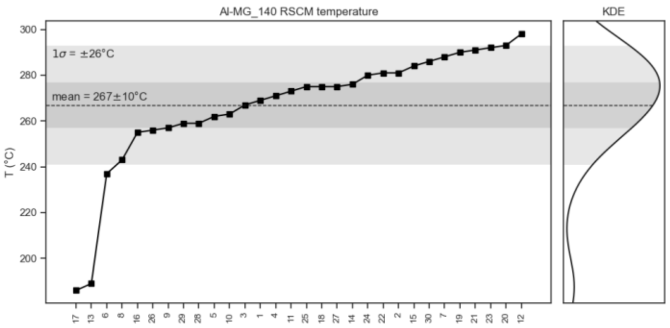
AI-MG_140 RSCM temperature
KDE
T (°C)
1σ = ±26°C
mean = 267±10°C
200
220
240
260
280
300

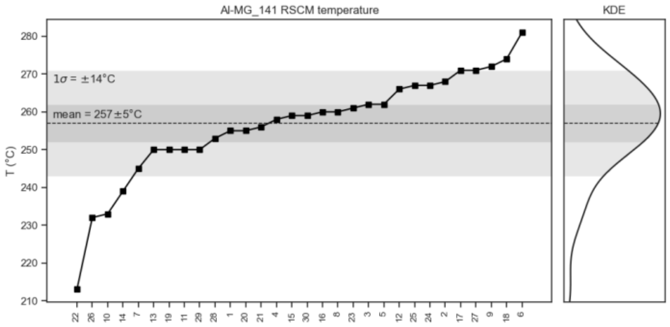
Al-MG_141 RSCM temperature
KDE
1σ = ±14°C
mean = 257±5°C
T (°C)
210
220
230
240
250
260
270
280

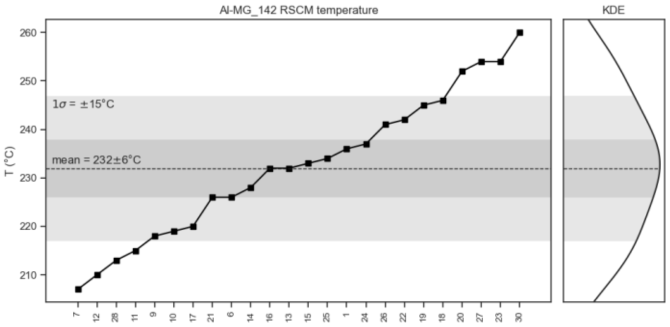
Al-MG_142 RSCM temperature
KDE
1σ = ±15°C
mean = 232±6°C
T (°C)
210
220
230
240
250
260

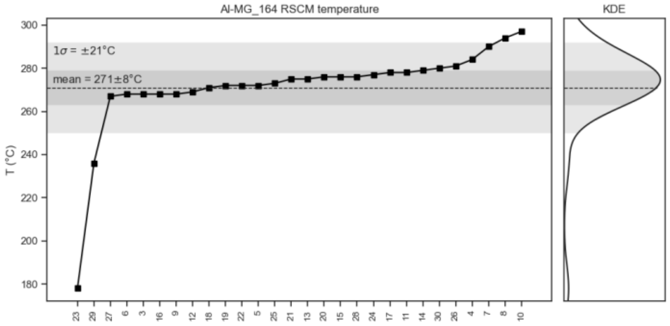
Al-MG_164 RSCM temperature
KDE
1σ = ±21°C
mean = 271±8°C
T (°C)
180
200
220
240
260
280
300

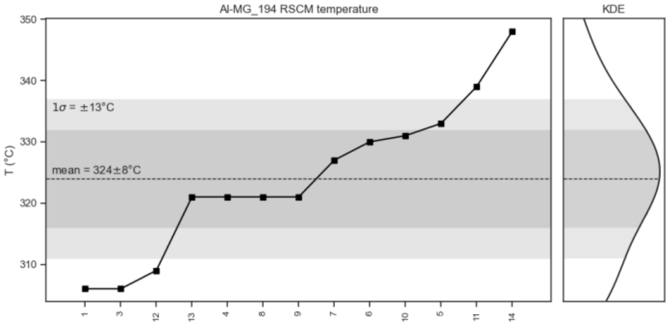
Al-MG_194 RSCM temperature
KDE
1σ = ±13°C
mean = 324±8°C
T (°C)
310
320
330
340
350

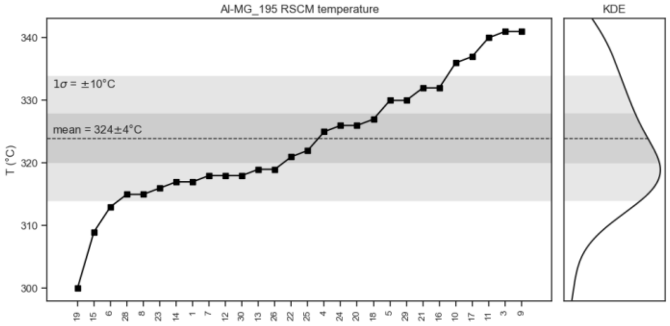
Al-MG_195 RSCM temperature
KDE
1σ = ±10°C
mean = 324±4°C
T (°C)
300
310
320
330
340

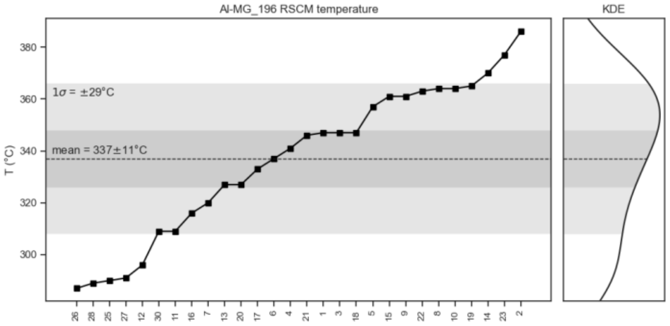
Al-MG_196 RSCM temperature
KDE
1σ = ±29°C
mean = 337±11°C
T (°C)
300
320
340
360
380

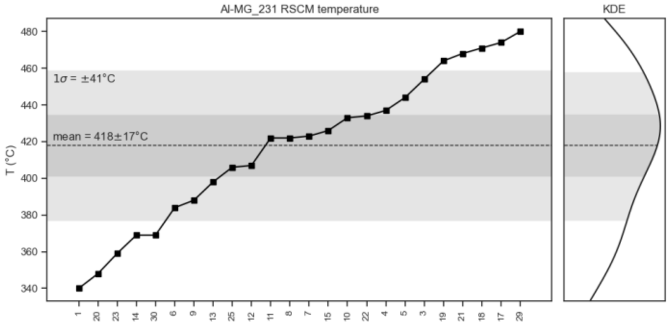
Al-MG_231 RSCM temperature
KDE
1σ = ±41°C
mean = 418±17°C
T (°C)
340
360
380
400
420
440
460
480

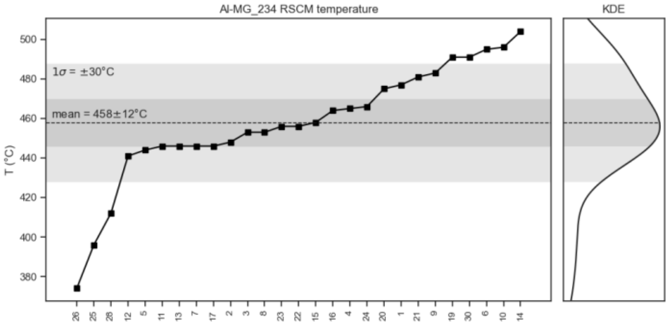
Al-MG_234 RSCM temperature
KDE
1σ = ±30°C
mean = 458±12°C
T (°C)
380
400
420
440
460
480
500

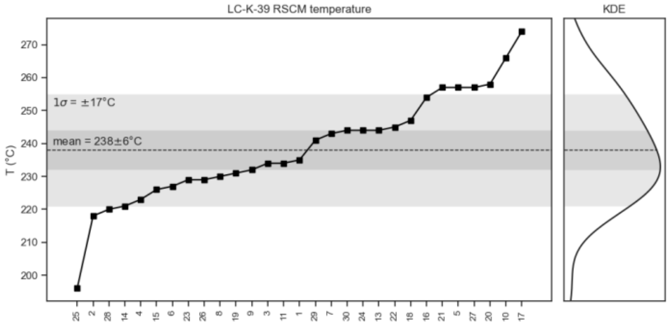
LC-K-39 RSCM temperature
KDE
1σ = ±17°C
mean = 238±6°C
T (°C)
200
210
220
230
240
250
260
270

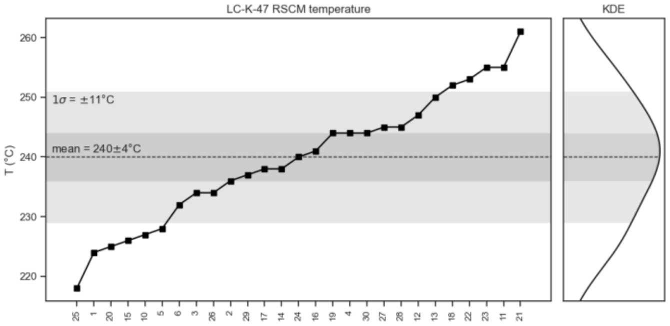
LC-K-47 RSCM temperature
KDE
1σ = ±11°C
mean = 240±4°C
T (°C)
220
230
240
250
260

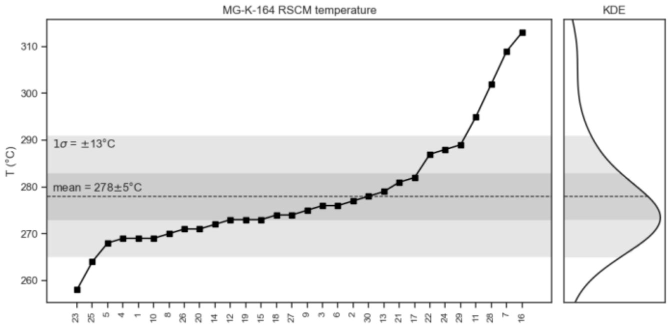

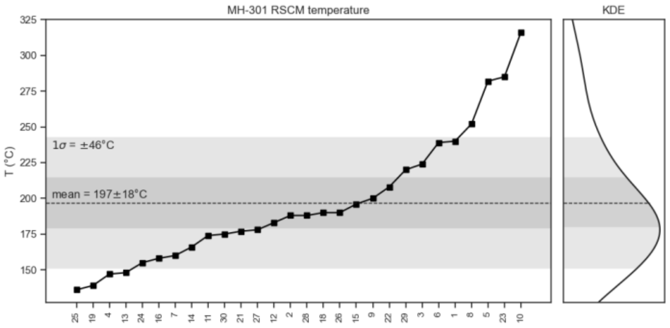

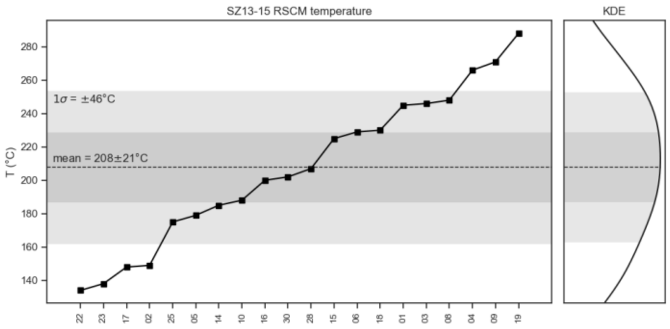

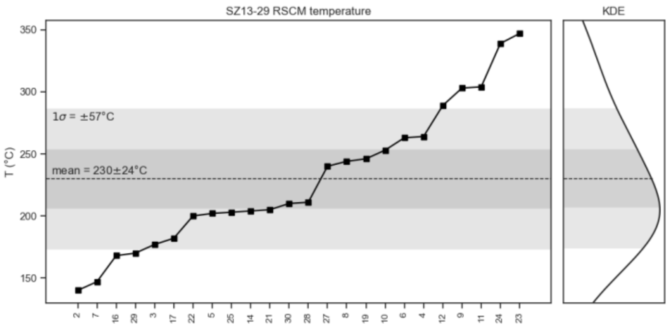

IFORS software configuration file (Lünsdorf et al. 2017) – a digital version is available in the enclosed digital data medium in folder: Appendix II/IFORS software/config_kosovo_v20220322.cfg

```
[Control]
start_wn = 800
stop_wn = 1900
seed = 0
repetitions = 1
plotting = yes
Gui = no
Cli = yes
smoothing = no
smooth_win_size = 11
shuffle_peak_pos = no

[Constraints]
min_width = 1
max_width = 60
min_dist = 5
baseline_mode = window_filter
polynom_order = 3
window_size = 0.5
alpha = 0.985
sigma_threshold = 0.01
noise_intensity = 2
max_peak_number = 100

[Readout_type]
Cm_readout = yes
Peak_parameters = no
Fitted_values = no

[Readout_opts]
mineral_phases = yes
plot_results = yes
print_mode = block
STA_range_start = 1000
STA_range_stop = 1800
```

```
[Ignored_peak_ranges]
cc_idx = 1080, 1093
cc_idx2 = 1070, 1080
cc_idx3 = 1435, 1445
cc_idx4 = 1744, 1760
dol_idx = 1093, 1100
plag_idx = 1095,1110
plag_idx2 = 1110, 1118
qz_idx = 460, 470
qz_idx2 = 1158, 1164
qz_idx3 = 1060, 1066
lower = 700, 1100
upper = 1700, 2000

[Estimate_temp]
p1 = 0.95
p2 = 0.9
model = cubic
plot = no
```

Appendix III

This appendix refers to Chapter IV: “Response of drainage pattern and basin evolution to tectonic and climatic changes along the Dinarides-Hellenides orogen”. Appendix III is also digital available on the enclosed digital data medium.

Cosmogenic Radio Nuclides

Sample Acquisition

For the depth-profile method to be successful, it is essential to use an artificial outcrop, such as a road-cut or an excavation-pit, to reduce the time of sidewise radiation to a negligible amount of a few decades or less (Hidy et al. 2010; Claude et al. 2019). Accordingly, two anthropogenic outcrops were chosen as target profiles. We collected depth profile samples at two different sampling sites on terrace levels T1 and T2, located at 283 m a.s.l. and 12 m above present-day river level, and 286 m a.s.l and 56 m, respectively. Profile TP-N was collected on the lower level T1 at an anthropogenic outcrop, most likely produced during a bridge across the Valbona River in the last century. The outcrop consists of well-rounded fluvial material from boulder to medium-sized pebbles with only minor calcitic cement between the grains resulting in an open-framework structure. A total of six samples from depths between 50 and 225 cm were collected. Each sample consists of ~350-500 g of 1 cm-sized pebbles, which sums up to 250-500 pebbles per sample. All samples were picked and mixed, integrating over a thickness of 10 cm (+/- 5 cm from the given depth) except for the sample in 80 cm depth, which contains pebbles from 15 cm of the profile (7.5 cm +/- the depth).

While sampling, only intact and well-rounded pebbles were taken to ensure a comparable transport and deposition history. The sediment was weakly consolidated, so blocks were broken out and then divided into individual pebbles using a small hammer. Broken and angular clasts could be part of much larger blocks with different histories or be part of slope talus from the nearby mountains rather than fluvial sediment.

Profile TP-S was collected in a freshly dug construction pit on terrace-level T2. The profile consists of seven sand matrix samples from a weakly consolidated sequence of the grey conglomerate. The outcrop's highest parts are covered with the red clay-rich lithology, and the entire profile is stained red. Seven samples containing around 1 kg of matrix material were collected from depths until 225 cm. As in profile TP-N, depth sections of 10 cm were sampled.

Table 1: Sample list for profiles TP-N and TP-S

Sample ID	Terrace Level	Grainsize	Weight
TP-N-50	1	Pebbles	347 g
TP-N-80	1	Pebbles	375 g
TP-N-105	1	Pebbles	350 g
TP-N-135	1	Pebbles	471 g
TP-N-180	1	Pebbles	502 g
TP-N-225	1	Pebbles	549 g
TP-S-40	2	Sand	1667 g
TP-S-70	2	Sand	1410 g
TP-S-90	2	Sand	758 g
TP-S-115	2	Sand	638 g
TP-S-145	2	Sand	813 g
TP-S-175	2	Sand	559 g
TP-S-225	2	Sand	852 g

Tab. S1/Appendix III: Sample list for profiles TB-N and TP-S

For the depth-profile method to be successful, it is essential to use an artificial outcrop, such as a road-cut or an excavation-pit, to reduce the time of sidewise radiation to a negligible amount of a few decades or less (Hidy et al. 2010; Claude et al. 2019). Accordingly, two anthropogenic outcrops were chosen as target profiles. We collected depth profile samples at two different sampling sites on terrace levels T1 and T2, located at 283 m a.s.l. and 12 m above present-day river level, and 286 m a.s.l and 56 m, respectively. Profile TP-N was collected on the lower level T1 at an anthropogenic outcrop, most likely produced during a bridge across the Valbona River in the last century. The outcrop consists of well-rounded fluvial material from boulder to medium-sized pebbles with only minor calcitic cement between the grains resulting in an open-framework structure. A total of six samples from depths between 50 and 225 cm were collected. Each sample consists of ~350-500 g of 1 cm-sized pebbles, which sums up to 250-500 pebbles per sample. All samples were picked and mixed, integrating over a thickness of 10 cm (+/- 5 cm from the given depth) except for the sample in 80 cm depth, which contains pebbles from 15 cm of the profile (7.5 cm +/- the depth).

While sampling, only intact and well-rounded pebbles were taken to ensure a comparable transport and deposition history. The sediment was weakly consolidated, so blocks were broken out and then divided into individual pebbles using a small hammer. Broken and angular clasts could be part of much larger blocks with different histories or be part of slope talus from the nearby mountains rather than fluvial sediment. Profile TP-S was collected in a freshly dug construction pit on terrace-level T2. The profile consists of seven sand matrix samples from a weakly consolidated sequence of the grey conglomerate. The outcrop's highest parts are covered with the red clay-rich lithology, and the entire profile is stained red. Seven samples containing around 1 kg of matrix material were collected from depths until 225 cm. As in profile TP-N, depth sections of 10 cm were sampled.

Sample Preparation at FU-Berlin

The sand fraction collected from TP-S was wet sieved to the grain size fraction between 250 and 500 μm. The pebbles from profile TP-N were leached for three days in 0.3 M HN03 to remove any secondary precipitated carbonates and matrix carbonate remnants. This is important, as meteoric ^{36}Cl could be incorporated into these secondary carbonates. After leaching, the pebbles were crushed in a jaw crusher and then sieved to the same size fraction, 250 to 500 μm. After sample preparation the same aliquots of samples were prepared and analyzed for main and trace elements composition and for Accelerator-Mass-Spectroscopy (AMS).

^{36}CL - dating routine

AMS measurements on the 6MV TANDEM were run at the LIP (Christl et al. 2013). Total Cl and 36Cl were measured from one target. Sample ratios of ^{35}Cl/^{36}Cl were normalized against the internal standard K382/4N (^{35}Cl/^{36}Cl = (17.36 ± 0.35) ×10-12) which is calibrated against KNSTD5000 (nominal ^{36}Cl/Cl ratio (5.00 ± 0.10)×10-12), (Phillips et al. 1991, 1996b, a; Sharma et al. 2000). Stable Chlorine was normalized against the natural ratio of ^{37}Cl/^{35}Cl=31.98%. Additionally, measured sample ^{35}Cl/^{36}Cl ratios were corrected for a chemical blank.

In addition to AMS measurements, main and trace element measurements were done to correct quantification of the ^{36}Cl production rate. These analyses were performed on the aliquots separated from the grain size fraction used in the AMS. For practical reasons, three composite samples per profile were grinded mixing two or three samples to obtain representative top, middle, and bottom composition. Main element analysis was performed using a handheld XRF in the Laboratory for Physical Geography at Freie Universität Berlin. Trace elements (U. Th, Gd, and Sm) were determined by high-resolution sector field ICP-MS at the German Research Center for Geoscience (GFZ) in Potsdam, Germany. Data results are summarized in Table S2/ Appendix III.

Table S2. Samples Chemical Composition: Main and trace element concentrations. Note that chemistry measurements were performed on amalgamated samples, given in comment.

Element	Mg	Al	Si	P	K	Ca	Ti	Mn	Fe	Sm	Gd	U	Th	Comment
Method	XRF									ICP-MS				
Unit	%	%	%	%	%	%	%	%	%	ppm	ppm	ppm	ppm	
TP-S 40	109,913	486,230	893,007	0.06520	109,913	2,222,683	0.00368	0.00044	0.07832	16,097	15,938	0.7280	17,185	TP-S High
TP-S 70	109,913	486,230	893,007	0.06520	109,913	2,222,683	0.00368	0.00044	0.07832	16,097	15,938	0.7280	17,185	TP-S High
TP-S 90	115,647	532,361	695,362	0.06781	115,647	2,412,557	0.00372	0.00033	0.08550	17,306	17,284	0.8444	19,755	TP-S Medium
TP-S 115	115,647	532,361	695,362	0.06781	115,647	2,412,557	0.00372	0.00033	0.08550	17,306	17,284	0.8444	19,755	TP-S Medium
TP-S 145	115,647	532,361	695,362	0.06781	115,647	2,412,557	0.00372	0.00033	0.08550	17,306	17,284	0.8444	19,755	TP-S Medium
TP-S 175	130,246	537,905	470,324	0.06702	130,246	2,678,605	0.00209	0.00013	0.04952	11,693	12,295	0.6957	11,419	TP-S Low
TP-S 225	130,246	537,905	470,324	0.06702	130,246	2,678,605	0.00209	0.00013	0.04952	11,693	12,295	0.6957	11,419	TP-S Low
TP-N 50	145,943	517,178	257,382	0.08023	145,943	2,957,946	0.00086	0.00002	0.02393	0.5357	0.5494	0.6718	0.4183	TP-N High
TP-N 80	145,943	517,178	257,382	0.08023	145,943	2,957,946	0.00086	0.00002	0.02393	0.5357	0.5494	0.6718	0.4183	TP-N High
TP-N 105	143,199	532,603	269,655	0.07554	143,199	2,926,443	0.00147	0.00097	0.03727	0.7107	0.7499	0.7702	0.5672	TP-N Medium
TP-N 135	143,199	532,603	269,655	0.07554	143,199	2,926,443	0.00147	0.00097	0.03727	0.7107	0.7499	0.7702	0.5672	TP-N Medium
TP-N 180	139,396	483,805	289,289	0.07397	139,396	2,961,963	0.00118	0.00002	0.02264	0.5388	0.5823	0.7242	0.4315	TP-N Low
TP-N 225	139,396	483,805	289,289	0.07397	139,396	2,961,963	0.00118	0.00002	0.02264	0.5388	0.5823	0.7242	0.4315	TP-N Low

Tab. S2/Appendix III: Main and trace element composition of the TCN samples.

Monte Carlo (MC) simulations

MC simulation was based on AMS-derived ^{36}Cl concentrations of the samples Accelerator-Mass-Spectroscopy (AMS) results for measured Cl isotope concentrations in all samples (Table S3/ Appendix III). Reported 1s uncertainties account for AMS reproducibility and counting statistics on concentrations), including depths and measurement uncertainty of the nuclide concentrations.

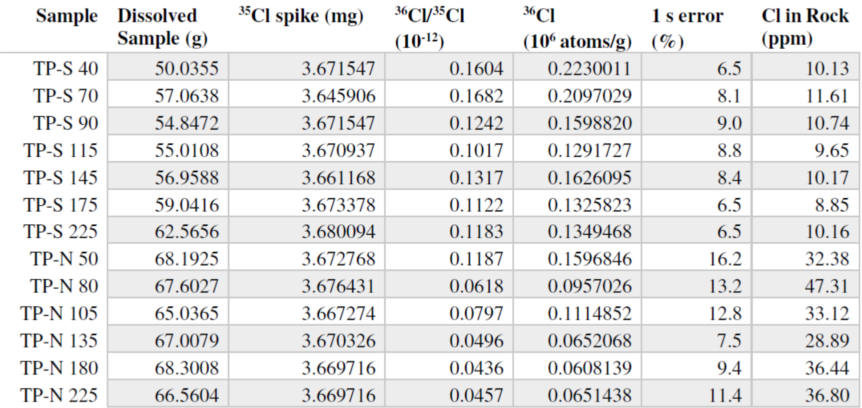

Sample	Dissolved Sample (g)	^{35}Cl spike (mg)	^{36}Cl/^{35}Cl (10^{-12})	^{36}Cl (10^{6} atoms/g)	1 s error (%)	Cl in Rock (ppm)
TP-S 40	50.0355	3.671547	0.1604	0.2230011	6.5	10.13
TP-S 70	57.0638	3.645906	0.1682	0.2097029	8.1	11.61
TP-S 90	54.8472	3.671547	0.1242	0.1598820	9.0	10.74
TP-S 115	55.0108	3.670937	0.1017	0.1291727	8.8	9.65
TP-S 145	56.9588	3.661168	0.1317	0.1626095	8.4	10.17
TP-S 175	59.0416	3.673378	0.1122	0.1325823	6.5	8.85
TP-S 225	62.5656	3.680094	0.1183	0.1349468	6.5	10.16
TP-N 50	68.1925	3.672768	0.1187	0.1596846	16.2	32.38
TP-N 80	67.6027	3.676431	0.0618	0.0957026	13.2	47.31
TP-N 105	65.0365	3.667274	0.0797	0.1114852	12.8	33.12
TP-N 135	67.0079	3.670326	0.0496	0.0652068	7.5	28.89
TP-N 180	68.3008	3.669716	0.0436	0.0608139	9.4	36.44
TP-N 225	66.5604	3.669716	0.0457	0.0651438	11.4	36.80

Tab. S3/Appendix III: Accelerator-Mass-Spectroscopy (AMS) results for measured Cl isotope concentrations in all samples. Reported 1s uncertainties account for AMS reproducibility and counting statistics on concentrations.

Uncertainty of the depth and thickness of the sampled sections is not propagated in the calculation. The authors of the model argue that systematic error in-depth measurement does not significantly alter the results (Hidy et al. 2010). Additionally, the XRF, respectively ICP-MS derived main and trace element data (Table S2/Appendix III), was used to account for the different production pathways of ^{36}Cl. These include high-energy neutrons, fast and negative muons, and thermal and epithermal neutrons (Alfimov and Ivy-Ochs 2009; Mair et al. 2019). Parameters regarding chlorine production were taken over from Mair et al. (2019), who used values for spallogenic production rates and epithermal production by Marrero et al. (2016), following Gosse and Philips (2001).

Topographic shielding was calculated following equations developed by Dunne et al. (1999) and using Topotoolbox 2 for MATLAB (Schwanghart and Scherler 2014) based on the 30 m 1 arc second SRTM digital elevation model (NASA JPL 2013). No correction for snow cover was applied, and the default value of 1 was used, as at the low elevation (280 m a.sl.) of the basin, no significant snow cover can be expected. A correction factor of 0.9539 was used by Çiner et al. (2019) for a nearby high elevation mountainous region (1300 m a.s.l.) and influenced ^{36}Cl exposure dating by less than 10%. The bulk density was not measured in situ but conservatively estimated to lie between 1.6 and 2.3, representing solid limestone and limestone with 35 % pore space. In order to avoid constraining the data with a wrong density estimate, an extensive range of values was tested. The production rate was scaled for the local conditions by using the scaling scheme of Lal (1991) and Stone (2000). Calculation of the muongenic production was fit into a depth of 4 m, per default assuming a density of 2.7g/cm3. As the used density is smaller than this, the muon fit is deeper than 4 m (Hidy et al. 2010). The upper limit for the depth profiles inheritance is constrained by the ^{36}Cl concentration of the lowermost sample in each profile.

The MC-simulation was then run until 106 solutions within the modal value of TP-P and TP-N confidence interval of the measured ^{36}Cl concentrations were achieved. The aim of this was to explore the possible range of parameters needed to find a solution so this range can be introduced into the MC simulation. Input parameters using for the MC modelling are reported in Table S4/Appendix III.

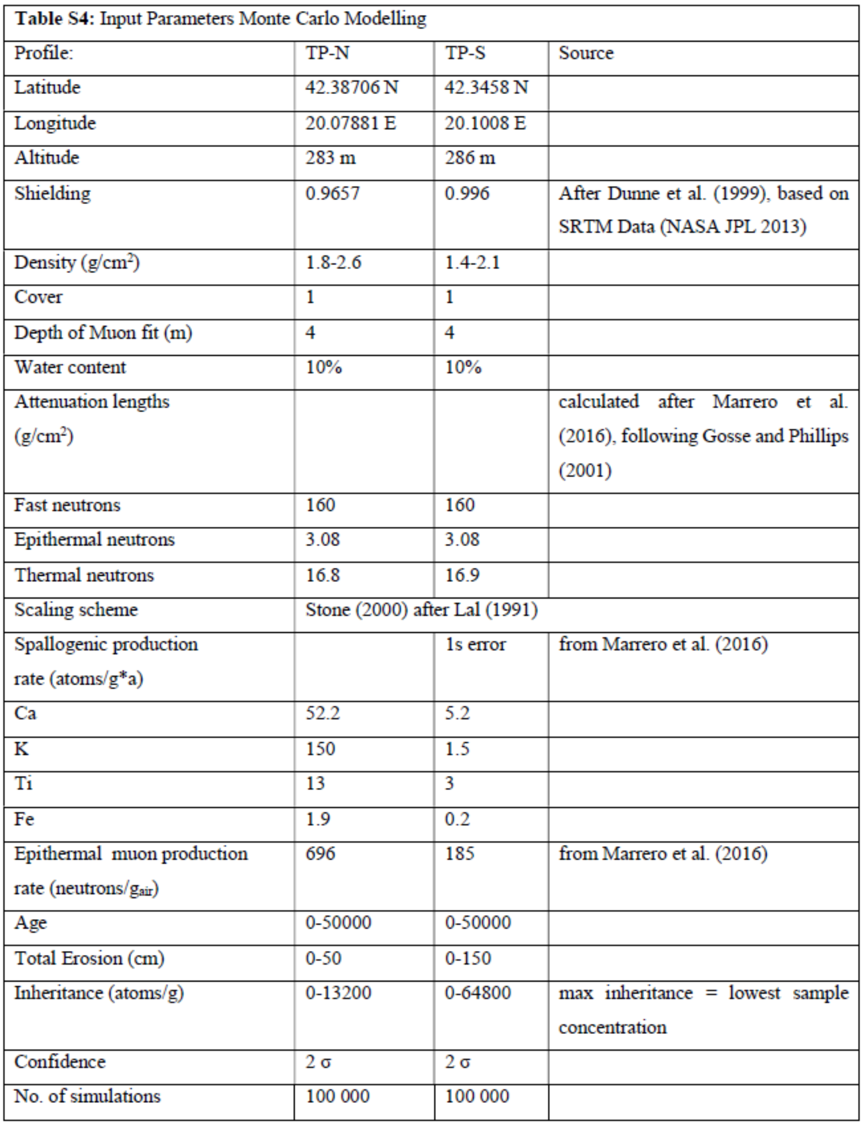

Table S4: Input Parameters Monte Carlo Modelling

Profile:	TP-N	TP-S	Source
Latitude	42.38706 N	42.3458 N	
Longitude	20.07881 E	20.1008 E	
Altitude	283 m	286 m	
Shielding	0.9657	0.996	After Dunne et al. (1999), based on SRTM Data (NASA JPL 2013)
Density (g/cm^2)	1.8-2.6	1.4-2.1	
Cover	1	1	
Depth of Muon fit (m)	4	4	
Water content	10%	10%	
Attenuation lengths (g/cm^2)			calculated after Marrero et al. (2016), following Gosse and Phillips (2001)
Fast neutrons	160	160	
Epithermal neutrons	3.08	3.08	
Thermal neutrons	16.8	16.9	
Scaling scheme	Stone (2000) after Lal (1991)		
Spallogenic production rate (atoms/g*a)		1s error	from Marrero et al. (2016)
Ca	52.2	5.2	
K	150	1.5	
Ti	13	3	
Fe	1.9	0.2	
Epithermal muon production rate (neutrons/g_{air})	696	185	from Marrero et al. (2016)
Age	0-50000	0-50000	
Total Erosion (cm)	0-50	0-150	
Inheritance (atoms/g)	0-13200	0-64800	max inheritance = lowest sample concentration
Confidence	2 σ	2 σ	
No. of simulations	100 000	100 000	

Tab. S4/Appendix III: Input parameters Monte Carlo modelling

Topographic Analysis

The DEMs files were clipped and converted in WGS 1984 UTM Zone 34 N and preprocessed to remove errors contained in the DEM to compute an elevation map in QGIS software (QGis 3.4.5 software, downloaded from https://qgis.org/de/site/). The swath width was fixed to 20 km with 200 parallel profiles separated by a distance of 100 m. We computed the mean elevation, describing the averaged topography between adjacent swath profiles, together with the minimum and maximum elevations describing the lateral variation of the topography perpendicular to the swath profile. The difference between the minimum, valley bottoms, and maximum elevations provide an estimate of the relief.

Fluvial Channels Analysis - K_{sn}

K_{sn} analysis was compared with available regional scale tectonic information. Figure S1/Appendix III shows the tectonic map modified by (Schmid et al. 2008) of the study area overlapped with normalized channel steepness indexes (K_{sn}). Figure S2 shows the knickpoint locations and the normalized channel steepness compared to (1) a geological map of the area (simplified Geological Map of Albania by Xhomo et al. (2002)) and (2) the extent of glaciation in the Albanian Alps, as reconstructed by Milivojević et al. (2008). Ksn values are positively correlated with more erosion-resistant lithologies. All segments with k_{sn} over 400 occur in the limestone domain (Figure S2/Appendix III top), while the shale, although at the same elevation, features less steep channels. All computed knickpoints are located in the limestone, suggesting a relationship between joints in the massive limestone banks and large steps in the river profile. Paleo glacial influence on knickpoint formation can be extrapolated in Figure S2/Appendix III below where extent of present day and LGM glaciers are displayed. Rivers crossing the SPNF are steep, but it is not possible to assign this to either active fault slip on the SPNF or the drastic change in relief and lithology created by the fault at some point in the past.

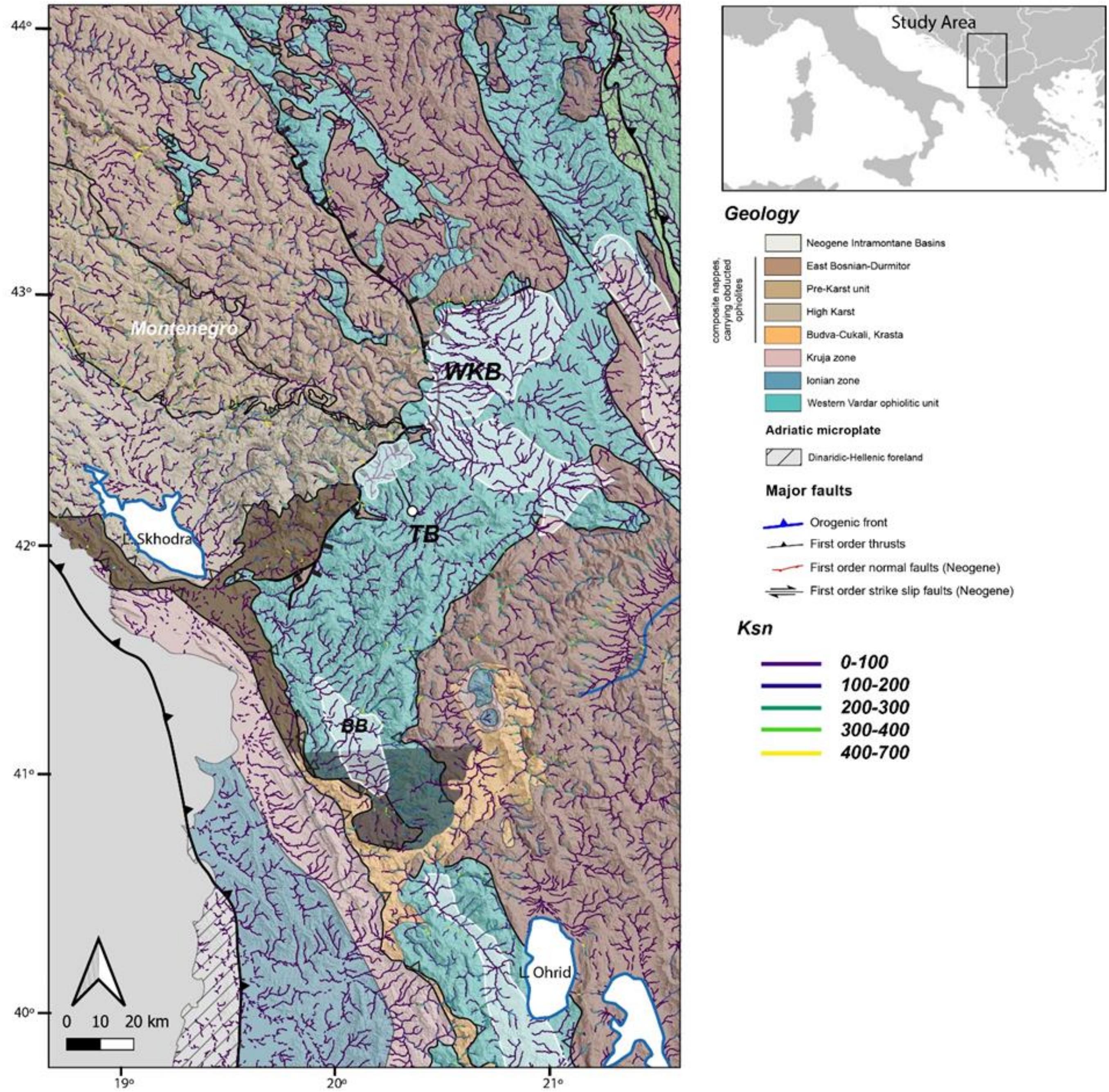

Fig. S1/Appendix III: Tectonic map of the study area with streams color-coded according to normalized channel steepness values (K_{sn}).

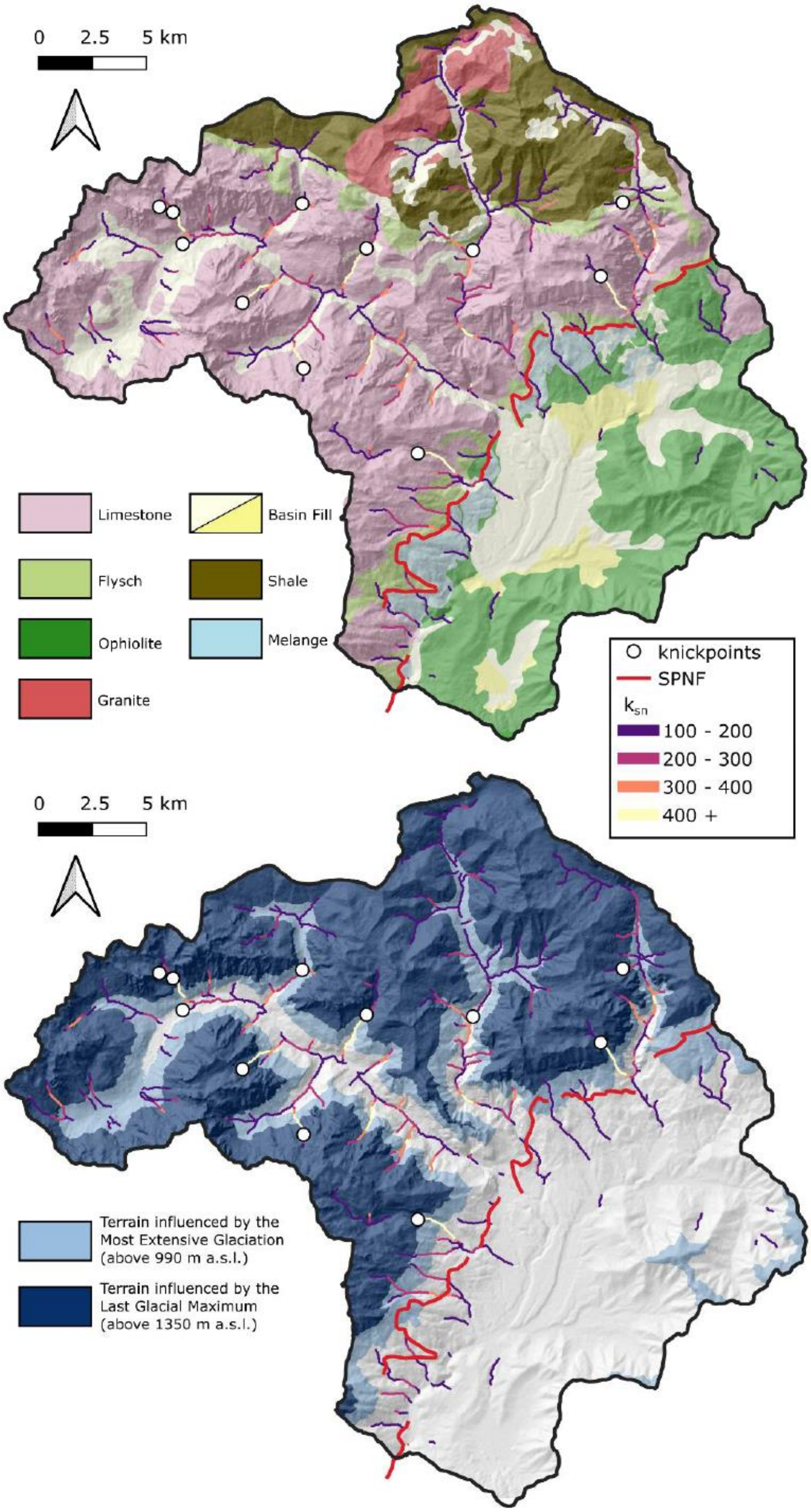

Fig. S2/Appendix III: Location of knickpoints in the study area and reaches with normalized steepness Ksn above 100. Top: Simplified geological map after Xhomo et al. (2002). Bottom: The lowest extent of glacial influence during the Most Extensive Glaciation (approx. 350 ka; above 990 m) and the LGM (22 ka; above 1350 m) as reconstructed by (Milivojević et al. 2008). Modified from Mittelbach (2020).

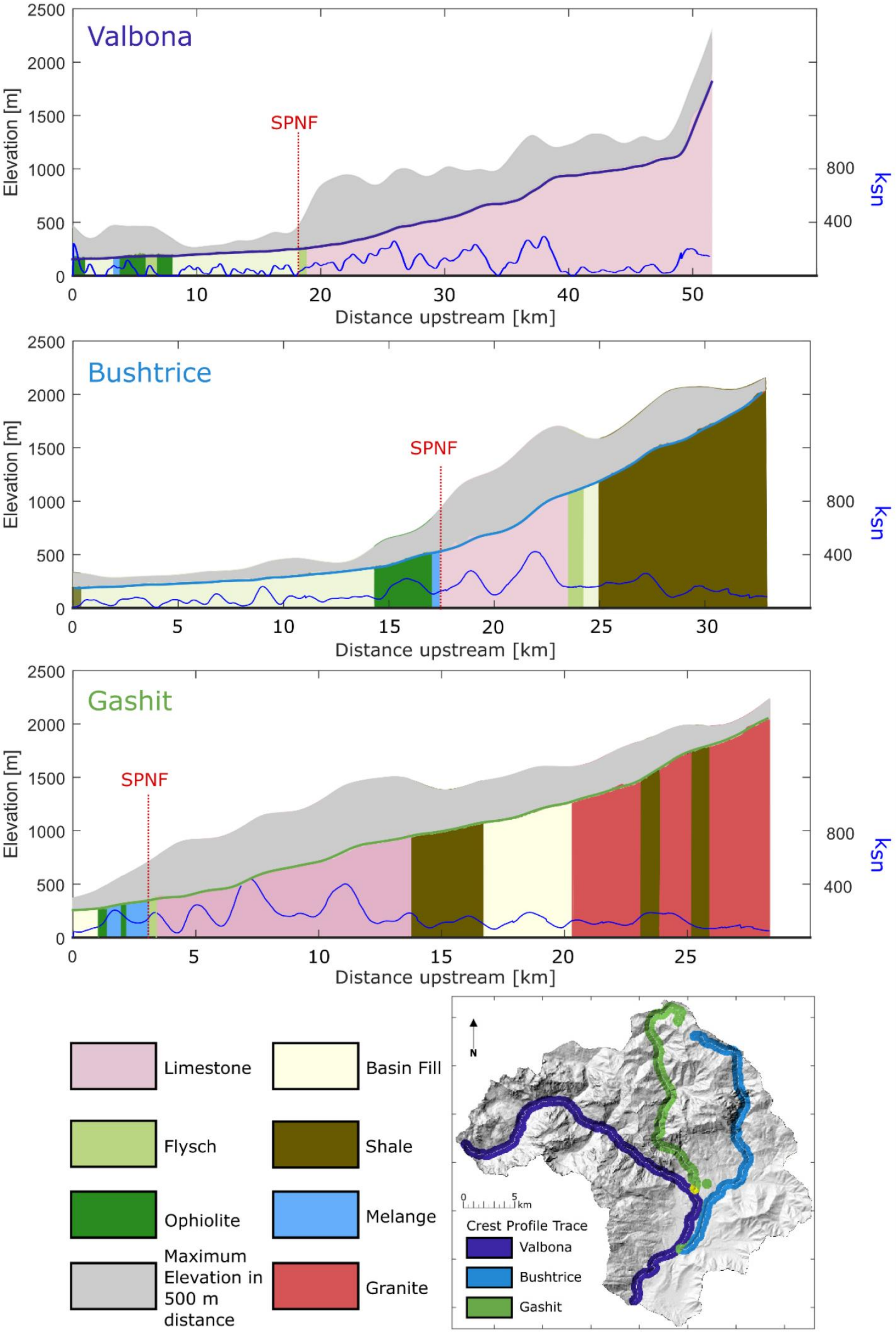

Fig. S3/Appendix III: Longitudinal river profiles and crest profiles of the highest elevation within 500 m orthogonally away into both directions from the river. Bedrock geology (Xhomo et al., 2002) along the stream. Blue line gives normalized channel steepness k_{sn} along stream. Modified from Mittelbach (2020).

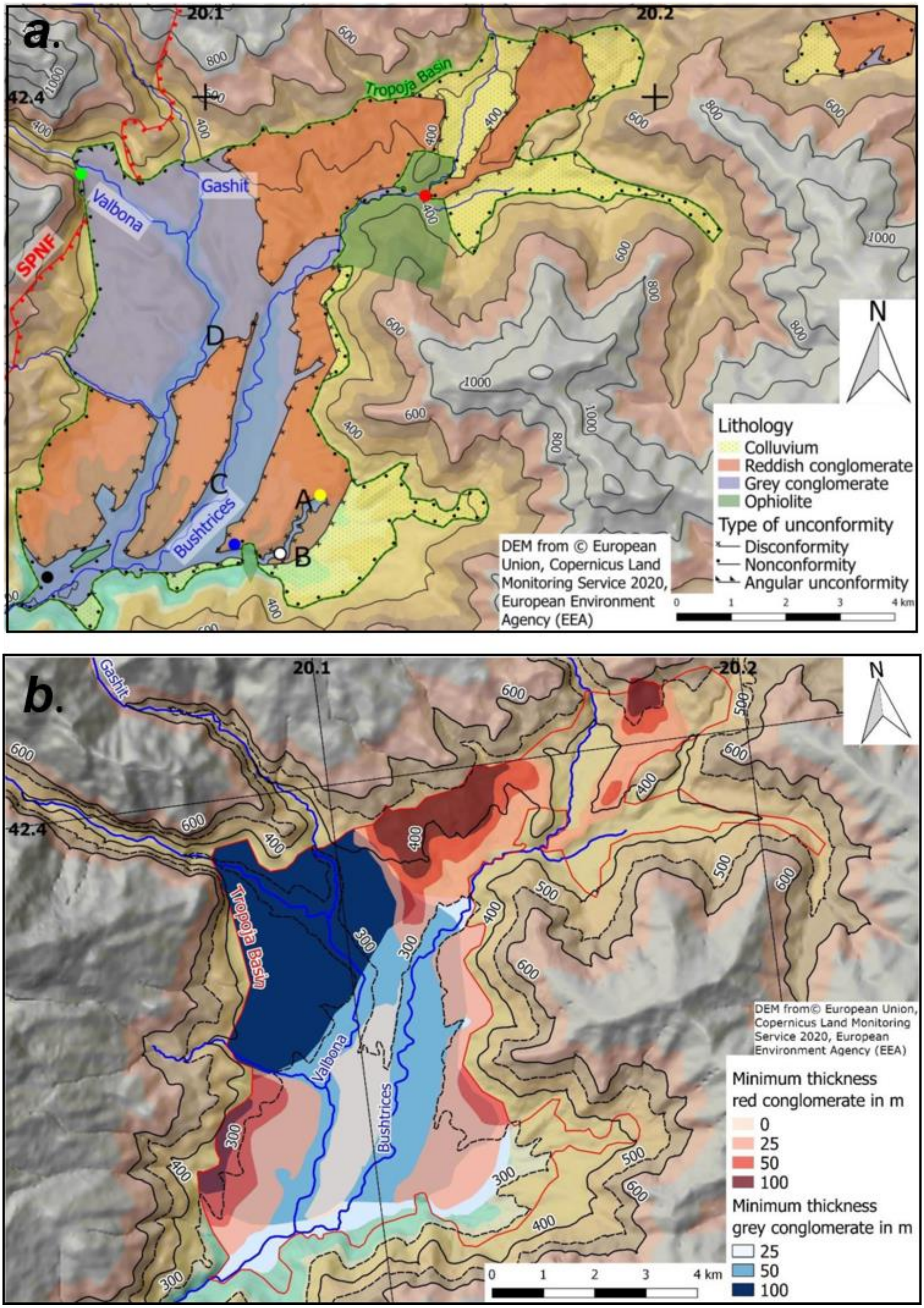

Fig. S4/Appendix III: A) Lithological contacts between the three units mapped in the TB. B) Minimum thickness of Unit 1 and Unit 2 here described as red conglomerate and grey conglomerate, from Simon (2021).

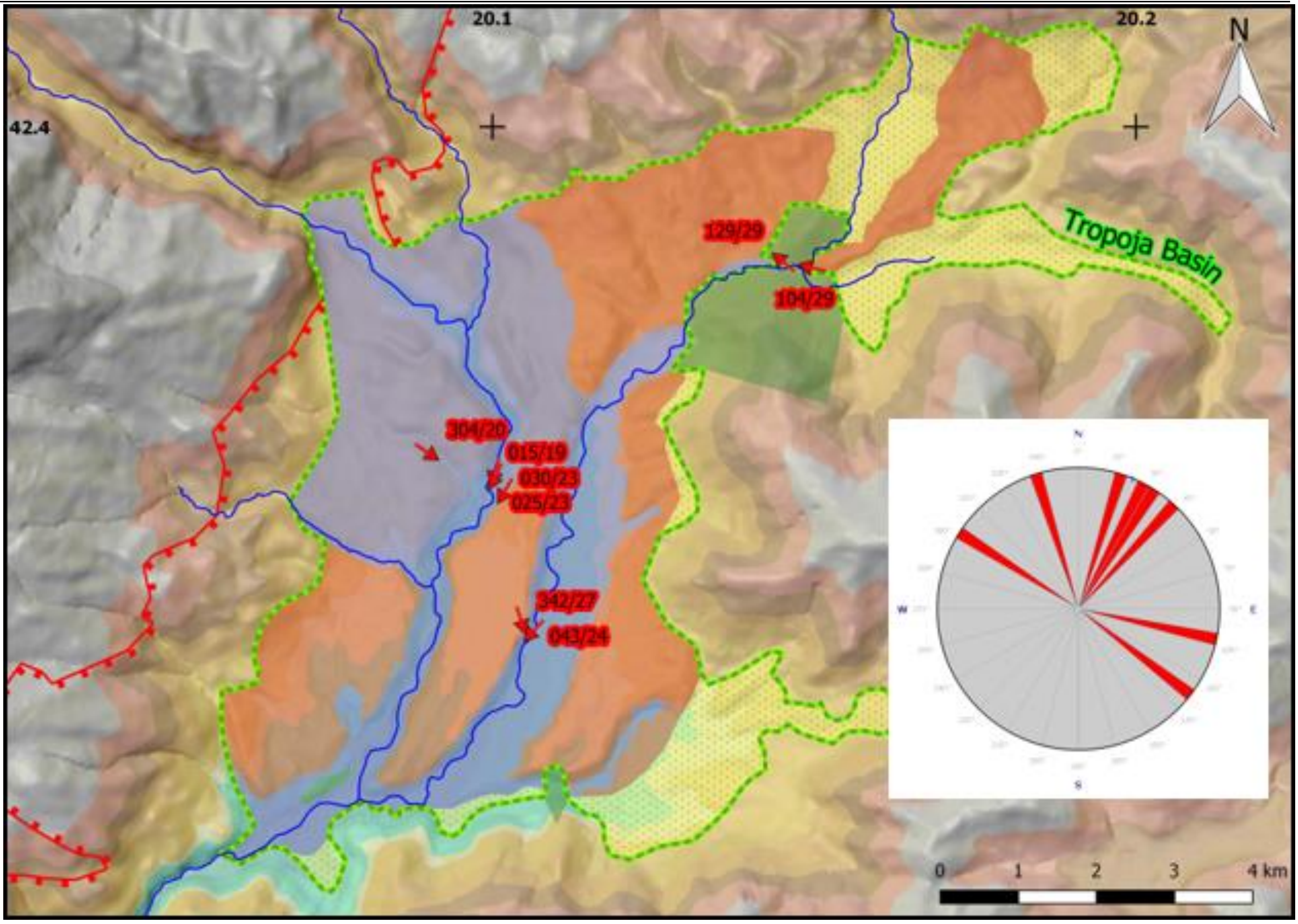

Fig. S5/Appendix III: Lithological distribution of TB sedimentary units and equal-area plot showing paleocurrent directions measured in the carbonatic pebbles of the carbonatic conglomerates (Unit 2). Red arrows indicate the mean of dip/dip dir. of the total measurement at each location. Lithologies are described in Figure S4a/Appendix III.